Arcady Zhukov Editor

High Performance Soft Magnetic Materials



Springer Series in Materials Science

Volume 252

Series editors

Robert Hull, Charlottesville, USA Chennupati Jagadish, Canberra, Australia Yoshiyuki Kawazoe, Sendai, Japan Richard M. Osgood, New York, USA Jürgen Parisi, Oldenburg, Germany Tae-Yeon Seong, Seoul, Korea, Republic of Shin-ichi Uchida, Tokyo, Japan Zhiming M. Wang, Chengdu, China The Springer Series in Materials Science covers the complete spectrum of materials physics, including fundamental principles, physical properties, materials theory and design. Recognizing the increasing importance of materials science in future device technologies, the book titles in this series reflect the state-of-the-art in understanding and controlling the structure and properties of all important classes of materials.

More information about this series at http://www.springer.com/series/856

Arcady Zhukov Editor

High Performance Soft Magnetic Materials



Editor
Arcady Zhukov
Basque Country University
San Sebastian, Spain

ISSN 0933-033X ISSN 2196-2812 (electronic) Springer Series in Materials Science ISBN 978-3-319-49705-1 ISBN 978-3-319-49707-5 (eBook) DOI 10.1007/978-3-319-49707-5

Library of Congress Control Number: 2016962022

© Springer International Publishing AG 2017

This work is subject to copyright. All rights are reserved by the Publisher, whether the whole or part of the material is concerned, specifically the rights of translation, reprinting, reuse of illustrations, recitation, broadcasting, reproduction on microfilms or in any other physical way, and transmission or information storage and retrieval, electronic adaptation, computer software, or by similar or dissimilar methodology now known or hereafter developed.

The use of general descriptive names, registered names, trademarks, service marks, etc. in this publication does not imply, even in the absence of a specific statement, that such names are exempt from the relevant protective laws and regulations and therefore free for general use.

The publisher, the authors and the editors are safe to assume that the advice and information in this book are believed to be true and accurate at the date of publication. Neither the publisher nor the authors or the editors give a warranty, express or implied, with respect to the material contained herein or for any errors or omissions that may have been made.

Printed on acid-free paper

This Springer imprint is published by Springer Nature
The registered company is Springer International Publishing AG
The registered company address is: Gewerbestrasse 11, 6330 Cham, Switzerland

Preface

Recent technological advances have been greatly affected by the development of advanced functional materials with improved physical properties. Advanced soft magnetic materials represent a key and fruitful area of research for functional materials. Many industrial sectors, such as magnetic sensors, microelectronics, security, automobiles, medicine, aerospace, energy harvesting and conversion, informatics, electrical engineering, magnetic recording, and medicine, demand magnetically soft materials with tuneable magnetic properties. These soft materials feature enhanced magnetic softness, giant magnetoimpedance effect, magnetic bistability, or inductive heating properties. Additionally, the miniaturization of modern magnetoelectronic devices tends to stimulate rapid development of soft magnetic materials with reduced dimensionality. Consequently the development of novel soft magnetic materials in the form of ribbons, wires, microwires, and multilayered thin films has gained significant attention of the scientific community.

In the area of soft magnetic materials, the discovery of the so-called giant magnetoimpedance effect in these materials makes them very attractive for a wide range of high-performance sensor applications for use in engineering, magnetic sensors, industry, and biomedicine. On the other hand, amorphous magnetic wires present magnetically bistable characteristics associated with a large Barkhausen jump. The magnetization reversal of these microwires runs through the quite fast domain wall (DW) propagation. Engineering of domain wall (DW) dynamics in nano- and microwires has become a challenge for fundamental physics and technological applications related to magnetic recording and magnetic sensors.

Therefore progress in the development of soft magnetic materials with low dimensionality, like ribbons, films, or wires, has drawn significant industry attention.

In all of these cases, a comprehensive understanding of the processing-structure—property relationship is of critical importance. Consequently, great efforts have been and continue to be focused on the origins of materials properties and on the prediction of novel, unusual macroscopic properties based on nano- and microstructures.

vi Preface

The present book on soft magnets was inspired by the recent progress in the development of novel soft magnetic materials including amorphous, nanocrystal-line, and nanostructured materials with improved magnetic and magneto-transport properties suitable for applications in various industrial sectors as well as in prospective applications.

The expert chapters from leading researchers from around the world cover a wide range of experimental and theoretical work highlighting the following main topics:

- · Soft magnetic materials
- · Amorphous and nanocrystalline magnetic materials
- · Tailoring of soft magnetic properties
- · Tuneable composites
- · Applications

The aim throughout is to provide the latest advances on recent developments in the field of soft magnetic materials paying particular attention to the tailoring of soft magnetic materials and optimization of their properties for industrial applications.

I hope that this publication will stimulate further interest in soft magnetic materials research. Last but not least, I would like to acknowledge all the contributing authors for their invaluable time, great contributions, and assistance with this book. Without such efforts we would not be able to accomplish and bring this special volume to the interested readers.

San Sebastian, Spain

Arcady Zhukov

Contents

1	Optimization of Soft Magnetic Properties	1
2	Tailoring of Soft Magnetic Properties and High Frequency Giant Magnetoimpedance in Amorphous Ribbons L. González-Legarreta, V.M. Prida, A. Talaat, M. Ipatov, V. Zhukova, Arcady Zhukov, LI. Escoda, J.J. Suñol, J. González, and B. Hernando	33
3	Melt Extracted Microwires	53
4	Giant Magneto-Impedance Effect in Amorphous Ferromagnetic Microwire with a Weak Helical Anisotropy N.A. Usov and S.A. Gudoshnikov	91
5	Tunable Magnetic Anisotropy and Magnetization Reversal in Microwires	111
6	Tunable Electric Polarization of Magnetic Microwires for Sensing Applications	131
7	Soft Ferromagnetic Microwires with Excellent Inductive Heating Properties for Clinical Hyperthermia Applications Rupin Singh, Javier Alonso, Jagannath Devkota, and Manh-Huong Phan	151

viii Contents

8	Magnetically Bistable Microwires: Properties and Applications	
	for Magnetic Field, Temperature, and Stress Sensing	169
	Rastislav Varga, Peter Klein, Rudolf Sabol, Kornel Richter,	
	Radovan Hudak, Irenej Polaček, Dušan Praslicka,	
	Miroslav Šmelko, Jozef Hudak, Ivan Mikita,	
	Giovanni Andrea Badini-Confalonieri,	
	Rhimou El Kammouni, and Manuel Vazquez	
In	ndex	213

Contributors

Javier Alonso Department of Physics, University of South Florida, Tampa, FL, USA

BCMaterials Edificio No. 500, Parque Tecnológico de Vizcaya, Derio, Spain

Giovanni Andrea Badini-Confalonieri Instituto de Ciencia de Materiales de Madrid, CSIC, Cantoblanco, Madrid, Spain

- **J.M. Blanco** Departamento de Física Aplicada, EUPDS, Basque Country University, UPV/EHU San Sebastian Spain, Bilbao, Spain
- **A.** Chizhik Departmento Facultad de Quimica, Universidad del País Vasco UPV/EHU, San Sebastian, Spain

Jagannath Devkota Department of Physics, University of South Florida, Tampa, FL, USA

Abdukarim Dzhumazoda National University of Science and Technology, MISIS, Moscow, Russian Federation

Rhimou El Kammouni Instituto de Ciencia de Materiales de Madrid, CSIC, Cantoblanco, Madrid, Spain

- LI. Escoda Girona University, Girona, Spain
- **J. González** Department of Materials Physics, University of the Basque Country, San Sebastián, Spain
- **L. González-Legarreta** Department of Physics, University of Oviedo, Oviedo, Spain
- **J. Gonzalez** Departmento Facultad de Quimica, Universidad del País Vasco UPV/EHU, San Sebastian, Spain

x Contributors

S.A. Gudoshnikov National University of Science and Technology "MISIS", Moscow, Russia

Pushkov Institute of Terrestrial Magnetism, Ionosphere and Radio Wave Propagation, Russian Academy of Sciences, IZMIRAN, Troitsk, Moscow, Russia

B. Hernando Department of Physics, University of Oviedo, Oviedo, Spain

Jozef Hudak Department of Aviation Technical Studies, Faculty of Aeronautics, Technical University of Košice, Košice, Slovakia

Radovan Hudak Department of Biomedical Engineering and Measurement, Faculty of Mechanical Engineering, Technical University of Košice, Košice, Slovakia

M. Ipatov Department of Material Physics, Basque Country University, UPV/EHU, San Sebastian, Spain

Departamento de Física Aplicada, EUPDS, Basque Country University, UPV/EHU San Sebastian Spain, Bilbao, Spain

Peter Klein Faculty of Science, Institute of Physics, UPJS, Košice, Slovakia

RVmagnetics s.r.o., Kosice, Slovakia

Dmitriy P. Makhnovskiy Robat Ltd., Macclesfield, UK

Ivan Mikita Department of Aviation Technical Studies, Faculty of Aeronautics, Technical University of Košice, Košice, Slovakia

Larissa V. Panina National University of Science and Technology, MISIS, Moscow, Russian Federation

Institute for Design Problems in Microelectronics, Moscow, Russian Federation

H.X. Peng Institute for Composites Science Innovation (InCSI), School of Materials Science and Engineering, Zhejiang University, Hangzhou, China

Manh-Huong Phan Department of Physics, University of South Florida, Tampa, FL, USA

Svetlana V. Podgornaya National University of Science and Technology, MISIS, Moscow, Russian Federation

Irenej Polaček Department of Biomedical Engineering and Measurement, Faculty of Mechanical Engineering, Technical University of Košice, Košice, Slovakia

Dušan Praslicka Department of Aviation Technical Studies, Faculty of Aeronautics, Technical University of Košice, Košice, Slovakia

V.M. Prida Department of Physics, University of Oviedo, Oviedo, Spain

Contributors xi

F.X. Qin Institute for Composites Science Innovation (InCSI), School of Materials Science and Engineering, Zhejiang University, Hangzhou, China

Kornel Richter Faculty of Science, Institute of Physics, UPJS, Košice, Slovakia

Rudolf Sabol Faculty of Science, Institute of Physics, UPJS, Košice, Slovakia

RVmagnetics s.r.o., Kosice, Slovakia

Rupin Singh Department of Physics, University of South Florida, Tampa, FL, USA

Miroslav Šmelko Department of Aviation Technical Studies, Faculty of Aeronautics, Technical University of Košice, Košice, Slovakia

A. Stupakiewicz Laboratory of Magnetism, University of Bialystok, Bialystok, Poland

J.J. Suñol Girona University, Girona, Spain

J.F. Sun School of Materials Science and Engineering, Harbin Institute of Technology, Harbin, China

A. Talaat Department of Material Physics, Basque Country University, UPV/EHU, San Sebastian, Spain

N.A. Usov National University of Science and Technology "MISIS", Moscow, Russia

Pushkov Institute of Terrestrial Magnetism, Ionosphere and Radio Wave Propagation, Russian Academy of Sciences, IZMIRAN, Troitsk, Moscow, Russia

Rastislav Varga Faculty of Science, Institute of Physics, UPJS, Košice, Slovakia RVmagnetics s.r.o., Kosice, Slovakia

Manuel Vazquez Instituto de Ciencia de Materiales de Madrid, CSIC, Cantoblanco, Madrid, Spain

H. Wang Institute for Composites Science Innovation (InCSI), School of Materials Science and Engineering, Zhejiang University, Hangzhou, China

Arcady Zhukov Department of Material Physics, Basque Country University, UPV/EHU, San Sebastian, Spain

Departamento de Física Aplicada, EUPDS, Basque Country University, UPV/EHU, San Sebastian, Spain

IKERBASQUE, Basque Foundation for Science, Bilbao, Spain

V. Zhukova Department of Material Physics, Basque Country University, UPV/EHU, San Sebastian, Spain

Departamento de Física Aplicada, EUPDS, Basque Country University, UPV/EHU San Sebastian Spain, Bilbao, Spain

Chapter 1 Amorphous and Nanocrystalline Glass-Coated Wires: Optimization of Soft Magnetic Properties

V. Zhukova, M. Ipatov, A. Talaat, J.M. Blanco, and Arcady Zhukov

1.1 Introduction

Soft magnetic wires presently considered as one of the most promising magnetic materials for industrial applications in various industrial sectors such as magnetic sensors, microelectronics, security and smart composites [1–7]. The main reason for this continuous interest is related to the possibility to obtain thin magnetic wires with extremely soft magnetic properties. Moreover magnetically soft microwire can also exhibit Giant Magnetoimpedance (GMI) effect that usually related to high circumferential magnetic permeability of magnetic wires [7–9]. Usually high magnetic permeability and GMI effect can be observed in magnetic wires with

V. Zhukova (☑) • M. Ipatov Department of Material Physics, Basque Country University, UPV/EHU, San Sebastian 20018, Spain

Departamento de Física Aplicada, EUPDS, Basque Country University, UPV/EHU, San Sebastian 20018, Spain e-mail: valentina.zhukova@ehu.eus

A. Talaat

Department of Material Physics, Basque Country University, UPV/EHU, San Sebastian 20018, Spain

J.M. Blanco

Departamento de Física Aplicada, EUPDS, Basque Country University, UPV/EHU, San Sebastian 20018, Spain

A. Zhukov

Department of Material Physics, Basque Country University, UPV/EHU, San Sebastian 20018, Spain

Departamento de Física Aplicada, EUPDS, Basque Country University, UPV/EHU, San Sebastian 20018, Spain

IKERBASQUE, Basque Foundation for Science, Bilbao, Spain

© Springer International Publishing AG 2017
A. Zhukov (ed.), *High Performance Soft Magnetic Materials*, Springer Series in Materials Science 252, DOI 10.1007/978-3-319-49707-5_1

1

vanishing magnetostriction coefficient [7–9]. Moreover amorphous character of magnetic wires prepared using rapidly quenching technique allows achievement of magnetic softness.

Phenomenologically the aforementioned GMI effect consists of large change of the impedance of magnetically soft conductor on applied magnetic field. GMI effect has been successfully explained in the terms of classical electrodynamics through the influence of magnetic field on penetration depth of electrical current flowing through the magnetically soft conductor [7-10].

Usually for characterization of the GMI effect the magneto impedance ratio, $\Delta Z/Z$, is used. The aforementioned GMI ratio, $\Delta Z/Z$, is defined as:

$$\Delta Z/Z = [Z(H) - Z(H_{\text{max}})]/Z(H_{\text{max}}),$$
 (1.1)

where H_{max} is the axial DC-field with maximum value up to few kA/m.

It is worth mentioning that, although discovery of the GMI effect has been attributed to first papers on amorphous wires where GMI effect has been described and explained [9, 10], the GMI effect has been described in 1930 in permalloy soft magnetic wire [7].

On the other hand, the other family of magnetic wires (basically with non-zero magnetostriction coefficient) can exhibit rectangular hysteresis loops. In this family of microwires the remagnetization process runs by the fast domain walls propagation along the wire [11–13]. Fast and controllable domain wall (DW) propagation in various families of magnetic wires has been proposed for quite promising applications in micro- and nanotechnology (magnetic memory, magnetic logic, magnetic TAGs, etc.) [14, 15].

In the case of glass-coated amorphous microwires exhibiting spontaneous magnetic bistability the DW propagation with a speed above 1 km/s can be easily achieved [11–13]. Therefore studies of DW dynamics in amorphous glass-coated microwires are quite important for understanding of the origin of fast DW propagation and ways to enhance the DW velocity in other materials.

Additionally a miniaturization of magnetic sensors allows reduction of the materials consumption and permits to find out new applications. Such trend in sensors miniaturization requires development of magnetic wires with reduced diameters [2, 3, 8].

Consequently studies of thin magnetically soft wires with enhanced magnetic softness, GMI effect and fast magnetization switching exhibiting rapid DW propagation attract attention during last two decades [8].

Up to know the thinnest magnetic wires are reported when utilizing the so-called Taylor–Ulitovsky method allowing preparation of glass-coated microwires with metallic nucleus diameters from 0.05 to 50 μm coated by glass with thickness ranging from 0.5 up to 30 μm [4]. The fabrication method essentially consists of the melting of the metallic alloy ingot inside the glass tube, forming the glass capillary and rapid quenching from the melt of the metallic nucleus completely coated by a glass [3, 16].

It is worth mentioning that although glass-coated microwires attracted interest during last two decades, the fabrication method is known along many years [17–21]. Initially the method for fabrication of glass-coated microwires has been introduced by Taylor [17]. Later it was modified by Ulitovsky. The modified method allowed preparation of long glass-coated microwires (the main modification was the introduction of the rotating bobbins that permitted to considerably enhance the length of glass-coated microwire). Initially this method has been developed for the preparation of Cu and Ag non-magnetic glass-coated microwires [17, 18]. Later few successful attempts of fabrication of Fe-based magnetic amorphous microwires have been reported in East Europe [19–21]. Thus considerable effect of annealing on hysteresis loop of FeP microwires and rectangular hysteresis loop in FeNiPB glass-coated microwires has been observed [22, 23].

The interest in thin magnetic wires was stimulated at the beginning of 1990 after reports on GMI effect in soft magnetic amorphous wires [9, 10] and proposed applications of the GMI effect in magnetic microsensors [6]. Consequently a number of papers on optimization of magnetic properties of glass-coated microwires have been published after 1995 [2–5, 24].

One of the features of the fabrication method is considerable difference of the thermal expansion coefficients of the glass and the metal results in appearance of considerable internal stresses [2–5, 16, 24]. These internal stresses considerably affect soft magnetic properties of amorphous materials [16]. Therefore in amorphous microwire (i.e. in the absence of magnetocrystalline anisotropy) the magnetoelastic anisotropy becomes the main factor that affects magnetic properties of glass-coated microwires.

The other important factor that affects soft magnetic properties of amorphous materials is the shape anisotropy. But in micrometric magnetic wires the influence of demagnetizing factor becomes negligible for the wire length below few mm.

Consequently, the main attention for engineering of magnetic properties of glass-coated microwires must be paid to the magnetoelastic anisotropy requires. The aforementioned magnetoelastic energy is essentially determined by the magnetostriction coefficient, λ_s and internal stresses, σ_i :

$$K_{\rm me} \approx 3/2\lambda_s\sigma_i,$$
 (1.2)

The magnetostriction constant depends mostly on the chemical composition and is vanishing in amorphous Fe–Co-based alloys with Co/Fe $\approx 70/5$ [25–27].

Consequently main possibilities to tailor magnetic properties of amorphous microwires are either internal stress or selection of the appropriate chemical composition of the metallic nucleus [16]. Internal stresses in principle can be modified by few different ways, i.e., by:

- · Heat treatment
- Chemical etching or mechanical removal of the glass coating or
- Controlling of the stresses through the modification of the ratio, ρ , between the metallic nucleus diameter, d and total microwire diameter, $D(\rho = d/D)$.

On the other hand, the alternative way of engineering of magnetic properties of magnetic microwires is controllable crystallization. It is well known that, the so-called nanocrystalline materials, i.e., two-phase materials consisting of nanosized crystallites embedded in an amorphous matrix can exhibit extremely soft magnetic properties.

Nanocrystalline magnetic materials are known 1988, when for the first time was reported that the presence of small additions of Cu and Nb in FeSiB-based alloys allows the obtaining of a two-phase material by the devitrification of the amorphous alloy after adequate annealing (i.e. at temperatures between the first and second crystallization processes) [28–30]. After first stage of crystallization, nanocrystalline material consists of small (around 10 nm) nanocrystallites embedded in the residual amorphous matrix.

Magnetic softness of nanocrystalline materials is thought to be originated by vanishing of the magnetocrystalline anisotropy (also known as a random anisotropy model) as well as by quite low magnetostriction constant of the two-phase materials when the grain size approaches 10 nm [29–31].

Recently successful attempts of improvement of magnetic softness and the GMI effect of thin magnetic wires by nanocrystallization of amorphous precursor have been reported [32–37].

In fact substitution of Co-rich amorphous microwires by less expensive Fe-rich microwires can be essentially promising from industrial application's point of view. Therefore, optimizing high GMI effect in Fe-rich glass-coated microwires is important from the viewpoint of the massive applications.

In this chapter we present our last results on optimization of GMI effect in amorphous and nanocrystalline glass-coated microwires.

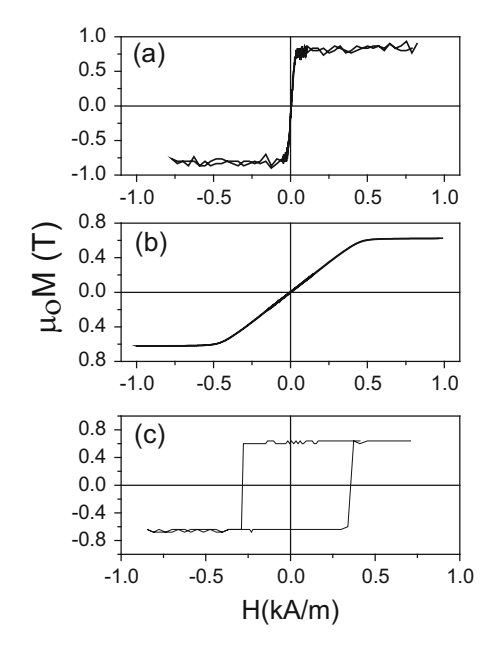
1.2 Engineering of Magnetic Properties and GMI Effect of Amorphous Microwires

Magnetic properties of glass-coated microwires essentially depend on chemical composition of the metallic nucleus [8]. The most drastic changes of the hysteresis loop have been reported for the $\text{Co}_x\text{Fe}_{1-x}$ ($0 \le x \le 1$) system [8, 24]. This compositional dependence is attributed to the change of the magnetostriction coefficient in the Co–Fe-based microwires [25–27]. As mentioned above in classical amorphous materials ($\text{Co}_x\text{Fe}_{1-x}$)₇₅Si₁₅B₁₀ the magnetostriction coefficient, λ_s , changes with x from -5×10^{-6} at x = 1, to $\lambda_s \approx 35 \times 10^{-6}$ at $x \approx 0.2$, achieving nearly zero values at Co/Fe about 70/5.

Consequently best soft magnetic properties are observed for nearly zero magnetostrictive Co-rich compositions (Co/Fe around 70/5).

On the other hand, microwires with Fe-rich metallic nucleus composition present rather different magnetic properties exhibiting rectangular hysteresis loops related with large and single Barkhausen jump.

Fig. 1.1 Hysteresis loop of amorphous Co-rich microwires with nearly zero magnetostriction (a) and negative magnetostriction (b) coefficients and Fe-rich microwire with positive magnetostriction (c)



In contrast to the Fe-rich glass-coated microwires presenting perfectly rectangular (usually also called as bistable) hysteresis loops, Co-rich amorphous microwires with negative magnetostriction coefficient exhibit nearly non-hysteretic behaviour [38]. In particular, hysteresis loops of magnetic microwires with nearly zero magnetostrictive compositions exhibit very low coercivities and quite large initial susceptibility [8].

Consequently generally magnetic properties and overall shape of hysteresis loops of amorphous microwires depend on composition of the metallic nucleus as well as on composition and thickness of the glass coating [39, 40, 41]. This can be illustrated by Fig. 1.1, where the hysteresis loops of three main groups of amorphous microwires (Fe-rich, Co-rich and Co-Fe-rich with positive, negative and vanishing magnetostriction constant, respectively) are shown.

Therefore the most common way for tailoring of the magnetic properties is the proper chemical composition selection.

But for further tuning of the properties the internal stresses can be taken into account.

As mentioned above, the internal stresses, σ_i , arising during simultaneous rapid quenching of metallic nucleus surrounding by the glass coating are the source of additionally magnetoelastic anisotropy. The strength of such internal stresses can be controlled by the ρ -ratio: strength of internal stresses increases decreasing ρ -ratio (i.e. increases with increasing of the glass volume) [40–43].

Consequently in each family of compositions the internal stresses influence is the other factor that affects the magnetic properties of microwires.

This influence is illustrated in Figs. 1.2 and 1.3.

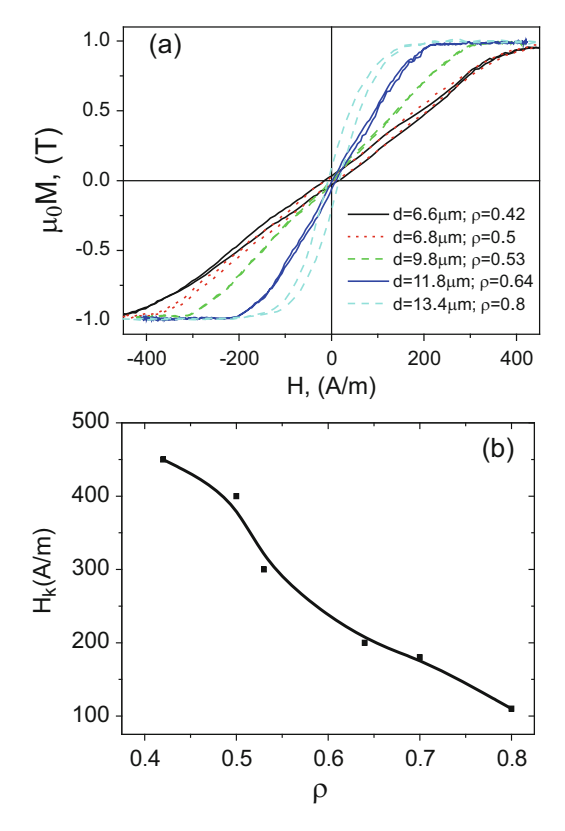


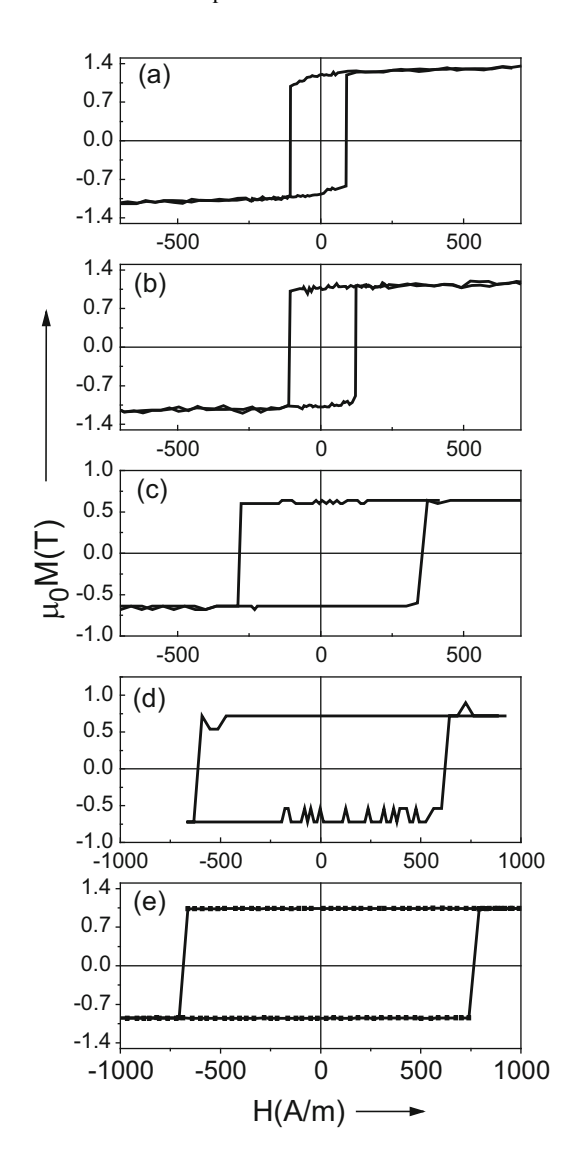
Fig. 1.2 Hysteresis loops of $Co_{67.1}Fe_{3.8}Ni_{1.4}Si_{14.5}B_{11.5}Mo_{1.7}$ microwires with different geometry (a) and dependence of H_k on ρ -ratio (b). Reprinted with permission from [45], A. Zhukov, M. Ipatov and V. Zhukova "Amorphous microwires with enhanced magnetic softness and GMI characteristics" EPJ Web of Conferences **29** 00052 (2012) DOI: 10.1051/ Owned by the authors, published by EDP Sciences, 2012 (Fig. 4)

Particularly the influence of the internal stresses on hysteresis loops of Co-rich (with vanishing λ_s -values) and Fe-rich (with positive λ_s -values) are shown in Figs. 1.2 and 1.3, where hysteresis loops of both families of microwires of the same chemical composition but with different ρ -ratios (different internal stresses) are shown.

The estimated values of the internal stresses in these glass-coated microwires arising from the difference in the thermal expansion coefficients of metallic nucleus and glass coating are of the order of 100–1000 MPa, depending strongly on the ρ -ratio [42–44], increasing with the glass coating thickness.

Such large internal stresses give rise to a drastic change of the magnetoelastic energy, K_{me} , given by Eq. (1.2) even for small changes of the glass-coating thickness at fixed metallic core diameter. Additionally, such a change of the ρ -

Fig. 1.3 Hysteresis loops of Fe-rich amorphous microwires with the same sample length and different metallic nucleus diameter d and total diameters D: Fe₇₀B₁₅Si₁₀C₅ microwires with $\rho = 0.63$; $d = 15 \, \mu m$ (a); $\rho = 0.48$; $d = 10.8 \, \mu \text{m}$ **(b)**; $\rho = 0.26$; $d = 6 \, \mu m$ **(c)**; $\rho = 0.16$; $d = 3 \, \mu \text{m}$ (**d**) and of Fe_{72.75}Co_{2.25}B₁₅Si₁₀ microwire with $\rho = 0.14$; $d \approx 1.4 \, \mu \text{m}$ (e). Reprinted with permission from [46]. Copyright (2012) SpringerOpen (Fig. 1)



ratio should be related to the change of the magnetostriction constant with stresses, σ (either applied or internal) [45, 46]:

$$\lambda_s = (\mu_o M_\sigma / 3)(d_\kappa / d\sigma) \tag{1.3}$$

where $\mu_o M_s$ is the saturation magnetization.

It is worth mentioning that residual stresses of glass-coated microwires arising during simultaneous solidification of metallic nucleus and glass coating, mostly have been estimated from the simulations of the process of simultaneous

solidification of metallic nucleus inside the glass tube [42–44] and experimental determination of such residual stresses is rather complex. In according to the simulation results these stresses present tensor character and the strongest stresses in most part of metallic nucleus value are the tensile stresses [42, 43].

Experimentally evidence of internal stresses is the dependence of hysteresis loops and particularly of magnetic properties (coercivity, remanent magnetization) on ρ -ratio [45, 46] as well as the applied stress dependence of the hysteresis loops [47–50] and effect of chemical etching of the glass on hysteresis loops [51, 52]. As can be appreciated from Fig. 1.3, considerable increasing of coercivity, H_c , and switching field, H_s , with decreasing of ρ -ratio is observed.

Direct confirmation of the magnetoelastic origin of observed changes of the hysteresis loops is the dependence of the measured effect of the switching field, H_s , on applied stresses, σ_a . Switching field, H_s , is defined as the field at which the large Barkhausen jump starts. It is worth mentioning that at low magnetic field amplitudes and frequencies the H_s is almost as same as coercivity, H_c . But the switching field, H_s , is usually almost independent on magnetic field amplitude, H_0 and frequency, f [53]. The difference between H_s and H_c was attributed to the DW dynamics, i.e., the time of domain wall propagation through the entire wire [54]. Therefore use of H_s for studying of stress dependence of hysteresis loops is more rigorous.

Similarly to the result presented in Fig. 1.3 a considerable and monotonic growth of H_s with σ_a is observed (Fig. 1.4). Consequently from comparison of Figs. 1.3 and 1.4 we can deduce that the internal stresses in glass-coated microwires are mostly of tensile origin and that the strength of internal stresses increase with ρ -ratio decreasing.

Similarly, after chemical etching of the glass coating we observed gradual changes of the hysteresis loop from almost unhysteretic and linear to almost rectangular in Co-rich microwires (Fig. 1.5).

Fig. 1.4 Effect of applied stresses on switching field of Fe₇₀B₁₅Si₁₀C₅ amorphous microwires with the different ρ -ratio: $\rho = 0.63$, d = 15 μm and $\rho = 0.48$, d = 10.8 μm. Reprinted with permission from [50]

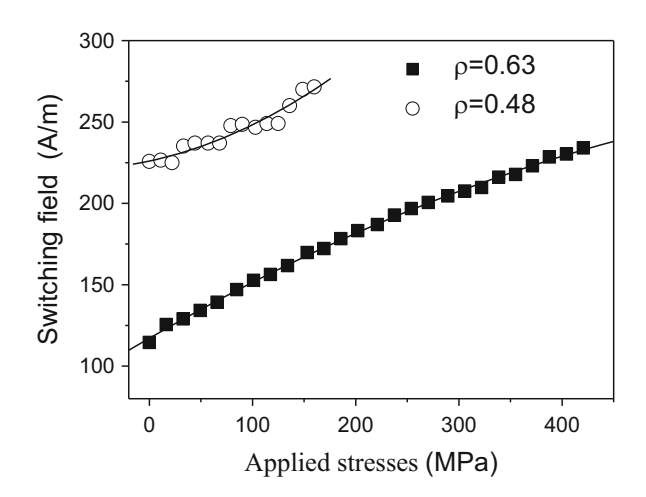
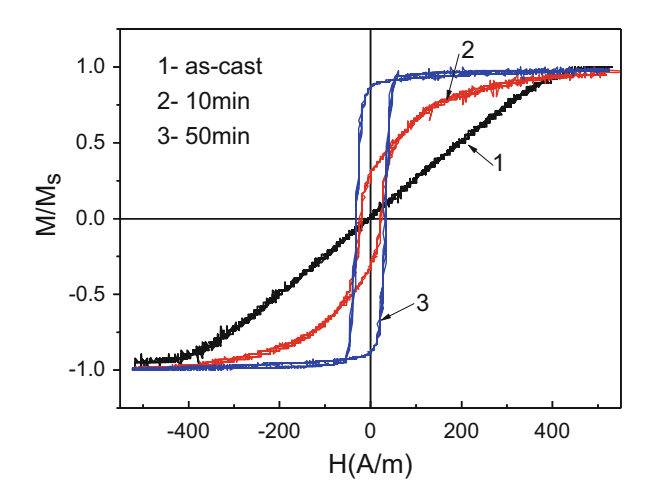


Fig. 1.5 Hysteresis loops of Co_{70.5}Mn_{4.5}Si₁₀B₁₅ microwire in the as-cast state (1) and chemically treated during 10 min (2) and 50 min (3)



Moreover quite recently we observed similar tendency after annealing of Co-rich microwires: annealing considerably affects magnetic properties of Co-rich microwires. Hysteresis loops becomes almost rectangular after annealing (see Fig. 1.6). As shown in Fig. 1.6 upon increasing the annealing time at fixed annealing temperature (250 °C in Fig. 1.6) the hysteresis loops become more and more rectangular. A similar tendency has been observed at different annealing temperatures [54, 55].

Consequently non-magnetic glass coating affects the hysteresis loops of ferromagnetic nucleus through the internal stresses induced by the glass coating inside the metallic nucleus.

Therefore, tailoring of the magnetoelastic energy, K_{me} , is essentially important for optimization of magnetic properties of glass-coated microwires [45–52].

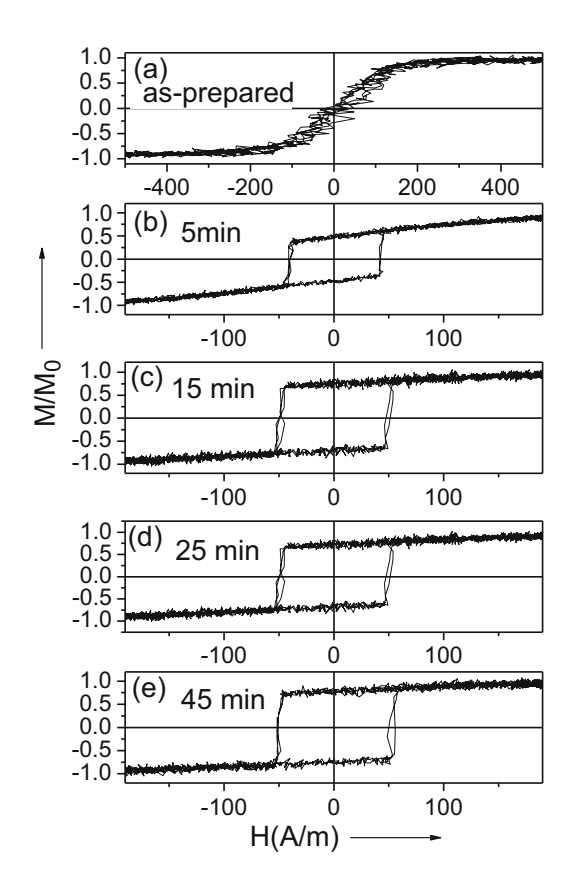
GMI effect is the highest in magnetically soft materials, i.e., in materials with high magnetic permeability. It is worth mentioning that the DC magnetic field dependence of GMI effect in magnetic materials with transverse magnetic anisotropy presents a maximum. The DC magnetic field that corresponds to the maximum GMI ratio, H_m , is attributed to the static magnetic anisotropy field, H_k . Consequently, there is close relation between the magnetic softness and magnetic field dependence of the GMI effect.

Moreover the parameter ρ must be considered as one of the factors that affect both soft magnetic properties and GMI of glass-coated microwires.

The influence of the ρ -ratio on GMI ratio and on $\Delta Z/Z$ magnetic field dependence is reported elsewhere [8, 41].

As can be appreciated, $\text{Co}_{67.1}\text{Fe}_{3.8}\text{Ni}_{1.4}\text{Si}_{14.5}\text{B}_{11.5}$ microwire with appropriate geometry and composition presents excellent magnetically soft properties with low coercivities (between 4 and 10 A/m, see Fig. 1.2) [8]. Magnetic anisotropy field, H_k , is found to be determined by the ρ -ratio, decreasing with ρ (Fig. 1.2b), as reported elsewhere [8, 41].

Fig. 1.6 Effect of annealing time on hysteresis loops of $Co_{69.2}Fe_{4.1}B_{11.8}Si_{13.8}C_{1.1}$ microwires annealed at $T_{ann} = 250$ °C. Reprinted with permission from [55], Fig. 6



Consequently, one can expect that the ρ -ratio must affect the GMI effect of studied samples.

Figure 1.7 presents results on magnetic field dependences of $\Delta Z/Z$ measured in $\text{Co}_{67.05}\text{Fe}_{3.85}\text{Ni}_{1.4}\text{B}_{11.33}\text{Si}_{14.47}\text{Mo}_{1.69}$ microwire samples with different ρ -ratios.

Indeed both maximum values of the GMI ratio, $\Delta Z/Z_m$, and the magnetic anisotropy field present considerable dependence on samples geometry. It is worth mentioning that for microwires with lowest glass coating thickness (largest ρ -ratio) $\Delta Z/Z_m \approx 600$ % has been observed [41].

Heat treatment is the usual way to relax the internal stresses. Therefore heat treatment is the other factor that considerably affects the GMI effect. As an example, the influence of current annealing on GMI ratio of Co-rich microwires is presented in Fig. 1.8. As can be seen from Fig. 1.8 after current annealing GMI ratio of Co₆₇Fe_{3.85}Ni_{1.45}B_{11.5}Si_{14.5}Mo_{1.7} microwire considerably increased [56].

On the other hand, heat treatment is not the method that always allows improvement of the GMI effect. Recently the influence of annealing on GMI effect of Co_{69.2}Fe_{4.1}B_{11.8}Si_{13.8}C_{1.1} microwires has been reported.

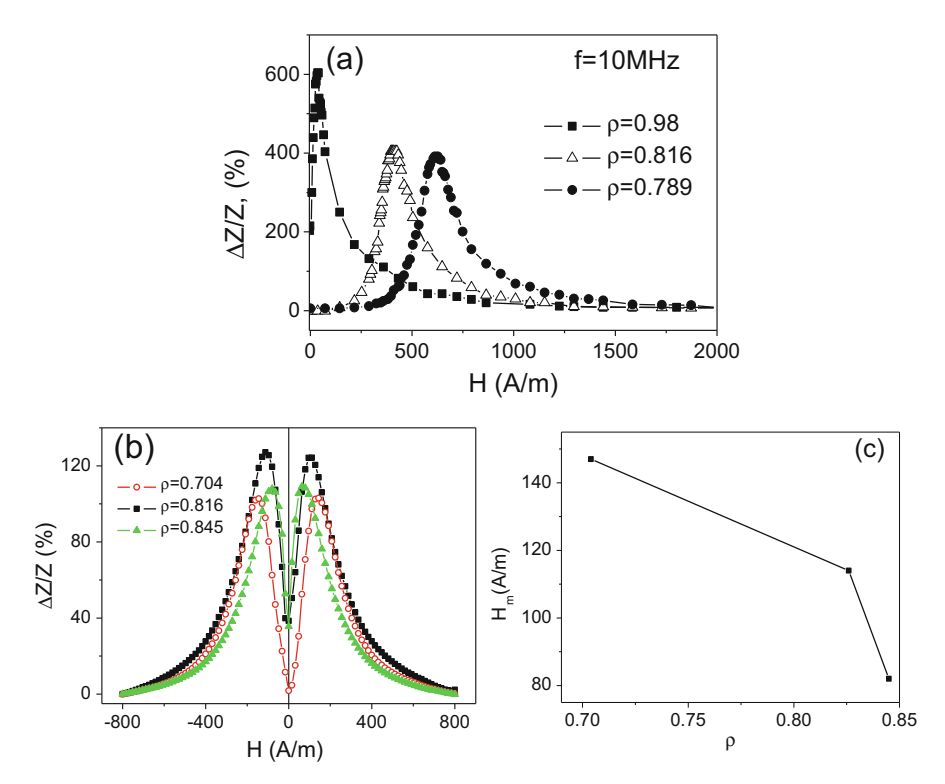


Fig. 1.7 Effect of ρ-ratio on GMI effect in $Co_{67.05}Fe_{3.85}Ni_{1.4}B_{11.33}Si_{14.47}Mo_{1.69}$ microwire samples with different ρ-ratios ((a), (b)) and dependence of field of maximums on ρ-ratio (c). Reprinted with permission from [41], V. Zhukova et al. "Optimization of Giant Magnetoimpedance in Co-Rich Amorphous Microwires" IEEE Trans. Magn., V 38, 5 part I, 2002 pp. 3090-3092. Copyright (2002) with permission from IEEE (Figure 4) and [7], A. Zhukov, M. Ipatov, M. Churyukanova, S. Kaloshkin, V. Zhukova, "Giant magnetoimpedance in thin amorphous wires: From manipulation of magnetic field dependence to industrial applications", J. Alloys Comp. 586 (2014) S279–S286. Copyright (2014) with permission from Elsevier (Figure 4a)

The aforementioned Co-rich microwires with low coercivity usually present high GMI effect. As an example, as-prepared $\text{Co}_{69.2}\text{Fe}_{4.1}\text{B}_{11.8}\text{Si}_{13.8}\text{C}_{1.1}$ amorphous microwires present soft magnetic behaviour with very low coercivity, H_c (about 8 A/m, see Fig. 1.9) and consequently high GMI ratio.

As mentioned above annealing considerably affects magnetic properties of studied samples: hysteresis loops becomes almost rectangular after annealing temperature (see Fig. 1.6).

GMI effect has been measured in as-prepared and annealed at 300 °C for 5 min $Co_{69.2}Fe_{4.1}B_{11.8}Si_{13.8}C_{1.1}$ samples. After annealing of $Co_{69.2}Fe_{4.1}B_{11.8}Si_{13.8}C_{1.1}$ microwire at this conditions present rectangular hysteresis loop but still with considerable magnetic permeability of the flat branches of the hysteresis loop (Fig. 1.10a). As can be appreciated from Fig. 1.10 the GMI ratio of annealed sample

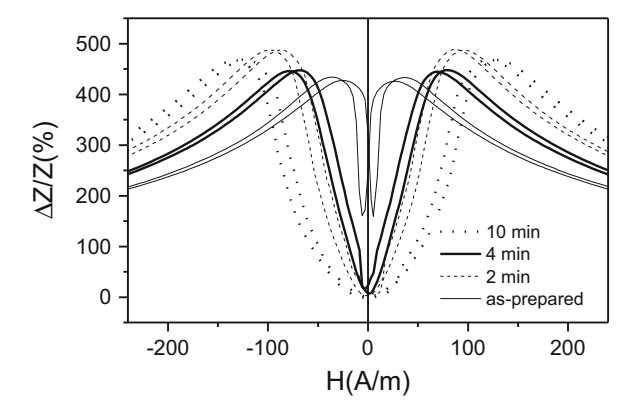


Fig. 1.8 $\Delta Z/Z(H)$ dependences of Co₆₇Fe_{3.85}Ni_{1.45}B_{11.5}Si_{14.5}Mo_{1.7} microwire measured at f=30 MHz and I=1 mA subjected to current annealing at 40 mA for different time. Reprinted with permission from [56], V. Zhukova, M. Ipatov, C. García, J. Gonzalez, J. M. Blanco and A. Zhukov, "Development of Ultra-Thin Glass-Coated Amorphous Microwires for High Frequency Magnetic Sensors Applications", *Open Materials Science Reviews*, I,(2007), pp.1-12

Fig. 1.9 Hysteresis loops (a) and $\Delta Z/Z(H)$ dependence (b) measured at 100 MHz in as-prepared $Co_{69.2}Fe_{4.1}B_{11.8}Si_{13.8}C_{1.1}$ microwire

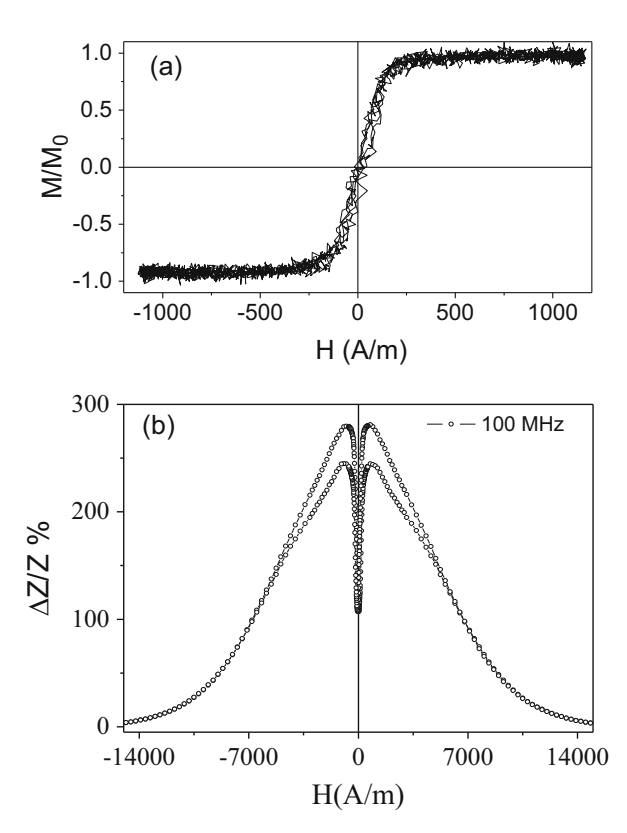
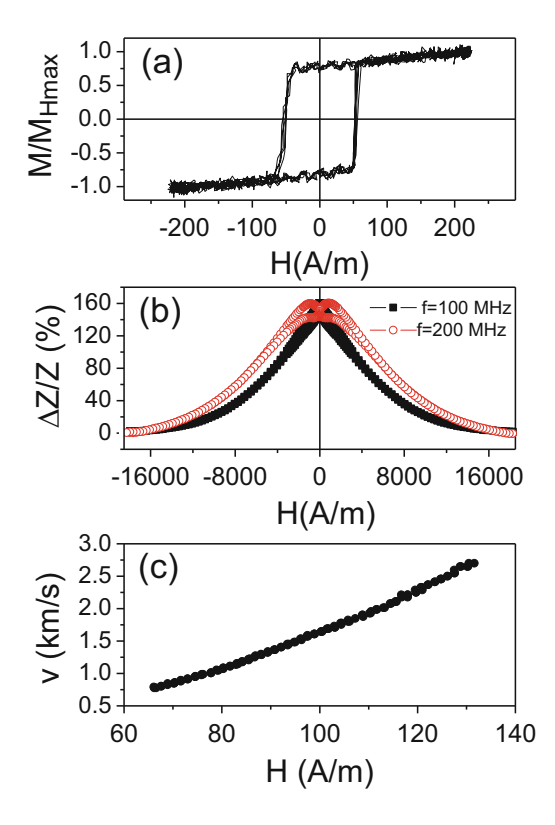


Fig. 1.10 Hysteresis loop (a) magnetic field dependence of the GMI ratio (b) and v(H)dependence (a) measured in of annealed at 300 °C for 5 min Co_{69.2}Fe_{4.1}B_{11.8}Si_{13.8} C_{1.1} microwires



at 300 °C for 5 min is lower than in as-prepared microwire ($\Delta Z/Z \approx 160$ %). Additionally a change of the magnetic field dependence of $\Delta Z/Z$ is observed: the field for maximum GMI is lower in the annealed microwire for all measured frequencies. As discussed elsewhere, the field for maximum GMI corresponds to the magnetic anisotropy field [45]. Additionally the magnetic field dependence of the GMI ratio is strongly affected by magnetic anisotropy [45].

On the other hand, the same sample presents also quite fast single domain wall propagation: we observed typical single wall propagation with nearly linear growth of velocity v with magnetic field, H. The maximum velocity observed in this sample was about 2.5 km/s (Fig. 1.10c).

As-compared with results reported in literature, the magnitudes of the GMI ratio and domain wall velocity presently studied in our microwire exhibit similar values of GMI ratio values (maximum value about 300 %) in the as-prepared state. After annealing the maximum value of the GMI ratio decreases almost twice (from 300 % to about 160 %) but still remains reasonable for practical applications. On the other hand, maximum wall velocity observed in our annealed sample is quite high (about 2.5 km/s) being similar to that reported for microwires with low and positive magnetostriction value [19, 41].

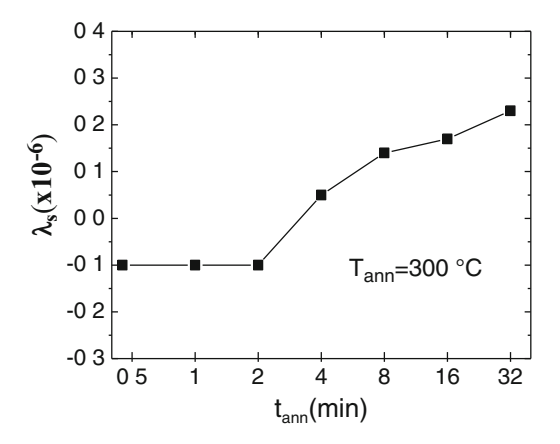


Fig. 1.11 Effect of annealing conditions on magnetostriction, λ_s of $Fe_{3.83}Co_{66.94}Ni_{1.44}B_{11.51}Si_{14.59}Mo_{1.69}$ microwires. Reprinted with permission from [57]

From the observed dependences we deduce that annealing induces an axial magnetic anisotropy.

But considerable GMI effect has been attributed to circular domain structure near the surface of annealed samples.

For explanation of the observed dependences few parallel phenomena have been proposed:

- 1. Effect of stress relaxation associated with the annealing affects the magnetostriction coefficient. Indeed recently direct measurements confirmed that considerable changes of the magnetostriction coefficient take place (see Fig. 1.11) [26, 57].
- 2. Tensile stress applied during annealing creates "back" stresses reducing the magnetostriction constant. Such "back" stresses have been considered for explanation of stress-induced anisotropy of Fe-rich microwires [58].

Perfectly rectangular hysteresis loops of Co-rich microwires observed after annealing (Fig. 1.10a) are quite similar to hysteresis loops of as-prepared Fe-rich microwires (Fig. 1.3): they exhibit similar coercivities and reducing the magnetic field amplitude below the switching field the hysteresis loop disappeared. Consequently we must assume that after annealing of Co-rich microwires we observe induced magnetic bistability.

Typical feature of microwires presenting magnetic bistability is the fast DW propagation within the inner axially magnetized core responsible for rectangular hysteresis loop.

Usually it is assumed that domain wall (DW) propagates along the wire with a velocity:

$$v = S(H - H_0) \tag{1.4}$$

where S is the DW mobility, H is the axial magnetic field and H_0 is the critical propagation field.

In previous papers on studies of DW dynamics in microwires exhibiting spontaneous magnetic bistability there are few typical features.

1.2.1 Domain Wall Dynamics Is Affected by the Internal Stresses

As the example, dependences of the DW velocity, v, on magnetic field, H for $Fe_{16}Co_{60}Si_{13}B_{11}$ and $Co_{41.7}Fe_{36.4}Si_{10.1}B_{11.8}$ amorphous microwires with the same ρ -ratio but with different magnetostriction coefficients are shown in Fig. 1.12. In this case, the effect of only magnetostriction constant is that higher magnetostriction constant (in according to [25–27] for $Co_{41.7}Fe_{36.4}Si_{10.1}B_{11}$ microwire $\lambda_s \approx 30 \times 10^{-6}$ should be considered, while for $Fe_{16}Co_{60}Si_{13}B_{11}$ composition $\lambda_s \approx 15 \times 10^{-6}$) results in smaller DW velocity at the same magnetic field and smaller DW mobility, S.

In order to evaluate the effect of ρ -ratio, i.e., effect of residual stresses on DW dynamics, measurements of v(H) dependences in the microwires with the same composition but with different ρ -ratios have been performed. Dependences of DW velocity on applied field for Fe₅₅Co₂₃B_{11.8}Si_{10.1} microwires with different ratios are shown in Fig. 1.13. Like in Fig. 1.12, at the same values of applied field, H, the domain wall velocity is higher for microwires with higher ρ -ratio, i.e., when the internal stresses are lower [46].

Additionally to evaluate the magnetoelastic contribution the v(H) dependences under applied stresses have been measured. Observed v(H) dependences for

Fig. 1.12 v(H) dependences for $Fe_{16}Co_{60}Si_{13}B_{11}$ and $Co_{41.7}Fe_{36.4}Si_{10.1}B_{11.8}$ microwires with $\rho=0.39$.

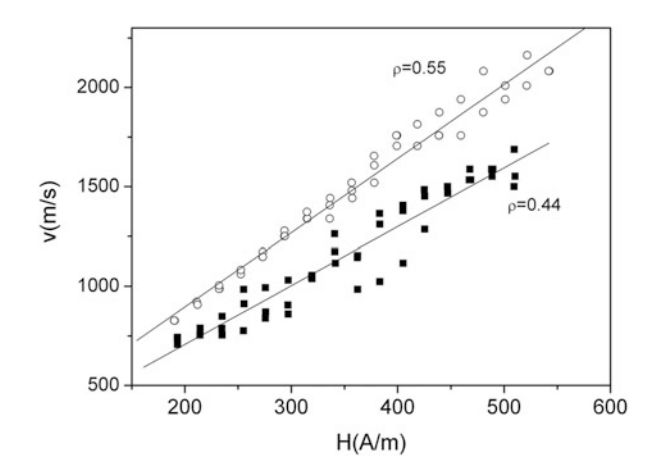


Fig. 1.13 v(H) dependences for Fe₅₅Co₂₃B_{11.8}Si_{10.1} microwires with different ratios ρ . Reprinted with permission from [46]

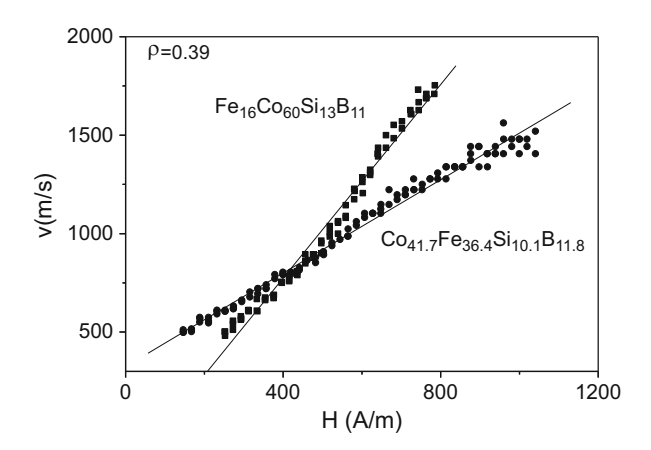
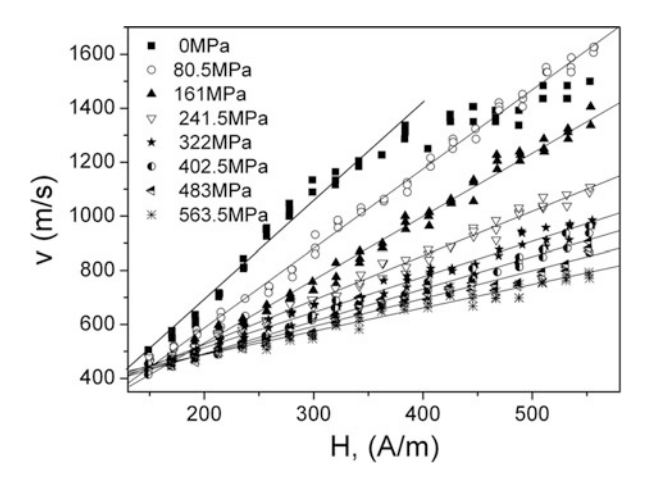


Fig. 1.14 v(H) dependences for $\mathrm{Co_{41.7}Fe_{36.4}Si_{10.1}B_{11.8}}$ microwires $(d\approx13.6~\mu\mathrm{m}, D\approx24.6~\mu\mathrm{m}, \rho\approx0.55)$ measured under application of applied stresses, σ_a . Reprinted with permission from [46]



 $\text{Co}_{41.7}\text{Fe}_{36.4}\text{Si}_{10.1}\text{B}_{11.8}$ microwire ($\rho \approx 0.55$) under applied stresses (see Fig. 1.14) present considerable decreasing of domain wall velocity, ν , at the same magnetic field value, H, under application of applies stress. Additionally, increasing of applied stress, σ_a , results in decreasing of DW velocity.

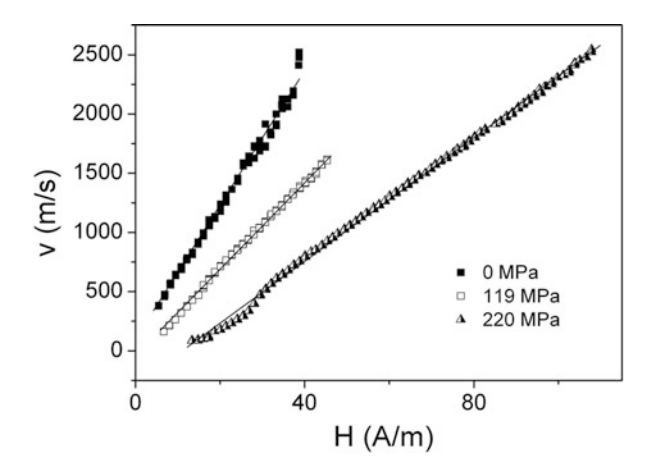
Finally v(H) dependences in low magnetostrictive $Co_{56}Fe_8Ni_{10}Si_{10}B_{16}$ microwire present considerable higher (almost twice) DW velocities than observed for microwires with higher magnetostriction constant DW at the same values of applied field (see Fig. 1.15).

The domain wall dynamics in viscous regime is determined by a mobility relation (1.4), where S is the domain wall mobility given by:

$$S = 2\mu_0 M_s / \beta \tag{1.5}$$

where β is the viscous damping coefficient, μ_0 is magnetic permeability of vacuum. Damping is the most relevant parameter determining the domain wall dynamics.

Fig. 1.15 v(H) dependences for $Co_{56}Fe_8Ni_{10}Si_{10}B_{16}$ microwires measured under application of applied stresses, σ_a . Reprinted with permission from [46]



Various contributions to viscous damping β have been considered and two of them are generally accepted [46]:

• Micro-eddy currents circulating nearby moving domain wall are the more obvious cause of damping in metals. However, the eddy current parameter β_e is considered to be negligible in high-resistive materials, like thin amorphous microwires.

The second generally accepted contribution of energy dissipation is magnetic relaxation damping, β_r , related to a delayed rotation of electron spins. This damping is related to the Gilbert damping parameter and is inversely proportional to the domain wall width δ_w [46],

$$\beta_r \approx \alpha M_s / \gamma \Delta \approx M_s (K_{\text{me}} / A)^{1/2}$$
 (1.6)

where γ is the gyromagnetic ratio, A is the exchange stiffness constant, K_{me} is the magnetoelastic anisotropy.

Consequently, we can assume that the magnetoelastic energy can affect domain wall mobility, *S*, as we experimentally observed in few Co–Fe-rich microwires.

In the case of only the magnetoelastic origin of the stress dependence of DW velocity, v, this dependence should exhibit an inverse square root dependence. In Fig. 1.16 we present our attempt to evaluate quantitatively observed $v(\sigma_a)$ dependence for Fe₅₅Co₂₃B_{11.8}Si_{10.2} microwires ($d = 13.2 \mu \text{m}$; $D = 29.6 \mu \text{m}$).

Experimental $v(\sigma_a)$ dependence exhibits decreasing of DW velocity, v, with applied stresses, σ_a (Fig. 1.16a), but this dependence does not fit well with inverse square root dependence on applied stress (Fig. 1.16b). Here we plotted obtained experimentally dependences as $\sigma_a(v^{-2})$. From Fig. 1.16b we can conclude that obtained $v(\sigma_a)$ dependences cannot be described by single $v(\sigma_a^{-1/2})$ dependence. One of possible reasons of such deviation from predicted dependence is that when applied stresses are of the same order, as the internal stresses with complex tensor

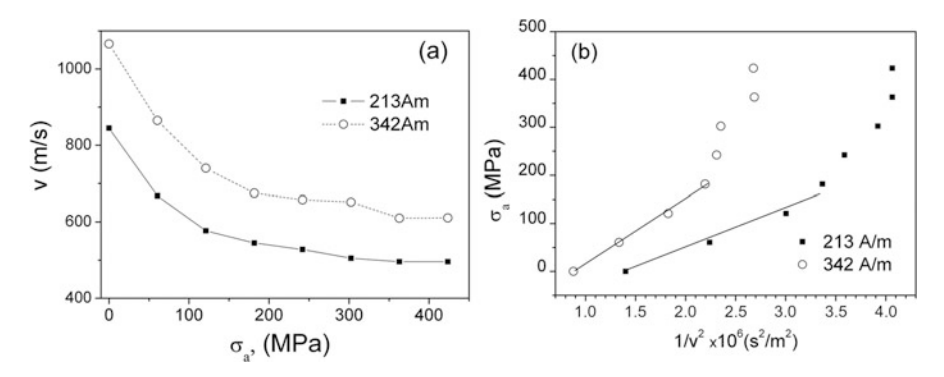


Fig. 1.16 $v(\sigma_a)$ dependences of Fe₅₅Co₂₃B_{11.8}Si_{10.2} microwires ($d=13.2 \mu \text{m}$; $D=29.6 \mu \text{m}$) (a) and $\sigma_a(1/v^2)$ dependence (b). Reprinted with permission from [46]

character [46]. The other reason can be related with stress dependence of magnetostriction previously observed in various amorphous alloys [46].

Consequently DW dynamics in as-prepared Fe-rich and annealed Co-rich samples measured under stress have been compared.

As can be appreciated from Fig. 1.17, a typical nearly linear growth of DW velocity has been observed in as-prepared Fe-rich and annealed Co-rich samples measured without stress.

Under applied stress drastic decreasing of DW velocity has been observed in Fe-rich microwires. On the other hand, in Co-rich microwires increasing of DW velocity takes place (Fig. 1.17).

We observed that annealing performed at 300 °C for 60 min in Fe₇₄B₁₃Si₁₁C₂ microwire considerably affects v(H) dependence: DW velocity measured at the same magnetic field considerably increases, the range of fields where linear v(H) dependence takes place is extended and DW mobility, S, increased from 4.02 to 4.65 m²/As (Fig. 1.17).

For explaining of the unusual features of Co-rich microwires with induced magnetic bistability we must consider that the origin of the magnetic bistability of amorphous glass-coated microwires is usually related to the fast magnetization switching of a large single axially magnetized domain [1]. In the case of Fe-rich microwires with spontaneous magnetic bistability is considered that large axially magnetized single domain is surrounded by the outer radially magnetized shell. This domain structure is determined by the stresses arising during the rapid solidification of the microwire [1, 54, 55].

In the case of the microwires with spontaneous magnetic bistability the annealing does not affect the character of hysteresis loop but considerably affects the DW dynamics. Thus annealing performed at 300 °C for 60 min in $Fe_{74}B_{13}Si_{11}C_2$ microwire considerably affects $\nu(H)$ dependence: DW velocity measured at the same magnetic field considerably increases, the range of fields

Fig. 1.17 Applied stress dependence of DW velocity of as-prepared $Fe_{70}B_{15}Si_{10}$ C_5 and annealed at $T_{\rm ann}=300~{\rm ^{\circ}C}$ for 45 min $Co_{69.2}Fe_{4.1}B_{11.8}Si_{13.8}C_{1.1}$ microwire. Reprinted with permission from [55]

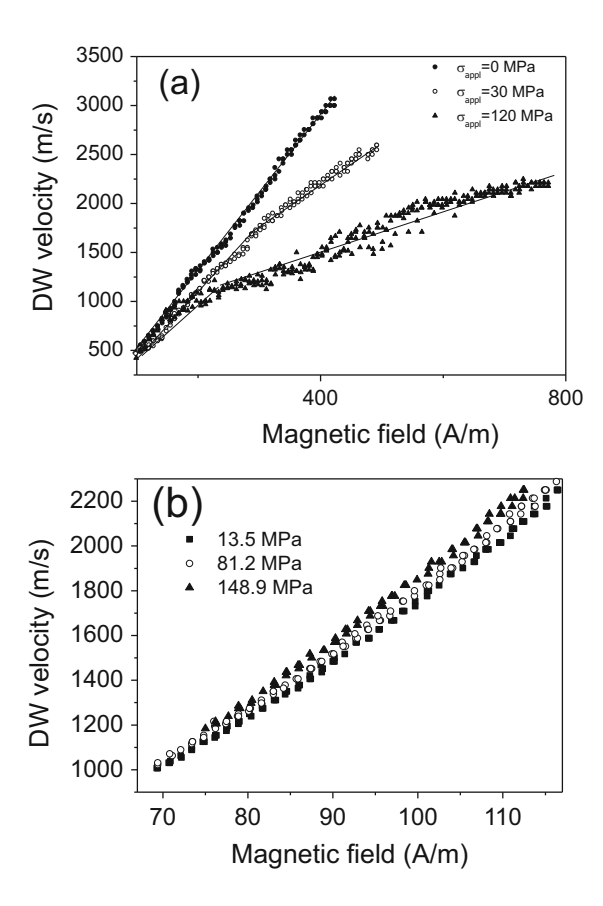
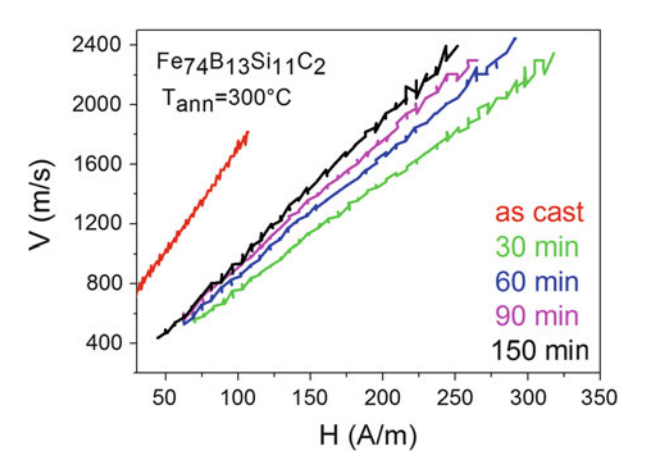


Fig. 1.18 Effect of annealing on v(H) dependence of Fe₇₄B₁₃Si₁₁C₂ microwire ($d=14.6~\mu\text{m}, \rho=0.55$). Reprinted with permission from [50]



where linear v(H) dependence takes place is extended and DW mobility, S, increased from 4.02 to 4.65 m²/As (Fig. 1.18).

Observed influence of sample annealing on DW dynamics in microwires with spontaneous magnetic bistability has been interpreted considering, partial internal stresses relaxation [50].

Increasing the annealing temperature above the crystallization temperature partial or complete crystallization can be achieved. Usually crystallization results in drastic magnetic hardening and deterioration of magnetic properties, but in some cases magnetic softness can be enhanced.

1.3 Effect of Partial Crystallization and Nanocrystallization on Magnetic Properties and GMI

As mentioned above although crystallization of amorphous materials usually results in degradation of their magnetic softness, in some cases crystallization can improve magnetically soft behaviour. This is the case of the so-called nanocrystalline alloys obtained by suitable annealing of amorphous metals. These materials have been introduced in 1988 by Yoshizawa and Yamauchi [28] and later have been intensively studied by a number of research groups [29–31]. As mentioned in the introduction the nanocrystalline structure of partially crystalline amorphous precursor is observed particularly in Fe-Si-B with small additions of Cu and Nb. Small additions of Cu and Nb allow inhibiting of the grains nucleation and decreasing of the grain growth rate [29–31]. Main interest in such nanocrystalline alloys is related to extremely soft magnetic properties combined with high saturation magnetization. Such soft magnetic character is thought to be originated because the magnetocrystalline anisotropy vanishes and the very small magnetostriction value when the grain size approaches 10 nm [28–31].

Recently considerable improvement of GMI effect in the case of glass-coated microwires is reported quite recently [34–37].

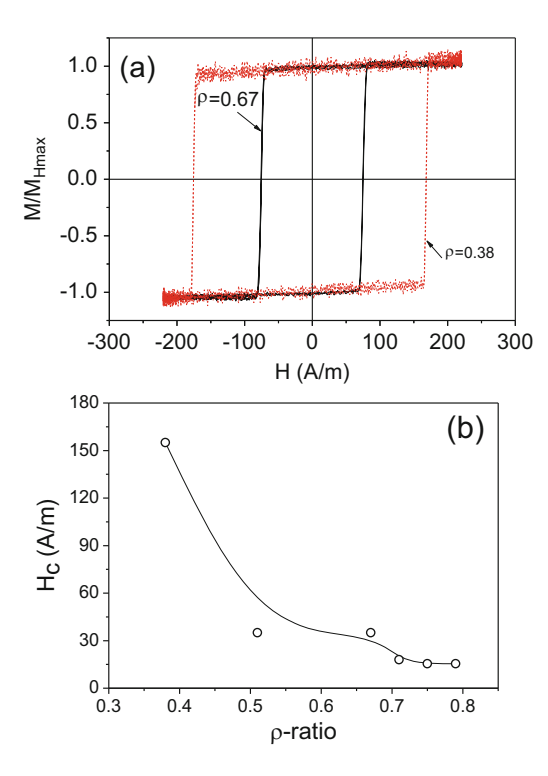
As-prepared Finmet-type $Fe_{73.4}Cu_1Nb_{3.1}Si_xB_{22.5-x}$ (x=11.5, 13.5 and 16.5) and $Fe_{73.4-x}Cu_1Nb_{3.1}Si_{13.4+x}B_{9.1}$ ($0 \le x \le 1.1$) microwires present rectangular hysteresis loops similarly to other Fe-rich amorphous microwires [34–36]. For illustration in Fig. 1.19a the hysteresis loops of $Fe_{70.8}Cu_1Nb_{3.1}Si_{14.5}B_{10.6}$ microwires with different ρ -ratios ($\rho=0.67$ and $\rho=0.38$) are provided.

The coercivity, H_c , of as-prepared Finemet-type microwires depends on ratio $\rho = d/D$ (Fig. 1.19b).

Figure 1.20a, b, c presents XRD spectra of some selected as-prepared $Fe_{70.8}Cu_1Nb_{3.1}Si_{16}B_{9.1}$, $Fe_{70.8}Cu_1Nb_{3.1}Si_{14.5}B_{10.6}$ and $Fe_{73.8}Cu_1Nb_{3.1}Si_{13}B_{9.1}$ microwires.

The first two peaks of the XRD spectra between 10° and 30° correspond to the glass layer and the other peaks at above 40° are related to the metallic nucleus. All

Fig. 1.19 Hysteresis loops (a) and $H_c(\rho)$ dependence (b) of Fe_{70.8}Cu₁Nb_{3.1}Si_{14.5} B_{10.6} as-prepared microwires. Reprinted with permission from [34]



 $Fe_{70.8}Cu_1Nb_{3.1}Si_{16}B_{9.1}$ and $Fe_{70.8}Cu_1Nb_{3.1}Si_{14.5}B_{10.6}$ samples present a completely amorphous structure (Figs. 1.20a, b).

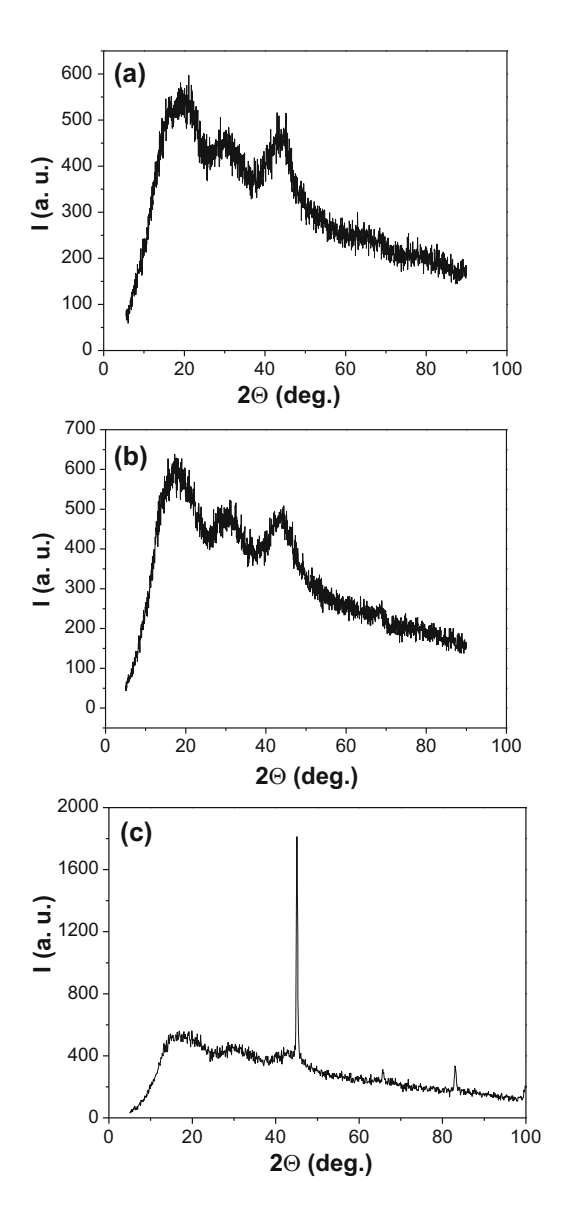
But some of Fe_{73.8}Cu₁Nb_{3.1}Si₁₃B_{9.1} microwires (see Fig. 1.20c) present a partially crystalline structure already in the as-prepared state.

Usually, the basic method to obtain a nanocrystalline structure from the amorphous state is achieving the crystallization of amorphous matrix by an appropriate heat treatment.

As-prepared samples have been annealed at different annealing temperatures, $T_{\rm ann}$, for fixed annealing time. Annealing results in considerable changes of the structure and magnetic properties.

Starting from $T_{\rm ann}$ ranging from 550 to 650 °C a main crystalline peak is appearing in the range between 42° and 45° which corresponds to the existence of α -Fe (Si) BCC crystal structure [34–36], as well as another two weak peaks appearing in the range between 65° and 85° (Fig. 1.21a). However, in the case of the Fe_{73.8}Cu₁Nb_{3.1}Si₁₃B_{9.1} microwire such crystalline peak has been observed in the as-prepared state (Fig. 1.21c) and consequently after annealing (Fig. 1.12b). Increasing the annealing temperature, $T_{\rm ann}$, this peak is getting higher and narrower which indicates an increase in both the bcc-Fe phase volume fraction and grain size growth, respectively.

Fig. 1.20 XRD patterns of as-prepared microwires: $Fe_{70.8}Cu_1Nb_{3.1}Si_{16}B_{9.1}$ with $\rho=0.75$ (a), $Fe_{70.8}Cu_1Nb_{3.1}$ $Si_{14.5}B_{10.6}$ with $\rho=0.81$ (b) and $Fe_{73.8}Cu_1Nb_{3.1}Si_{13}B_{9.1}$ with $\rho=0.6$ (c)



From the Deybe–Sherrer equation (Eq. (1.7)), one can obtain the value of the grain size (D).

$$D = k\lambda/\epsilon\cos 2\Theta \tag{1.7}$$

where ϵ is the half height width of the crystalline peak and 2Θ is the angular position of the maximum crystalline peak. We found that the average grain size, D, in the

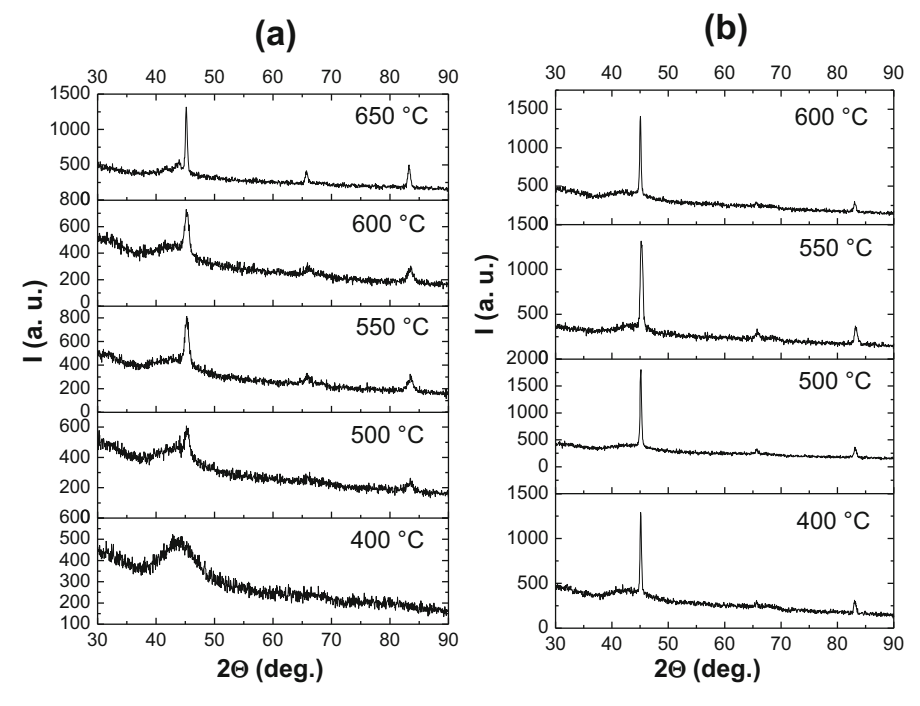
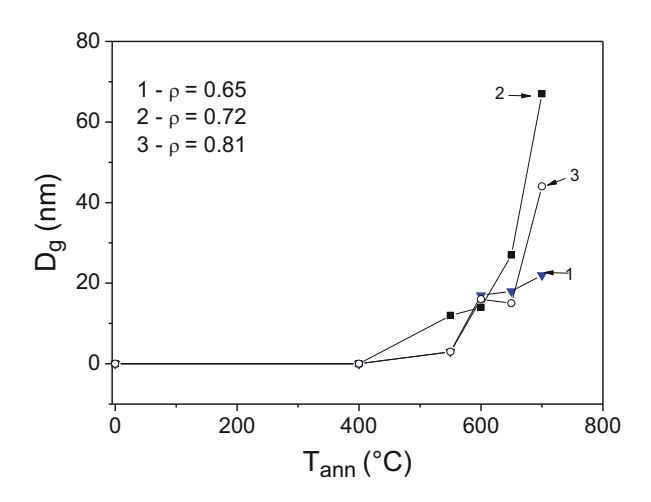


Fig. 1.21 XRD patterns of annealed microwires $Fe_{70.8}Cu_1Nb_{3.1}Si_{14.5}B_{10.6}$ with $\rho=0.81$ (a) and $Fe_{73.8}Cu_1Nb_{3.1}Si_{13}B_{9.1}$ with $\rho=0.6$ (b). Annealing temperatures are indicated within each pattern

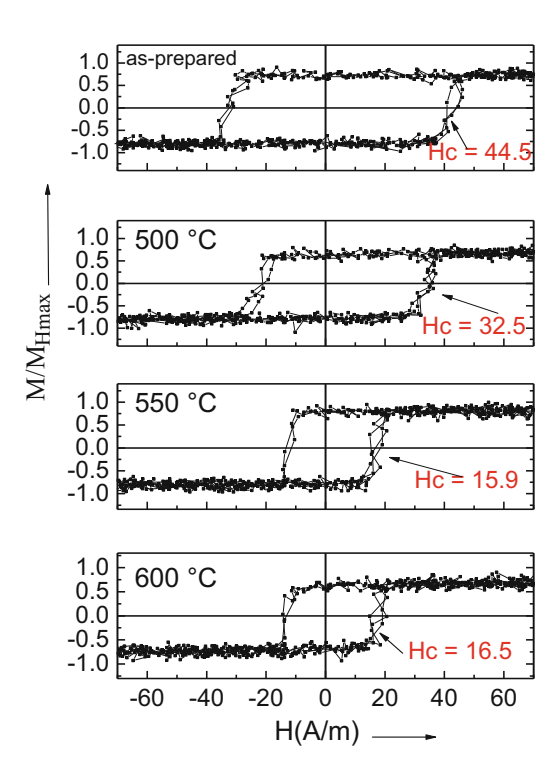
Fig. 1.22 Dependence of average grain size on annealing temperature for $Fe_{70.8}Cu_1Nb_{3.1}Si_{14.5}B_{10.6}$ microwires with various ρ -ratios



range of 550 °C $\leq T_{\rm ann} \leq 600$ °C is between 12 and 17 nm. By increasing $T_{\rm ann} \geq 650^\circ$, D rapidly increases achieving values above 30 nm (see Fig. 1.22).

Strong dependence of magnetic properties on the sample's geometry in as-prepared state has been observed for all compositions. Hysteresis loops (plotted

Fig. 1.23 Hysteresis loops of as-prepared and annealed Fe_{70.8}Cu₁Nb_{3.1}Si_{14.5}B_{10.6} microwires, with $\rho = 0.81$, at different temperatures measured at fixed magnetic field amplitude of 225 A/m



as the normalized magnetization $M/M_{H_{\rm max}}$ versus applied magnetic field H) of as-prepared microwires present rectangular shape typical for amorphous Fe-rich microwires (Fig. 1.19a). As can be appreciated from Fig. 1.19b the coercivity, H_c , is drastically affected by the ρ -ratio. Strong $H_c(\rho)$ dependence can be explained taking into account the influence of the internal stresses on coercivity. As mentioned above the strength of internal stresses is a function of ρ -ratio.

Hysteresis loops of as-prepared and annealed $Fe_{70.8}Cu_1Nb_{3.1}Si_{14.5}B_{10.6}$ microwires ($\rho=0.81$) at different temperatures are presented in Fig. 1.23. It is worth mentioning that the coercivity decreases upon increasing the annealing temperature, while the rectangular character of hysteresis loops is observed for all samples even annealed at below certain temperature.

In Fig. 1.24 we plotted coercivity dependence on annealing temperature for $Fe_{70.8}Cu_1Nb_{3.1}Si_{14.5}B_{10.6}$ glass-coated microwire with different ρ -ratio.

According to these data, a tendency towards decreasing H_c values is observed at the range of 500–550 °C. Above $T_{\rm ann}\approx 600$ °C the magnetic bistability disappears (hysteresis loops cannot be considered perfectly rectangular). Similar behaviour associated with devitrification and magnetic softening has been previously reported in other Finemet-type microwires [34–36].

Consequently magnetic softening with lowest value of coercivity and switching field is obtained in the samples treated at 500–600 °C which could be ascribed to the

Fig. 1.24 Dependence of the coercivity, H_c , for the Fe_{70.8}Cu₁Nb_{3.1}Si_{14.5}B_{10.6} glass-coated microwire with selected ρ -ratio on annealing temperature

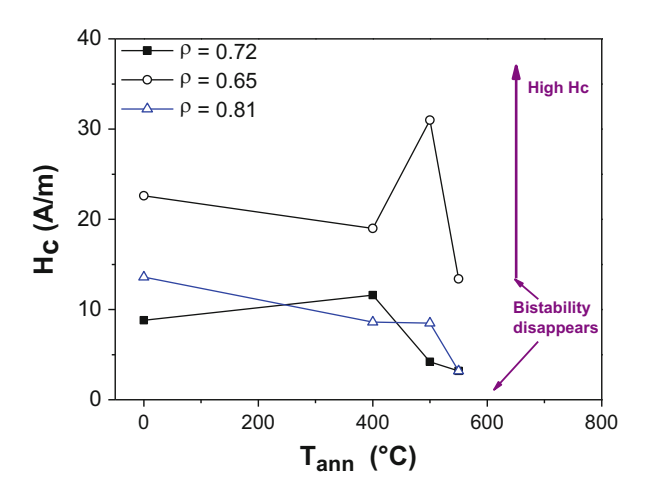
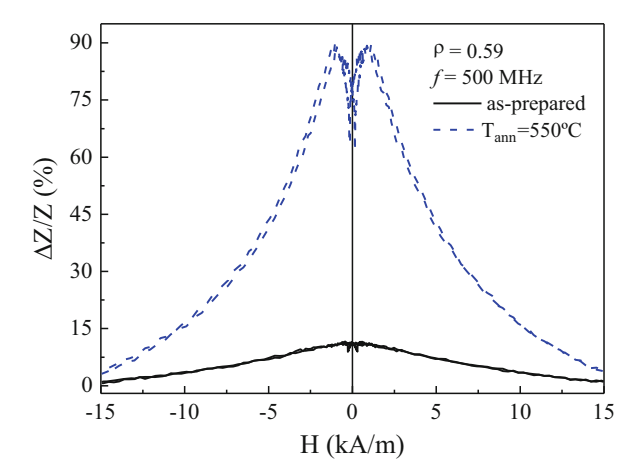


Fig. 1.25 Effect of annealing at 550 °C for 1 h on $\Delta Z/Z(H)$ dependence of Fe_{70.8}Cu₁Nb_{3.1}Si₁₆B_{9.1} microwire with $\rho=0.59$ measured at 500 MHz in comparison with the GMI response of the as-prepared sample



fact that the first crystallization process has been developed, leading to fine α -Fe (Si) nanocrystals with grain size around 10–20 nm (compare Figs. 1.21 and 1.22). This behaviour is similar to that one widely reported for FINEMET ribbons [29–31].

GMI ration has been measured in as-prepared and annealed samples. As it was expected, samples with amorphous structure in as-prepared samples exhibit a rather small GMI effect (below 5 % see Fig. 1.25) similar to other Fe-based glass-coated microwires with positive magnetostriction. In contrast, nanocrystalline $Fe_{70.8}Cu_1Nb_{3.1}Si_{16}B_{9.1}$ microwires annealed at 550 °C exhibit higher GMI effect ($\Delta Z/Z \approx 90$ %, see Fig. 1.25).

Indeed like all Fe-based microwires, studied FeCuNbSiB microwires exhibit high positive magnetostriction. Consequently the stress distribution arising from simultaneous rapid quenching of metallic nucleus inside the glass coating must result in a longitudinal easy magnetization direction axis [1]. The resulting domain

V. Zhukova et al.

structure (with low circular magnetic permeability typical for magnetically bistable samples) usually exhibits a small GMI effect. Therefore, GMI effect in the as-cast FINEMET microwires with positive magnetostriction is low.

A noticeable change in the GMI has been observed after the appearance of nanocrystallites (Fig. 1.25). As discussed elsewhere, after the nanocrystallization the average magnetostriction constant takes nearly zero values [29–31, 34–36], thanks to the control of the crystalline volume fraction:

$$\lambda_{s,\text{eff}} = V_{\text{cr}}\lambda_{s,\text{cr}} + (1 - V_{\text{cr}})\lambda_{s,\text{am}}$$
(1.8)

being $\lambda_{s,\rm eff}$ the saturation magnetostriction coefficient and $V_{\rm cr}$ the crystalline volume fraction.

The other family of microwires with nanocrystalline structure is the Hitpermtype microwires [59]. Hysteresis loops of all as-prepared microwires present rectangular shapes typical for Fe-rich amorphous microwires (see Fig. 1.26). As-prepared Hitperm-type microwires present much higher coercivity values as—compared with Finemet-type microwires (Fig. 1.26b). For comparison the microwires with similar ρ -ratio, i.e., with similar value of the internal stresses were compared.

In contrast to Finemet-type microwires, for as-prepared Fe_{38.5}Co_{38.5}B₁₈Mo₄Cu₁ microwires ($\rho=0.6$) a noticeable peak appears at $2\theta\approx45^\circ$ that corresponds to α -FeCo phase with an average grain size of about 33.3 nm randomly distributed in an amorphous matrix (Fig. 1.27b). The diffraction spectra must be attributed to the superposition of the peaks corresponding to the crystalline and amorphous phases.

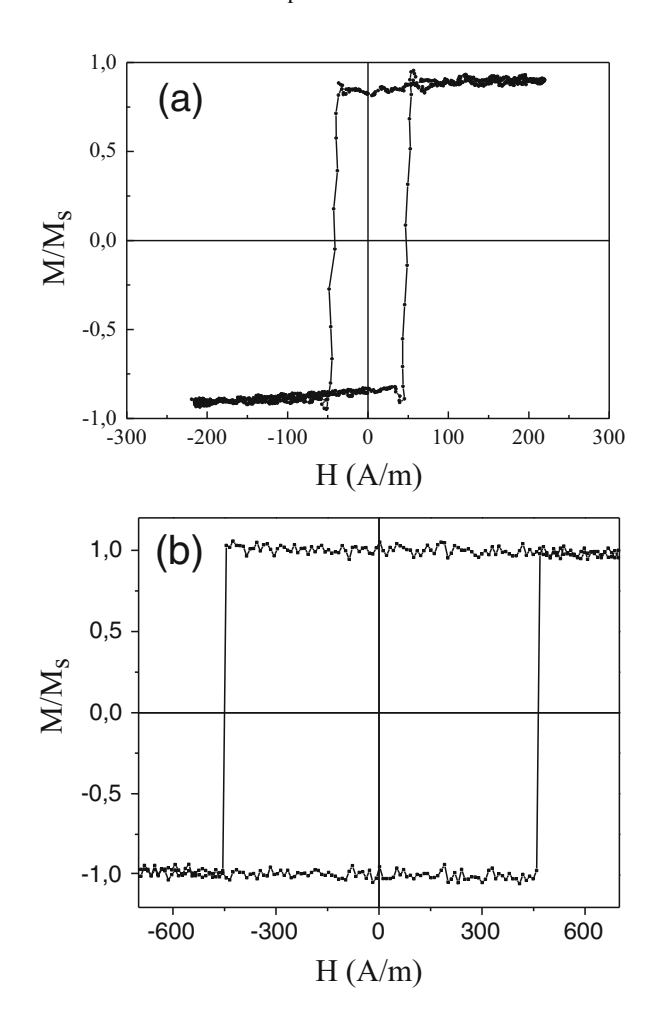
The nanocrystalline structure of Fe_{38.5}Co_{38.5}B₁₈Mo₄Cu₁ microwires maintains after annealing at $T_{\rm ann} \le 600$ °C (with $20 \le D \le 30$ nm).

It is worth mentioning that in contrast to Finemet-type nanocrystalline materials the magnetostriction of Hitperm-type materials remained highly positive due to the positive magnetostriction sign of the α -FeCo nanocrystallites. Consequently, we measured (DW) velocities, ν , of as-prepared and annealed Hitperm-type glass-coated microwires as shown in Fig. 1.28 where is presented as annealing affects to DW dynamics of Fe_{38.5}Co_{38.5}B₁₈Mo₄Cu₁ microwires. Magnetic field range at which we observed single DW propagation becomes more extended in the annealed samples. This extended magnetic field region for single DW propagation must be related to stress relaxation and related magnetic softening observed after annealing.

Both as-prepared and annealed at 450 °C samples present non-linear v(H) dependences. One of the possible explanations of such non-linearity could be attributed to the change of domain wall structure. The other reason for non-linearity can be associated with the defects [37, 46].

Consequently, after the devitrification of FINEMET and HITPERM-type microwires magnetic softness, enhanced GMI effect and high velocity of DW propagation can be observed.

Fig. 1.26 Hysteresis loops of as-prepared Fe_{70.8}Cu₁Nb_{3.1}Si₁₆B_{9.1} microwires with $\rho=0.62$ (a) and Fe_{38.5}Co_{38.5}B₁₈Mo₄Cu₁ with $\rho=0.60$ (b)



1.4 Conclusions

Studies of magnetic properties and GMI effect of amorphous Co–Fe-rich microwires reveal that selecting its appropriate chemical composition and geometry they present high GMI effect. Hysteresis loops and magnetic field dependences of GMI effect are affected by the magnetoelastic anisotropy.

Magnetic properties of amorphous microwires are strongly affected by the annealing. In Co-rich microwires after annealing rectangular hysteresis loops and coexistence of GMI effect and fast domain wall propagation can be observed. Observed changes are discussed considering effect of annealing on the magneto-striction coefficient. Similarly in Fe-rich microwires annealing affects the DW dynamics.

V. Zhukova et al.

Fig. 1.27 XRD patterns of Hitperm Fe_{38.5}Co_{38.5}B₁₈Mo₄Cu₁ microwire ($\rho \approx 0.6$) annealed at different temperatures for 1 h. Reprinted with permission from [59]

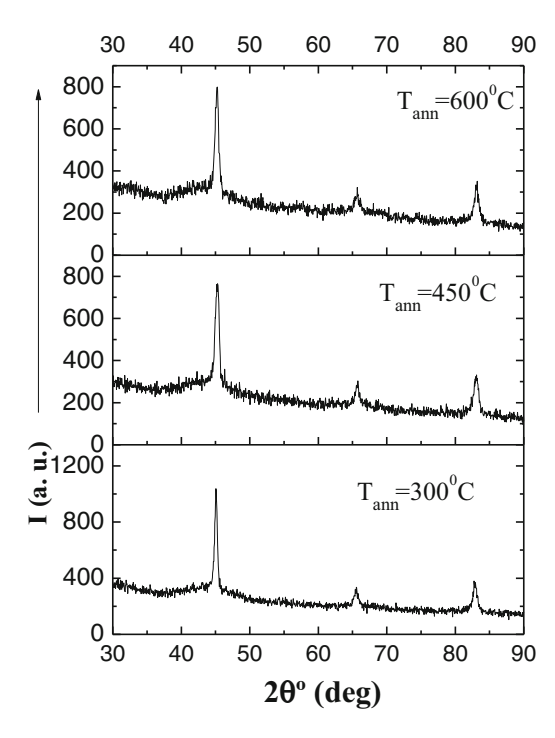
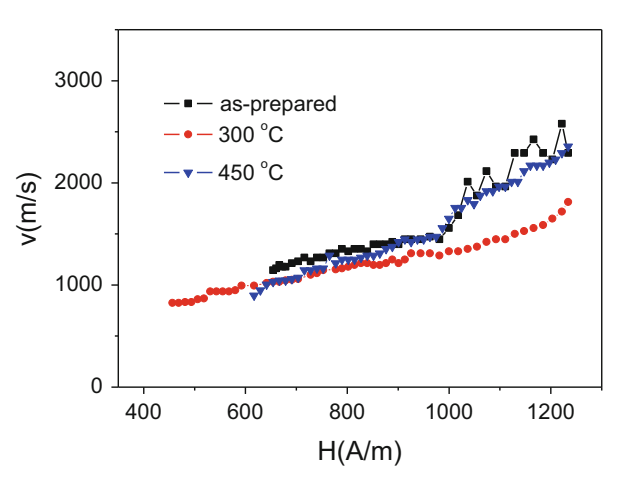


Fig. 1.28 DW velocities dependences of magnetic field measured in as-prepared and annealed Hitperm Fe_{38.5}Co_{38.5}B₁₈Mo₄Cu₁ microwires at different temperatures



Investigations of magnetic properties of Finemet-type Fe-Cu-Nb-Si-B microwires reveal that annealing considerably affects the hysteresis loops and GMI effect of this family of microwires. Magnetoelastic anisotropy affects soft magnetic properties of as-prepared FeCuNbSiB microwires. We observed magnetic softening and a considerable increasing of the GMI effect in Finemet-type FeCuNbSiB with nanocrystalline structure even in as-prepared microwires. After

an adequate annealing of Finemet-type microwires we observed a GMI ratio of about 100 %. The nanocrystallization of FeCuNbSiB microwires is a key factor for the optimization of the GMI effect.

In Hitperm-like $Fe_{38.5}Co_{38.5}B_{18}Mo_4Cu_1$ microwires rectangular hysteresis loops and fast domain wall dynamics have been observed.

Referencess

- Zhukova, V., Ipatov, M., Zhukov, A.: Thin magnetically soft wires for magnetic microsensors. Sensors. 9, 9216–9240 (2009)
- 2. Phan, M.-H., Peng, H.-X.: Giant magnetoimpedance materials: fundamentals and applications. Prog. Mater. Sci. **53**, 323–420 (2008)
- Zhukov, A., Zhukova, V.: Magnetic Properties and Applications of Ferromagnetic Microwires with Amorphous and Nanocrystalline Structure. Nova Science Publishers, New York (2009) ISBN: 978-1-60741-770-5
- Chiriac, H., Corodeanu, S., Lostun, M., Ababei, G., Óvári, T.-A.: Magnetic behavior of rapidly quenched submicron amorphous wires. J. Appl. Phys. 107, 09A301 (2010)
- Chiriac, H., Ovari, T.A.: Amorphous glass-covered magnetic wires: preparation, properties, applications. Prog. Mater. Sci. 40, 333 (1997)
- Honkura, Y.: Development of amorphous wire type MI sensors for automobile use. J. Magn. Magn. Mater. 249, 375–381 (2002)
- 7. Harrison, E.P., Turney, G.L., Rowe, H.: Electrical properties of wires of high permeability. Nature. **135**, 961 (1935)
- Zhukov, A., Ipatov, M., Churyukanova, M., Kaloshkin, S., Zhukova, V.: Giant magnetoimpedance in thin amorphous wires: from manipulation of magnetic field dependence to industrial applications. J. Alloys Compd. 586(Suppl. 1), S279–S286 (2014)
- Panina, L.V., Mohri, K.: Magneto-impedance effect in amorphous wires. Appl. Phys. Lett. 65, 1189–1191 (1994)
- Beach, R.S., Berkowitz, A.E.: Giant magnetic-field dependent impedance of amorphous FeCoSiB wire. Appl. Phys. Lett. 64(26), 3652 (1994)
- Varga, R., Zhukov, A., Zhukova, V., Blanco, J.M., Gonzalez, J.: Supersonic domain wall in magnetic microwires. Phys. Rev. B. 76, 132406 (2007). doi:10.1103/Phys Rev B.76.132406
- Ekstrom, P.A., Zhukov, A.: Spatial structure of the head-to-head propagating domain wall in glass-covered FeSiB microwire. J. Phys. D: Appl. Phys. 43, 205001 (2010). doi:10.1088/0022-3727/43/20/205001
- Gudoshnikov, S.A., Grebenshchikov, Y.B., Ljubimov, B.Y., Palvanov, P.S., Usov, N.A., Ipatov, M., Zhukov, A., Gonzalez, J.: Ground state magnetization distribution and characteristic width of head to head domain wall in Fe-rich amorphous microwire. Phys. Status Solidi A. 206(4), 613 (2009). doi:10.1002/pssa.200881254
- Hayashi, M., Thomas, L., Rettner, C., Moriya, R., Jiang, X., Parkin, S.: Dependence of Current and Field Driven Depinning of Domain Walls on Their Structure and Chirality in Permalloy Nanowires. Phys. Rev. Lett. 97, 207205 (2006). doi:10.1103/PhysRevLett. 97.207205
- Faulkner, C.C., Allwood, D.A., Cowburn, R.P.: Tuning of biased domain wall depinning fields at Permalloy nanoconstrictions. J. Appl. Phys. 103, 073914 (2008). doi:10.1063/1.2905318
- Larin, V.S., Torcunov, A.V., Zhukov, A., González, J., Vazquez, M., Panina, L.: Preparation and properties of glass-coated microwires. J. Magn. Magn. Mater. 249(1-2), 39–45 (2002)
- 17. Taylor, G.F.: Phys. Rev. 24, 6555–6560 (1924)
- Ulitovski, A.V., Maianski, I.M., Avramenko, A.I.: Author's Certification Patent No. 128,427, 3 Sept 1950

- Wiesner, H., Schneider, J.: Structure transformation in Fe-based amorphous alloy. Phys. Status Solidi A. 32(2), 655–659 (1975)
- Wiesner, H., Schneider, J., Gemperle, R.: Annealing effects on the magnetic properties of rapidly quenched transition metal alloys. Phys. Status Solidi A. 36(1), K59 (1976)
- 21. Gemperle, R., Kraus, L., Schneider, J.: Magnetization reversal of amorphous $Fe_{80}P_{10}B_{10}$ microwires. Czech. J. Phys. B. **28**, 1138 (1978)
- 22. Kraus, L., Schneider, J., Wiesner, H.: Ferromagnetic resonance in amorphous alloys prepared by rapid quenching from the melt. Czech. J. Phys. B. 26, 601 (1976)
- 23. Kraus, L., Schneider, J.: Magnetostriction of Amorphous (Fe1-xNix)80P10B10 Alloys. Phys. Status Solidi A. 39, K161 (1977)
- 24. Zhukov, A., Zhukova, V.: Magnetic Sensors Based on Thin Magnetically Soft Wires with Tuneable Magnetic Properties and its Applications. International Frequency Sensor Association (IFSA) Publishing, Ronda de Ramon Otero Pedrayo (2014). ISBN-10: 84-617-1866-6
- Konno, Y., Mohri, K.: Magnetostriction measurements for amorphous wires. IEEE Trans. Magn. 25, 3623–3625 (1989)
- Zhukov, A., Churyukanova, M., Kaloshkin, S., Sudarchikova, V., Gudoshnikov, S., Ipatov, M., Talaat, A., Blanco, J.M., Zhukova, V.: Magnetostriction of Co-Fe-based amorphous soft magnetic microwires. J. Electron. Mater. 45, 226–234 (2015). doi:10.1007/s11664-015-4011-2
- Zhukov, A., Zhukova, V., Blanco, J.M., Cobeño, A.F., Vazquez, M., Gonzalez, J.: Magnetostriction in glass-coated magnetic microwires. J. Magn. Magn. Mater. 258-259, 151–157 (2003)
- 28. Yoshizawa, Y., Yamauchi, K.: Fe-based soft magnetic alloy composed of ultrafinegrain structure. Mater. Trans. JIM. **31**, 307–314 (1990)
- 29. Herzer, G.: Grain size dependence of coercivity and permeability in nanocrystalline ferromagnets. IEEE Trans. Magn. **26**, 1397–1402 (1990)
- McHenry, M.E., Willard, M.A., Laughlin, D.E.: Amorphous and nanocrystalline materials for applications as soft magnets. Prog. Mater. Sci. 44, 291–433 (1999)
- Herzer, G.: Anisotropies in soft magnetic nanocrystalline alloys. J. Magn. Magn. Mater. 294, 99–106 (2005)
- 32. Zhukova, V., Cobeño, A.F., Zhukov, A., Blanco, J.M., Larin V. and Gonzalez J.: Coercivity of glass-coated Fe_{73,4-x}Cu₁Nb_{3.1}Si_{13.4+x}B_{9.1} (0≤x≤1.6) microwires. Nanostruct. Mater. 11(8), 1319–1327 (1999)
- 33. Dudek, C., Adenot-Engelvin, A.L., Bertin, F., Acher, O.: J. Non-Cryst. Solids. 353, 925 (2007)
- Zhukov, A.P., Talaat, A., Ipatov, M., Blanco, J.M., Gonzalez-Legarreta, L., Hernando, B., Zhukova, V.: Effect of nanocrystallization on magnetic properties and GMI effect of microwires. IEEE Trans. Magn. 50(6), 2501905 (2014)
- Talaat, A., Zhukova, V., Ipatov, M., del Val, J.J., Gonzalez-Legarreta, L., Hernando, B., Blanco, J.M., Zhukov, A.: Effect of nanocrystallization on giant magnetoimpedance effect of Fe based microwires. Intermetallics. 51, 59–63 (2014)
- 36. Talaat, A., Zhukova, V., Ipatov, M., Blanco, J.M., Gonzalez-Legarreta, L., Hernando, B., del Val, J.J., Gonzalez, J., Zhukov, A.: Optimization of the giant magnetoimpedance effect of Finemet-type microwires through the nanocrystallization. J. Appl. Phys. 115, 17A313 (2014)
- Chiriac, H., Ovari, T.A., Marinescu, C.S.: Giant magneto-impedance effect in nanocrystalline glass-covered wires. J. Appl. Phys. 83, 6584 (1998)
- 38. Vázquez, M., Zhukov, A.: Magnetic properties of glass coated amorphous and nanocrystalline microwires. J. Magn. Magn. Mater. **160**, 223–228 (1996)
- 39. Usov, N.A., Antonov, A.S., Lagar'kov, A.N.: Theory of giant magneto-impedance effect in amorphous wires with different types of magnetic anisotropy. J. Magn. Magn. Mater. 185, 159 (1998)
- 40. Pirota, K.R., Kraus, L., Chiriac, H., Knobel, M.: Magnetic properties and GMI in a CoFeSiB glass-covered microwire. J. Magn. Magn. Mater. **21**, L243–L247 (2000)

- Zhukova, V., Chizhik, A., Zhukov, A., Torcunov, A., Larin, V., Gonzalez, J.: Optimization of giant magneto-impedance in Co-rich amorphous microwires. IEEE Trans. Magn. 38(5), 3090–3092 (2002)
- 42. Velázquez, J., Vazquez, M., Zhukov, A.: Magnetoelastic anisotropy distribution in glass-coated microwires. J. Mater. Res. 11, 2499–2505 (1996)
- Antonov, A.S., Borisov, V.T., Borisov, O.V., Prokoshin, A.F., Usov, N.A.: Residual quenching stresses in glass-coated amorphous ferromagnetic microwires. J. Phys. D: Appl. Phys. 33, 1161–1168 (2000)
- 44. Chiriac, H., Ovari, T.-A., Zhukov, A.: Magnetoelastic anisotropy of amorphous microwires. J. Magn. Magn. Mater. **254-255**, 469–471 (2003)
- 45. Zhukov, A., Ipatov, M., Zhukova, V.: Amorphous microwires with enhanced magnetic softness and GMI characteristics. EPJ Web Conf. 29, 00052 (2012)
- Zhukov, A., Blanco, J.M., Ipatov, M., et al.: Manipulation of domain wall dynamics in amorphous microwires through the magnetoelastic anisotropy. Nanoscale Res. Lett. 7, 223 (2012). doi:10.1186/1556-276X-7-223
- 47. Zhukov, A.P., Vázquez, M., Velázquez, J., et al.: The remagnetization process of thin and ultrathin Fe-rich amorphous wires. J. Magn. Magn. Mater. 151, 132–138 (1995)
- 48. Aragoneses, P., Blanco, J.M., Dominguez, L., et al.: The stress dependence of the switching field in glass-coated amorphous microwires. J. Phys. D: Appl. Phys. 31, 3040–3045 (1998)
- Aragoneses, P., Blanco, J.M., Cobeño, A.F., Dominguez, L., Gonzalez, J., Zhukov, A., Larin, V.: Stress dependence of the switching field in Co-rich amorphous microwires. J. Magn. Magn. Mater. 196-197, 248–250 (1999)
- 50. Zhukov, A., Ipatov, M., Blanco, J.M., Chizhik, A., Talaat, A., Zhukova, V.: Fast magnetization switching in amorphous microwires. Acta Phys. Pol., A. 126, 7–11 (2014)
- 51. Garcia-Prieto, M.J., Pina, E., Zhukov, A.P., et al.: Glass coated Co-rich amorphous microwires with improved permeability. Sens. Actuators, A. **81**(1-3), 227–231 (2000)
- 52. Zhukov, A., Gonzalez, J., Blanco, J.M., et al.: Induced magnetic anisotropy in Co-Mn-Si-B amorphous microwires. J. Appl. Phys. 87, 1402–1408 (2000)
- Zhukov, A., Vázquez, M., Velázquez, J., et al.: Frequency dependence of coercivity in rapidly quenched amorphous materials. J. Mater. Sci. Eng. A. 226-228, 753-756 (1997)
- 54. Zhukov, A., Talaat, A., Ipatov, M., Blanco, J.M., Zhukova, V.: Tailoring of magnetic properties and GMI effect of Co-rich amorphous microwires by heat treatment. J. Alloys Compd. 615, 610–615 (2014)
- 55. Zhukov, A., Talaat, A., Blanco, J.M., Ipatov, M., Zhukova, V.: Tuning of magnetic properties and GMI effect of Co-based amorphous microwires by annealing. J. Electron. Mater. **43**(12), 4532–4539 (2014). doi:10.1007/s11664-014-3348-2
- Zhukova, V., Ipatov, M., García, C., Gonzalez, J., Blanco, J.M., Zhukov, A.: Development of ultra-thin glass-coated amorphous microwires for high frequency magnetic sensors applications. Open Mater. Sci. J. 1, 1–12 (2007)
- Churyukanova, M., Semenkova, V., Kaloshkin, S., Shuvaeva, E., Gudoshnikov, S., Zhukova, V., Shchetinin, I., Zhukov, A.: Magnetostriction investigation of soft magnetic microwires. Phys. Status Solidi A. 213, 363–367 (2016). doi:10.1002/pssa.201532552
- 58. Zhukov, A.: Design of magnetic properties of Fe-rich, glass-coated magnetic microwires for technical applications. Adv. Funct. Mater. 16(5), 675–680 (2006)
- Zhukova, V., Talaat, A., Ipatov, M., Del val, J.J., Blanco, J.M., Gonzalez-Legarreta, L., Hernando, B., Varga, R., Klein, P., Churyukanova, M., Zhukov, A.: Optimization of soft magnetic properties in nanocrystalline Fe-rich glass-coated microwires. JOM. 67, 2108 (2015). doi:10.1007/s11837-015-1546-x

Chapter 2 Tailoring of Soft Magnetic Properties and High Frequency Giant Magnetoimpedance in Amorphous Ribbons

L. González-Legarreta, V.M. Prida, A. Talaat, M. Ipatov, V. Zhukova, Arcady Zhukov, LI. Escoda, J.J. Suñol, J. González, and B. Hernando

2.1 Introduction

Among several industrial sectors nowadays demanding advanced soft magnetic materials such as magnetic sensors and actuators are one of the most active [1]. Amorphous soft magnetic thin films, microwires, and ribbons present excellent magnetic properties not only interesting from the basic point of view but also suitable for technological applications [2]. In the absence of magneto-crystalline anisotropy the magnetoelastic anisotropy of amorphous materials is the main factor determining their magnetic properties. This magnetoelastic anisotropy, $K_{\rm me}$, given by the equation: $K_{\rm me} \sim 3/2\lambda_s\sigma_i$, is affected by internal stresses, σ_i , and magnetostriction coefficient, λ_s , is the saturation magnetostriction [3]. Giant magnetoimpedance, GMI, is one of the most promising effects for technical applications [1, 4, 5] being proposed for several magnetic sensor applications [6, 7]. Rapidly solidified Co-based alloys displaying nearly zero magnetostriction

L. González-Legarreta • V.M. Prida • B. Hernando (🖂)

Department of Physics, University of Oviedo, Ave. Calvo Sotelo s/n, 33007 Oviedo, Spain e-mail: grande@uniovi.es

A. Talaat • M. Ipatov • V. Zhukova • J. González

Department of Materials Physics, University of the Basque Country, Paseo Manuel de Lardizábal 3, 20018 San Sebastián, Spain

A. Zhukov

Department of Materials Physics, Basque Country University, UPV/EHU, San Sebastian 20018, Spain

Departamento de Física Aplicada, EUPDS, Basque Country University, UPV/EHU, San Sebastian 20018, Spain

IKERBASQUE, Basque Foundation for Science, Bilbao, Spain

L. Escoda • J.J. Suñol

Girona University, Campus Montilivi, ed. PII, Lluís Santaló s/n, 17003 Girona, Spain

[©] Springer International Publishing AG 2017

exhibit soft magnetic properties that may be enhanced by controlled annealing treatment [8–12]. From the perspective of highly sensitive magnetic sensor and in order to achieve a suitable GMI response, we have investigated the effects of stress and current annealing on magnetic and magnetoimpedance properties of near-zero magnetostriction of $\text{Co}_{66.3}\text{Fe}_{3.7}\text{Si}_{12.0}\text{B}_{18.0}$ and $\text{Co}_{71.25}\text{Fe}_{3.75}\text{Si}_{10}\text{B}_{15}$ amorphous alloy ribbons.

2.2 Giant Magnetoimpedance Effect

The so-called giant magnetoimpedance (GMI) effect is the large change in the ac impedance of a soft ferromagnetic conductor induced by a dc magnetic field [13, 14]. This change is usually defined by the GMI ratio as:

$$\Delta Z/Z(\%) = 100\% \times \frac{Z(H) - Z(H_{\text{max}})}{Z(H_{\text{max}})}$$
(2.1)

where Z(H) and $Z(H_{\rm max})$ represent the impedance in an applied field H and in an external magnetic field sufficient to saturate magnetically the sample, respectively. In practice, the value of $H_{\rm max}$ is the maximum field available for the experimental equipment.

GMI effect can be explained by means of Maxwell equations of electrodynamics together with the Landau–Lifshitz–Gilbert equation of the magnetization dynamics [15]. Analytically, it is difficult to obtain the exact solution of the problem by solving simultaneously these equations. However, at low-intermediate frequencies the problem can be treated with a quasi-static approximation. In this case, assuming the material relationship between the induction and magnetic field is linear, $B = \mu H$, the diagonal and off-diagonal components of the impedance tensor [16] for an infinite planar film with thickness, d, are [17]:

$$Z_{zz} = R_{\rm dc}\xi\cot\xi\tag{2.2}$$

$$Z_{yz} = -i\omega\mu_{zy} \frac{(1-\cos\xi)}{(2\xi\sin\xi)}$$
 (2.3)

where $R_{\rm dc}$ is the dc electrical resistance, $\xi = (1 - i)\delta/(2d)$, and δ is the penetration depth in a magnetic medium,

$$\delta = \sqrt{2\rho/\omega\mu_{yy}} \tag{2.4}$$

where ρ is the electrical resistivity and $\omega = 2\pi f$ is the angular frequency of the driving ac current. The components of permeability tensor are $\mu_{yy} = \mu_0 (1 + \cos^2 \theta \chi_t)$ and $\mu_{zy} = -\mu_0 \sin \theta \cos \theta \chi_t$, where θ is the angle between the total magnetic field H and the magnetization M of the sample, and the transverse susceptibility χ_t is

obtained by solving Landau–Lifshitz–Gilbert equation [15]. When $I_{\rm dc}=0$, the component of permeability $\mu_{\rm yy}$ is constant.

At high frequencies, $f \sim \text{GHz}$, the quasi-static approximation is no longer applied and ferromagnetic resonance (FMR) takes place. Therefore, the nonlinearity of Landau–Lifshitz equation must be taken into account, since nonlinear effects should appear [18]. A complete GMI description including dynamical effects with different degrees of approximations has been reported by several authors [15, 19]. In this frequency range, the resonance frequencies satisfy the Kittel resonance condition for a thin film magnetized along the in-plane uniaxial easy axis [18, 20]:

$$f^{2} = (\gamma^{2}\mu_{0}^{2}/4\pi^{2}) [(H + H_{K}) (H + H_{K} + M_{S})]$$
 (2.5)

where γ is the gyromagnetic ratio of the electron, H_K the anisotropy field, and M_S the respective saturation magnetization. γ is expressed as:

$$\gamma = g \frac{\mu_0 e}{2m_e} \tag{2.6}$$

where m_e and e are the mass and charge of the electron, respectively, and g is the Landé splitting factor.

As have been mentioned above, GMI depends on the frequency of the ac driving current, which flows through the sample, being possible classify the effect into four frequency regimes.

- 1. Very low frequencies ($f \sim 10 \text{ kHz}$): the skin effect is rather weak. This is due to the skin depth at these frequencies that is usually larger than the thickness of the sample. The principal contribution to the transverse magnetic permeability (μ_t) and hence to the GMI effect comes from the inductive voltage. It is called magnetoinductive effect.
- 2. Low frequencies ($f \sim 10$ MHz): the skin effect is strong and changes of the transverse magnetic permeability and hence to the GMI are caused by domain walls movement and magnetization rotation.
- 3. Intermediate frequencies ($f \sim 1000$ MHz): the GMI effect is also originated by the skin effect. However, at these frequencies the domain walls are strongly damped. Thus the magnetization rotation must be considered as responsible for the transverse magnetic permeability change induced by the external magnetic field [14].
- 4. High frequencies ($f \sim \text{GHz}$): the magnetization rotation is strongly influenced by the gyromagnetic effect and ferromagnetic relaxation. At this frequency range, strong changes of the sample impedance are attributed to the ferromagnetic resonance (FMR) [14].

2.3 Amorphous Ribbons Production

Soft ferromagnetic amorphous ribbons were produced by melt spinning at cooling rates of 10^3 – 10^6 K/s. This technique avoids prolonged conventional annealing stages. Complementary heat treatments of ribbons as stress annealing or current annealing will be discussed in Sect. 2.4.3.

2.3.1 Melt Spinning

Melt spinning process is often performed by rapid cooling of a bulk master alloy. This primary alloy can be prepared from high purity elements by arc melting under Ar atmosphere. Samples should be remelted several times to assure alloy compositional homogeneity [21]. Amorphous Co- or Fe-rich soft ferromagnetic amorphous alloys are produced by rapid quenching from the melt in vacuum or in inert atmosphere. Figure 2.1 shows a schema (left) of the melt spinning procedure. The as-prepared ribbons can be annealed in a vacuum chamber or in a furnace. It is known that annealing can modify the structure and MI response of the amorphous soft ferromagnetic materials through: (a) the structural relaxation and stress release of the amorphous phase [22], (b) the growth of a crystallized layer at the sample surface [23], or (c) the nanocrystallization in the bulk material [24]. In the literature, many annealing temperature and times were applied [24, 25]. Furthermore, it is possible to anneal ribbons by laser or by microwave [26]. One option to improve magnetic anisotropy during the quenching production is two apply a magnetic field during the fabrication process (field-quenched sample) [27].

After annealing, the samples were cooled in furnace until the chamber temperature is near room temperature or rapidly quenched in water or ice. Cooling is usually performed under vacuum (at a low partial pressure to the order of 10^{-3}

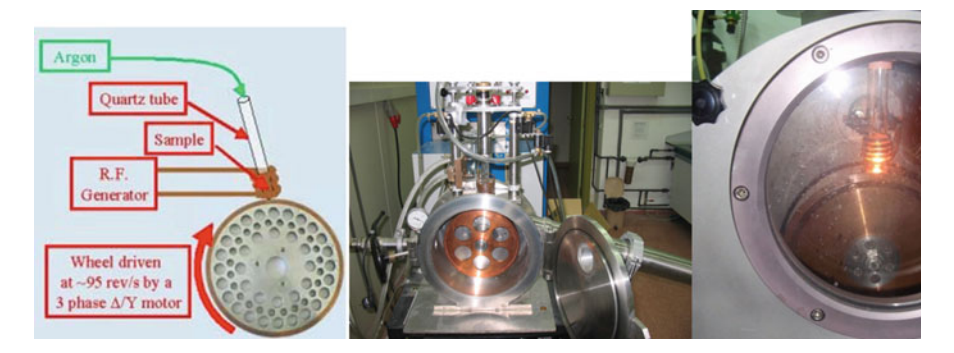


Fig. 2.1 Experimental melt spinning equipment and schema of the melt spinning process

Torr) or under inert atmosphere. Sometimes samples were annealed in air to develop an oxide coating on the surface and to evaluate the effect of the oxide [28]. The structure of the annealed samples remains amorphous or is nanocrystalline. Concerning nanocrystallization, one of the problems is that it renders these alloys extremely brittle limiting their practical application [29].

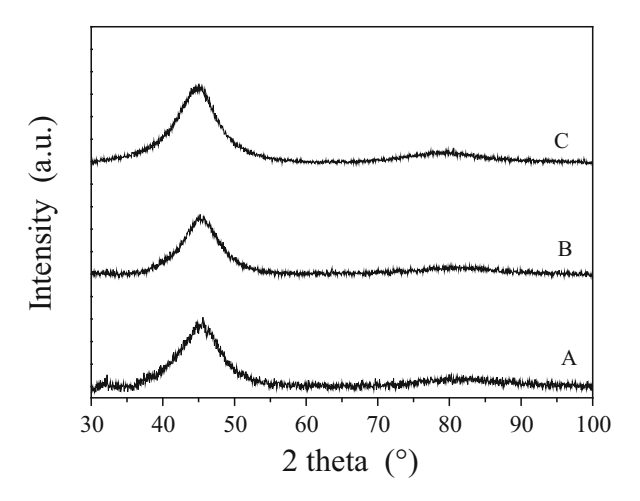
2.3.2 Structural Characterization

In order to get confirmation of the amorphous microstructure of the alloy, X-ray or neutron diffraction measurements were performed at room temperature. Figure 2.2 shows the amorphous X-ray diffraction patterns of three Co-rich ribbons produced by melt spinning. The as-quenched samples presented a broad hump, which is characteristic of the amorphous phase.

The existence of the amorphous phase can also be checked by high-resolution transmission microscopy (HRTEM) [30]. Furthermore, transmission Mössbauer spectroscopy (TMS) is useful in Fe-rich samples [31]. Figure 2.3 shows a micrograph (obtained by scanning electron microscopy, SEM) of the wheel surface of a ribbon flake (*left*) and a typical HRTEM amorphous halo (*right*).

In order to check thermal stability of the amorphous phase against crystallization thermal analysis experiments are usually performed. As an example, Fig. 2.4 shows the differential scanning calorimetry (DSC) heating scans of two amorphous ribbons [27].

Fig. 2.2 X-ray diffraction patterns at room temperature of three Co-rich amorphous ribbons produced by melt spinning



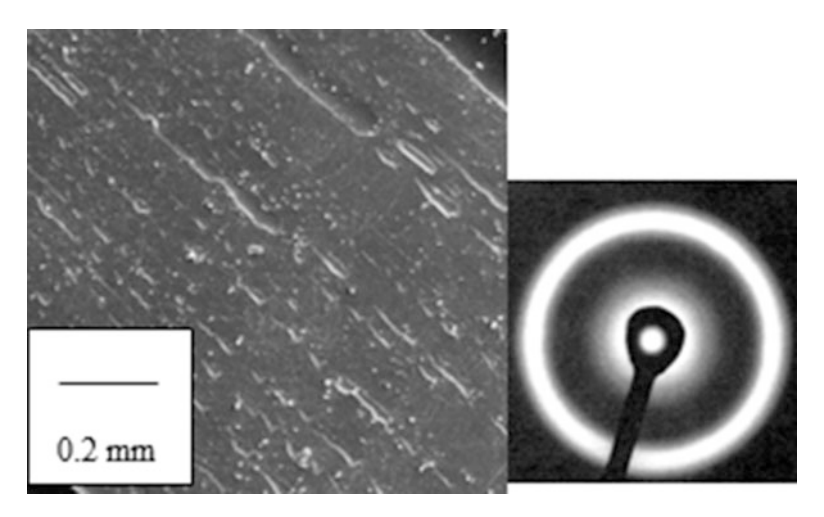


Fig. 2.3 SEM micrograph of the wheel surface of a ribbon (*left*) and an HRTEM amorphous halo (*right*)

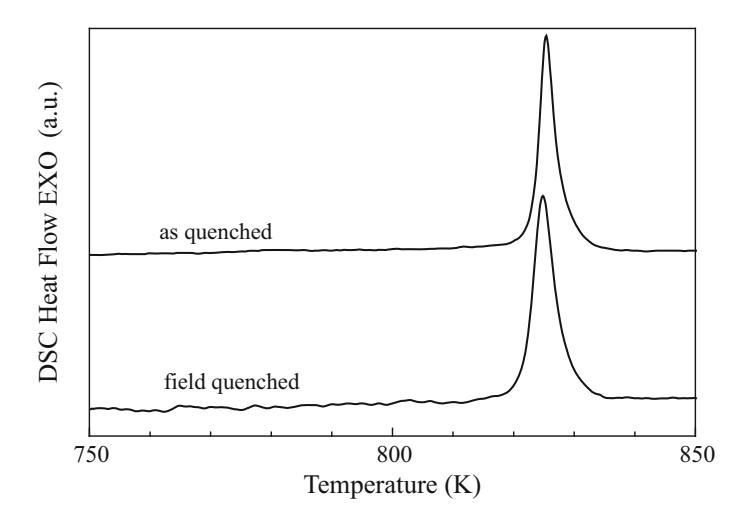


Fig. 2.4 DSC heating scans of two amorphous soft ferromagnetic ribbons produced by melt spinning: conventional quenching (up), quenching under magnetic field (down)

2.4 Experimental Techniques

2.4.1 Magnetic Characterization: Hysteresis Loops and Magnetostriction

Hysteresis loops for all ribbons were measured along the ribbon axis at a frequency value of 50 Hz using the conventional induction technique. Isothermal M(H) loops at room temperature for the three stress-annealed $Co_{66.3}Fe_{3.7}Si_{12.0}B_{15.0}$ samples

show an almost ideal behavior, with a constant slope nearly up to saturation and a quasi-absence of hysteresis effect. All samples exhibit an induced anisotropy perpendicular to the ribbon axis, and a saturation magnetization, $\mu_0 M_S$, of 0.53 T. Sample 1 has the smallest effective anisotropy field of 360 A/m, while the effective anisotropy fields of 530 A/m and 550 A/m were determined for samples 2 and 3, respectively. The anisotropy fields were estimated with an accuracy of the 0.5 % in all cases [32]. Magnetostriction coefficients were obtained by the small angle magnetization rotation (SAMR) technique [33].

2.4.2 Measurement of GMI Effect

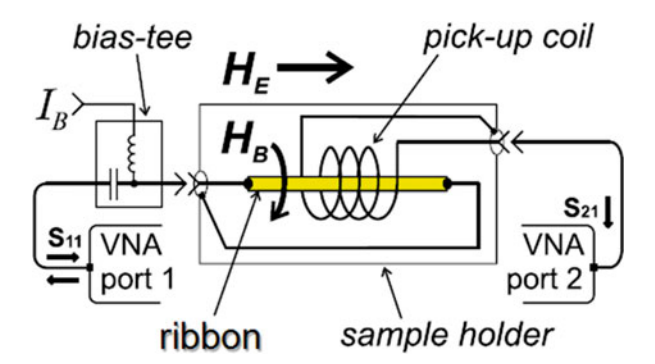
The set-up in this work used to measure the giant magnetoimpedance of Co-based amorphous ribbons is shown in Fig. 2.5.

Impedance components measurements were carried out on the as-quenched and annealed Co-based 1 cm long ribbons soldered to a specially designed micro-strip sample holder. The sample holder is placed inside a long solenoid, which generates a homogenous magnetic field H_E up to 20 kA/m along the ribbon axis. In addition, this system allows the application of a transversal bias field H_B created by dc bias current I_b applied to the sample by a bias-tee element. This system is connected to a vector network analyzer N5230A (VNA), which allows measuring simultaneously the longitudinal and off-diagonal impedance component of the sample in the frequency range of 100–3500 MHz [34]. The longitudinal impedance component is obtained from the reflection coefficient S_{11} by:

$$Z_{zz} = Z_0 \frac{(1 + S_{11})}{(1 - S_{11})} \tag{2.7}$$

where $Z_0 = 50 \Omega$ is the characteristic impedance of the electric coaxial line. The off-diagonal impedance Z_{yz} component is measured through the transmission coefficient S_{21} as a voltage induced in a 2 mm long pick-up coil wound around the ribbon sample (see Fig. 2.5).

Fig. 2.5 Experimental set-up for measuring the GMI response of Co-based ribbons



The analyzer power output in all measurements presented here was 10 dBm that corresponds to a 1.4 mA high frequency driving current passing through the ribbon.

2.4.3 Thermal Treatments: Stress Annealing and Current Annealing

One of the most interesting aspects concerning to the research to get a larger GMI effect is the reduction of the skin effect by choosing magnetic materials with large permeability and small skin depth [19]. For the last purpose we need that the transverse component (in the case of ribbons) of the magnetic susceptibility to be very sensitive to the external magnetic field in order to the skin depth effect can be modified by the action of the magnetic field reflecting in strong changes of the electrical impedance owing the variation of the effective cross section to the electrical transport. These modifications of the transverse component of the magnetic susceptibility can be reached by submitting the amorphous ribbons to thermal treatment under the action of a stress and/or magnetic field, which can develop a uniaxial magnetic anisotropy with the magnetization easy axis transverse to the longitudinal direction of the ribbon [35, 36].

In this work, the studied $Co_{66.3}Fe_{3.7}Si_{12.0}B_{18.0}$ and $Co_{71.25}Fe_{3.75}Si_{10}B_{15}$ amorphous alloy ribbons present transverse induced magnetic anisotropy by stress and current annealing, respectively.

For $Co_{66.3}Fe_{3.7}Si_{12.0}B_{18.0}$ ribbon, which exhibits in the as-quenched state a saturation magnetostriction at room temperature of the order of $\lambda_S \sim -0.18 \times 10^{-6}$, we took three pieces, which were submitted to the following stress-annealing treatment:

- 1. Sample 1: tensile stress annealing at 400 °C with 300 MPa during 1 h, without pre-annealing.
- 2. Sample 2: pre-annealing at 340 $^{\circ}$ C during 1 h, followed by a tensile stress annealing at 340 $^{\circ}$ C with 300 MPa during 1 h.
- 3. Sample 3: pre-annealing at 360 $^{\circ}$ C during 1 h, followed by a tensile stress annealing at 360 $^{\circ}$ C with 300 MPa during 1 h.

In all thermal treatments the tensile stress was applied along the ribbon axis. After annealing, these samples changed the magnetostriction coefficient to $+0.04 \times 10^{-6}$, $+0.17 \times 10^{-6}$, and $+0.11 \times 10^{-6}$, respectively.

For $\text{Co}_{71.25}\text{Fe}_{3.75}\text{Si}_{10}\text{B}_{15}$ amorphous ribbon, which exhibits in the as-quenched state a saturation magnetostriction at room temperature of the order of $\lambda_S \sim -6 \times 10^{-7}$, we took different pieces which were submitted to current annealing [37], i.e., a dc electrical current (440–680 mA) was passing along the ribbon during 5 min. An estimation of the temperature produced by the annealing can be obtained from [35] and Fig. 2.2. Then, for the current intensity range here employed that the averaged temperature within the sample was ranging in (274–427 °C), being something lower at

dc borders of the ribbon because of dissipative effects. Besides, the dc current flowing along the ribbon generates a maximal transverse magnetic field from 6.9×10^3 A/m up to 10.6×10^3 A/m.

These thermal treatments develop a macroscopic uniaxial magnetic anisotropy that will play a drastic role regarding the giant magnetoimpedance effect of these treated ribbons.

2.5 Results and Discussion

Here it will be presented the results of the magnetoimpedance response of near-zero magnetostriction of $Co_{71.25}Fe_{3.75}Si_{10}B_{15}$ and $Co_{66.3}Fe_{3.7}Si_{12.0}B_{18.0}$ amorphous ribbons exhibiting a macroscopic uniaxial magnetic anisotropy induced by current annealing (440–680 mA during 5 min) in the first ribbon and by stress-annealing treatment (300 MPa applied tensile stress at different temperature, i.e., 340, 360, and 400 °C, during 1 h) in the second one, in the frequency range from 100 MHz up to 3500 MHz.

2.5.1 Induced Anisotropy Influence on GMI Components in Stress-Annealed Co-Based Amorphous Ribbons

To explore the effect of induced anisotropy by stress annealing on GMI components of Co_{66.3}Fe_{3.7}Si_{12.0}B_{18.0} amorphous alloy ribbon, we have submitted to some pieces of the ribbon at three different treatments, aforementioned.

Firstly, we have studied the diagonal impedance for the three ribbons in the frequency range of 100-3500 MHz. The absolute value of the longitudinal impedance, Z_{zz} , measured as a function of the applied field for selected values of the frequency for the three samples is shown in Fig. 2.6. It can be observed that for the sample 1 (Fig. 2.6a), which does not have been submitted to any pre-annealing, the impedance evolves to a symmetric two-peaks behavior with respect to H as the frequency increases. Meanwhile, the impedance behavior for samples 2 and 3 (Fig. 2.6b, c, respectively), which have been submitted to a stress relaxation followed by stress annealing at different temperatures, displays different features. The GMI response shows a not enough well-defined two-peaks pattern at low frequencies below 150 MHz for sample 2, but above this frequency a two-peaks pattern emerges clearly. Meanwhile, sample 3 displays an asymmetric two-peaks behavior below 150 MHz, which vanishes as the frequency increases. The different features observed in these annealed ribbons can be explained by the influence of the respective anisotropy induced by each performed annealing under tensile stress on their susceptibility. The two-peaks behavior is more defined and the GMI effect displays its maximum value for sample 1 annealed at 400 °C without previous stress

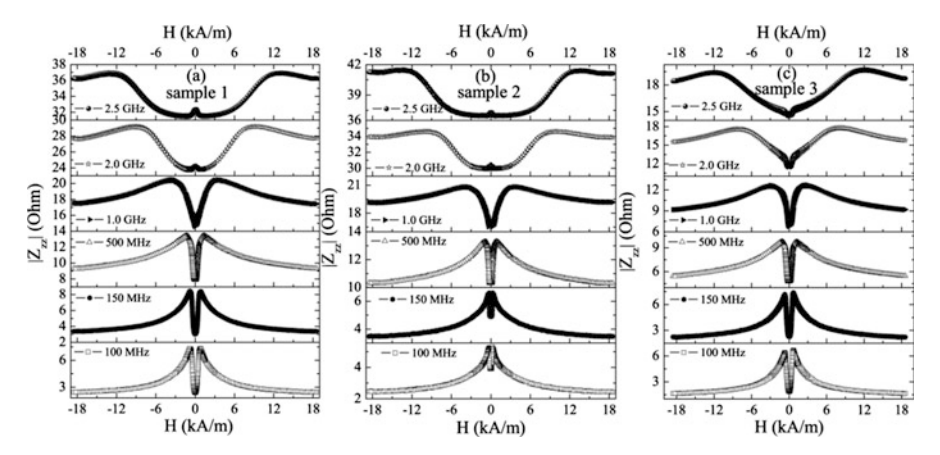
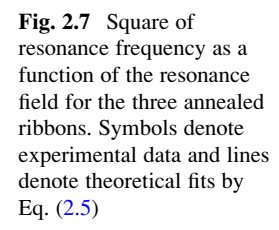


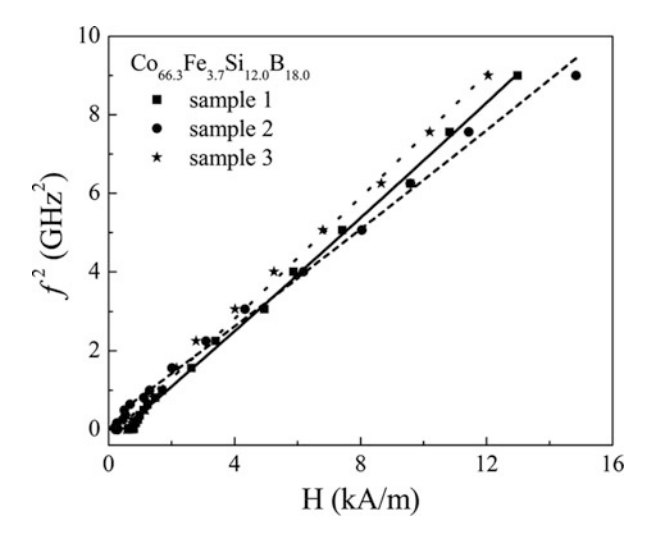
Fig. 2.6 Magnetic field dependence of diagonal impedance component at selected frequencies for stress-annealed Co_{66.3}Fe_{3.7}Si_{12.0}B_{18.0} samples

relaxation, indicating the optimum conditions for induced anisotropy and lower magnetostriction coefficient in comparison with the other two annealed samples. Higher anisotropy fields are detected in stress-annealed samples 2 and 3 as a consequence of the smaller magnitude of the non-recoverable plastic contribution to the induced anisotropy arising from the pre-annealing. Furthermore, the asymmetric character of the GMI in sample 3 could be attributed to the partial crystallization taken place at the surface of this ribbon annealed at 360 °C during 2 h, as a consequence of the different anelastic contribution to the stress-induced anisotropy in the crystallized surface of this sample in comparison with the other two annealed ribbons [32].

Concerning the frequency dependence with the field corresponding to the Z_{zz} maximum, it is observed that the MI peaks are shifted to higher magnetic fields as the frequency is raised. This shift is related to the variation of the skin depth with the frequency-dependent magnetic permeability. In fact, the presence of stress-induced anisotropy with the easy magnetization direction perpendicular to the ribbon axis leads to significantly high values of the transverse magnetic permeability for these samples. In addition, this shift results an evidence of the ferromagnetic resonance contribution to the impedance [38]. Studying the position of the FMR peaks, i.e., the frequency at which appears a maximum of the impedance for each applied field, the data can be fitted by the well-known FMR expression described above (Eq. (2.5)). The results for the three samples are displayed in Fig. 2.7.

It shows a good agreement between the fitting of the resonance frequencies and the Kittel resonance condition (Eq. (2.5)). The experimental results provide us the anisotropy effective fields of $H_K = 290$ A/m for sample 1, $H_K = 550$ A/m for sample 2, and $H_K = 650$ A/m for sample 3. These values are comparable to derived ones from hysteresis loops measured along the ribbon axis at 50 Hz [32].





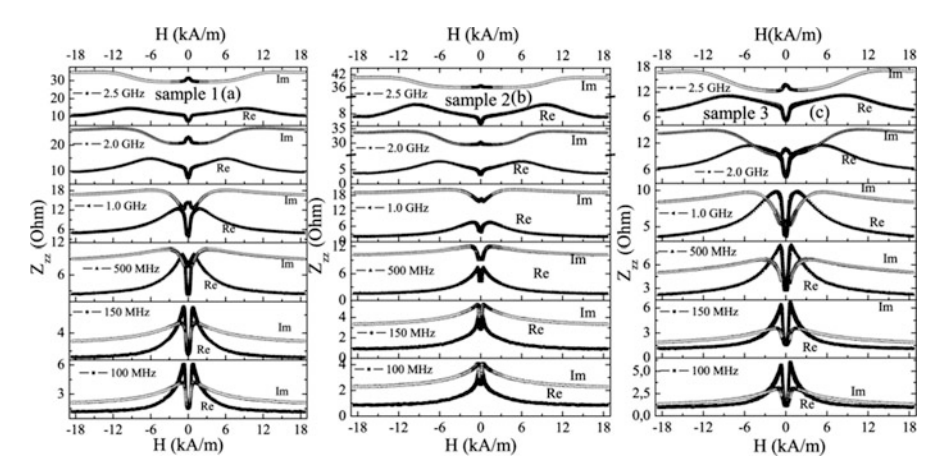


Fig. 2.8 Real (R) and imaginary (χ) parts of the impedance as a function of the applied magnetic field for several frequencies for the three stress-annealed samples

The effect of FMR is even more evident when the field dependence of real (R) and imaginary (X) part of diagonal impedance is plotted. In Fig. 2.8, it can be observed that at low frequency (below 500 MHz), the R and X impedance components show a parallel trend. However, at high frequency, when the maximum in the real part occurs then a slope change in the imaginary part vs. applied field is displayed, according to the characteristic behavior of the imaginary impedance component at resonance [38].

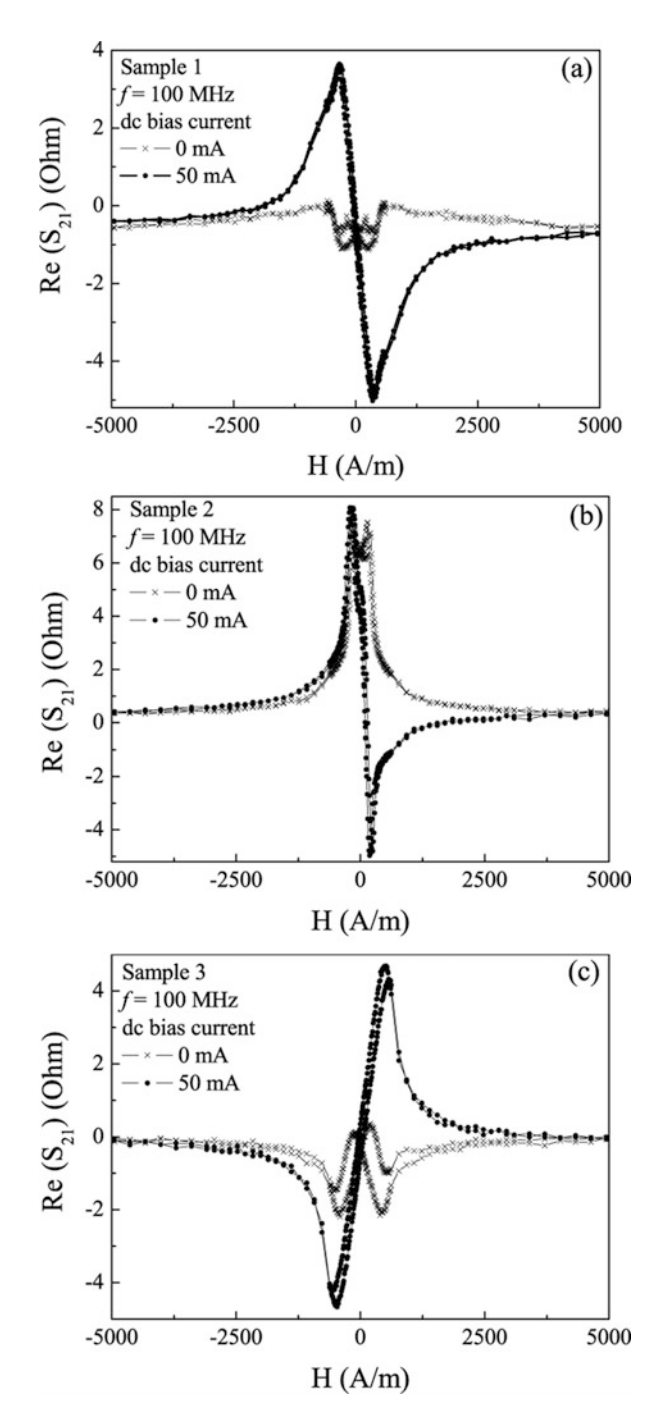
We have also explored the off-diagonal impedance component for these three ribbons. The off-diagonal GMI is a cross-magnetization process that is due to the appearance of a longitudinal magnetization when the sample is transverse

magnetized by the excitation current pass through it, i.e., a non-zero off-diagonal component of the permeability tensor is present in the ferromagnetic conductor [39, 40].

The reactance of the pick-up coil for $S_{21}(H)$ detection starts to affect the measurements as the frequency increases, therefore we present the off-diagonal measurements at lower frequencies than the longitudinal ones. Figure 2.9 shows the real part of off-diagonal impedance $Z_{vz}(H) \sim S_{21}(H)$ measured at 100 MHz with different dc bias currents I_b for all samples. The amplitude of bias current I_b was small to prevent the ribbon overheating and crystallization. For $I_b = 0$, the off-diagonal impedance shows symmetric peaks for applied field values in the vicinity of the anisotropy field $\pm H_K$, for each ribbon. In this case, the total response should be zero for all field range; however, these symmetric peaks are due to the small residual helical anisotropy, which remains in the samples after been submitted to stress annealing [41]. With $I_b = 50$ mA the off-diagonal response significantly increases and becomes antisymmetric with respect to the field H, having almost linear behavior in the field range of ± 500 A/m, for the three samples. This behavior can be explained as follows. The transverse dc field created by the bias current makes one or the opposite (depending on the current direction) transverse magnetization direction more favorable. Domains with magnetization lying along the bias field increase at the expense of domains with magnetization aligned against this field. If it is sufficiently large, domains with magnetization lying along the bias field collapse forming a single domain structure. Then, both the axial external magnetic field and the transverse dc bias field determine the re-magnetization process [42, 43]. Besides, if this field is sufficiently high, the field dependence of the off-diagonal impedance becomes asymmetric and anhysteretic [44] as it is shown in Fig. 2.9. The quasi-linear behavior near H = 0 of $Z_{vz}(H)$ is rather interesting for field sensors [17, 34, 44].

The frequency dependence of diagonal and off-diagonal impedance components is completely different. In Fig. 2.10 the maximum values of $|Z_{zz}|$ and S_{21} as a function of frequency are represented for the three samples. As can be observed in it the diagonal impedance component increases monotonously; however, the off-diagonal one shows a maximum. This different behavior should be explained from Eqs. (2.2) and (2.3). The diagonal impedance is inversely proportional to skin depth, thus when the frequency increases and δ decreases, $|Z_{zz}|$ increases. However, the off-diagonal impedance is directly proportional to $(\omega \mu_{zy} \delta)$. There is a competition between the magnetic induction term $(\omega \mu_{zy})$, which increases with the frequency, and the skin depth δ that decreases with the frequency. As a consequence the off-diagonal impedance exhibits a peak [17].

Fig. 2.9 Real part of the off-diagonal impedance (in terms of S_{21} -parameter) dependencies on external axial magnetic field with the dc bias current as a parameter at f = 100 MHz for (a) sample 1, (b) sample 2, and (c) sample 3



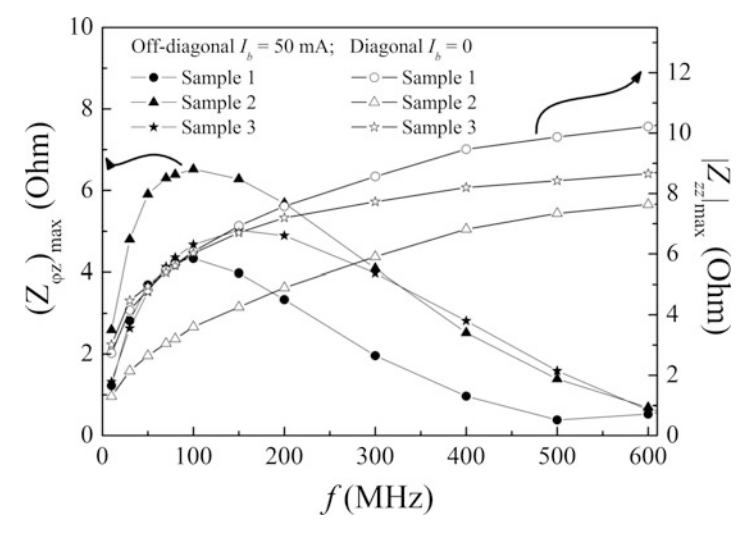


Fig. 2.10 Frequency dependence of maximum off-diagonal and diagonal impedance components for the three annealed samples. Symbols denote experimental data and lines are guides for the eye

2.5.2 Influence of Current Annealing on GMI Effect in Co-Rich Amorphous Ribbons

Joule annealing requires short annealing time to enhance soft magnetic behavior exhibited by Co-based nearly zero magnetostriction coefficient [45], and the references therein. To study the current-annealing effect on the longitudinal magnetoimpedance of the $\text{Co}_{71.25}\text{Fe}_{3.75}\text{Si}_{10}B_{15}$ ribbon, 1 cm long pieces of the as-quenched ribbon were Joule annealed with a dc electrical current (440–680 mA) passing during 5 min along the ribbon. This annealing process develops a transverse magnetic anisotropy of average value of around 100 J/m, although of inhomogeneous character, that enhances the transverse susceptibility [11, 46].

Figure 2.11 shows 3-D variation of the electrical giant magnetoimpedance ratio, $\Delta Z/Z(H, I_{\rm ann})$, as a function of the applied magnetic field with the annealing current intensity, $I_{\rm ann}$, as a parameter, at selected frequencies between 100 and 3500 MHz of the ac electrical current flowing along the ribbon. It can be seen that a two-peaks response (symmetrically with respect to H) is present in all the frequency range for all samples. The value of H corresponding to the peaks ($\Delta Z/Z$ maximum value) is linked to the average value of the anisotropy field, H_K , at high frequency values, and to the anisotropy distribution in the sample. As it is expected, as a general rule, the evolution of $\Delta Z/Z(\%)$ with the frequency for the current-annealed ribbons shows that the maximum increases with the frequency, remaining the two-peaks behavior.

To remark the effect of current-annealing intensity on the GMI response, we have plotted the variations of $\Delta Z/Z(\%)$ as a function of $I_{\rm ann}$ in Fig. 2.12 at different values of the driving current frequency. As can be observed, this $\Delta Z/Z(\%)$ variation

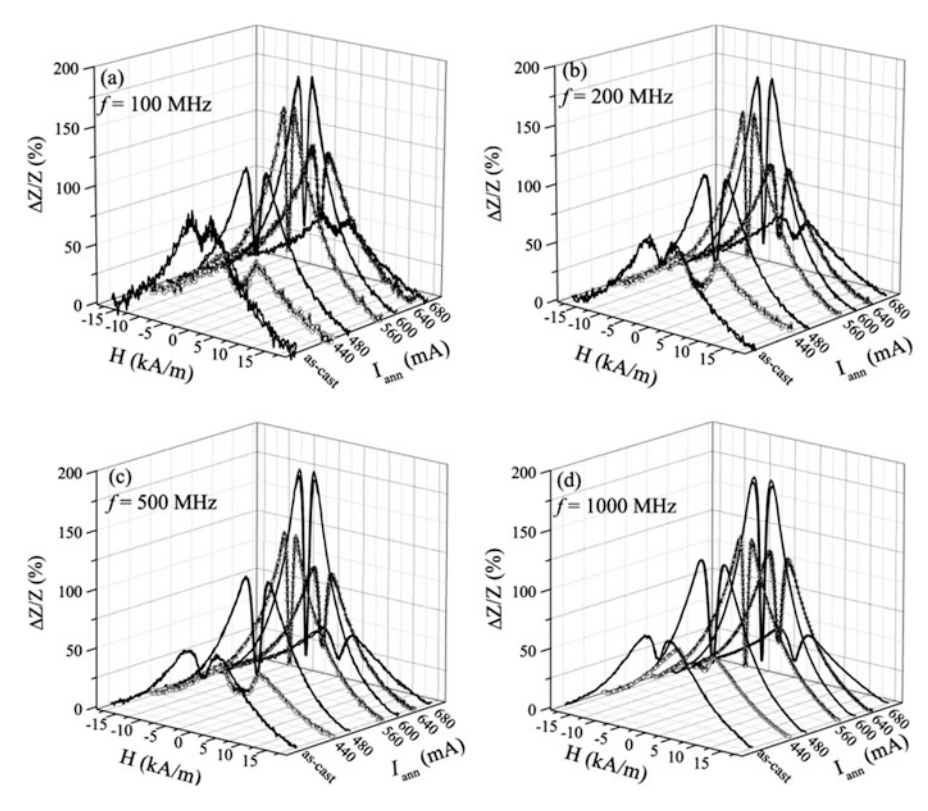


Fig. 2.11 GMI ratio as a function of the magnetic field applied along the ribbon axis at different values of the driving current frequency: (a) 100 MHz, (b) 200 MHz, (c) 500 MHz, and (d) 1000 MHz for Joule annealed Co_{71.25}Fe_{3.75}Si₁₀B₁₅ ribbons at different current intensities

Fig. 2.12 Frequency dependence of the GMI ratio as a function of the annealing current I_{ann} . Symbols denote experimental data and lines are guides for the eye

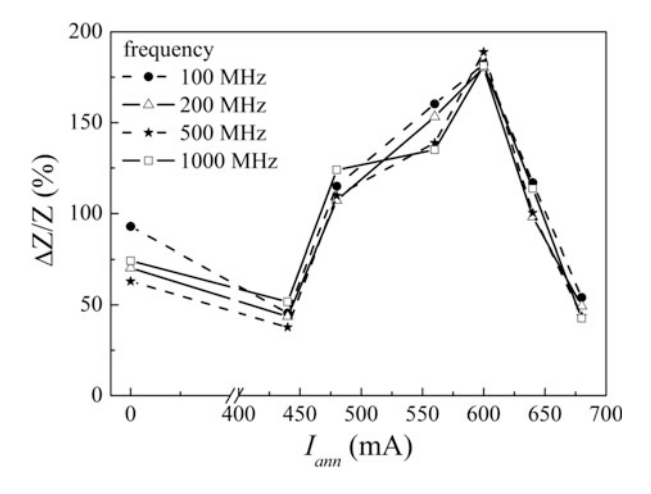
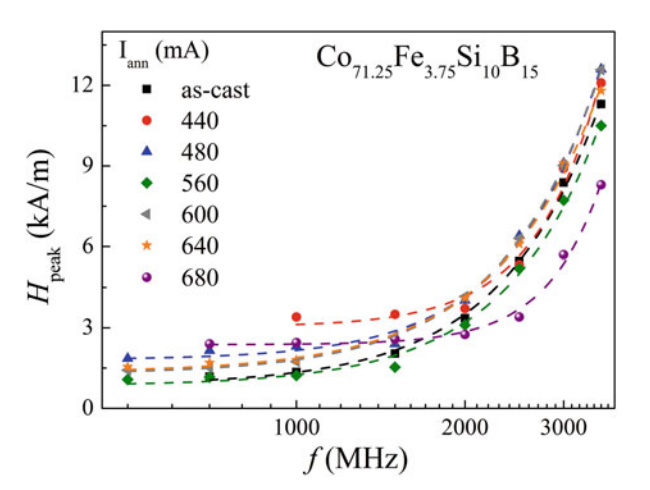


Fig. 2.13 Frequency dependence of the magnetic field, $H_{\rm peak}$, where GMI ratio presents a maximum for current-annealed ${\rm Co_{71.25}Fe_{3.75}Si_{10}B_{15}}$ ribbons. Symbols denote experimental data and lines are guides for the eye



presents a maximum around 600 mA, which is the intensity of current annealing to develop the maximum transverse induced magnetic anisotropy such has been reported in [37, 46].

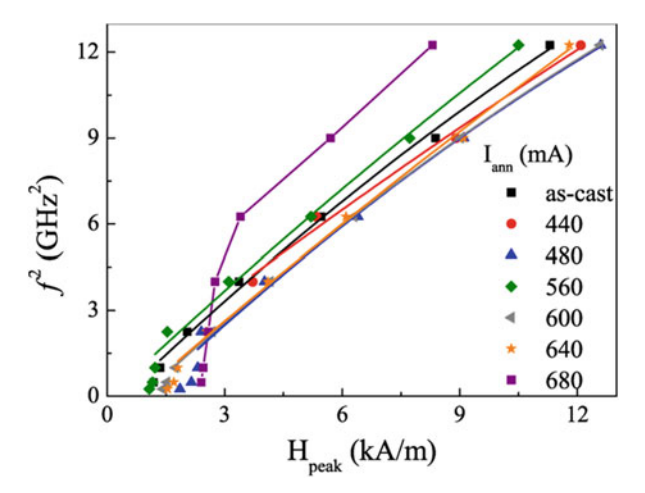
Furthermore, the frequency dependence of the value of the magnetic field, $H_{\rm peak}$, where the GMI ratio presents the maximum value, is represented in Fig. 2.13 for all as-cast and current-annealed ribbons. It can be seen that the $H_{\rm peak}$ value increases with the frequency for all samples.

Maximum GMI response and $H_{\rm peak}$ value depend on the annealing current intensity, since both features are strongly connected to the anisotropy field. The origin of the $H_{\rm peak}$ shift as the frequency increases is related to the change in skin depth through the frequency-dependent magnetic permeability. As increasing the driving frequency of the ac electric current along the ribbon, a decrease of the surface layer thickness is produced and transverse permeability should drastically change. The application of a longitudinal magnetic field large enough for saturating the sample modifies the transverse permeability by the reorientation of the static magnetization, and by the own permeability change simultaneously. As a consequence, the effective skin depth increases, providing an impedance decreasing.

As mentioned above, the $H_{\rm peak}$ value corresponding to the maximum of the magnetoimpedance of all the samples is shifted towards larger field values when the frequency is increased. This is a conclusive evidence of the ferromagnetic resonance contribution to the GMI effect [38]. Studying the position of the FMR peaks, i.e., the frequency at which appears a maximum of the impedance for each field H, we can observe that data are well fitted by the above mentioned FMR expression, Eq. (2.5), except for the Joule annealed sample with 680 mA current intensity (see Fig. 2.14).

It is worthwhile mentioning that this ribbon showed a clear trace of the first stage of crystallization as was shown in [37].

Fig. 2.14 Square of frequency as a function of $H_{\rm peak}$ for current-annealed ${\rm Co_{71.25}Fe_{3.75}Si_{10}B_{15}}$ amorphous ribbons. Symbols denote experimental data and lines denote theoretical fits by Eq. (2.5)



2.6 Conclusions

Giant magnetoimpedance response of Co-rich amorphous Co_{71,25}Fe_{3,75}Si₁₀B₁₅ and Co_{66.3}Fe_{3.7}Si_{12.0}B_{18.0} alloy ribbons results to be rather sensitive to currentannealing and stress-annealing treatments, respectively, as a consequence of the induction of different uniaxial anisotropy transverse to the ribbon axis, affecting drastically the soft magnetic character of the sample. Two-peaks behavior of the GMI effect is observed in all current-annealed ribbons. The effect is enhanced as increasing the intensity of the annealing current (up to 600 mA at which $\Delta Z/Z$ ratio achieves its maximum value). This behavior is explained in terms of the frequency dependence of skin depth and the dispersion of easy axes through the ribbon thickness. Moreover, the macroscopic magnetic anisotropy induced by this thermal treatment has an inhomogeneous character as a consequence of the non-uniform transverse field created by the electric current through the ribbon cross section during the annealing. In the case of stress-annealing ribbons, the GMI response is sharper and narrower as a consequence of the more uniform induced anisotropy in comparison with the as-quenched ribbon, which has to be considered as key-factor for sensing applications. Two-peaks behavior in the GMI effect is observed for the ribbon stress annealed at 400 °C, while in those samples submitted to a previous stress relaxation the two-peaks behavior show some peculiarities. The ribbon pre-annealed at 340 °C displays two-peaks behavior but emerging at frequency above 150 MHz, while the sample pre-annealed at 360 °C shows an asymmetry in the GMI effect. Finally, ferromagnetic resonance effects at high frequencies are detected in all studied ribbons.

Acknowledgements This work was financially supported by the Spanish MINECO Ref. MAT2013-47231-C2-1-P, Ref. MAT2013-47231-C2-2-P, and Ref. MAT2013-48054-C2-2-R, Asturias Government Ref. FC-15-GRUPIN14-085, Basque Government under Saiotek 13 PROMAGMI (SPE13UN014), and DURADMAG (S-PE13UN007). Technical and human support provided by SGIker (UPV/EHU, MICINN, GV/EJ, ERDF, and ESF) is gratefully acknowledged.

References

- Jiles, D.C.: Recent advances and future directions in magnetic materials. Acta Mater. 51, 5907 (2003)
- Hasegawa, R.: Advances in amorphous and nanostructured materials. J. Optoelectron. Adv. Mater. 6, 503 (2004)
- Zhukov, A., Ipatov, M., Churyukanova, M., Kaloshkin, S., Zhukova, V.: Giant magnetoimpedance in thin amorphous wires: from manipulation of magnetic field dependence to industrial applications. J. Alloys Compd. 586, S279 (2014)
- Panina, L.V., Mohri, K.: Magneto-impedance effect in amorphous wires. Appl. Phys. Lett. 65, 1189 (1994)
- 5. Beach, R., Berkowitz, A.: Giant magnetic field dependent impedance of amorphous FeCoSiB wire. Appl. Phys. Lett. **64**, 3652 (1994)
- Honkura, Y.: Development of amorphous wire type MI sensors for automobile use. J. Magn. Magn. Mater. 249, 375 (2002)
- Mohri, K., Uchiyama, T., Shen, L.P., Cai, C.M., Panina, L.V.: Amorphous wire and CMOS IC-based sensitive micro-magnetic sensors (MI sensor and SI sensor) for intelligent measurements and controls. J. Magn. Magn. Mater. 249, 351 (2002)
- Marín, P., López, M., Vlad, A., Hernando, A., Ruiz-González, M.L., González-Calbet, J.M.: Magnetic field driving custom assembly in (FeCo) nanocrystals. Appl. Phys. Lett. 89, 033508 (2006)
- 9. Ohodnicki, P.R., Laughlin, D.E., McHenry, M.E., Keylin, V., Huth, J.: Temperature stability of field induced anisotropy in soft ferromagnetic Fe, Co-based amorphous and nanocomposite ribbons. J. Appl. Phys. **105**, 07A322 (2009)
- 10. Chaturvedi, A., Laurita, N., Leary, A., Phan, M.-H., McHenry, M.E., Srikanth, H.: Giant magnetoimpedance and field sensitivity in amorphous and nanocrystalline $(Co_{1-x}Fe_x)_{89}Zr_7B_4$ (x = 0, 0.025, 0.05, 0.1) ribbons. J. Appl. Phys. **109**, 07B508 (2011)
- 11. Laurita, N., Chaturvedi, A., Bauer, C., Jayathilaka, P., Leary, A., Miller, C., Phan, M.-H., McHenry, M.E., Srikanth, H.: J. Appl. Phys. **109**, 07C706 (2011)
- Manna, S.K., Srinivas, V.: Magnetic and magnetoimpedance studies on controlled Joule annealed amorphous Co₇₃Fe_{4.5}Ni_{0.5}Mn_{0.5}Nb_{0.5}Si_{4.2}B_{16.8} alloy. J. Appl. Phys. 115, 17A324 (2014)
- 13. Knobel, M., Vazquez, M., Kraus, L.: Giant magnetoimpedance. In: Buschow, K. (ed.) Handbook of Magnetic Materials, pp. 497–563. Elsevier, North-Holland (2003)
- 14. Phan, M.-H., Peng, H.-X.: Giant magnetoimpedance materials: fundamentals and applications. Prog. Mater. Sci. **53**, 323 (2008)
- 15. Kraus, L.: Theory of giant magneto-impedance in the planar conductor with uniaxial magnetic anisotropy. J. Magn. Magn. Mater. **195**, 764 (1999)
- Makhnovskiy, D.P., Panina, L.V., Mapps, D.: Field-dependent surface impedance tensor in amorphous wires with two types of magnetic anisotropy: helical and circumferential. Phys. Rev. B. 63, 144424-1–144424-17 (2001)
- Kraus, L.: Off-diagonal magnetoimpedance in stress-annealed amorphous ribbons. J. Magn. Magn. Mater. 320, e746–e749 (2008)
- Kraus, L., Vázquez, M., Infante, G., Badini-Confalonieri, G., Torrejón, J.: Nonlinear magnetoimpedance and parametric excitation of standing spin waves in a glass-covered microwave. Appl. Phys. Lett. 94, 062505 (2009)
- 19. Panina, L.V., Mohri, K., Uchiyama, T., Noda, M., Bushida, K.: Giant magneto-impedance in Co-rich amorphous wires and films. IEEE Trans. Magn. 31, 1249 (1995)
- Ciureanu, P., Britel, M., Ménard, D., Akyel, C., Yelon, A., Rouabhi, M., Cochrane, R.W.: Anisotropic behavior of permalloy wires using the giant magnetoimpedance effect. J. Magn. Magn. Mater. 196–197, 391 (1999)
- Crisan, O., Le Breton, J.M., Filoti, G.: Nanocrystallization of soft magnetic Finemet-type amorphous ribbons. Sens. Actuators A. 106, 246 (2003)

- Zhang, K., Zhou, D.W., Han, B., Lv, Z., Xun, X.C., Du, X.B., Liu, Y.Q., Yao, B., Zhang, T., Li, B.H., Wang, D.: Annealing temperature dependence of magnetic properties and magnetoimpedance effect in CoZrB alloys. J. Alloys Compd. 464(28), (2008)
- 23. Allia, P., Tiberto, P., Baricco, M., Vinai, F.: dc Joule annealing of amorphous metallic ribbons: experimental aspects and model. Rev. Sci. Instrum. **64**, 1053 (1993)
- 24. Sahoo, T., Majundar, B., Srivinas, V., Srinivas, M., Nath, T.K., Agarwal, G.: Improved magnetoimpedance and mechanical properties on nanocrystallization of amorpous Fe_{68.5}Si_{18.5}Cu₁Nb₃B₉ ribbons. J. Magn. Magn. Mater. **343**, 13 (2013)
- Hoque, S.M., Haque, A., Rahman, M.O., Nghi, N.H., Hakim, M.A., Akther, S.: Ultra-soft magnetic properties and giant magneto-impedance of Co₆₈Fe_{4.5}Si_{12.5}B₁₅. J. Non-Cryst. Solids. 357, 2109 (2011)
- 26. Kotagiri, G., Ramarao, S.D., Markandeyulu, G.: Magnetoimpedance studies on laser and microwave annealed Fe₆₆Ni₇Si₇B₂₀ ribbons. J. Magn. Magn. Mater. **382**, 43 (2015)
- González, L., Bonastre, J., Sánchez, T., Santos, J.D., Sánchez, M.L., Chiznik, A., Domínguez, L., Ipatov, M., Zhukova, V., Zhukov, A., González, J., Suñol, J.J., Hernando, B.: Magnetoimpedance response in Co-based amorphous ribbons obtained under the action of a magnetic field. IEEE Trans. Magn. 48, 4375 (2012)
- Kim, C.G., Jang, K.J., Kim, H.C.: Asymmetric giant magnetoimpedance in field-annealed Co-based amorphous ribbon. J. Appl. Phys. 15, 5447–5449 (1999)
- 29. Gupta, P., Gupta, A., Franco, V., Conde, A.: Joule heating as a technique for obtaining uncoupled soft and hard magnetic phases in a Finemet alloy. J. Appl. Phys. **101**, 133909 (2007)
- Shari, F., Beitollahi, A., Shabestari, S.G., Ghanaatshoar, M., Tehranchi, M.M., Mohseni, S.M., Roozmeh, S.E., Wanderka, N., Florillo, F.: Structural characterization and magnetoimpedance effect in amorphous and nanocrystalline Al Ge-substituted FeSiBNbCu ribbons. J. Magn. Magn. Mater. 312, 35–42 (2007)
- 31. Bonastre, J., Suñol, J.J., Bruna, P., Sato, K., Santos, J.D., Hernando, B.: Influence of a magnetic field applied during the quenching process on the spin density and nanoscale of an amorphous Fe-B ribbon. Mater. Lett. **87**, 131–134 (2012)
- 32. Talaat, A., Ipatov, M., Zhukova, V., Zhukov, A.P., González, J., González-Legarreta, L., Prida, V.M., Hernando, B.: High frequency magnetoimpedance response of stress annealed Co_{66.3}Fe_{3.7}Si_{12.0}B_{18.0} amorphous alloy ribbons. J. Appl. Phys. **114**, 023904 (2013)
- Narita, K., Yamasaki, J., Fukunaga, H.: Measurement of saturation magnetostriction of a thin amorphous ribbon by means of small-angle-magnetization-rotation. IEEE Trans. Magn. 16, 435 (1980)
- 34. Ipatov, M., Zhukova, V., Zhukov, A., González, J.: Expanding the longitudinal magnetoimpedance sensor range by direct bias current. J. Appl. Phys. 113, 203902 (2013)
- Nielsen, O.V.: Effects of longitudinal and torsional stress annealing on the magnetic anisotropy in amorphous ribbon materials. IEEE Trans. Magn. 21, 2008 (1985)
- Blanco, J.M., Barbón, P.G., Pierna, A.R., González, J.: Compositional dependence of the stress plus field induced anisotropy in Co-Ni-Si-B and Co-Fe-Ni-Si-B amorphous alloy ribbons. J. Non-Cryst. Solids. 136, 91 (1991)
- Vázquez, M., González, J., Hernando, A.: Induced magnetic anisotropy and change of the magnetostriction by current annealing in Co-based amorphous alloys. J. Magn. Magn. Mater. 53, 323 (1986)
- 38. Barandiarán, J.M., García-Arribas, A., de Cos, D.: Transition from quasistatic to ferromagnetic resonance regime in giant magnetoimpedance. J. Appl. Phys. **99**, 103904 (2006)
- Antonov, A.S., Iakubov, I.A., Lagarikov, A.N.: Longitudinal-transverse linear transformation of the HF-current in soft magnetic materials with induced anisotropy. IEEE Trans. Magn. 33, 3367 (1997)
- Buznikov, N.A., Kim, C.G., Kim, C.O., Yoon, S.S.: Asymmetric off-diagonal magnetoimpedance in field-annealed amorphous ribbons: analysis of bias current effect. J. Magn. Magn. Mater. 309, 216 (2007)

- 41. Malátek, M., Kraus, L.: Off-diagonal GMI sensor with stress-annealed amorphous ribbon. Sens. Actuators A. **164**, 41–45 (2010)
- 42. Ipatov, M., Zhukova, V., Zhukov, A., Gonzalez, J., Zvezdin, A.: Low field hysteresis in the magnetoimpedance of amorphous microwires. Phys. Rev. B. 81, 134421 (2010)
- 43. Ipatov, M., Zhukova, V., Zhukov, A., Gonzalez, J.: Magnetoimpedance sensitive to dc bias current in amorphous microwires. Appl. Phys. Lett. 97, 252507 (2010)
- 44. Ipatov, M., Zhukova, V., Gonzalez, J., Zhukov, A.: Symmetry breaking effect of dc bias current on magnetoimpedance in microwire with helical anisotropy: application to magnetic sensors. J. Appl. Phys. **110**, 086105 (2011)
- Manna, S.K., Srinivas, V.: Magnetic and magnetoimpedance studies on controlled Joule annealed amorphous Co₇₃Fe_{4.5}Ni_{0.5}Mn_{0.5}Nb_{0.5}Si_{4.2}B_{16.8} alloy. J. Appl. Phys. 115, 17A324 (2011)
- 46. Ipatov, M., González-Legarreta, L., Garcia, J., Chizhik, A., Domínguez, L., Zhukova, V., Zhukov, A., Hernando, B., González, J.: Induced giant magnetoimpedance effect by current annealing in ultra thin Co-based amorphous ribbons. IEEE Trans. Magn. 49, 1009 (2012)

Chapter 3 Melt Extracted Microwires

H. Wang, F.X. Qin, H.X. Peng, and J.F. Sun

3.1 Introduction to Melt Extraction Technique

Amorphous microwires as a new category of advanced materials possess many excellent mechanical and magnetic properties, and have received considerable attention from both the research and industry community. Significant efforts have been devoted to the optimization of fabrication process, tailoring of mechanical and magnetic properties, sensor and microwave applications [1–6]. To now, amorphous wires can be prepared by several methods such as glass coating (Taylor-wire technique) [7, 8], in-water quenching [9–12], and melt extraction technology (MET) [13–16]. Compared with others, the solidification rate of wires prepared by melt extraction is the highest, which endows the resultant wires many excellent mechanical and magnetic properties. To our best recollection, there is no dedicated monograph on melt extraction microwires yet. Therefore, in this chapter, we will focus on the melt-extracted amorphous microwires, detailing the fabrication process, wire formation mechanism, mechanical and magnetic properties, thus provide some technical base for its application in sensor and multifunctional composites.

The concept of melt extraction was firstly introduced by Maringer [17] in 1974 to produce metallic microwires. The basic principle can be briefed as follows: a high-speed wheel with a sharp edge is employed to contact the molten alloy surface and then a molten layer can be rapidly extracted and cooled down to be form of wires. During the extraction process, the solidification rate of metallic wires can

Institute for Composites Science Innovation (InCSI), School of Materials Science and Engineering, Zhejiang University, Hangzhou 310027, China e-mail: faxiangqin@zju.edu.cn

J.F. Sun

School of Materials Science and Engineering, Harbin Institute of Technology, Harbin 150001, China

H. Wang • F.X. Qin (⋈) • H.X. Peng

54 H. Wang et al.

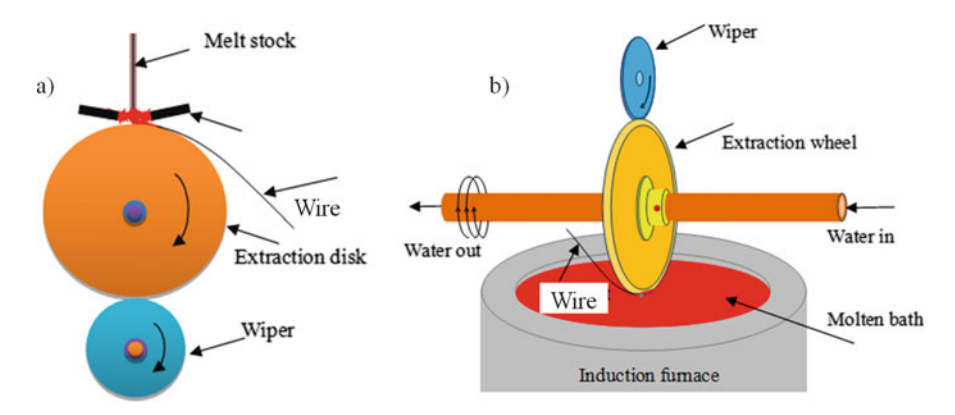


Fig. 3.1 Schematic illustrations of melt extraction technique, (a) pendant drop and (b) crucible melt extraction method

reach up to 10^5 – 10^6 K/s; it has been widely used to fabricate amorphous metallic wires and a few ceramic microwires, e.g., CaO/Al₂O₃ and Al₂O₃/Y₂O₃ [18-20]. Because it does not require any liquid cooling mediums, MET can also be used to fabricate some highly reactive alloys such as aluminum, titanium, zirconium, and magnesium wires [13, 21, 22]. Melt extraction technique was divided into pendant drop melt extraction (PDME) [23–25] and crucible melt extraction (CME) [13, 15, 22, 26] according to the source of molten materials, as shown in Fig. 3.1. For PDME (Fig. 3.1a), the source of molten material is a droplet formed on the end of master alloy, the liquid metal solidifies on the extracted wheel edge and then releases spontaneously in the form of solidified microwires. There is no reaction between crucible and melt during the fabrication process. However, the alloy was melted by oxy-acetylene flame which will lead to the oxidation of solidified microwires, meanwhile, the molten drop was hanged in the air and sensitive to ambient environment such as the oxy-acetylene flame and rotation of wheel will result in the molten instability. The CME facility is schematically shown in Fig. 3.1b. Unlike PDME, the master alloy was put in a crucible below the metal wheel and remelted by induction heating. The diameter of the fabricated microwires was controlled by adjusting the extracted wheel speed and the insert depth between the wheel and melt. By reducing the size of the crucible, ultra fine, ultra soft magnetic and high reactive metallic and amorphous microwires, for example, Co-based, Fe-based, Ti-based, Al-based, and Cao-Al₂O₃-ZrO₂ wires were fabricated in McGill University [18, 26–31] and Tohoku University [32–34] over the last few decades.

3.2 Casting Method: Production and Processing

Melt extraction requires bringing the liquid metal puddle into contact with a V-shaped rotating wheel edge. The metal solidifies on the edge, adheres, and then releases in the form of solid powder, wire, or microwire depending on the process

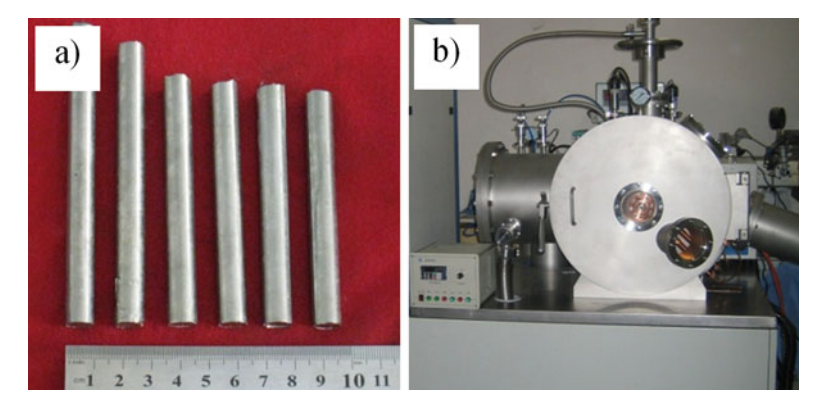


Fig. 3.2 (a) Quaternary alloy ingots and (b) overview of melt extraction setup

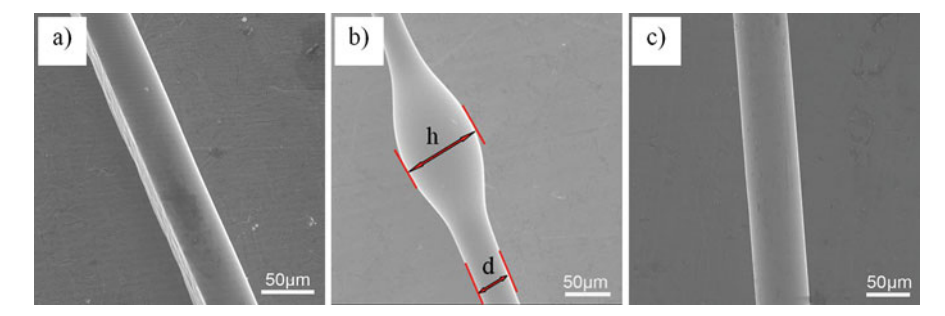


Fig. 3.3 SEM images of the melt-extracted microwires showing (a) uniform with concaved track wire; (b) wire with Rayleigh waves; (c) fine and uniform wire

parameters, viscosity of the melts and the wettability between molten and extracted wheel. The ingot with a diameter of 8–10 mm was prepared in argon atmosphere by arc melting, as shown in Fig. 3.2a. Processing optimization was performed using a home-built crucible melt extraction facility using a copper wheel with diameter of 160 mm and 60° knife-edge (Fig. 3.2b).

3.2.1 Process Parameter and Optimization

During the optimization of different melt extraction process parameters, wires of three different geometrical morphologies are obtained: one is uniform wire but with concaved track, the second is wire with Rayleigh waves, and the third is fine and uniform wire, as shown in Fig. 3.3a–c, respectively. The diameter of the uniform circular part of wires and the thickness of the nonuniform part of Rayleigh waves are defined as d and h, respectively, as shown in Fig. 3.3b. The dimensions of wires,

56 H. Wang et al.

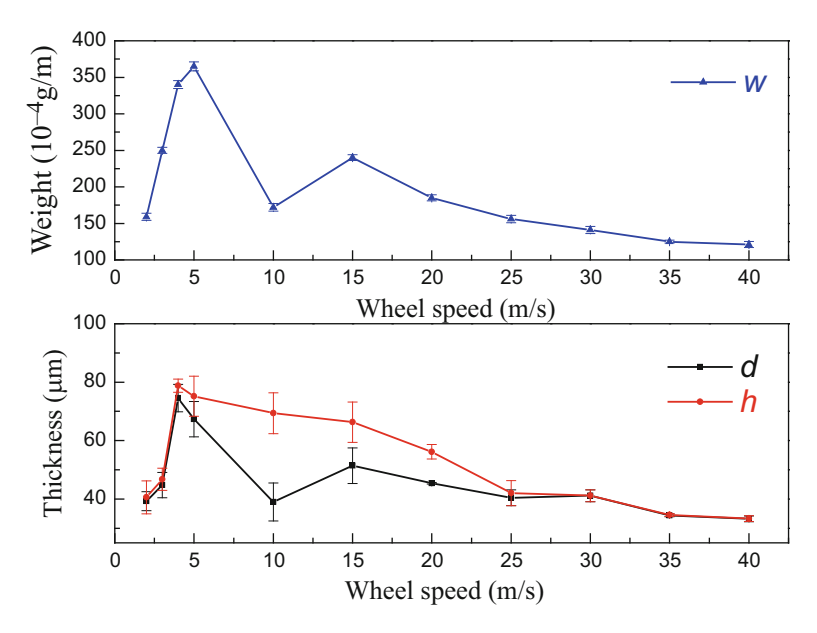


Fig. 3.4 The weight per meter w, wire diameter d, Rayleigh wave thickness h as a function of wheel velocity

i.e., d and h, are measured for at least 50 wire samples for SEM images to obtain the average for each data point. The weight of the extracted wires, w, i.e., extracted layer, was examined for ten samples each with length of 10 cm.

The variation of wire diameters *vs* wheel velocity passes through a maximum and then decreases with the increase of wheel velocity, shown in Fig. 3.4. For the weight of the extracted wires, the minimum of w occurs at a wheel velocity of 10 m/s, where the gap between d and h reaches maximum. These two plots can be divided into three regions according to the wheel speed: (a) low-speed region (2–5 m/s), (b) intermediate speed region (5–30 m/s), and (c) high-speed region (30–40 m/s). At low- and high-speed regions, wires exhibit a uniform diameter; while in the medium region, Rayleigh waves are found and h decreases with an increase of the wheel velocity. Obviously, there are some fluctuations of d, h, and w in the medium region. With an increase in wheel velocity, Rayleigh waves form and become larger; i.e., the difference between d and h increases and reaches a maximum at a wheel velocity of 10 m/s, where a larger number of particles formed.

It was considerred previously that the diameter of the wires or the thickness of the ribbon decreases with the increase of the wheel velocity, but in our test, the result is abnormal at low speeds. This phenomenon was also found in the melt extraction of ceramic material by Allahverdi [29] and Taha [35] in the melt spinning process of Al-Cu alloy. The abnormal behavior at low velocity may be caused by increasing wheel vibration when the wheel velocity increases within the low-speed range. The deeper the wheel penetrates into the molten, the larger the

diameters will be. On the other hand, as the wheel velocity increases (less than 10 m/s), the concave tracks on the extracted wire become wider. Therefore, the increasing vibration is the most likely reason for this abnormal behavior. With the increasing velocity ($V_{\rm s} > 10 \text{ m/s}$), the Rayleigh waves become smaller and the thickness of the wires decreases. The formation of the Rayleigh waves can be found elsewhere [36–38]. In the high-speed region ($V_{\rm s} > 30 \text{ m/s}$), fine and uniform wires with a diameter of less than 40 lm are obtained. The production of high-quality wires in the high-speed region has been reported by A. Inoue [39] for the melt extraction of Fe-Si-B and Co-Si-B alloys.

The Rayleigh instability is well known for a jet of liquid. Surface tension destabilizes the jet stream, and finally breaks it up into fine droplets. In the melt extraction process, since heat transfer and supercooling are simultaneously occurring with the extraction, the destabilizing effect of the surface tension cannot readily result in the wire or the stream may even break up. Hence, wires can be obtained, and frozen Rayleigh waves are observed on the free surface of the extracted wires, as illustrated by Allahverdi et al. [40] in Amorphous CaO-Al₂O₃ wire extraction (Fig. 3.5).

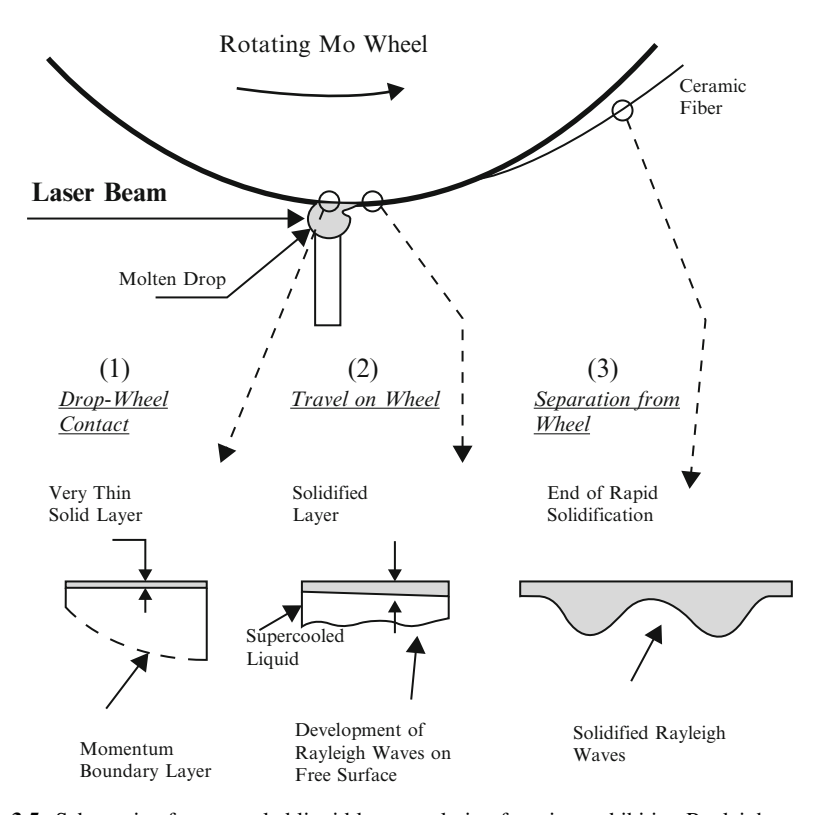


Fig. 3.5 Schematic of supercooled liquid layer evolution for wires exhibiting Rayleigh waves

58 H. Wang et al.

The molten feed rate together with the wheel velocity affects the roundness of the wire and the formation of Rayleigh waves obviously. The faster the molten feeds, the thicker it immerses into the copper wheel, which promoted heat transformed into it. When it happened, the molten supercooled below the melting point, and solidification occurred adjacent to the wheel tip, leading to the formation of the concave; meanwhile, on the free surface of the extracted layer, heat transferred to the supercooled region and surface tension acted as a dominant factor, tending to minimize the surface of the liquid layer, and some Rayleigh waves may occur when it experienced some improper cooling rate. Therefore, the coexistence of concave and Rayleigh waves narrows down the operating window of MET very and limits its applications.

On the other hand, as viscosity and surface tension relate closely to the temperature and superheat degree (difference value between actual temperature and melting point $T_{\rm m}$) of the melt, they also have effects on the melt-extracted process. Once the melting point of molten alloy is higher than the extracted wheel, melting and hot corrosion of the wheel will happen during the extraction process. As a result, the microstructures and compositions of the microwires had been modified, thereby reducing accuracy of wheel and stability of melt-extracted process. Figure 3.6 shows the TEM micromorphology of Co-based microwires with melting temperature of ~120 K above the melting. The microwires show two phases of amorphous state and nano-crystal state (~10 nm) with obvious boundary as displayed in Fig. 3.6a. Compositions of the amorphous and nano-crystal phases identified by EDS and shown as Co_{89.58}Fe_{5.43}Si_{3.87}B_{1.12} Co_{20.54}Fe_{1.21}Si_{1.84}Cu_{76.41}, respectively. The nano-crystal phases were further explored as Cu with FCC structure, which indicates that the rim of Cu wheel was melt caused by excessively high temperature during the melt-extracted process and leads to the changes in compositions and properties of microwires.

According to the processes mentioned above, the optimized parameters of meltextracted Co-based microwires are listed as follows:

- 1. Linear velocity of wheel ranged from 25 to 30 m/s;
- 2. Feeding speed ranged from 60 to 90 µm/s;
- 3. The melting temperature determined as $T_m + 50 \text{ K}$;
- 4. Wheel fabricated by pure Cu and preheated at 100 °C;
- 5. The melt-extracted process operated in Ar atmosphere.

We have fabricated Co-based micromicrowires with excellent qualities such as high roundness and good uniformity, the maximum length of an extracted microwire is large than 2000 mm. The micromicrowires so fabricated are displayed in Fig. 3.7.

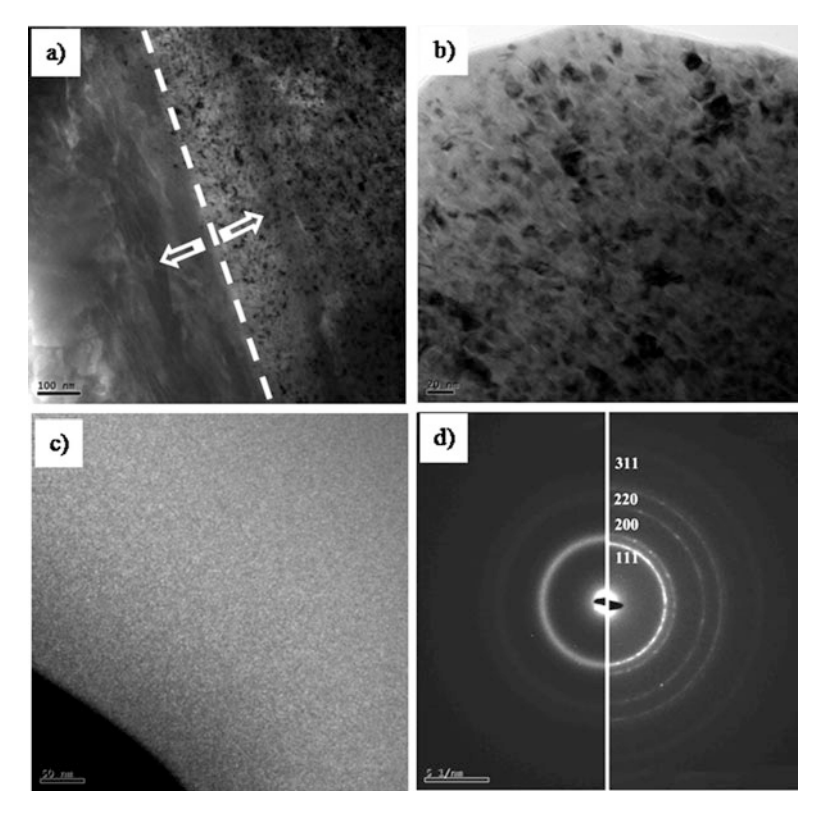


Fig. 3.6 TEM analyses of the extracted Co-based microwires with high molten temperature (a) TEM analysis of dual phase; (b) nanocrystals; (c) amorphous phase; (d) SAED for the amorphous and nanocrystals structures

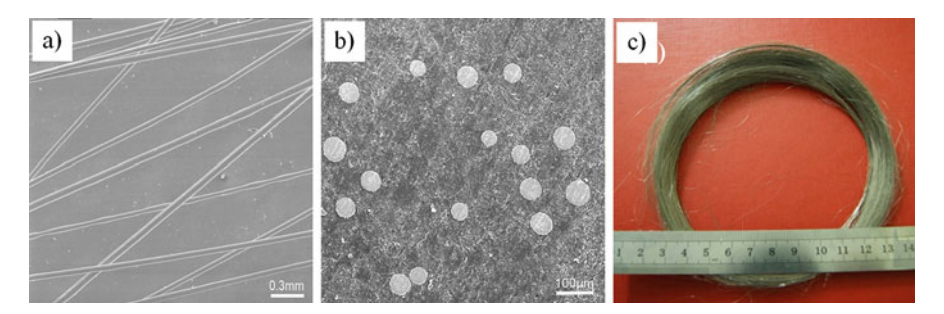


Fig. 3.7 Images of melt-extracted Co-based microwires (a) Longitudinal image; (b) Cross-section and (c) Macro-morphology

60 H. Wang et al.

3.2.2 Puddle Deformation Behavior

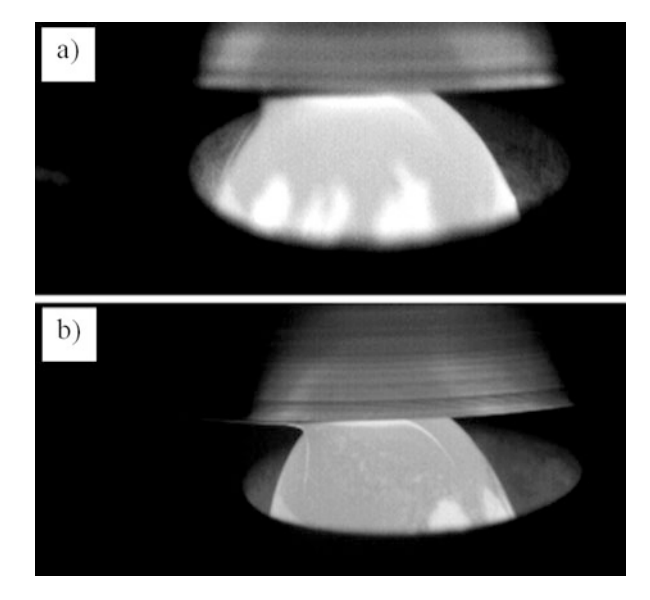
The contact geometry between the tip of the rotary wheel and molten provides us with some insight into the formation mechanism of melt extraction metallic wires. Figure 3.8a, b shows the contact geometry at wheel velocities of 2 and 30 m/s, where uniform wires were fabricated. From Fig. 3.8a, due to the surface tension of the molten materials and the decrease in temperature, the dragged molten tends to shrink with lower energy and a gap is observed in the front of the contact area. As the speed is increased, as shown in Fig. 3.8b, the shear force between the wheel and the molten becomes greater; a sharp frontier was seen in front of the contact area, which plays an important role in the formation of amorphous wires.

In fact, wetting of the copper by molten alloy plays a pivotal role in producing amorphous wires. In an isothermal static wetting, the wettability can be expressed by Young's equation as follows:

$$\cos \theta = (\gamma_{sv} - \gamma_{sl})/\gamma_{lv} \tag{3.1}$$

where γ is the surface energy or surface tension; and the subscripts s,l, and ν indicate the solid, liquid, and vapor, respectively. Once the contact interface begins to move, the conditions are generally complicated. This is because the dynamic forces generated by motion change the surface tension, altering the balance in the Young's equation. In the optimization of process parameters, the surface tension of molten acts as a hindrance to limit the fluid of molten and tends to increase as the temperature decreases. In the low velocity region, part of the solidification occurs on the wheel tip and reduces the temperature of the molten.

Fig. 3.8 Contact geometry between molten drop and rotating wheel (a) 2 m/s; (b) 30 m/s [14]



In this region, surface tension evolving with temperature acts as a dominant force to produce metallic wires. The mechanism of wire formation may be influenced by the heat transfer from the molten to the wheel tip; in the high-speed region, wettability of this process is promoted by dynamic shear force and overcomes the surface tension obstacle. The contact time $\Delta t \approx 46$ ms at a wheel velocity of 35 m/s, during which short period of time, no solidification occurred as revealed in the high-speed video recorder. In this region, fine and uniform wires with circular cross-section were fabricated, which indicates that the wires were in liquid state upon leaving the molten before the solidification completely took place after they were extracted and flew in the argon atmosphere. This is different from the previous result that solidification is almost completed when the extracted layer leaves the wheel during the melt spinning of amorphous ribbons. The accelerated layer is almost liquid, which promoted the momentum penetration into the layer.

During melt extraction, wetting is a dynamic process due to the rotating wheel and there is an additional shear force involved. Moreover, the extraction also includes heat transfer and solidification process. These factors make the puddle and wetting behaviors in the melt extraction process quite distinct. Figure 3.9a shows the contact geometry in extraction process, $L_{\rm c}$ and δ are the contact length and the thickness of the extracted layer, respectively. In this dynamic state, the wheel tip is moving and a shear force is applied which is due to drag forces at the wheel/liquid interface. Figure 3.9b gives the changes of $L_{\rm c}$ and δ versus extracted wheel speed. The contact length increases gradually with the wheel speed, while the thickness of the extracted layer decreases rapidly till a wheel velocity of 5 m/s prior to a gradual increase.

With reference to Eq. (3.1), it seems any term that is capable of increasing the numerator of Eq. (3.1), i.e. $(\gamma_{sv} - \gamma_{sl})$, or decreases the denominator γ_{lv} , would be able to improve the wetting behavior. Shear force generated during extraction process increases the numerator because it spreads the droplet on the wheel tip and decreases the apparent downstream contact angle. The variation of contact angle, as a result of shear stress, is similar to the hysteresis of contact angle of a drop on an inclined surface.

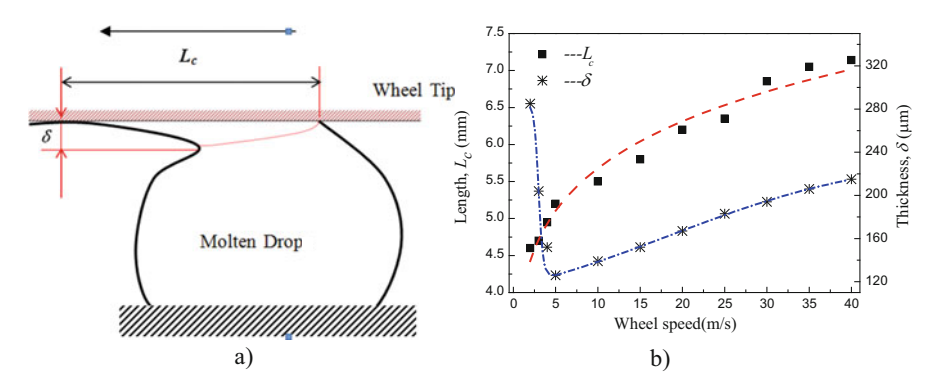


Fig. 3.9 Schematic illustration of the contact geometry (a) and the evolution of L_c , δ versus wheel velocity (b)

3.2.3 Wires Formation Mechanism

The possible modes of the small-sized metallic samples formation have been described by Kavesh [41] and can fall into the following two mechanisms: (I) thermal transport controlling, (II) momentum transport controlling. According to the boundary layer theory of Schlichting [42, 43], these two limiting cases can be discussed as below:

- (I) Thermal transport controlling: If heat propagates much faster than momentum, a solid layer will form at the wheel tip and grow into the liquid puddle. The solid layer will travel with the rotating wheel and a concave will be formed on the wire cross-section.
- (II) Momentum transport controlling: In this reverse case, the momentum transfer is much faster than the thermal transfer, a liquid layer will be dragged out of the puddle by the rotating wheel to solidify further downstream. When the liquid stream is divorced from the wheel tip, high circular wires are thus produced.

Schlichting has performed an analysis and showed that the depth of the thermal boundary layer δ_t and momentum layer δ_u in the liquid near the solid boundary is given by:

$$\delta_t \propto L_c / (\text{Pr} \cdot \text{Re})^{0.5},$$
 (3.2)

$$\delta_u \propto L_c/\text{Re}^{0.5},$$
 (3.3)

where L_c is the contact length of the extracted layer, and Pr is the Prandtl number of the liquid, and Re is the Reynolds number of the liquid. We can then obtain the correlation between δ_t and δ_u :

$$\delta_t/\delta_u \propto 1/\text{Pr}$$
 (3.4)

For the metallic liquid, $\Pr \ll 1$, and we can see that $\delta_t \gg \delta_u$, wire dimension is determined by the heat transfer. Based on the IR measurement for the cooling rate in the puddle, it was concluded that almost the ideal cooling conditions exist with a heat transfer coefficient in excess of 10^6 W/m²K. Outside the puddle, the cooling rates decrease substantially to 10^4 W/m²K. The ideal cooling conditions on the puddle area suggest that the mechanism of wire formation is controlled by thermal transport rather than momentum transport. However, Sun and Davies believed that the assumption of the ideal cooling region at puddle–substrate interface is unrealistic. They stated that both the thermal and momentum transports control the wire formation mechanism. There are still several discrepancies, and it seems both the thermal and momentum transport mechanisms involved in the wire formation depend on the selected processing parameters.

The unique structure and property correlates closely with its cooling experience during wire formation melt extraction process. However, owing to the typically minor deformation puddle, the limited dwell time, and the high rotation velocity of

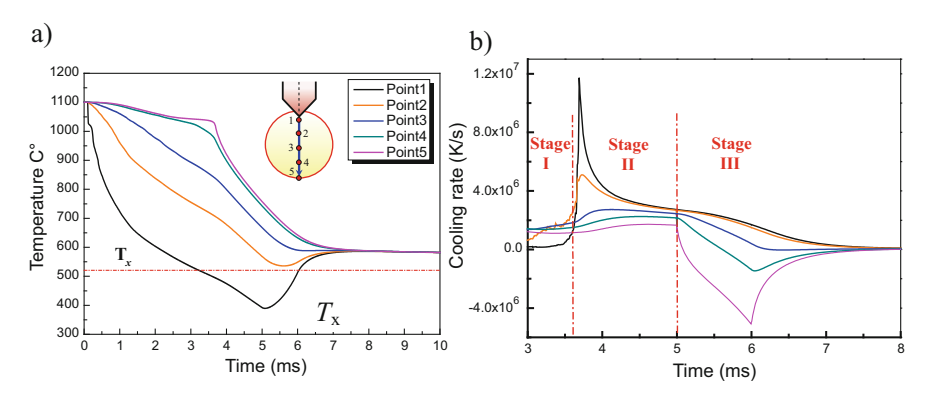


Fig. 3.10 Temperature and cooling rate distribution at different testing points (a) temperature distribution; (b) cooling rate profile [44]

the wheel in a MET process, it is rather difficult to investigate the process experimentally. In order to establish the correlation between temperature distributions i.e., the cooling rate and microstructure evolution during extraction process, a finite element analysis (FEA) was conducted in a ProCASTTM software. Figure 3.10a shows temperature distribution on the cross-section of the extracted wire with five different positions, from copper wheel contacted regions to the free surface. It is readily shown that the temperature near the wheel tip decreases dramatically in the first microsecond and decreases a little slower for the following time. The larger reduction of temperature near the wheel tip is responsible for the formation of concaves on the surface in Fig. 3.3a. The same changing tendency is also obtained for other cooling regions. Figure 3.10b shows the corresponding cooling rate distribution across the microwire. Excluding the larger drop of temperature in the instantaneous contact interval, the cooling experience of the whole extracted layer is herein divided into three stages, namely, (I) formation and moving within the puddle, (II) dwelling on the wheel tip, and (III) the separation from the wheel. In the first stage (before 3.6 ms), a thin liquid layer is accelerated in the puddle due to the combination of momentum and heat transfer by the extracted wheel. The cooling rate in this stage is very small, in that the whole layer moves within the puddle and the heat can transfer instantaneously from the remaining liquid to the thin accelerated layer. When the melt layer was extracted out of the puddle (3.6 ms, starting point of stage II), the temperature of the most part of the layer is above its crystallization temperature T_x (except for point 1, seen in Fig. 3.10a), indicating the extracted layer remains almost liquid after leaving the droplet. The layer dwells along the rotating direction and heat transfers from molten layer to the wheel tip. Thin amorphous layer solidifies along the wheel tip because of its high cooling rate (exceeding the order of 10⁶ K/s), leading to the formation of shallow concave near the contact with the copper wheel. It should be noted that the temperature in this stage (3.6–5 ms) within the layer is still above its crystallization temperature, and the layer remains liquid after leaving the wheel, where surface tension acts as a dominant effect on the formation of circular microwire.

3.3 Mechanical Properties

3.3.1 Tensile Property and Fracture Reliability

Quasi-static tensile tests were performed on an INSTRON 3343 micro-tensile testing setup with a load cell of 10 N at room temperature. The ASTM standard of D3379-75 with a regularly rectangle gauge length of 10 mm was chosen for preparing tensile samples. Uniaxial tensile tests were conducted at room temperature with a constant strain rate of 4.2×10^{-4} s⁻¹. Figure 3.11a-c shows the tensile strength-strain curve and fracture morphology of Co-based extracted wires with diameters of about 60 and 40 μ m, respectively. The tensile strength of the thin uniform circular wire is approximately 3700 MPa, a little higher than the previous results, processed by glass-covered amorphous wires [45]. While for the wire with

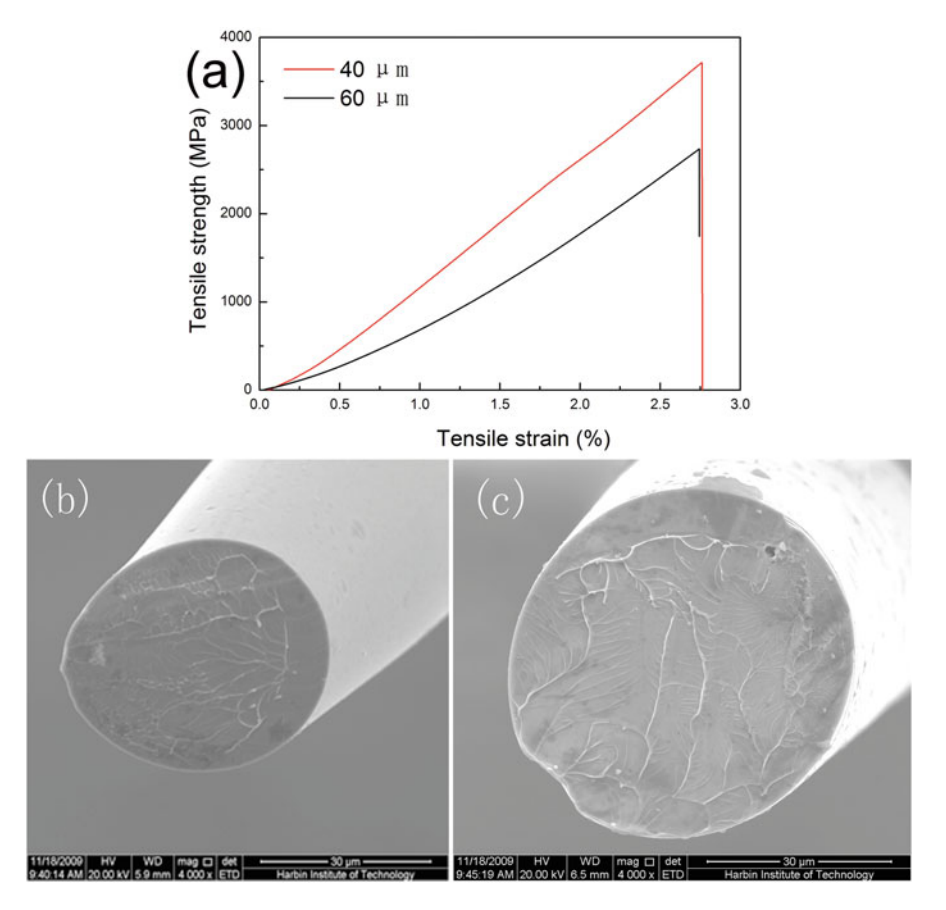


Fig. 3.11 Tensile behavior (a) and fracture morphologies of Co-based wires with diameters of 40 μm (b) and 60 μm (c)

diameter of 60 μ m, its tensile property of approximately 2850 MPa is much lower than the previous one. The higher tensile strength can be explained by the low stress concentration, perfect geometry, and high amorphous nature. From Fig. 3.11b, c, it can be seen that both the fracture figures are composed of two regions: a relatively featureless zone produced by shear slip and a vein pattern produced by the rupture of the cross-section remaining after the initial shear displacement. However, the former wire of 40 μ m fractures along the maximum shear plane, which is declined by about 45 deg to the tensile direction, and some molten droplets form at the initial part of the vein pattern; for 60- μ m wires, tensile fracture occurs on a shear plane at 90° to the transverse section.

The strength data of brittle materials have been known to exhibit a wider degree of scatter compared to that of ductile materials, implying the reliability of structural applications. The statistical method commonly used to describe the distribution of fracture stresses in brittle materials is that given by Weibull [46]. The cumulative probability function of the Weibull distribution is expressed as follows:

$$P_{\rm f} = 1 - \exp\left[-\int_{V} \left(\frac{\sigma - \sigma_{\mu}}{\sigma_{0}}\right)^{m} d_{V}\right] \tag{3.5}$$

where $P_{\rm f}$ is the probability of failure at a given uniaxial stress or lower, and can be calculated using the equation: $P_i = \frac{i-0.3}{N+0.5}$, where N is the total number of the samples tested and i is the sample ranking in ascending order of failure stress. The threshold value σ_{μ} is the value below which no specimen is expected to fail. The term σ_0 refers to a characteristic strength defined as the stress at which the $P_{\rm f}$ is 63.2%. The m is a parameter known as Weibull modulus, and V is the volume of the tested samples.

After rearranging, Eq. (3.1) can be written as

$$\ln\left\{\ln\left[\frac{1}{(1-P_{\rm f})}\right]\right\} = m\ln\left(\sigma - \sigma_{\mu}\right) - m\ln\sigma_{0} \tag{3.6}$$

When $\sigma_{\mu}=0$, the distribution becomes the two-parameter Weibull distribution

$$\ln\left\{\ln\left[\frac{1}{(1-P_{\rm f})}\right]\right\} = m\ln(\sigma) - m\ln\sigma_0 \tag{3.7}$$

Weibull modulus m, threshold value σ_{μ} and characteristic strength σ_0 thus can be obtained by fitting experimental data $\left(\ln\left(\sigma_f\right), \ln\left\{\ln\left[\frac{1}{(1-P_i)}\right]\right\}\right)$ with two-parameter and three-parameter method.

Eighteen samples were tested for these extracted microwires and displayed in Fig. 3.12. The apparent fracture strength σ_f ranges from 2843 to 3558 MPa, with a mean value of 3197 MPa and a variance of 235 MPa. The strength variation for these microwires results from the distribution of the strength-limiting flaws. For as-cast microwires, the flaws could stem from the concaves, casting pores,

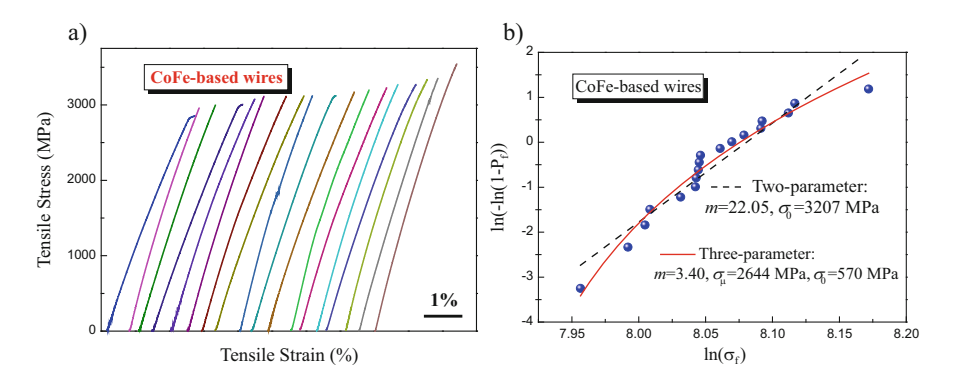


Fig. 3.12 (a) Tensile stress-strain curves and (b) Weibull statical analysis of Co-based microwires

inclusions or surface irregularities. Note that the existence of these flaws results in a severe deterioration of their mechanical properties, especially tensile strength and fracture reliabilities. Figure 3.12b shows the Weibull plots in the fashion suggested by Eqs. (3.6) and (3.7) for the extracted Co-based microwires. The data fits yield the following estimated parameters that describe the distributions:

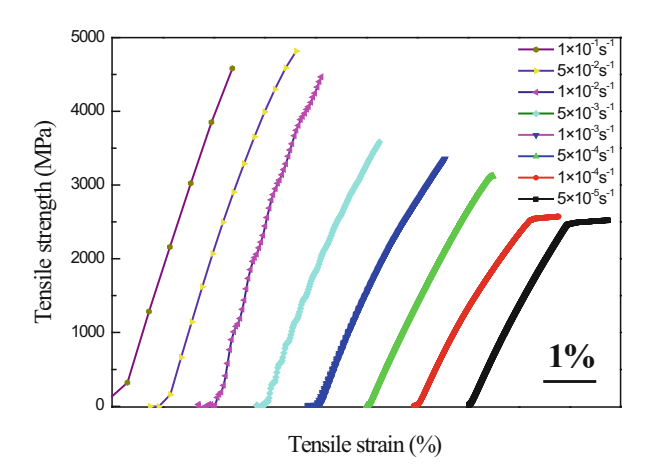
Two-parameter: m = 22.05, $\sigma_0 = 3207$ MPa

Three-parameter: m = 3.40, $\sigma_{\mu} = 2644$ MPa, $\sigma_{0} = 570$ MPa

3.3.2 Strain Rate Dependence

Understanding of the dynamic failure mechanism in microwires is important for the application of this class of materials to a variety of engineering problems. This is true for design environments in which components are subject to different loading rates. Typical tensile stress-strain curves of Co-based amorphous microwires on the range 5×10^{-5} to 1×10^{-1} s⁻¹ are shown in Fig. 3.13. The fracture stress increased gradually with increasing strain rate. The fracture stress increased from 2500 to 4500 MPa when the applied strain increased from 5.0×10^{-5} to 1.0×10^{-1} s⁻¹, indicating a positive strain rate sensitivity. The stress–strain curves at 5.0×10^{-2} and 1.0×10^{-1} s⁻¹ exhibit linear slope till failure and no anelastic post-yielding were observed. With the decrease of strain rate, lower than $5.0 \times 10^{-2} \text{s}^{-1}$, the stress-strain curve initially deforms elastically and further deviates from the linear deformation part, showing a nonlinear deformation behavior prior to fracture. With further reduction of the applied strain rate, the curves deformed at 1.0×10^{-4} and $5.0 \times 10^{-5} \text{ s}^{-1}$ exhibit completely different shapes. After reaching the maximum stress, relatively large plastic flow with no strain hardening, typical of "ductile" failure, was observed in the tensile curves. Maximum tensile plasticity over 1 % can be observed in this low strain range. Unlike most strain rate responses of bulk

Fig. 3.13 Tensile stress strain curves of Co-based amorphous microwires at different strain rates



metallic glasses, it is important to note that no serrated flow, mainly caused by the shear band initiation and propagation, was observed on the tensile curves over a wider strain range, indicating that the "ductile" failure behavior for the amorphous microwires at the low strain rate does not depend on the formation of new shear band

Fractured specimens were examined to investigate the deformation behavior of microsized Co-based amorphous microwires. Figure 3.14a, c, e are the side views of the specimen fractured at the strain rate of 5.0×10^{-5} , 1.0×10^{-4} , and 5.0×10^{-3} s⁻¹, respectively. The whole three samples sheared off nearly at 54° to the tensile axis, essentially independent of strain rate in the present studies. The fracture characteristics of amorphous microwires yield the Mohr–Coulomb criterion rather than Von Mises rule. The side surface Fig. 3.14a, c, e appears to be smooth, no clear sign indicating the operation of other shear bands. The formation and propagation of one major shear band dominates the fracture of the sample, in accordance with previous observation as in Fig. 3.13. The fracture surface of the specimen at corresponding strain rate is shown in Fig. 3.14b, d, f. Smooth tearing deformation region, i.e. shear offset, and vein-like morphology is readily seen over the three specimens. The lengths of shear offset decrease with the applied strain rate while the density of vein-like pattern gives an opposite tendency.

The deformation and fracture behaviors of amorphous microwires are strongly dependent on the strain rate. The larger strain rate it imposed, the higher fracture strength it behaves. This result revealed in Co-based amorphous microwires is consistent with the report of Mukai et al. [47] on the $Pd_{40}Ni_{40}P_{20}$ BMG in tension test. However, the tensile plasticity exhibits a contrary tendency. A possible explanation for the behavior as seen in Fig. 3.13 could be related to the creation, coalescence, and diffusion of free volume in these materials, whereas the creation and diffusion of free volume are influenced greatly by the applied strain rate. Spaepen et al. [48] developed a general constitutive equation to characterize the plastic deformation of amorphous alloys, which can be written as

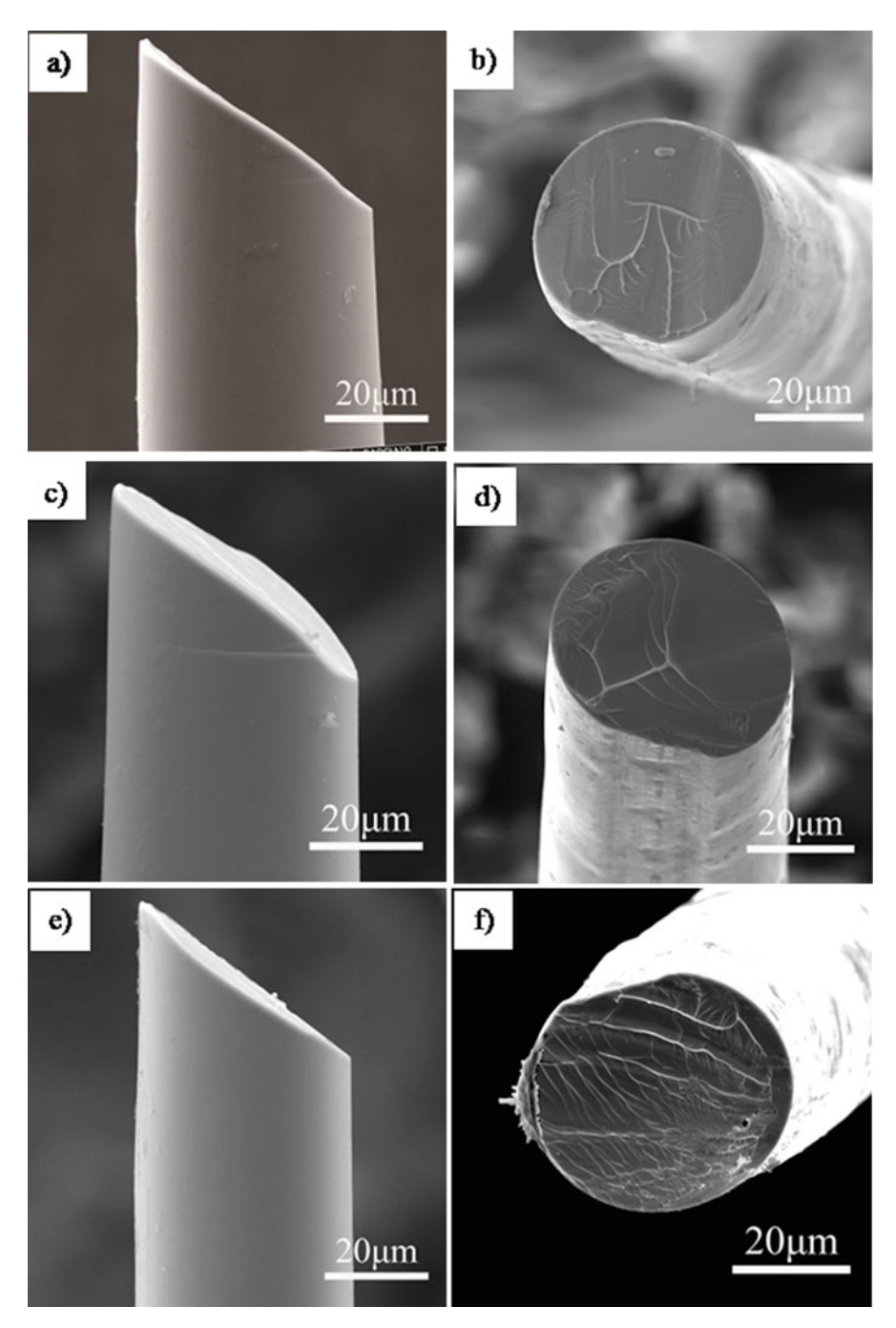


Fig. 3.14 SEM images revealing fracture features of Co-based amorphous microwires with different strain rates (a), (b) 5.0×10^{-5} s⁻¹ (c), (d) 1.0×10^{-4} s⁻¹ (e), (f) 5.0×10^{-3} s⁻¹

$$\dot{\gamma} = \frac{\dot{\tau}}{\mu} + 2f \cdot \exp\left(-\frac{\alpha}{\xi}\right) \cdot \exp\left(-\frac{\Delta G}{k_B T}\right) \cdot \sinh\left(\frac{\tau \Omega}{2k_B T}\right)$$
(3.8)

where $\dot{\gamma}$ is the shear strain rate, $\dot{\tau}$ the applied shear stress, ξ the concentration of the free volume, α a geometrical factor of order unity, f the frequency of atomic vibration, ΔG the activation energy, Ω the atomic volume, k_B the Boltzmann's constant, μ the shear modulus, and T the absolute temperature. Apart from the thermodynamic and geometrical factor, the concentration of the free volume ξ also plays an important role in the deformation of amorphous alloys. The concentration of the free volume is the competition result between continuous creation by an applied shear stress and annihilation by structural relaxation due to atom rearrangement. The creation of free volume increases gradually with shear strain rate, while the free volume annihilation rate yields an opposite tendency. For those relatively high strain rates, the creation rate of free volume exceeds the annihilation rate, resulting in the decrease of viscosity or the increase of temperature on the shear plain and finally catastrophic failure. With the applied strain rate decreasing further, below $1.0 \times 10^{-4} \text{s}^{-1}$, the free volume annihilation rate exactly balances the stress-driven creation rate. As a result, the total net concentration of free volume remains constant, leading to a global tensile plasticity in Co-based amorphous microwires.

The absence of serrated flow and the existence of a pure slip region before final fracture in melt-extracted Co-based amorphous microwires indicate that the tensile fracture behavior of such small specimens over a wider strain range was dominated by the initiation and propagation of one major shear band. For the shear banding process of amorphous alloys, there exist two counteracting mechanisms: shearinduced accumulation of free volume within the shear band, leading to the stress drop in the stress-strain curve, and structure-induced annihilation, which can counteract the aforementioned softening effect. By analogy to the three structure evolution stages raised by Wu et al. [49] during deformation of bulk metallic glasses, we suggest that the whole tensile process of Co-based amorphous microwires can be divided into four stages: (1) elastic tensile deformation, (2) nonlinear tensile deformation, (3) stable propagation of shear band and uniform tensile plasticity, (4) final fast propagation and failure of shear band, as shown in Fig. 3.15. At the first stage, specimen deformed elastically with the applied stress and the density of the free volume increased gradually. In stage II, the excess free volumes agglomerate on the shear plane and shear band starts to form, sub-nanometer voids are coalesced from free volume at the same time due to the applied tensile stress. The formation of tiny voids probably consumes the applied strain energy and decreases the stress area thus gives rise to the nonlinear deformation behavior, which has been already confirmed in some small-sized metallic glasses. With shear deformation proceeding, in stage III for the low strain rate condition, the stress-driven creation rate of free volume is exactly balanced by the annihilation due to structure relaxation. Free volume has sufficient time to restructure and reconfigure to accommodate the applied strain rate. At the same time, the

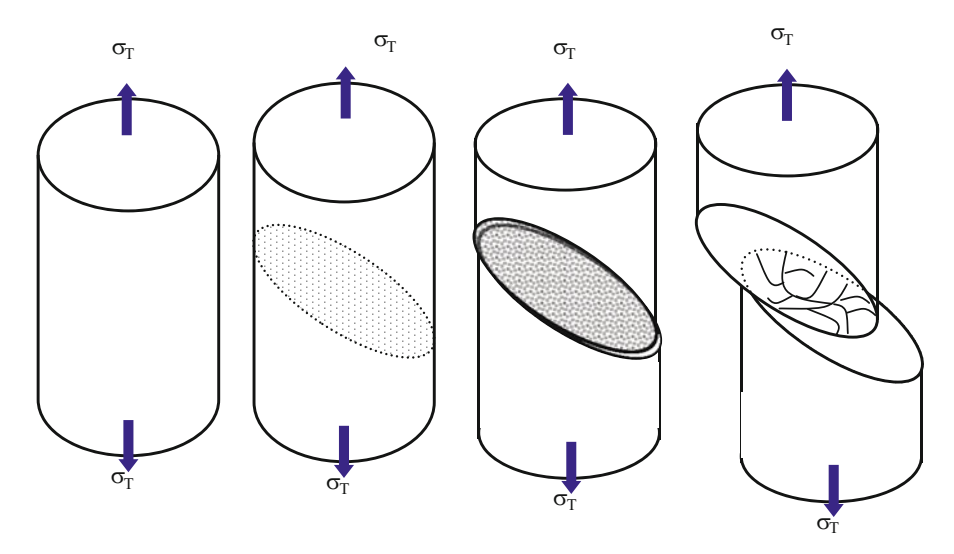


Fig. 3.15 Schematic illustrations of tensile deformation and fracture process for Co-based amorphous microwire

voids agglomerated start to induce the formation of a local crack and slip steadily, resulting in the formation of shear offset on the fracture surface. The slow and stable propagation of shear crack yields a steady development of shear offset, leading to a global tensile plasticity in Co-based amorphous microwires. For the high strain rate condition, the balance between creation and annihilation of free volume will not occur. In the fourth stage, when the size of shear offset develops to a critical length, the shear band becomes unstable; any fluctuation of stress or free volume change will trigger the rapid prorogation and final fast fracture of sample. The propagation behavior in these amorphous microwires is too fast to be observed experimentally. Vein patterns observed in Fig. 3.14b, d, f are the results of rapid propagation and fracture of shear band. The critical shear offset, i.e., the size of the smooth region on the fracture surface of amorphous samples after deformation, and tensile plasticity of amorphous microwires are strongly dependent on the imposed strain rate. The critical shear offset can be regarded as a parameter directly reflecting the stability of shear deformation. Therefore, it is suggested that the shear deformation capability of an amorphous microwire is related to its critical shear offset: the global plastic deformation of the amorphous microwire increases with increasing critical shear offset. For the Co-based amorphous microwires in the present work, decreasing strain rate will enlarge the critical shear offset and improve their plastic deformation dramatically.

3.3.3 Cold-Drawn Property

The continuous near-circular Co-based wires with diameter of about 60 μ m were fabricated by the melt extraction method. The diameter of the extracted wires was reduced step by step through a number of drawing processes using diamond dies without any intermitting annealing, as schematically shown in Fig. 3.16a [50]. The cross-section area reduction ratio, $R = (D_0^2 - D_1^2)/D_0^2$, where D_1 is the diameter after drawing and D_0 is the original diameter, was controlled within 4% per step.

Co-based metallic wires were easily drawn to a cross-section area reduction of about 75% without rupture. The outer surface of cold-drawn wire with different *R* values is shown in Fig. 3.16b. All of the drawing wires exhibit smooth surfaces without any visible scratches, while the grooves and fluctuations in the as-quenched wire, as indicated by the arrows, can be seen occasionally on the surface. Note that the existences of these flaws severely deteriorate their mechanical properties. After the drawing process, it can be seen that the grooves and flaws were removed; wires became more circular and round.

The effect of cold drawing on the mechanical performance of melt-extracted amorphous wires was investigated and the representative tensile stress—strain curves for microwires with different R values are presented in Fig. 3.17. The cold-drawn wires exhibit noticeable tensile plasticity as compared with the as-quenched sample (a). The tensile strain and tensile strength increase gradually with cross-section reduction until R = 51 % and then decrease with further deformation. Cold-drawn microwire with R = 51 % exhibits the highest tensile strength of 4320 MPa and a maximum tensile ductility of 1.09 %. It should be noted that curves (a), (b), and (c) possess similar elastic modulus, as calculated from the slope of these curves, while the modulus becomes slightly larger for samples (d), (e), and (f), indicating somewhat different structures of these two groups of wires.

To verify the wire's usefulness as a fine engineering material, it is necessary to evaluate its mechanical properties in the context of prevalent materials of same

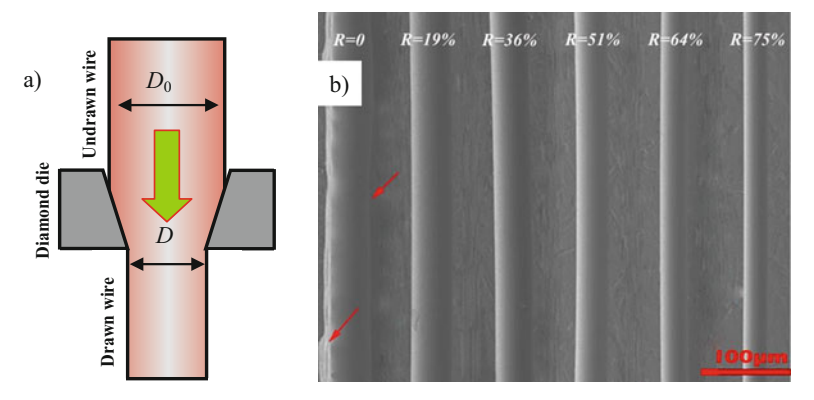
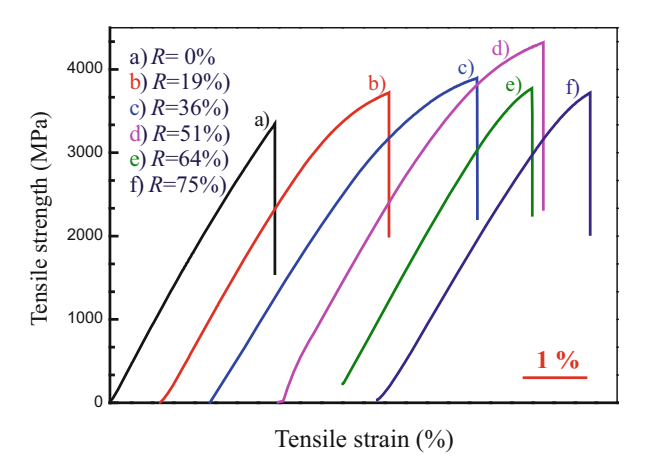


Fig. 3.16 Principle of diamond cold drawing (a) and SEM images of melt-extracted wires with different cross-area reduction (b) [50]

Fig. 3.17 Stress-strain curves for the metallic wires with different cross-section reductions



scale. The engineering stress–strain curve of the present 51% cold-drawn wire together with a series of Zr-based [51, 52], Pd-based [53, 54], Fe-based [3], Mg-based [55], Ni-based [56, 57], and Co-based amorphous microwires [58] are compiled and presented in Fig. 3.18a. It can be clearly seen that, compared with other microwires fabricated by in-rotating-water quenching, glass coating and even conventional melt extraction methods, the present microwire exhibits the largest fracture absorption energy (fracture toughness), as characterized by the area underneath the stress–strain curves. Figure 3.18b compares the tensile stress versus tensile strain data for all of those above-mentioned wires and the microwire in the present study exhibits the highest tensile strength and the largest tensile ductility of all discussed samples.

Figure 3.19 presents X-ray diffraction patterns of the as-quenched and cold-drawn samples. Most of these samples exhibit consistent feature, i.e., a broad diffuse halo except for a small crystal peak overshadowed by the background noise for the 64% drawn wires, indicating that cold drawing is an effective way to reduce the diameter of the melt-extracted microwire without changing its macroscale structure constitute. This is especially important for the sensing application of wires, since they prefer to be thinned down to fine diameter in meeting the requirement of miniaturization but without compromising the mechanical integrity. It should be noted that the conventional XRD technique is unable to detect phases whose content is less than about 5 wt% (depending on crystal symmetry), the microscale structural change (if any) induced during cold-drawing process needs to be further clarified by electron microscopy.

Figure 3.20a–c gives the high-resolution transmission electron microscopy (HRTEM) images for the as-cast, R = 51% and R = 64% cold-drawn wires. No contrast and lattice fringe can be detected in Fig. 3.20a, demonstrating that the as-cast wire is fully amorphous without any nanocrystals. Compared with the as-cast structure, isolated nanocrystallites with an average size of 4 nm distributed homogeneously in the amorphous matrix were observed for the R = 51% sample (Fig. 3.20b). The degree of nanocrystallization becomes higher and more obvious

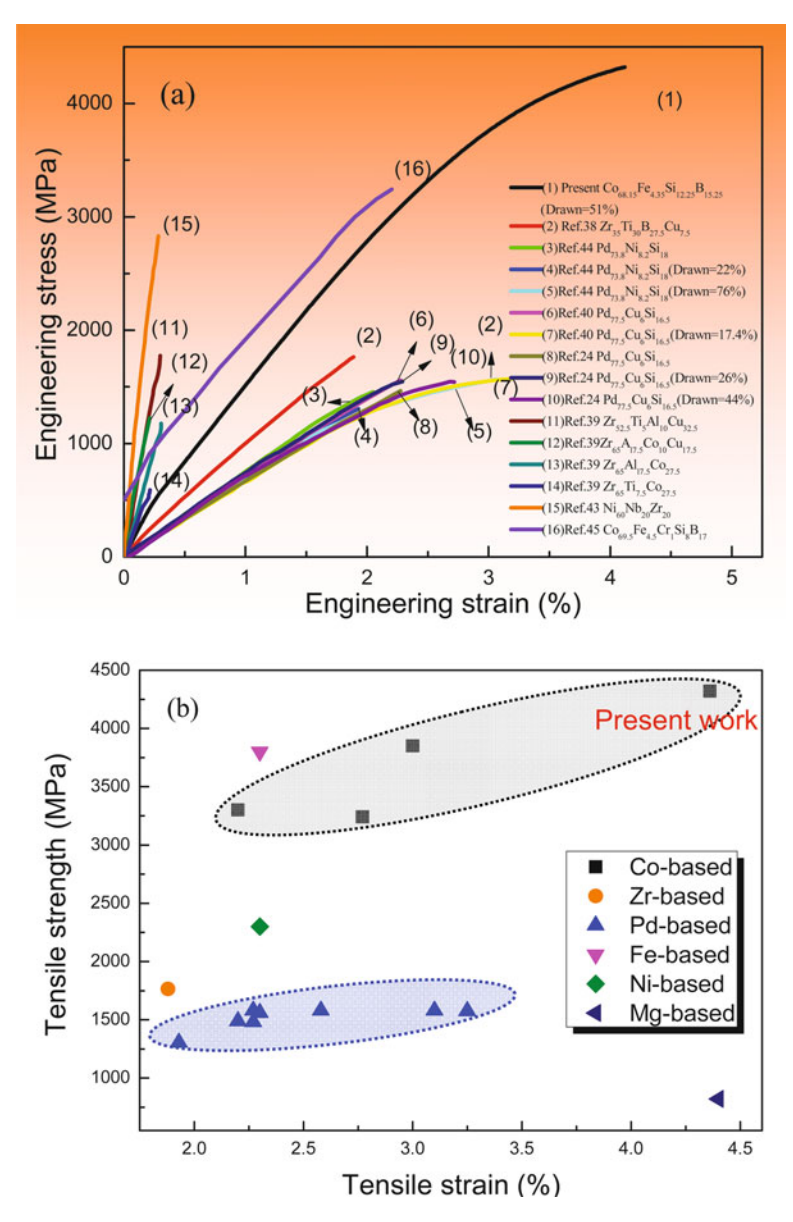
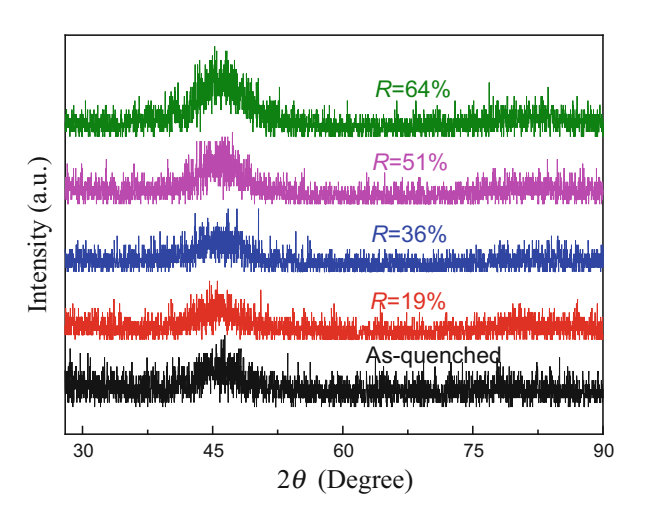


Fig. 3.18 (a) Tensile stress-strain curves for a series of amorphous microwires; (b) Tensile strength plotted against the tensile ductility at room temperature

for the R = 64% wire as seen in Fig. 3.20c. These inhomogeneities embedded in the amorphous matrix are believed to arrest the fast extension of shear band and stabilize the sample against the catastrophic failure, resulting in the enhanced ductility.

Fig. 3.19 X-ray diffraction patterns of the as-quenched and cold-drawn microwires



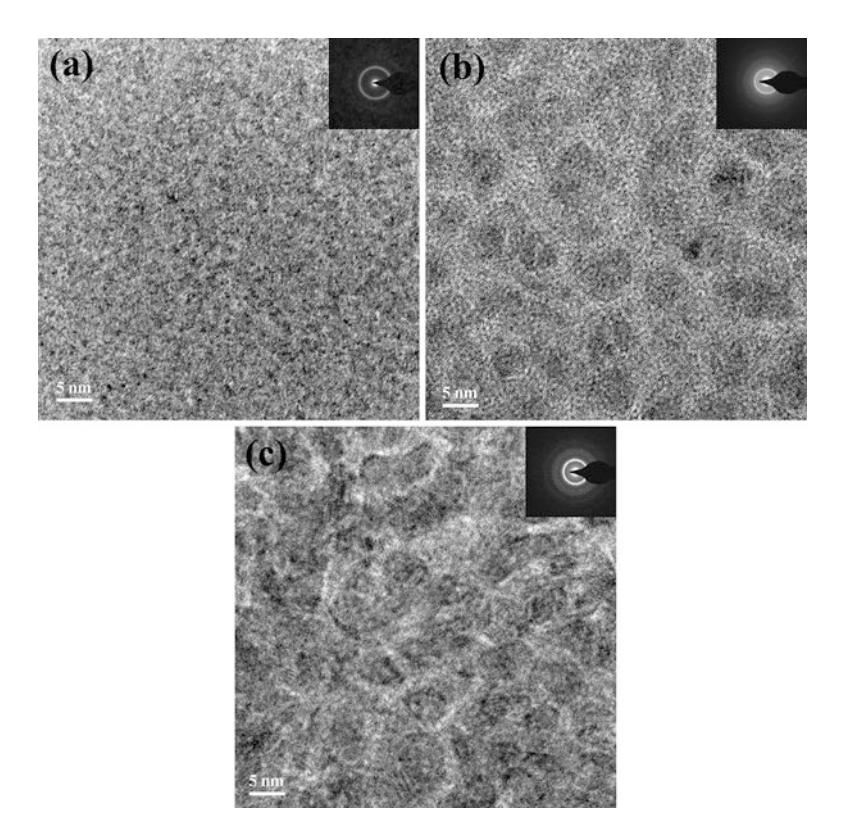


Fig. 3.20 High-resolution transmission electron microscope patterns of the different cold-drawn extracted microwires (a) as-quenched, (b) 51% and (c) 75% cold-drawn microwires

In another perspective, residual stress generated in the drawing process can also affect their mechanical properties. The axial residual stress σ_x and circumferential residual stress σ_n can be given by:

$$\sigma_{x} = \frac{B}{B-1}\sigma_{y} \left[1 - \left(\frac{D}{D_{0}} \right)^{2(B-1)} \right], \tag{3.9}$$

$$\sigma_n = \frac{B}{B-1} \sigma_y \left[\left(\frac{D}{D_0} \right)^{2(B-1)} - \frac{1}{B} \right],$$
 (3.10)

where *B* is constant and related to the geometry of die, σ_y is the yield strength of the sample, *D* and D_0 represent the diameter at position *x* and initial diameter.

Because of its low deformability, the area reduction ratio of Co-based metallic wires was limited to 4% per each step, thus the stress of the wires when extracted out of the diamond die can be calculated as: $\sigma_x = 0.115\sigma_y$, $\sigma_n = 0.885\sigma_y$, respectively. Bear in mind that the compressive surface residual stress is beneficial for the increase of hardness and fracture strength, while the tensile residual stress has the opposite effect [25, 48–50]. Thus $\sigma_n \gg \sigma_x$, suggesting that the circumferential compressive stress benefits the mechanical performance of the drawn wires.

3.4 Magnetic Behavior

3.4.1 Giant Magnetoimpedance

Giant magnetoimpedance refers to a significant change of ac impedance occurred to a soft magnetic material carrying a driving ac current when it is submitted to a dc magnetic field [5]. This effect has aroused much research interest due to its promising applications in various sensing devices. Among other GMI materials, microwires are recognized most privileged sensing element with extraordinary GMI effect for high-performance sensing applications [59]. Therefore, much research efforts have been devoted to modulation and optimization of the microwires' microstructure and domain structure for better GMI effect.

The giant magnetoimpedance (GMI) effects of the microwires fabricated at different cooling speeds mentioned above were systematically studied and Fig. 3.21 exhibits their GMI results measured at different frequencies: 0.1, 0.5, 1, 5, 10, and 15 MHz. The GMI ratios ($\Delta Z/Z_{\rm max}(\%)$) of Co-based microwires fabricated by Cu wheel at 5 m/s and 30 m/s are 27 % and 8.1 % at 0.1 MHz, respectively, and 97 % and 78.6 % at 0.5 MHz, respectively. The GMI ratios increase with the Cu wheel speeds (>1 MHz) and the maximum GMI ratio at 30 m/s reaches 360 % at 10 MHz, then the value declined slightly at 15 MHz. The Mo wheel has relatively lower thermal conductivity compared with Cu wheel thus resulting in the difference in microstructures. The GMI ratio for microwires

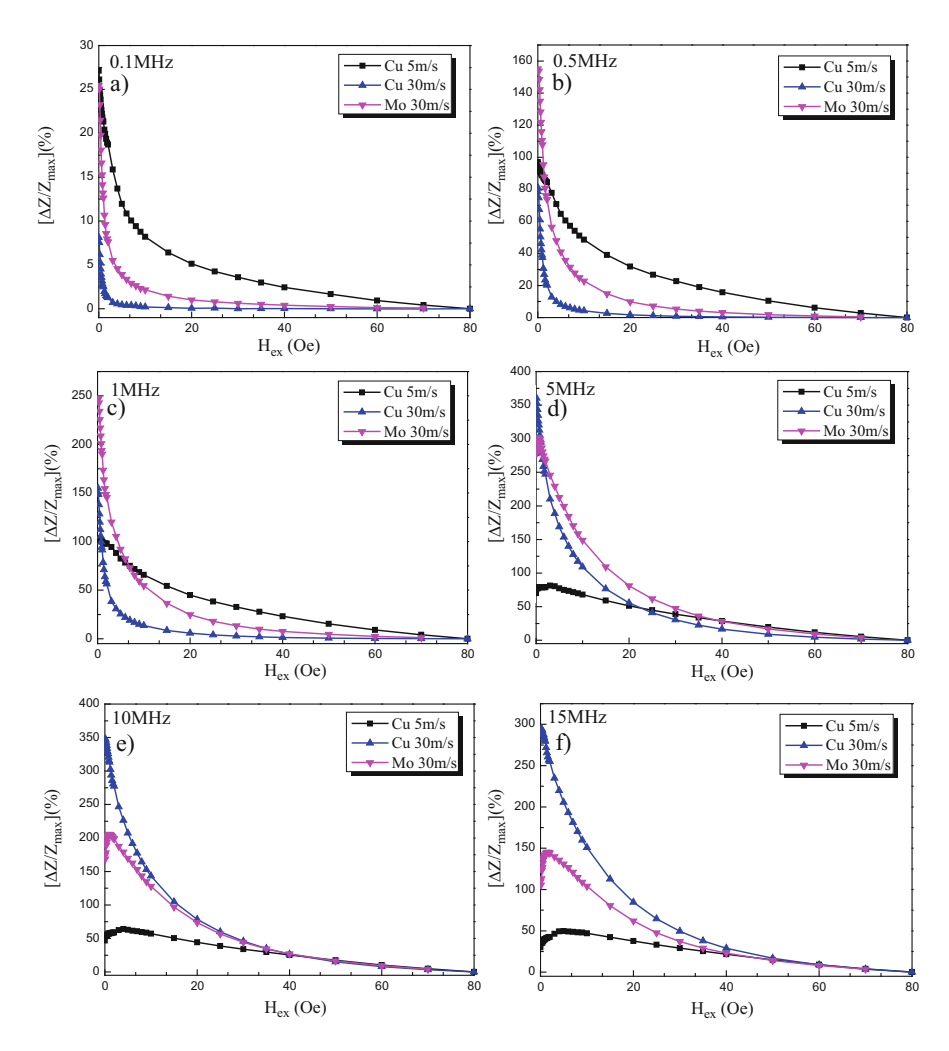


Fig. 3.21 Magnetic field dependence of GMI ratio $\Delta Z/Z_{\rm max}$ at different frequencies for the different extracted micromicrowires (a) f=0.1 MHz; (b) f=0.5 MHz; (c) f=1 MHz; (d) f=5 MHz; (e) f=10 MHz; (f) f=15 MHz

obtained under Mo 30 m/s is larger than that of Cu 30 m/s microwires when measured frequencies is lower than 1 MHz but the GMI ratio becomes lower when the applied frequencies larger than 5 MHz. It has been reported that the GMI curves show typical symmetry under the applied positive and negative magnetic fields with single peaks and double peaks behaviors. The GMI ratios of Cu 30 m/s microwires exhibit monotonically decreasing with the increase of applied

field for all measured frequencies, while the GMI curves of Mo 30 m/s and Cu 5 m/s microwires show double peaks behavior for frequencies larger than 5 MHz and their equivalent magnetic anisotropy fields increased to larger than 2 Oe.

Commonly, the GMI effects of melt-extracted micromicrowires show high dependence on their compositions, measurements, distribution of residual stresses, and microstructures. The residual stresses in the microwires increased with the solidification rate which related to the revolving speed of wheel, moreover the stress distribution on the surface of the wires is nonuniform due to the unilateral heat transfer during the melt-extracted process thus result in the change of stress anisotropy. The large residual stresses lead to large magnetoelastic energy which results in the difficulties in magnetic domain switching or moving, so the microwires fabricated at high wheel speed exhibit relatively hard magnetization and small GMI ratios at low applied fields. The magnetocrystalline anisotropy of Mo 30 m/s microwires and Cu 5 m/s microwires increases due to the hard magnet phases Fe₃Si, Co₂B, and Co₂Si which obstruct magnetic domain switching or moving as pinning points, then reduces both the magnetic conductivity and GMI effect, thus the GMI curves show typical double peak behaviors.

The dependence of the GMI ratios at 10 and 15 MHz as a function of applied axial magnetic field H, for different R values, i.e., as-cast, 19, 36, 51, 64 %, is presented in Fig. 3.22. One can see that, at both frequencies, all the wires including the as-cast wire show double-peak features. The shape of curves and the amplitude of GMI ratio $(\Delta Z/Z)$ as well as the anisotropy field (H_k) at which the maximum GMI ratio occurs depend intimately on the cross-section area reduction. To clearly elucidate the role of each drawing step on the GMI characteristics of microwires, we plotted the field dependence of maximum GMI ratio $((\Delta Z/Z)_{max})$ and anisotropy field (H_k) . The $(\Delta Z/Z)_{\text{max}}$ decreased dramatically after the initial drawing process, for example, from 134 % to 88 % at 10 MHz for R = 19 %. With further deformation, the $(\Delta Z/Z)_{\text{max}}$ starts to increase and reaches a maximum of 160 % at 7 Oe for R = 51% before decreases again with increasing R up to 64%. The anisotropy field (H_k) undergoes a rapid increase from 1 Oe to 5 Oe at 10 MHz after the first drawing step before a relatively small increase of 2 Oe with further drawing. Afterwards the anisotropy field levels off at 7 Oe. Overall the simple cold-drawing process proves to be capable of enhancing the GMI ratio by 30% and the anisotropy field by a factor of 7 in comparison with those of as-cast wire, respectively. The effect of each cold-drawing step remains the same trend at both frequencies. Yet it should be noted that at 15 MHz the maximum improvement of GMI ratio is 44 %, much larger than 26 % at 10 MHz, whereas the maximum increase of anisotropy field is quite similar, i.e., 6 and 6.6 Oe, respectively. Such a simultaneous large improvement of maximum GMI ratio and anisotropy field is particularly important for the magnetic sensing application which requires a strong response and a wide measurement range.

Compared with the as-cast microwire, melt-extracted microwires after cold drawing exhibit a higher GMI ratio except for an initial drop for the $R=19\,\%$ sample. The distribution of stress generated in the quenching process and the added external stress throughout the wire volume as well as the microstructural evolution

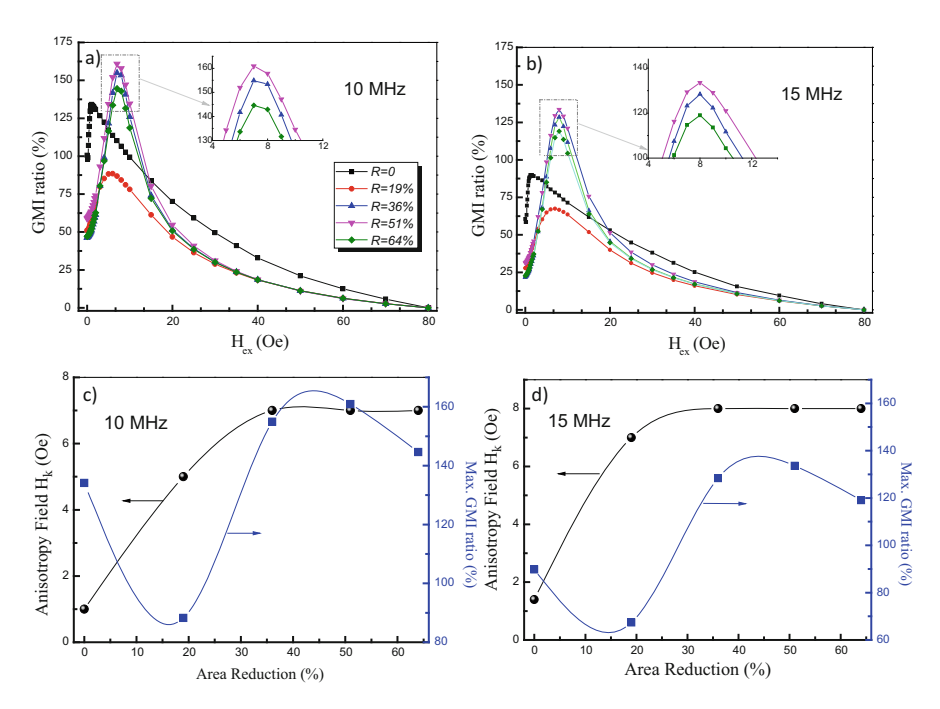


Fig. 3.22 Field dependence of the GMI ratio $\Delta Z/Z$ and maximum GMI ratio and anisotropy field at different frequencies for the as-quenched and cold-drawn wires (a), (c) 10 MHz; (b), (d) 15 MHz

during drawing process play decisive roles in the determination of its magnetization configuration, and hence its magnetic performance. In this section, we discuss the effect of the longitudinal tensile stress and circumferential compressive residual stress generated during drawing process and the size of those mechanical-induced nanocrystals on the evolution of magnetic domain configuration. The magnetic anisotropy of amorphous wires is mainly determined by magnetoelastic interactions due to the absence of magnetocrystalline anisotropy (for R < 51 %) and negligible shape anisotropy. The magnetoelastic energy density of an amorphous can be formulated as [60]:

$$w_{m-el} = -\frac{3}{2} \lambda_s \left(\sigma_{rr}^{(q)} \alpha_r^2 + \sigma_{\varphi\varphi}^{(q)} \alpha_{\varphi}^2 + \sigma_{zz}^{(q)} \alpha_z^2 \right), \tag{3.11}$$

where λ_s is the saturation magnetostriction constant, $\sigma_{ii}^{(q)}$ are the diagonal components of the residual stress tensor in cylindrical coordinates (r, φ, z) ; and α_i are the components of the unit magnetization vector. The residual quenching stress throughout the wire is assumed to be a function of reduced wire radius x (r/r_0), and can be reasonably approximated by means of the following simplified relations [55]:

$$\sigma_{rr}^{(q)}/\sigma_{\rm v} = a(1-x^2),$$
 (3.12)

$$\sigma_{\varphi\varphi}^{(q)}/\sigma_{y} = a(1-3x^{2}), \tag{3.13}$$

$$\sigma_{zz}^{(q)}/\sigma_{y} = b(1 - 2x^{2}), \tag{3.14}$$

where a and b are the constants relevant to the material property.

Figure 3.23a illustrates such radial dependence of residual stress. There exists an intersection at x_1 for $\sigma_{\varphi\varphi}^{(q)}/\sigma_y$ and $\sigma_{zz}^{(q)}/\sigma_y$. The inner core and out shell is then classified at this point for an as-prepared amorphous wire with negative magnetostriction, and x_1 is the inner core radius, where the easy axis is along the wire due to $\sigma_{zz}^{(q)}/\sigma_y < \sigma_{\varphi\varphi}^{(q)}/\sigma_y$; for outer surface $(r>x_1)$, $\sigma_{zz}^{(q)}/\sigma_y>\sigma_{\varphi\varphi}^{(q)}/\sigma_y$ results in a circumferential anisotropy. The corresponding core—shell domain structure for the as-cast wire is shown in Fig. 3.23b, consisting of the outer shell circular domains and inner core axial domains. While for the cold-drawn wires, the existence of circumferential compressive stress and longitudinal tensile stress will cause a change in the volume fraction of outer shell circular domains and inner core axial domains, i.e., the outer shell domains become larger and the inner core domains are reduced accordingly, as depicted in Fig. 3.23c, but the domain configuration remains unchanged. This can be mathematically interpreted as the movement of intersection x_1 for the $\sigma_{\varphi\varphi}^{(q)}/\sigma_y$ and $\sigma_{zz}^{(q)}/\sigma_y$. As demonstrated in a previous study [61], a larger GMI

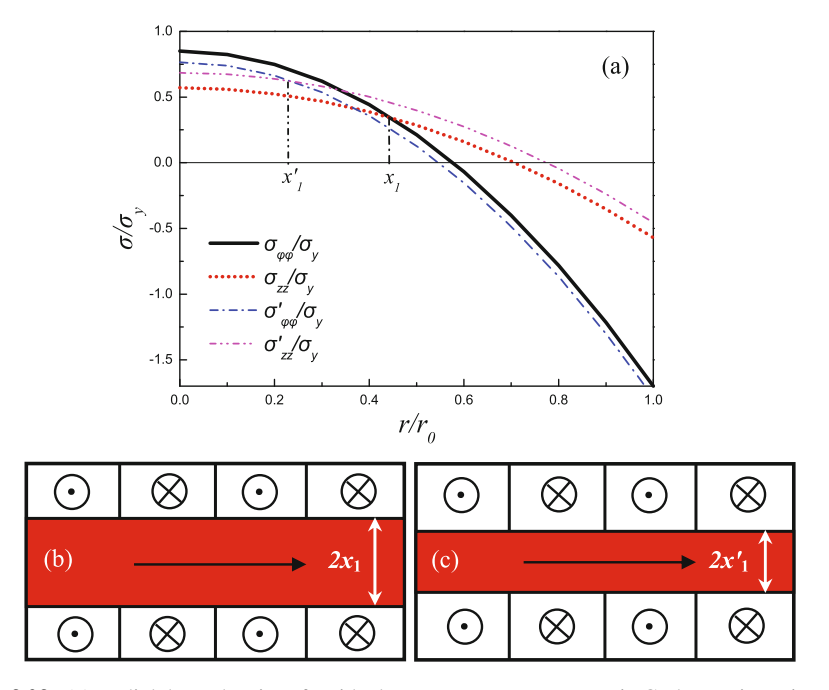


Fig. 3.23 (a) Radial dependencies of residual stress tensor components in Co-base microwire and the corresponding domain structure for the (b) as-quenched and (c) cold-drawn samples

effect in Co-rich amorphous wire was achieved by an external axial tensile stress due to the rearrangement of the domain wall induced by tensile stress and the increase in circular anisotropy and permeability. The coupling effect of external axial tensile stress and residual quenched axial stress σ_{zz} will cause the intersection x_1 move to the left, increasing the outer shell circular domains. In analogy, the circumferential compressive residual stress will cause a smaller $\sigma_{\varphi\varphi}$, similarly result in the intersection moving slightly to the left, i.e. point x_1' . As such, the axial residual tensile stress and circumferential compressive stress induced by cold-drawing process together increase the volume of outer shell and hence the circumferential permeability, giving rise to an improved GMI ratio.

Based on the above analyses, one would expect a monolithic increase of GMI ratio with further drawing process, however, Fig. 3.22 shows a complex field dependence of maximum GMI ratio. Thus the residual stress can only explain the increase of GMI from R = 19 to 51%. To understand the large reduction of GMI for the initial drawing steps, one need to consider the imperfect geometries of wires, which are expected to act as defects to cause stress concentration at the surface during the cold-drawing process, as schematically shown in Fig. 3.24. Along with the SEM images in Fig. 3.16b, it can be seen that the inhomogeneous surface of as-cast wire is forced into several stress-concentrated local regions, which will result in the inhomogeneities of magnetoanisotropy energy in the surface and deteriorate the soft magnetic properties. As exactly a surface related property, GMI effect is reduced sharply.

In another perspective, as discussed above, mechanical-induced nano-scale crystals formed during the cold-drawing process have a significant effect on the GMI properties. Isolated small-sized nanocrystals of less than 4 nm embedded in the amorphous matrix for the 51 % drawn sample yields a maximum GMI ratio of

Fig. 3.24 Schematic illustration of the residual stress distribution in the microwires with different deformation degree (a) as-cast; (b) R = 19%; (c) R = 51%





about 160% at 10 MHz. This phenomenon can be attributed to the residual stress generated during the drawing process, as the effect of crystalline anisotropy is negligible in this case. When the deformation is beyond the observed critical point of R = 51%, we can see from Fig. 3.20c that the size of these Co-rich nanocrystals become larger, with diameter exceeding 10 nm, and these crystals become nearly touched with each other. The existence of these nanocrystals with large size causes an increase of magnetocrystalline anisotropy and the magnetic hardness, deteriorating the soft magnetic property and hence the reduction of GMI ratio.

The last point deals with the effect of deformation on the anisotropy field which is governed by the magnetostriction constant λ_s , saturation magnetization M_s and the difference between σ_{zz} and $\sigma_{\phi\phi}$ and can be expressed as [62]:

$$H_k = \frac{3\lambda_s}{M_s} \left(\sigma_{zz} - \sigma_{\varphi\varphi} \right) \tag{3.15}$$

As the difference between σ_{zz} and $\sigma_{\phi\phi}$ increases with cold-drawing process as shown in Fig. 3.10, the anisotropy field then increases accordingly. However, instead of a linear increase with increasing reduction area, the anisotropy field became constant after R=36%. In a reverse way of reasoning, this suggests the difference between σ_{zz} and $\sigma_{\phi\phi}$ could become smaller. Indeed, as shown in a previous study [63], the circumferential stress exhibits a peak feature with increasing reduction area, i.e., the stress increases first and then decreases. This explains the observed evolution of anisotropy field with the wire area reduction. It is desirable to conduct a similar quantitative analysis for the present wires, which will be addressed in future work.

3.4.2 Magnetocaloric Property

Magnetic cooling technique has drawn much attention since it involves no environmental hazardous gas that is essential for conventional gas-compression technique. The cooling technique is realized through the adiabatic temperature change or the isothermal entropy change in response to an applied magnetic field in a material, i.e. magnetocaloric effect [64]. In comparison with the gas-compression cycle, the magnetic cooling cycle has much higher efficiency [65]. Therefore, significant research efforts have been devoted to exploring new MCE materials and devices. As compared to other form of MCE materials, microwires have the following advantages [46, 66]: (1) large surface area to volume ratio, which ensures a high cooling efficiency. (2) large aspect ratio, which means small demagnetization factor; (3) wire bundles have large operation frequency and favor a high-performance active magnetic refrigeration system.

Obviously, compared with bulk metallic glass (BMG), a strongly shape anisotropy appears due to the unique shape of the microwires and which may resulting in the anisotropy of magnetic properties. In order to investigating the influence of

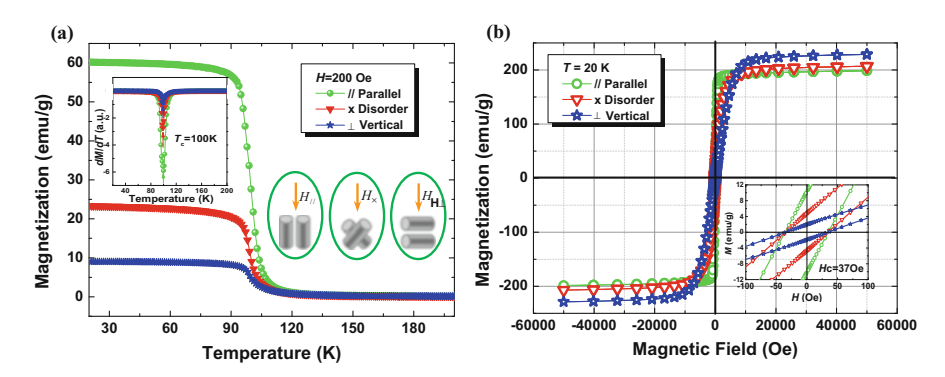


Fig. 3.25 (a) Temperature dependences of FC magnetization taken at a field of 200 Oe for three different microwire arrangements, *insets* are the plot of dM/dT vs. T (*left hand*) and schematic diagrams (*right hand*) of three different microwire arrangements. (b) Magnetic hysteresis loops (M-H) for three microwire samples with different arrangements taken at 20 K, the *inset* shows the M-H loops at low applied magnetic field

microwire shape anisotropy, three different microwire arrangements were designed and performed: the microwires were arranged parallel (//), disorder (×), and vertical (\bot) versus the direction of applied field, respectively, as schematically shown in inset (right hand) of Fig. 3.25a. The temperature dependence field-cooled (FC) taken at 200 Oe of three different arrangements was displayed in Fig. 3.25. Therefore, it can be observed that the microwires undergo a paramagnetic to ferromagnetic (PM-FM) transition. The Curie temperature T_C , defined by the minimum in dM/dT, is determined to be about 100 K, as plotted and shown in inset (left hand) of Fig. 3.25a. It is noticeable that the magnetization is much larger and the PM-FM transition is broader for the axis of microwires (//) arranging parallel to the applied field. Figure 3.25b displays the magnetic hysteresis loops (M-H) taken at 20 K of different microwires arrangements. As coupled with inset in the Fig. 3.25b, micromicrowires exhibit a soft ferromagnetic characteristic ($H_C \sim 37$ Oe), which is desirable for magnetic refrigeration applications. The square shape of the M-H loop (//) indicates that the easy magnetization direction is parallel to the micromicrowire axis. Remarkably, the M-H loop (\perp) of microwire axis arranging vertical to test field displays the largest saturation magnetization in large applied field ($M_s = 229 \text{ emu/g}, \Delta H = 5 \text{ T}$), ~15 % larger than that of parallel to the applied field ($M_s = 199 \text{ emu/g}, \Delta H = 5 \text{ T}$).

Figure 3.26a–c shows the isothermal magnetizations (M-H) curves for the three microwire arrangements in the applied field. The results for all above cases are displayed in Fig. 3.26a–c. Further to explore the nature of the magnetic phase transitions in the present samples, Arrott plots have been constructed based on the M-H data (Fig. 3.26d–f). As displayed, the sign of the slope of M^2 vs H/M is determined by the nature of a PM to FM transition, and the positive slope corresponding to a second order transition for all the microwire samples. Notably, due to the shape anisotropy of the microwires, the magnetizations of all

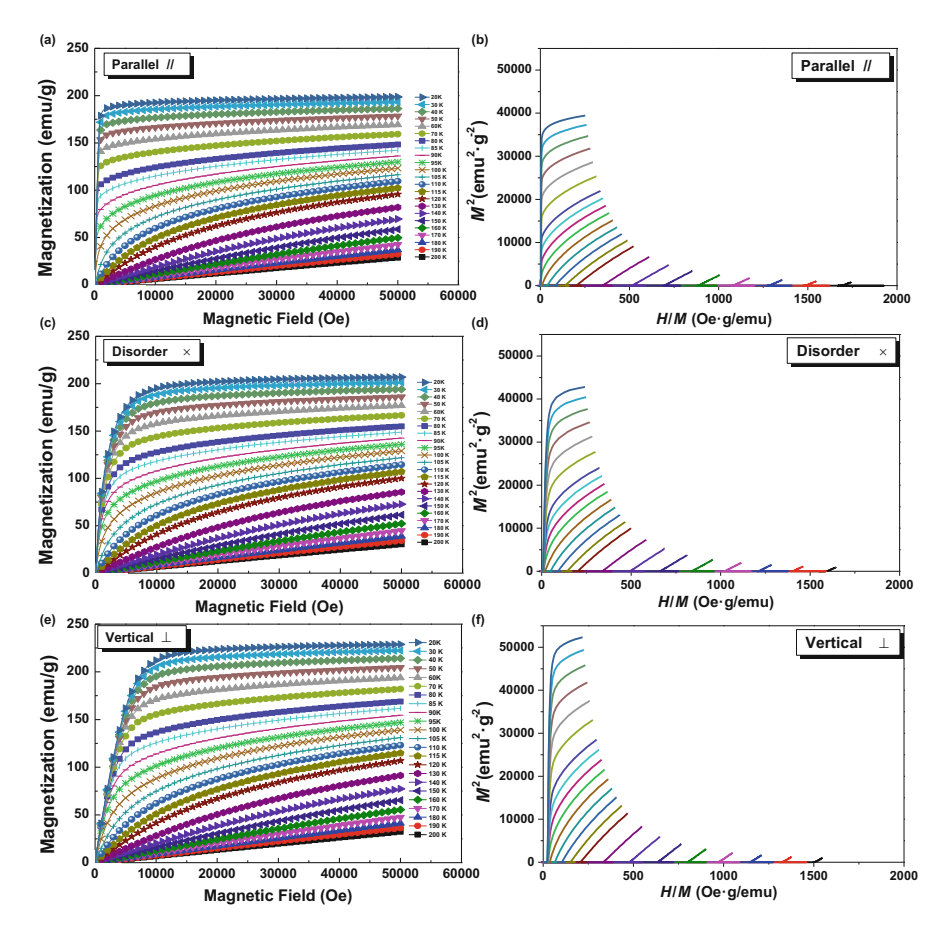


Fig. 3.26 Isothermal magnetization curves at different fixed temperatures between 20 and 200 K

temperatures can easilyreach its saturation state at low magnetic fields for the case (//) of microwire sample parallel arrangement compared with the other two cases (\times or \perp). The obtained exciting results indicated that a larger isothermal magnetic entropy change ($-\Delta S_m$) can be induced by a low magnetic fields for the // sample. Just this characteristic is favorable for practical applications of magnetic refrigerators, i.e. more economical permanent magnets can be provided as a magnetic field source instead of using expensive superconducting magnets.

The magnetic entropy change $(-\Delta S_{\rm m})$ of the samples has been calculated from the *M-H* isotherms by integrating throughout the whole magnetic fields:

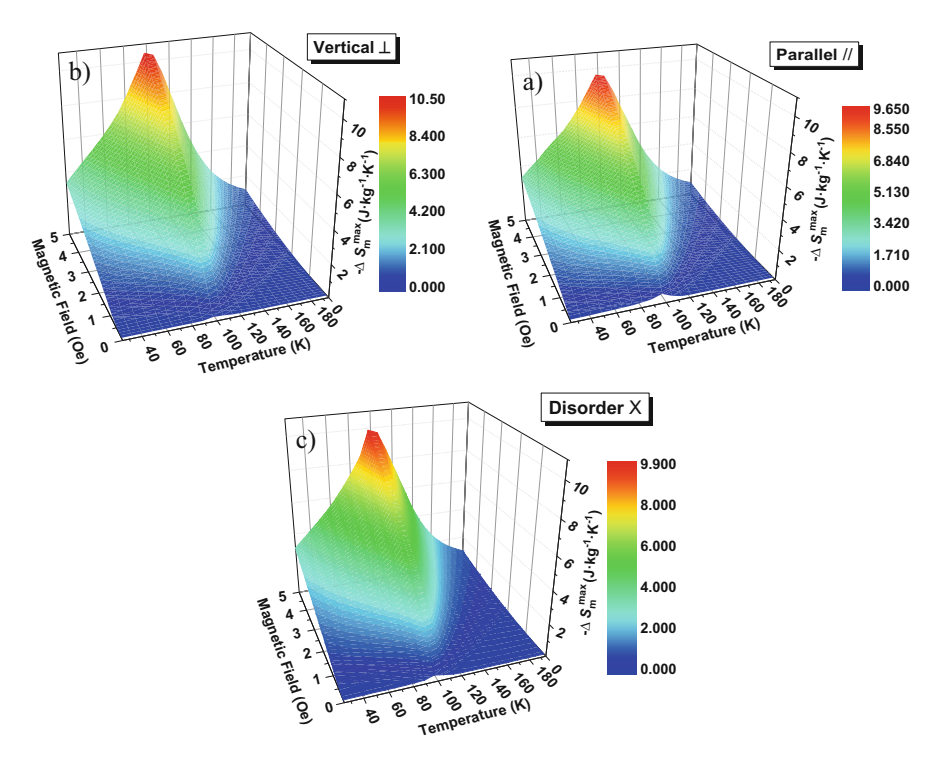


Fig. 3.27 Temperature dependence of magnetic entropy change $(-\Delta S_m)$ for different field changes up to 5 T (a) for the "//" sample, (b) for the "×" sample and (c) for the " \perp " sample

$$\Delta S_m(T, H) = S(T, H) - S(T, 0) = \int_0^{H_{\text{max}}} \left(\frac{\partial M}{\partial T}\right)_H dH$$
 (3.16)

where H represents the magnetic field, M denotes the magnetization, and T is the temperature. Then the results of $-\Delta S_m$ vs. T under different magnetic fields for the three microwire samples are plotted in Fig. 3.27a–c. As desired, all microwire samples with different arrangement all display large values of magnetic entropy change $(-\Delta S_m)$ around the T_C and broad magnetic entropy change peaks. Remarkably, a larger peak value of isothermal magnetic entropy change $(-\Delta S_m^{\max})$ and broader $-\Delta S_m$ vs. T curves were achieved at a low magnetic fields (<2 T) for the // sample compared with the other two cases. Mostly interested, the \bot sample shows a superior peak value of magnetic entropy change $(-\Delta S_m^{\max}, \sim 10.6 \text{ J} \cdot \text{Kg}^{-1} \cdot \text{K}^{-1})$ at 5 T) than the other sample at large applied magnetic field (>2 T).

3.5 Conclusions

The melt extraction technique can be fruitfully employed to fabricate amorphous, nanocrystalline, and dual-phase amorphous/nano-crystal metallic wires by controlling process parameters during fabrication process and post treatment like annealing and drawing. These microwires exhibited excellent mechanical and magnetic properties, which depend both on the composition design, process optimization and post treatments. The following conclusions can be drawn from previous works:

- (a) Wire extraction mainly resulted in three geometries: uniform wires with concaved track at extracted wheel speed 5 m/s, wires exhibiting Rayleigh waves between 5 and 30 m/s, uniform wires with circular cross-sections at higher wheel speed 30 m/s. The formation of wavy wires is due to the Rayleigh instabilities and surface tension effect which tend to reduce the free surface area of the extracted liquid layer.
- (b) Wetting is a key parameter in the melt extraction process. Wetting behavior during melt extraction is distinct and different from conventional sessile drop method and dynamic wetting behavior. Besides the existence of shear force acting at the contact between the wheel tip and molten, supercooling or solidification occurs during the extraction process and, therefore, extraction could be processed.
- (c) Analysis of the controlling mechanism in the melt extraction process shows that, both thermal and viscous, i.e., momentum transport mechanism, are involved in the different process conditions. The controlled mechanism in the optimum process region is momentum transport.
- (d) The extracted amorphous microwires exhibit high mechanical properties and fracture reliability. The fracture strength of Co-based microwires with diameter of 40 μm is approximately 3700 MPa. The Weibull modulus is 22.05 for the two-parameter Weibull static calculation, and the threshold value can be reached as high as 2644 MPa for the three-parameter Weibull static calculation.
- (e) The fracture strength of the Co-based amorphous microwire gradually increased with the strain rates, while the tensile plasticity increased with decreasing strain rate. At strain rates below $1.0 \times 10^{-4} \, \mathrm{s}^{-1}$, due to the balance of creation and annihilation of free volume, large dimensions of shear offset were formed on the fracture surface, leading to a pronounced tensile plasticity in Co-based amorphous microwires.
- (f) The Co-based microwires can be successfully cold drawn with up to 75% cross-section area reduction. Tensile ductility, tensile strength as well as the GMI effect of the drawn wires increased with cold drawing and reached a peak of 1.09%, 4320 MPa and 160%, respectively, at 51% cross-section area reduction and followed by a reduction with further deformation.
- (g) Nano-sized crystallites precipitated during drawing can stabilize the shear bands and arrest its fast propagation, leading to an enhanced ductility. The residual stress not only accelerates the amorphous-to-nanocrystalline phase

transformation but also contributes to the mechanical and magnetic properties. Both GMI ratio and anisotropy field are significantly improved after cold drawing.

(h) Amorphous Gd-based microwires show excellent magnetocaloric properties due to the short-range order structure and size effect. The design and fabrication of a magnetic bed made of these multiple single parallel-arranged microwires would be a very promising approach for active magnetic refrigeration for nitrogen liquefaction.

The simultaneous achievement of high mechanical and magnetic properties opens up abundant possibilities of producing a variety of magnetic, stress and biological sensors or microwires enabled multifunctional composites.

Acknowledgement The authors gratefully acknowledge the financial support from the Natural Science Foundation of China (NSFC 51371067, 51671171 and 51501162) and Zhejiang Provincial Natural Science Foundation of China (LY16E010001). HW also acknowledges useful discussions with Hongxian Shen, Jingshun Liu, Shuling Zhang, and Lunyong Zhang from the Harbin Institute of Technology, PR China.

References

- Strom-Olsen, J.: Fine wires by melt extraction. Mater. Sci. Eng. A Struct. Mater. Prop. Microstruct. Process. 178, 239–243 (1994)
- Vazquez, M., Hernando, A.: A soft magnetic wire for sensor applications. J. Phys. D Appl. Phys. 29, 939–949 (1996)
- 3. Waseda, Y., Ueno, S., Hagiwara, M., Aust, K.: Formation and mechanical properties of Fe-and Co-base amorphous alloy wires produced by in-rotating-water spinning method. Prog. Mater. Sci. **34**, 149–260 (1990)
- Chiriac, H., Ovari, T.A.: Amorphous glass-covered magnetic wires: preparation, properties, applications. Prog. Mater. Sci. 40, 333–407 (1996)
- 5. Phan, M.-H., Peng, H.X.: Giant magnetoimpedance materials: fundamentals and applications. Prog. Mater. Sci. **53**, 323–420 (2008)
- Qin, F.X., Peng, H.-X.: Ferromagnetic microwires enabled multifunctional composite materials. Prog. Mater. Sci. 58, 183–259 (2013)
- 7. Donald, I.W., Metcalfe, B.L.: Preparation, properties and applications of some glass-coated metal filaments prepared by the Taylor-wire process. J. Mater. Sci. 31, 1139–1149 (1996)
- 8. Zhukov, A., Zhukova, V., Blanco, J.M., Gonzalez, J.: Recent research on magnetic properties of glass-coated microwires. J. Magn. Magn. Mater. **294**, 182–192 (2005)
- 9. Ochin, P.: Shape memory thin round wires produced by the in rotating water melt-spinning technique. Acta Mater. **54**, 1877–1885 (2006)
- Yamasaki, J., et al.: Magnetic properties of Co-Si-B amorphous wires prepared by quenching in-rotating water technique. IEEE Trans. J. Magn Jpn. 4, 360–367 (1989)
- 11. Chiriac, H., Ovari, T.A., Vazquez, M., Hernando, A.: Magnetic hysteresis in glass-covered and water-quenched amorphous wires. J. Magn. Magn. Mater. 177–181, 205–206 (1998)
- 12. Hagiwara, M., Inoue, A., Masumoto, T.: Mechanical properties of Fe-Si-B amorphous wires produced by in-rotating-water spinning method. Metall. Mater. Trans. A 13, 373–382 (1982)
- Maringer, R.E., Mobley, C.E.: Advances in melt extraction. Rapid Quenched Metals III. 446, 49–56 (1978)

- Wang, H., Xing, D., Wang, X., Sun, J.: Fabrication and characterization of melt-extracted Co-based amorphous wires. Metall. Mater. Trans. A 42A, 1103–1108 (2010)
- 15. Allahverdi, M., Drew, R.: Melt Extraction of Oxide Ceramic Wires. Montreal, McGill University (1991)
- Inoue, A., Amiya, K., Yoshii, I., Kimura, H.M., Masumoto, T.: Production of Al-based amorphous alloy wires with high tensile strength by a melt extraction method. Mater. Trans. JIM 35, 485–488 (1994)
- 17. Maringer, R.E., Mobley, C.E.: Casting of metallic filament and wire. J. Vac. Sci. Technol. 11, 1067 (1974)
- Allahverdi, M., Drew, R.A.L., Rudkowska, P., Rudkowski, G., Strom-Olsen, J.O.: Amorphous CaO-Al₂O₃ wires by melt extraction. Mater. Sci. Eng. Struct. Mater. Prop. Microstruct. Process. A207, 12–21 (1996)
- Shen, T.D., Schwarz, R.B.: Lowering critical cooling rate for forming bulk metallic glass. Appl. Phys. Lett. 88, 091903 (2006)
- Allahverdi, M., Drew, R., Strom-Olsen, J.: Wetting and melt extraction characteristics of ZrO₂-Al₂O₃ based materials. J. Am. Ceram. Soc. 80, 2910–2916 (1997)
- 21. Maringer, R.E., Mobley, C.E.: Melt extraction of metallic filament and staple wire. AIChE Symp. Ser. **74**, 16–19 (1978)
- 22. Engineering, M.: Fine metallic and ceramic wires by melt extraction. Techniques 1, 158–162 (1994)
- Baik, N.I., Choi, Y., Kim, K.Y.: Fabrication of stainless steel and aluminum wires by PDME method. J. Mater. Process. Technol. 168, 62–67 (2005)
- 24. Arkhangel'skij, V.M., Mitin, B.S.: Problems in wire producing by pendant drop melt extraction. Stal', 71–76 (2001)
- Archangelsky, W., Prischepov, S.V., Vasiliev, V.A.: Adhesion interaction on melt extraction from pendant drop. Mater. Sci. Eng. A Struct. Mater. Prop. Microstruct. Process. 304, 598–603 (2001)
- Strom-Olsen, J.: Fine fibres by melt extraction. Mater. Sci. Eng. A Struct. Mater. Prop. Microstruct. Process. A178, 239–243 (1994)
- 27. Allahverdi, M., Drew, R.A.L., Strom-Olsen, J.: Melt extraction and properties of ZrO₂ · Al₂O₃-based wires. Ceram. Eng. Sci. Proc. **16**, 1015–1025 (1995)
- 28. Rudkowski, P., Strom-Olsen, J.O., Rudkowska, G., Zaluska, A., Ciureanu, P.: Ultra fine, ultra soft metallic fibres. IEEE Trans. Magn. 31, 1224–1228 (1995)
- 29. Allahverdi, M., Drew, R.A.L., StromOlsen, J.O.: Melt-extracted oxide ceramic fibres The fundamentals. J. Mater. Sci. 31, 1035–1042 (1996)
- Allahverdi, M., Drew, R.A.L., StromOlsen, J.O.: Wetting and melt extraction characteristics of ZrO2-Al₂O₃ based materials. J. Am. Ceram. Soc. 80, 2910–2916 (1997)
- Strom-olsen, J.O., Rudkowska, G., Rudkowski, P., Allahverdi, M., L. Drew, R.A. Fine metallic and ceramic fibres by melt extraction. Mater. Sci. Eng. A Struct. Mater. Prop. Microstruct. Process. 179–180, 158–162 (1994)
- 32. Katsuya, A., Inoue, A., Masumoto, T.: Production and properties of amorphous alloy wires in Fe-B base system by a melt extraction method. Mater. Sci. Eng. A Struct. Mater. Prop. Microstruct. Process. **226**, 104–107 (1997)
- Zhang, T., Inoue, A.: A new method for producing amorphous alloy wires. Mater. Trans. JIM 41, 1463–1466 (2000)
- 34. Inoue, A., Amiya, K., Katsuya, A., Masumoto, T.: Mechanical properties and thermal stability of Ti- and Al-based amorphous wires prepared by a melt extraction method. Mater. Trans. JIM 36, 858–865 (1995)
- 35. Taha, M.A., El-Mahallawy, N.A., Abdel-Gaffar, M.F.: Geometry of melt-spun ribbons. Mater. Sci. Eng. A A134, 1162–1165 (1991)
- 36. Tanner, B.R.I.: Note on the Rayleigh Problem for a Visco-Elastic Fluid. 13, 573-580 (1962)
- 37. Saasen, B.A., Tyvand, P.A.: Rayleigh-Taylor instability and Rayleigh-type waves on a Maxwell-fluid. J. Appl. Math. 41, 284–293 (1990)

- 38. Olson, B.J., Cook, A.W.: Rayleigh-Taylor shock waves. Phys. Fluids 19, 128108 (2007)
- 39. Akihisa, I.: Preparation of amorphous Fe-Si-B and Co-Si-B alloy wires by a melt extraction method and their mechanical and magnetic properties. Mater. Trans. **36**, 802–809 (1995)
- Allahverdi, M., Drew, R.A.L., Rudkowska, P., Rudkowski, G., StromOlsen, J.O.: Amorphous CaO · Al₂O₃ wires by melt extraction. Mater. Sci. Eng. A Struct. Mater. Prop. Microstruct. Process. 207, 12–21 (1996)
- 41. Kavesh, S.: Melt spinning of metal wires. AIChE Symp. Ser. 74, 1–15 (1978)
- 42. Schlichting, H., Gersten, K.: Boundary-Layer Theory, Berlin: Springer Verlag, (2000)
- 43. Schlichting, H.: Theory of Boundary Layer. Nauka, Moscow (1969)
- 44. Wang, H., Qin, F.X., Xing, D.W., et al.: Fabrication and characterization of nano/amorphous dualphase FINEMET microwires. Mater. Sci. Eng. B 178(20), 1483–1490 (2013)
- 45. Khandogina, E.N., Petelin, A.L.: Magnetic, mechanical properties and structure of amorphous glass coated microwires. J. Magn. Magn. Mater. 249, 55–59 (2002)
- 46. Qin, F.X., et al.: Mechanical and magnetocaloric properties of Gd-based amorphous microwires fabricated by melt-extraction. Acta Mater. **61**, 1284–1293 (2013)
- 47. Mukai, T., Nieh, T.G., Kawamura, Y., Inoue, A., Higashi, K.: Effect of strain rate on compressive behavior of a Pd₄₀Ni₄₀P₂₀ bulk metallic glass. Intermetallics **10**, 1071–1077 (2002)
- 48. Spaepen, F.: A microscopic mechanism for steady state inhomogeneous flow in metallic glasses. Acta Metall. 25, 407–415 (1977)
- Wu, F.F., Zhang, Z.F., Mao, S.X.: Size-dependent shear fracture and global tensile plasticity of metallic glasses. Acta Mater. 57, 257–266 (2009)
- Wang, H., et al.: Relating residual stress and microstructure to mechanical and giant magnetoimpedance properties in cold-drawn Co-based amorphous microwires. Acta Mater. 60, 5425–5436 (2012)
- 51. Yi, J., et al.: Micro-and nanoscale metallic glassy wires. Adv. Eng. Mater. 12, 1117-1122
- 52. Nagase, T., Kinoshita, K., Nakano, T., Umakoshi, Y.: Fabrication of Ti-Zr binary metallic wire by Arc-Melt-Type melt-extraction method. Mater. Trans. **50**, 872–878 (2009)
- 53. Takayama, S.: Drawing of Pd77. 5Cu6Si16. 5 metallic glass wires. Mater. Sci. Eng. 38, 41–48 (1979)
- 54. Masumoto, T., Ohnaka, I., Inoue, A., Hagiwara, M.: Production of Pd-Cu-Si amorphous wires by melt spinning method using rotating water. Scripta Metall 15, 293–296 (1981)
- 55. Zberg, B., Arata, E.R., Uggowitzer, P.J., Lofler, J.F.: Tensile properties of glassy MgZnCa wires and reliability analysis using Weibull statistics. Acta Mater. 57, 3223–3231 (2009)
- Nagase, T., Ueda, M., Umakoshi, Y.: Preparation of Ni-Nb-based metallic glass wires by arcmelt-type melt-extraction method. J. Alloys Compd. 485, 304–312 (2009)
- Metals, O., Centre, D.: Production of Ni-Pd-Si and Ni-Pd-P amorphous wires and their mechanical and corrosion properties. Development 20, 97–104 (1985)
- Wu, Y., et al.: Nonlinear tensile deformation behavior of small-sized metallic glasses. Scr. Mater. 61, 564–567 (2009)
- 59. V'azquez, M.: Advanced magnetic microwires. In: Handbook of Magnetism and Advanced Magnetic Materials, vols 1–34. John Wiley & Sons, Ltd (2007)
- Antonov, A.S., Borisov, V.T., Borisov, O.V., Prokoshin, A.F., Usov, N.A.: Residual quenching stresses in glass-coated amorphous ferromagnetic microwires. J. Phys. D Appl. Phys. 33, 1161 (2000)
- 61. Zhang, S.L., Sun, J.F., Xing, D.W., Qin, F.X., Peng, H.X.: Large GMI effect in Co-rich amorphous wire by tensile stress. J. Magn. Magn. Mater. 323, 3018–3021 (2011)
- 62. Antonov, A.S., et al.: Residual quenching stresses in amorphous ferromagnetic wires produced by an in-rotating-water spinning process. J. Phys. D Appl. Phys. **32**, 1788–1794 (1999)
- 63. Wu, Y., Wu, H.H., Hui, X.D., Chen, G.L., Lu, Z.P.: Effects of drawing on the tensile fracture strength and its reliability of small-sized metallic glasses. Acta Mater. **58**, 2564–2576 (2010)
- 64. Provenzano, V., Shapiro, A.J., Shull, R.D.: ErratumReduction of hysteresis losses in the magnetic refrigerant Gd₅Ge₂Si₂ by the addition of iron. Nature **435**, 528–528 (2005)

- 65. Jeong, S.: AMR (Active Magnetic Regenerative) refrigeration for low temperature. Cryogenics **62**, 193–201 (2014)
- 66. Dong, J.D., Yan, A.R., Liu, J.: Microstructure and magnetocaloric properties of melt-extracted La–Fe–Si microwires. J. Magn. Magn. Mater. **357**, 73–76 (2014)

Chapter 4 Giant Magneto-Impedance Effect in Amorphous Ferromagnetic Microwire with a Weak Helical Anisotropy

N.A. Usov and S.A. Gudoshnikov

4.1 Introduction

Amorphous ferromagnetic glass-coated microwires are very promising for a number of technical applications, in particular, for creation of sensitive magnetic field sensors [1–3]. Currently, the technology of manufacturing of glass-coated microwires with diameters from a few to tens of micrometers is well developed [4]. This allows production of samples of a perfect cylindrical shape, with controlled diameters and composition. It is well known [5–7] that the magnetic anisotropy of amorphous ferromagnetic microwires is determined mainly by residual quenching stress arising during rapid solidification of the metal alloys. Therefore, the magnetic properties of microwires with a small positive or negative magnetostriction constant λ_s are radically different. In particular, the Co-rich glass-coated microwires with $\lambda_s < 0$ are magnetized circularly in the ground state, and show the Giant Magneto-Impedance (GMI) effect [8–25] with a very large GMI ratio. The GMI effect is used [26–28] to develop a new generation of sensitive sensors of weak magnetic fields.

Note that in the microwires with a small negative magnetostriction, having a nearly circular magnetic anisotropy, there are actually two different GMI effects, i.e., diagonal and off-diagonal GMI effects [14, 20]. The diagonal GMI effect is a dramatic change in the complex resistance of the microwire at alternating current as a function of external magnetic field applied along the microwire axis. The off-diagonal GMI effect is the appearance of a voltage in the receiving coil wound on the microwire, when the ac current flows along the wire axis.

N.A. Usov (⋈) • S.A. Gudoshnikov National University of Science and Technology "MISIS", 119049 Moscow, Russia

Pushkov Institute of Terrestrial Magnetism, Ionosphere and Radio Wave Propagation, Russian Academy of Sciences, IZMIRAN, Troitsk, 142190 Moscow, Russia e-mail: usov@izmiran.ru

The off-diagonal GMI effect is especially interesting for the creation of a highly sensitivity magnetometer, as the voltage induced in the receiving coil is directly proportional to the component of the applied magnetic field parallel to the wire axis.

The initial circular magnetization of amorphous Co-rich microwire determines the high sensitivity of GMI wire characteristics to the longitudinal external magnetic field [2, 3, 14, 18]. At the same time, in most Co-rich microwires the helical magnetic anisotropy [18, 29, 30] was found. Recently it has been shown [29, 30] that the presence of even a weak helical anisotropy contribution significantly influences the electromagnetic properties of Co-rich amorphous microwires. Thus, to understand completely the electrodynamic properties of amorphous Co-rich microwires it is necessary: (1) to calculate the distribution of residual quenching stresses over the microwire cross section; (2) to describe the magnetostatic wire properties in a weak external magnetic field, taking into account the contribution of helical anisotropy; (3) to develop the electrodynamics of microwire considering the tensor nature of the wire magnetic permeability and its strong dependence on the external magnetic field and the phenomenological magnetic damping constant. These issues are discussed in Sects. 4.2, 4.3, and 4.4 of this paper. In Sect. 4.5 the basic parameters that determine the slop of the off-diagonal component the wire impedance as a function of external magnetic field are discussed. This question is important to create a sensitive sensor of weak magnetic fields working on the off-diagonal GMI effect. In the same section we discuss briefly the possible impact of the magnetic defects and bamboo domain walls separating the circular magnetic domains magnetized in opposite directions, on the GMI characteristics of Co-rich amorphous microwire.

4.2 The Nature of the Magnetic Anisotropy in Amorphous Ferromagnetic Microwires

4.2.1 The Density of the Magneto-Elastic Energy

It is well known [5–7] that the distribution of easy anisotropy axes in amorphous ferromagnetic microwires and ribbons are determined mainly by magneto-elastic interaction. The latter is significant in amorphous alloys due to the presence of large residual quenching stresses. The latter arise during rapid quenching of the samples from the melt.

For amorphous Co-rich microwire with negative magnetostriction constant, $\lambda_s < 0$, the density of the magneto-elastic energy can be written [7] in the cylinder coordinates (ρ, φ, z) as a diagonal quadratic form

$$w_{m-el} = K \left[\widetilde{\sigma}_{\rho\rho} \alpha_{\rho}^2 + \widetilde{\sigma}_{\varphi\varphi} \alpha_{\varphi}^2 + \left(\widetilde{\sigma}_{zz} + \widetilde{\sigma}_{zz}^{(a)} \right) \alpha_z^2 \right], \quad K = \frac{3}{2} |\lambda_s| \sigma_0, \tag{4.1}$$

where K is the nominal anisotropy constant of the wire, $\sigma_0 = 100$ MPa is a characteristic amplitude of residual quenching stress, $\tilde{\sigma}_{ij} = \sigma_{ij}/\sigma_0(i,j=\rho,\varphi,z)$ are the reduced tensor components of the residual quenching stress in cylindrical coordinates, and $\tilde{\sigma}_{zz}^{(a)} = \sigma_{zz}^{(a)}/\sigma_0$ is the reduced applied tensile stress.

Note that Eq. (4.1) describes the magneto-elastic energy density of the amorphous microwire with a strictly circular type magnetic anisotropy. For a description of the magnetic properties of microwires with a weak helical anisotropy it is necessary to introduce in Eq. (4.1) a small off-diagonal correction term [29, 30]. This point will be discussed further in Sect. 4.3.2.

The calculation of the residual quenching stresses in glass-coated microwires show as a rule [31, 32], that the azimuthal component of the residual stress tensor has the smallest value within the ferromagnetic wire nucleus, $\tilde{\sigma}_{\phi\phi} < \tilde{\sigma}_{\rho\rho}, \tilde{\sigma}_{zz}$. Therefore, the magneto-elastic energy, Eq. (4.1), has a minimum when the unit magnetization vector points in the azimuthal direction, so that $\vec{\alpha} = (0, \pm 1, 0)$. This means that for a microwire with negative magnetostriction the easy anisotropy axis has azimuthal direction.

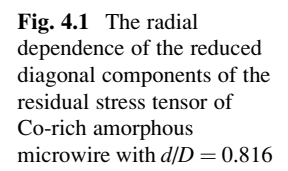
Evidently, the deviation of the unit magnetization vector in the radial direction is energetically unfavorable because it leads to the appearance of the demagnetizing fields and associated magnetostatic energy. On the other hand, for the deviation of the unit magnetization vector in the longitudinal direction one has the relation $\alpha_{\varphi}^2 = 1 - \alpha_z^2$. For such a process, the magneto-elastic energy density (4.1) takes the form

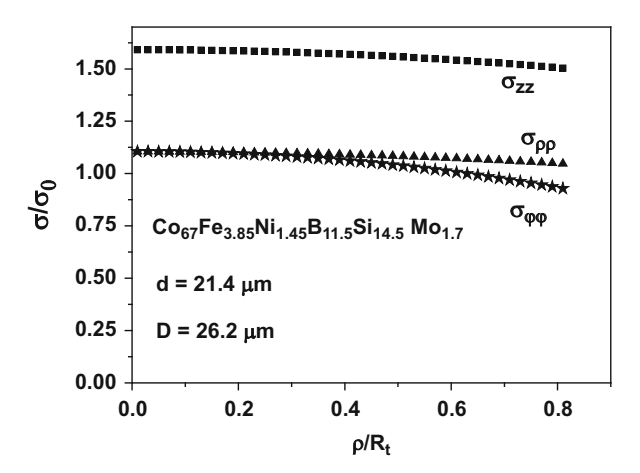
$$w_{m-el} = K \left[\widetilde{\sigma}_{\varphi\varphi} + \left(\widetilde{\sigma}_{zz} - \widetilde{\sigma}_{\varphi\varphi} + \widetilde{\sigma}_{zz}^{(a)} \right) \alpha_z^2 \right]. \tag{4.2}$$

Therefore, the longitudinal direction is difficult for this type of microwires, the corresponding effective magnetic anisotropy constant being $K_{ef} = K(\tilde{\sigma}_{zz} - \tilde{\sigma}_{\varphi\varphi} + \tilde{\sigma}_{zz}^{(a)})$. It follows from this expression that the magnetostatic properties of amorphous glass-coated Co-rich microwire are determined mainly by three physical parameters, namely the saturation magnetization M_s , the magnetostriction constant λ_s , and the characteristic amplitude of the residual quenching stress $\Delta \tilde{\sigma} = \tilde{\sigma}_{zz} - \tilde{\sigma}_{\varphi\varphi}$. The effective anisotropy field of the microwire can be defined as $H_{a,ef} = H_a(\Delta \tilde{\sigma} + \tilde{\sigma}_{zz}^{(a)})$, where $H_a = 2K/M_s = 3l\lambda_s |\sigma_0/M_s$ is the nominal anisotropy field of the microwire.

4.2.2 The Estimation of Residual Quenching Stress

As noted above, the magnetoelastic interactions are essential in amorphous microwires due to the presence of significant residual quenching stresses. An adequate calculation of the residual stresses in amorphous glass-coated ferromagnetic wires has been carried out [7] based on the theory of viscoelastic medium [33].





In fact, the theory of viscoelasticity generalizes the usual elasticity theory [34] and at the same time takes into account the relaxation of the internal shear stresses at elevated temperatures, when the viscosity of the solidifying alloy is still not very large. Thermoelastic stresses [5.6] are significant only below the glass transition point, where the process of stress relaxation can be neglected. These stresses are taken into account automatically in the approach developed in [7].

Due to axial symmetry of the microwire, in the cylindrical coordinates (ρ, φ, z) only the diagonal components of the residual stress tensor, $\sigma_{\rho\rho}(\rho)$, $\sigma_{\varphi\varphi}(\rho)$ and $\sigma_{zz}(\rho)$ are nonzero. In addition, these components depend only on the radial coordinate. As an example, Fig. 4.1 shows the radial dependence of the diagonal components of the residual stress tensor calculated for Co-rich microwire of composition $\text{Co}_{67}\text{Fe}_{3.85}\text{Ni}_{1.45}\text{B}_{11.5}\text{Si}_{14.5}\text{Mo}_{1.7}$ with inner and outer diameters $d=21.4~\mu\text{m}$ and $D=26.2~\mu\text{m}$, respectively. The diagonal components are normalized to the characteristic amplitude of the residual quenching stress, $\sigma_0=100~\text{MPa}$, the radial coordinate being normalized to the outer wire radius $R_t=D/2$.

As Fig. 4.1 shows, in a glass-coated microwire the reduced diagonal components of the residual stress tensor show only weak radial dependence due to appreciable difference of the thermal conductivities of the metallic nucleus and the glass shell, respectively. As discussed above, the effective anisotropy constant of amorphous Co-rich microwire is determined by the reduced difference of the diagonal stress components $\Delta \tilde{\sigma} = \tilde{\sigma}_{zz} - \tilde{\sigma}_{\varphi\varphi}$ calculated at the surface of the metallic nucleus, at $\rho = R$.

The experimental evaluation of the amplitude of the residual quenching stress in amorphous Co-rich microwire can be obtained by means of small angle magnetization rotation (SAMR) method [35]. In the SAMR method [36, 37] the wire is initially magnetized along its axis in a sufficiently strong magnetic field, $H_{0z} >> H_{a,ef}$, which exceeds the wire effective anisotropy field $H_{a,ef}$. Then, the nearly uniform wire magnetization is subjected to the influence of a circular magnetic field of alternating current, $I(t) = I_0 \sin(\omega t)$, of frequency f flowing through

the wire. Here $\omega = 2\pi f$ is the angular frequency, and I_0 is the ac current amplitude. The magnetic field of ac current causes the magnetization oscillations of the wire circular magnetization component, and accordingly, the oscillations of the longitudinal magnetization component. This leads to the generation of the electro-motive force (EMF) signal in the receiving coil wound on the microwire

$$E = -\frac{1}{c} \frac{\partial \Phi}{\partial t} = -\frac{4\pi M_s N}{c} \int \frac{\partial \alpha_z}{\partial t} ds,$$

where *N* is the number of turns in the receiving coil. The EMF signal occurs at the doubled frequency 2f, because circular component of the magnetization vector is small, $\alpha_{\varphi} << 1$. Thus, the longitudinal component of the unit magnetization vector is approximately equal $\alpha_z = \sqrt{1 - \alpha_{\varphi}^2} \approx 1 - \alpha_{\varphi}^2/2$. For the second EMF harmonic induced in the receiving coil the following expression has been obtained [35]:

$$E_{2f}(H_{0z},t) = E_{2f}(H_{0z})\sin(2\omega t), \tag{4.3}$$

the amplitude of the second EMF harmonic being

$$E_{2f}(H_{0z}) = \frac{C_{2f}}{\left(H_{a,ef} - H_{0z}\right)^2}; \quad C_{2f} = \frac{4\pi^2 M_s N\omega I_0^2}{c^3}; \tag{4.4}$$

One has to remember that Eq. (4.4) is valid only in magnetic field stronger than the effective wire anisotropy field, $H_{0z} > H_{a,ef}$, so that the condition $\alpha_{\varphi} << 1$ is satisfied. Otherwise, the magnetization of the Co-rich microwire is twisted in azimuthal direction, contrary to the initial assumption of nearly uniform magnetization of the amorphous microwire. The numerator C_{2f} in Eq. (4.4) depends only on single material parameter of the microwire, namely the saturation magnetization. The latter for the microwire of composition $Co_{67}Fe_{3.85}Ni_{1.45}B_{11.5}Si_{14.5}Mo_{1.7}$ with inner and outer diameters $d=21.4~\mu m$ and $D=26.2~\mu m$ has been independently measured as $M_s=500~emu/cm^3$. Using the values of the other parameters of the experiment [35] (the number of turns of the receiving coil N=630, $I_0=4~mA$, f=5~kHz) one obtains the value $C_{2f}=0.63~mV$.

Then, one can determine the experimental values of the wire effective anisotropy fields at various tensile stresses by comparing the experimental dependence of the amplitude of the second EMF harmonic as a function of the applied magnetic field with Eq. (4.4). These values were found to be $H_{a,ef}=1.0,\,1.2,\,1.4,\,$ and 1.6 Oe for mechanical loads $m=0.5,\,1.5,\,2.5,\,$ and 3.5 g, respectively. It is easy to see that the effective anisotropy field of the microwire does increase proportionally to the applied tension. Using the theoretical expression $H_{a,ef}=H_a\left(\Delta\widetilde{\sigma}+\widetilde{\sigma}_{zz}^{(a)}\right),\,$ and knowing the sequence of values $\widetilde{\sigma}_{zz}^{(a)}$ that correspond to the applied mechanical loads m, one can determine the nominal anisotropy field of the wire, $H_a=0.87$ Oe, and the reduced residual stress $\Delta\widetilde{\sigma}=1.03$. This value is slightly higher than the

theoretically estimated amplitude of characteristic quenching stress, $\Delta \widetilde{\sigma}_{th} = 0.75$. This may be due to the uncertainty in a number of parameters adopted in the calculation, such as the heat transfer coefficient between the wire and the cooling liquid that is not strictly known. But in any case, the experimental and theoretical values for the characteristic amplitude of the residual quenching stress turn out to be close.

4.3 Stationary Magnetization Distribution in Co-rich Microwire and Its Evolution in the External Magnetic Field

4.3.1 Amorphous Wire with a Circular Type of Magnetic Anisotropy

To describe the magnetostatic properties of amorphous Co-rich microwire with a purely circular type of magnetic anisotropy (4.1) it is necessary to solve the corresponding equilibrium micromagnetic equation [38] for the unit magnetization vector

$$\left[\vec{\alpha}, \vec{H}_{ef}\right] = 0; \quad M_s \vec{H}_{ef} = C\Delta \vec{\alpha} - \frac{\partial w_{m-el}}{\partial \vec{\alpha}} + M_s \left(\vec{H}_0 + \vec{H}'\right), \tag{4.5}$$

with the boundary condition, $\partial \vec{\alpha}/\partial n=0$, at the surface of the metallic nucleus. Here n is a unit outward normal to the metallic nucleus surface, \vec{H}_{ef} is the wire effective magnetic field, C is the exchange constant, \vec{H}_0 is the external magnetic field applied to the wire, and \vec{H}' is the demagnetizing field of the volume and surface magnetic charges.

Due to the axial symmetry of the residual stress tensor, in the ground micromagnetic state the radial component of the unit magnetization vector is zero, whereas other components depend only on the radial coordinate, so that

$$\vec{\alpha}(\vec{r}) = (0, \alpha_{\varphi}(\rho), \alpha_{z}(\rho)). \tag{4.6}$$

It is easy to see that for the magnetization distribution (4.6) the demagnetizing field of the wire vanishes, $\vec{H}' = 0$. Next, the exchange energy contribution to the effective magnetic field is given by

$$H_{ex,\phi} = \frac{C}{M_s} \left\{ \frac{1}{\rho} \frac{\partial}{\partial \rho} \left(\rho \frac{\partial \alpha_{\varphi}}{\partial \rho} \right) - \frac{\alpha_{\varphi}}{\rho^2} \right\}; \tag{4.7a}$$

$$H_{ex,z} = \frac{C}{M_s} \frac{1}{\rho} \frac{\partial}{\partial \rho} \left(\rho \frac{\partial \alpha_z}{\partial \rho} \right), \tag{4.7b}$$

whereas the contribution of the magneto-elastic energy, Eq. (4.1), is calculated as

$$H_{m-el,\varphi} = -\frac{\partial w_{m-el}}{M_s \partial \alpha_{\varphi}} = -H_a \widetilde{\sigma}_{\varphi\varphi} \alpha_{\varphi}; \tag{4.8a}$$

$$H_{m-el,z} = -\frac{\partial w_{m-el}}{M_s \partial \alpha_z} = -H_a \widetilde{\sigma}_{zz} \alpha_z. \tag{4.8b}$$

The distribution of the wire magnetization also depends on the amplitude of the external uniform magnetic field applied along the wire axis

$$\vec{H}_0 = (0, 0, H_{0z}). \tag{4.9}$$

Taking into account Eqs. (4.6)–(4.9), the equilibrium micromagnetic equation (4.5) can be reduced to the relation

$$\alpha_z(\rho)H_{ef,\varphi}(\rho) - \alpha_{\varphi}(\rho)H_{ef,z}(\rho)^{ef,zef,z} = 0, \tag{4.10}$$

where the effective magnetic field components are equal to $H_{ef,\varphi} = H_{ex,\varphi} + H_{m-el,\varphi}$ and $H_{ef,z} = H_{ex,z} + H_{m-el,z} + H_{0z}$, respectively. The components of the unit magnetization vector $\alpha_{\varphi}(\rho)$ and $\alpha_{z}(\rho)$ can be obtained from Eq. (4.10) as the functions of the applied magnetic field H_{0z} . For the numerical solution of Eq. (4.10) one can use the iterative scheme [31] that mimics the dynamic relaxation process to a steady micromagnetic state according to the time dependent Landau–Lifshitz–Gilbert (LLG) equation.

The numerical solution shows that amorphous Co-rich microwire with a purely circular type of magnetic anisotropy is completely saturated in applied magnetic field $|H_{0z}| \ge H_{a,ef}$. In the interval $|H_{0z}| < H_{a,ef}$ the longitudinal component of the unit magnetization vector of the wire varies approximately linearly, $\alpha_z = H_{0z}/H_{a,ef}$, while its circular component is given by $\alpha_{\varphi} = \pm \sqrt{1 - \alpha_z^2}$. It is important to note that for a wire with purely circular type of magnetic anisotropy both signs of the circular magnetization component are completely equivalent.

4.3.2 Amorphous Wire with a Weak Helical Anisotropy. Effect of Magnetic Field of DC Current

The model of amorphous microwire with a purely circular magnetic anisotropy was used [14] to explain the main features of the GMI effect observed experimentally in Co-rich amorphous microwires. The model [14] explains the presence of both diagonal Z_{zz} and off-diagonal $Z_{\varphi z}$ components of the GMI tensor and the strong dependence of these components on a weak external magnetic field. However, the circular model [14] turned out to be too idealized. As pointed out in [16, 21], it

cannot accurately describe the dependence of the GMI tensor components on frequency and other parameters. The main drawback of this model is the assumption of a strictly circular type of magnetic anisotropy of Co-rich microwire. As shown in Sect. 4.3.1, the wire with a strictly circular type of magnetic anisotropy, Eq. (4.1), is completely saturated in a longitudinal magnetic field $H_{0z} = H_{a,ef}$. Accordingly, the off-diagonal component of the GMI tensor $Z_{\varphi z}$ exists only in the range of fields $|H_{0z}| < H_{a,ef}$. In addition, at the point $H_{0z} = H_{a,ef}$ the effective wire permeability μ_{ef} has a pole, $\mu_{ef} \sim 1/\kappa$, where κ is the phenomenological magnetic damping constant. This phenomenological parameter is used in the calculation of the magnetic moment dynamics according to the LLG equation. Thus, within a circular model one has a divergence $\mu_{ef} \to \infty$ when $\kappa \to 0$. In the experiment, however, the pole in the effective permeability at $H_{0z} = H_{a,ef}$ can be eliminated due to the presence of various defects and inhomogeneities that increase the magnetic damping parameter.

Another possibility is a spatial dispersion of the magnetic permeability tensor [15, 16, 21]. It was shown [21] that taking into account spatial dispersion one can adequately describe the frequency dependence of the GMI tensor components at sufficiently high alternating current frequencies, $f > 500 \, \mathrm{MHz}{-1} \, \mathrm{GHz}$. However, it can be shown that in a general case, the effect of the spatial dispersion is not significant, at least at moderate frequencies, $f \leq 50{-}100 \, \mathrm{MHz}$.

For a more precise description of the properties of amorphous Co-rich microwires at moderate frequencies, a natural generalization of the model [14], namely the model of a microwire with a weak helical anisotropy has been introduced [29]. The presence of a weak off-diagonal correction in the magneto-elastic energy density eliminates the pole in the magnetic permeability of the wire, as in this case the process of the wire saturation occurs gradually in the whole range of magnetic fields larger than the wire anisotropy field. As a result, in a whole range of applied magnetic fields essential for the GMI effect the circular magnetization component and the off-diagonal component of the GMI tensor are nonzero.

The properties of amorphous ferromagnetic microwires with helical anisotropy were considered in many studies [16, 18, 23–25]. However, the helical magnetic anisotropy was introduced ad-hoc, assuming that the easy anisotropy axis on the wire surface has a fixed angle with respect to the wire axis. However, as soon as the magnetic anisotropy of the microwire is related with the residual quenching stress [5–7], the description of the helical anisotropy should also be based on this fact. To describe the properties of microwire with a weak helical anisotropy a small off-diagonal correction, $\tilde{\sigma}_{qz}(\rho) \approx (0.01-0.05)\rho/R$, to the residual stress tensor has been introduced in Ref. 29. The magneto-elastic energy density of a microwire with a weak helical anisotropy has been postulated in the form

$$w_{m-el} = K_e \left[\widetilde{\sigma}_{\rho\rho} \alpha_{\rho}^2 + \widetilde{\sigma}_{\varphi\varphi} \alpha_{\varphi}^2 + \widetilde{\sigma}_{zz} \alpha_{z}^2 + 2\widetilde{\sigma}_{\varphi z} \alpha_{\varphi} \alpha_{z} \right]; \qquad K_e = \frac{3}{2} |\lambda_s| \sigma_0.$$
 (4.11)

The amplitude of the off-diagonal component, $\tilde{\sigma}_{\varphi z}(R) \sim (0.01-0.05)$, is an adjustable parameter that must be determined from the experimental data.

As a typical example of the wire with helical anisotropy, let us consider the same wire of composition $\text{Co}_{67}\text{Fe}_{3.85}\text{Ni}_{1.45}\text{B}_{11.5}\text{Si}_{14.5}\text{Mo}_{1.7}$ which was studied in Sect. 4.3.1. The unit magnetization vector of the microwire with helical anisotropy satisfies the same micromagnetic Eq. (4.5) with the difference, that now the contribution of the magneto-elastic energy to the effective magnetic field of the microwire is calculated as

$$H_{m-el,\phi} = -\frac{\partial w_{m-el}}{M_s \partial \alpha_m} = -H_a \left[\widetilde{\sigma}_{\varphi\varphi} \alpha_{\varphi} + \widetilde{\sigma}_{\varphi z} \alpha_z \right]; \tag{4.12a}$$

$$H_{m-el,z} = -\frac{\partial w_{m-el}}{M_s \partial \alpha_z} = -H_a \left[\widetilde{\sigma}_{zz} \alpha_z + \widetilde{\sigma}_{\varphi z} \alpha_{\varphi} \right]. \tag{4.12b}$$

To study the influence of the magnetic field of a dc bias current $I_{\rm dc}$, flowing through the wire, one has to take into account the corresponding contribution to the effective magnetic field of the wire

$$\vec{H}_{\rm dc} = (0, H_{\varphi}(\rho), 0); \qquad H_{\varphi}(\rho) = H_{0\varphi} \frac{\rho}{R}. \tag{4.13}$$

Here $H_{0\varphi} = 2I_{\rm dc}/cR$ is the magnetic field of a dc bias current at the surface of the metallic nucleus of radius R, c being the speed of light. The same iterative scheme can be used to solve the LLG equation with the components of effective magnetic field appropriate for the wire with weak helical anisotropy.

The numerical calculation of the magnetization reversal process for a wire with weak helical anisotropy shows [29] that due to magnetomechanical coupling between the longitudinal α_z and circular α_{φ} components of the unit magnetization vector, the jump of the circular magnetization component occurs at some critical value of the external magnetic field H_{0z}^{*}. However, the magnetiz field of a dc bias current can stabilize the behavior of the circular magnetization component and prevent its jump during the wire magnetization reversal. This important fact has recently been confirmed experimentally [20, 24, 25].

As numerical simulation shows, the components $\alpha_{\varphi}(\rho)$ and $\alpha_{z}(\rho)$ are slowly varying functions of the radial coordinate near the surface of the metallic nucleus. Due to the presence of the skin effect the later region determines the high-frequency properties of the amorphous microwire. Therefore, further it will suffice to analyze the behavior of these components only at $\rho = R$.

Figure 4.2a shows the behavior of the circular component $\alpha_{\varphi}(R)$ at the surface of the metallic nucleus during the wire magnetization reversal in the applied magnetic field, which is gradually reduced from $H_{0z}=5$ Oe to -5 Oe. As shown in Fig. 4.2a, at $H_{0z}=5$ Oe, when the component $\alpha_z\approx 1$, the sign of the circular magnetization component is determined by the sign of the off-diagonal stress component $\sigma_{\varphi z}$. Indeed, when $\alpha_z\approx 1$ the minimum of the magneto-elastic energy, Eq. (4.11), is reached for $\alpha_{\varphi}<0$, if $\sigma_{\varphi z}>0$, and for $\alpha_{\varphi}>0$ if $\sigma_{\varphi z}<0$.

When the applied magnetic field decreases to zero, the α_{φ} component retains its sign. As Fig. 4.2a shows, in the low field range, $H_{0z} \approx 0$, the longitudinal

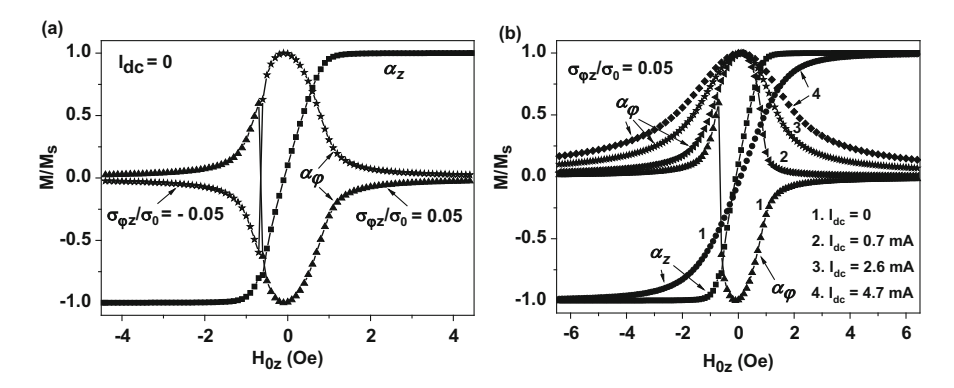


Fig. 4.2 The dependence of the circular component of the unit magnetization vector at the surface of the metallic nucleus on: (a) the sign of a small off-diagonal correction of the residual stress tensor; (b) on the value of the dc bias current flowing through the microwire

component α_z is close to zero. Therefore the influence of the term $2K_e\widetilde{\sigma}_{\varphi z}\alpha_{\varphi}\alpha_z$ is not essential. As a result, in the range of magnetic fields $|H_{0z}| < |H_{0z}|^*$ there may exist stable stationary states with both directions of magnetization rotation. However, in the field $|H_{0z}| \ge |H_{0z}|^*$, when the α_z component becomes sufficiently large in absolute value, the helical correction to the magneto-elastic energy is essential, so that one of the directions of magnetization rotation, which corresponds to the larger magneto-elastic energy, becomes unstable.

In Fig. 4.2a the jump of the circular magnetization component occurs in the field $H_{0z}^* = -0.67$ Oe for both signs of the off-diagonal residual stress component $\sigma_{\varphi z}$. As Fig. 4.2a shows, the jump of the $\alpha_{\varphi}(R)$ component leads only to a minor feature in the longitudinal $\alpha_z(R)$ component. It can be shown that the dependence of the $\alpha_z(R)$ component on the applied magnetic field is almost identical to that of average longitudinal wire magnetization, $m_z = M_z(H_{0z})/M_s$. Therefore, the location of the jump of the circular magnetization can hardly be detected experimentally by measuring the dependence $m_z(H_{0z})$. However, as we shall see in Sect. 4.4.2, the jump of the circular magnetization component leads to the corresponding jump of the off-diagonal GMI component.

Naturally, the circular magnetic field of the dc bias current can stabilize the behavior of the α_{φ} component during magnetization reversal process in applied axial magnetic field H_{0z} . As Fig. 4.2b shows, already at $I_{\rm dc}=0.7$ mA, when the circular magnetic field at the metallic nucleus surface is only given by $H_{0\varphi}=0.13$ Oe, the jump of the circular magnetization component is absent. In addition, this component becomes positive, $\alpha_{\varphi}>0$, showing the magnetization rotation parallel the direction of the circular magnetic field of the bias current. A further increase of the bias current up to $I_{\rm dc}=4.7$ mA only leads to an increase in the wire effective anisotropy field. Similarly, the stabilization of the negative circular component, $\alpha_{\varphi}<0$, occurs for the negative bias currents, $I_{\rm dc}\leq-0.7$ mA.

4.4 Giant Magneto-Impedance in Amorphous Co-rich Microwire

4.4.1 Amorphous Wire with a Circular Type of Magnetic Anisotropy

The magnetic permeability of a Co-rich microwire with purely circular magnetic anisotropy was shown [14] to be a tensor whose components depend significantly on the applied magnetic field even in a range of small magnetic fields, on the order of the wire anisotropy field. As a result, the electromagnetic properties of the wire are characterized by the GMI tensor, which has both diagonal and off-diagonal components. Recently it has become clear that in experimental samples there are always deviations from precise cylindrical symmetry. These deviations may be related with a slightly asymmetric distribution of residual quenching stresses, or small deviations from the ideal cylindrical shape of the sample, etc. It seems hardly possible to prepare an amorphous microwire with a purely circular type of magnetic anisotropy. Rather, the experimental samples show a weak helical anisotropy. The latter can be adequately described on the basis of the approach developed in Sect. 4.3.2. As we shall see in Sect. 4.4.2, the presence of a weak helical anisotropy leads to some changes in the permeability tensor components of the wire and as a consequence, to a change in its electrodynamic properties.

4.4.2 Amorphous Wire with a Weak Helical Anisotropy

As shown in [29], the jump of the circular magnetization component is only weakly reflected in the behavior of the diagonal component of the GMI tensor, $Z_{zz}(H_{0z})$. However, it leads to a jump of the off-diagonal component $Z_{\varphi z}(H_{0z})$ because its sign is determined [14] by the sign of the circular magnetization component.

The calculation of the GMI tensor components for a wire with helical anisotropy is similar to that carried out [14] for a wire with a purely circular anisotropy. Maxwell's equations for the high-frequency field components e_z , e_{φ} , h_z , h_{φ} , and h_{ρ} are given by

$$-\frac{\partial e_z}{\partial \rho} = ik_0 \left(h_{\varphi} + 4\pi M_s \alpha_{\varphi}^{(1)} \right);$$

$$-\frac{1}{\rho} \frac{\partial}{\partial \rho} \left(\rho e_{\varphi} \right) = ik_0 \left(h_z + 4\pi M_s \alpha_z^{(1)} \right); \quad h_{\rho} + 4\pi M_s \alpha_{\rho}^{(1)} = 0, \quad (4.14)$$

where $k_0 = \omega/c$, $\omega = 2\pi f$ is the angular frequency, and the high-frequency correction to the unit magnetization vector is given by

$$\vec{\alpha}^{(1)} = \left(\alpha_{\rho}^{(1)}, \alpha_{\varphi}^{(1)}, \alpha_{z}^{(1)}\right). \tag{4.15}$$

The unperturbed unit magnetization vector of the microwire can be written as $\vec{\alpha}^{(0)} = (0, \sin \theta, \cos \theta)$, where $\sin \theta = \alpha_{\varphi}^{(0)}(R)$ and $\cos \theta = \alpha_{z}^{(0)}(R)$. It follows from the normalization condition that

$$\sin\theta\alpha_{\omega}^{(1)} + \cos\theta\alpha_{z}^{(1)} = 0. \tag{4.16}$$

The correction (4.15) can be obtained by means of solving the linearized LLG equation

$$-i\omega\vec{\alpha}^{(1)} = -\gamma \left[\vec{\alpha}^{(1)}, \vec{H}_{ef}^{(0)}\right] - \gamma \left[\vec{\alpha}^{(0)}, \vec{H}_{ef}^{(1)}\right] - i\kappa\omega \left[\vec{\alpha}^{(0)}, \vec{\alpha}^{(1)}\right], \tag{4.17}$$

where γ is the gyromagnetic ratio and κ is the magnetic damping constant. Nonzero components of the unperturbed effective magnetic field are given by

$$H_{ef,\varphi}^{(0)} = -H_a \left[\widetilde{\sigma}_{\varphi\varphi} \sin \theta + \widetilde{\sigma}_{\varphi z} \cos \theta \right] + H_{0\varphi}; H_{ef,z}^{(0)} = -H_a \left[\widetilde{\sigma}_{zz} \cos \theta + \widetilde{\sigma}_{\varphi z} \sin \theta \right] + H_{0z}.$$

$$(4.18)$$

In Eq. (4.18) we neglect the exchange energy contribution and take into account a slow radial dependence of the stress tensor components, setting $\tilde{\sigma}_{ij} \approx \tilde{\sigma}_{ij}(R)$ near the surface of the metallic nucleus. The first-order high-frequency corrections to the effective magnetic field are

$$\begin{split} H_{ef,\rho}^{(1)} &= h_{\rho}; \qquad H_{ef,\varphi}^{(1)} &= h_{\varphi} - H_{a} \Big[\widetilde{\sigma}_{\varphi\varphi} \alpha_{\varphi}^{(1)} + \widetilde{\sigma}_{\varphi z} \alpha_{z}^{(1)} \Big]; \\ H_{ef,z}^{(1)} &= h_{z} - H_{a} \Big[\widetilde{\sigma}_{zz} \alpha_{z}^{(1)} + \widetilde{\sigma}_{\varphi z} \alpha_{\varphi}^{(1)} \Big]. \end{split} \tag{4.19}$$

Solving Eqs. (4.16)–(4.19) one can prove that the right-hand sides of Eq. (4.14) can be written as

$$h_{\varphi} + 4\pi M_s \alpha_{\varphi}^{(1)} = \left(1 + \mu_{ef} \cos^2 \theta\right) h_{\varphi} - \mu_{ef} \sin \theta \cos \theta h_z;$$

$$h_z + 4\pi M_s \alpha_z^{(1)} = -\mu_{ef} \sin \theta \cos \theta h_{\varphi} + \left(1 + \mu_{ef} \sin^2 \theta\right) h_z.$$
(4.20)

Here the effective magnetic permeability μ_{ef} is given by $\mu_{ef} = \omega_m/D$, where

$$D = \omega_{h0z} \cos \theta + \omega_{h0\varphi} \sin \theta - \omega_K (\widetilde{\sigma}_{zz} - \widetilde{\sigma}_{\varphi\varphi}) \cos 2\theta - 4\omega_K \widetilde{\sigma}_{\varphi z} \sin \theta \cos \theta - i\kappa \omega + \frac{\omega^2 \sin \theta}{\omega_{h0\varphi} - \omega_K \widetilde{\sigma}_{\varphi z} \cos \theta + (\omega_m - \omega_K \widetilde{\sigma}_{\varphi\varphi} - i\kappa \omega) \sin \theta}.$$

$$(4.21)$$

In Eq. (4.21) the following frequencies are introduced: $\omega_m = 4\pi M_s \gamma$, $\omega_K = \gamma H_a$, $\omega_{h0z} = \gamma H_{0z}$, $\omega_{h0\omega} = \gamma H_{0\omega}$.

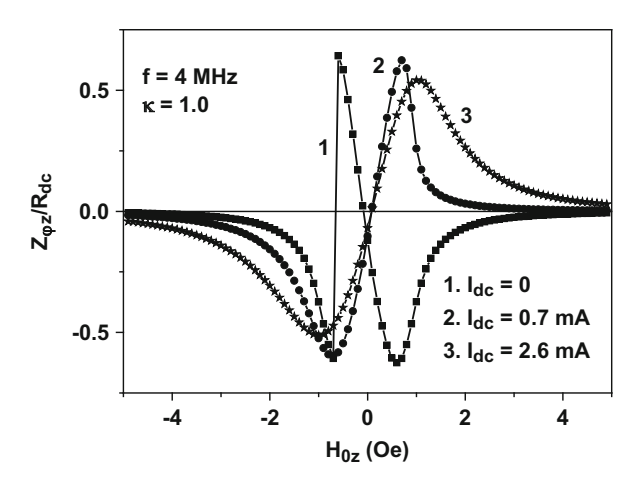
It is easy to see that the original electrodynamics problem, Eq. (4.14), reduces exactly to the system of Maxwell's equations for a wire with a purely circular anisotropy [14] with the following differences. First, there is another equilibrium micromagnetic equation for the magnetic moment distribution, which follows from Eqs. (4.12a), (4.12b), and (4.13). It takes into account the peculiarities of the magnetization reversal process for a wire with helical anisotropy, which are discussed in detail in Sect. 4.3.2. In addition, for this wire the new Eq. (4.21) is obtained for the effective magnetic permeability. In Eq. (4.21) the pole of the magnetic permeability is virtually eliminated by the presence of the off-diagonal residual stress component $\tilde{\sigma}_{\varphi z}$.

The diagonal and off-diagonal GMI components are determined [14] by the relations $Z_{zz}(f,H_{0z}) = e_z(R)/I_0$ and $Z_{\varphi z}(f,H_{0z}) = e_{\varphi}(R)/I_0$, respectively, where I_0 is a total current flowing through the wire cross section. The calculation of these components is carried out in this paper according to the formulas given in Ref. 14, taking into account Eq. (4.21) for the effective magnetic permeability of the wire with helical anisotropy. Besides, the unperturbed components of the unit magnetization vector, $\sin\theta$ and $\cos\theta$, are determined as a function of H_{0z} using the micromagnetic simulation, as described in Sect. 4.3.2.

The calculations based on Eqs. (4.14)–(4.21) show [29] that in contrast to the wire with a purely circular anisotropy, for a wire with a weak helical anisotropy the position and the magnitude of the maximum of the diagonal component $Z_{zz}(f,H_{0z})$ depend strongly on the frequency, even at moderate frequencies, $f \sim 1$ –20 MHz. At the same time, a strong dependence of $Z_{zz}(f,H_{0z})$ on the damping constant κ which is characteristic for the wire with purely circular anisotropy disappears for the wire having weak helical anisotropy. Both features are in agreement with the experiment.

Much more interesting, however, is the behavior of the off-diagonal GMI component as a function of $I_{\rm dc}$. As Fig. 4.3 shows, in the absence of the

Fig. 4.3 The dependence of the off-diagonal GMI component of amorphous wire with helical anisotropy on the amplitude of the dc bias current



bias current, $I_{\rm dc}=0$, the $Z_{\varphi z}(H_{0z})$ component abruptly changes sign at the same point $H_{0z}^{*}=-0.67$ Oe, where the jump of the α_{φ} component occurs. Curve 1 in Fig. 4.3 is obtained assuming that the applied magnetic field is reduced from 7.5 Oe up to -7.5 Oe. When the applied field increases in the opposite direction, from -7.5 Oe to 7.5 Oe, a similar jump of the $Z_{\varphi z}$ component occurs in the positive field, $H_{0z}^{*}=+0.67$ Oe. Thus, the existence of the jump of the off-diagonal GMI component clearly indicates the presence of the off-diagonal residual stress component $\sigma_{\varphi z}$ in the wire magneto-elastic energy. However, the circular magnetic field of the dc bias current of sufficient amplitude, $I_{\rm dc} \geq 0.7$ mA, can stabilize the dependence $Z_{\varphi z}(H_{0z})$. The slope of the curve $Z_{\varphi z}(H_{0z})$ is very sharp in the range of weak magnetic fields. This fact can be used [20, 27, 28] to design sensitive magnetic field sensor based on the measurement of the off-diagonal GMI component, stabilized by circular magnetic field of the dc bias current.

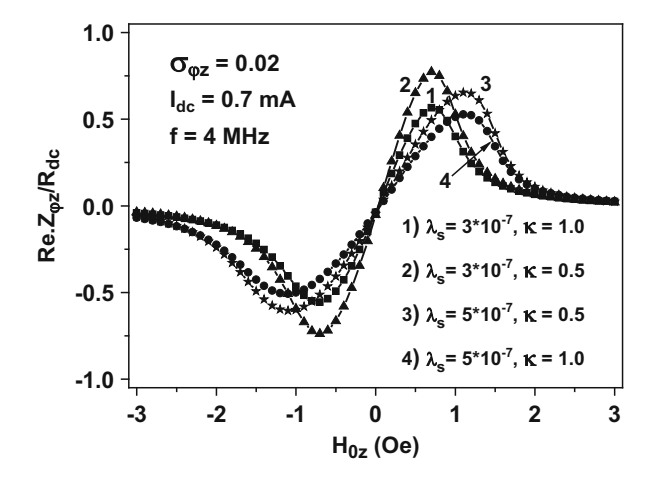
4.5 Optimization of the GMI Characteristics of Co-rich Amorphous Microwire

4.5.1 The Main Parameters that Determine the Slope of the Off-Diagonal GMI Component as a Function of Applied Magnetic Field

When an ac current flows along the microwire, the EMF induced in the receiving coil, $E=2\pi R_c Ne_{\varphi}(R_c)$, is proportional to the number of the coil turns N, and the amplitude of the circumferential component of the high-frequency electric field in the coil, $e_{\varphi}(R_c)$, where R_c is the coil radius. It can be shown [29, 30], that the circumferential component of the electric field outside the microwire decreases approximately inversely proportional to the radial coordinate, so that $e_{\varphi}(R_c)=Re_{\varphi}(R)/R_c$, where R is the radius of the metallic nucleus of the microwire. On the other hand, in the linear regime with respect to the ac current amplitude I_0 the circumferential electric field component is proportional to the off-diagonal component of the microwire impedance, $e_{\varphi}(R)=I_0Z_{\varphi z}(f_1H_{0z})$. Therefore, the EMF induced in the receiving coil is given by $E=2\pi RNI_0Z_{\varphi z}(f_1H_{0z})$.

Thus, one can see that the sensitivity of the GMI sensor to the applied magnetic field, apart from the obvious parameters N and I_0 , is determined also by the magnetic field dependence of the off-diagonal impedance component $Z_{\varphi z}(f,H_{0z})$. It follows from the theory [14, 29], that in a range of applied magnetic fields $|H_{0z}| < H_{a,ef}$, the off-diagonal impedance component $Z_{\varphi z}(f,H_{0z})$ is nearly proportional to the applied magnetic field, $Z_{\varphi z}(f,H_{0z}) \approx \xi H_{0z}$. However, the coefficient $\xi = dZ_{\varphi z}/dH_{0z}$ depends on the frequency of the ac current f, as well as on many other parameters, such as the distribution of the residual quenching stress over the wire cross section, the magnetostriction constant λ_s , the effective magnetic damping κ , and the amplitude of the dc bias current I_{dc} . Therefore, the analysis of the

Fig. 4.4 The off-diagonal component of the GMI tensor as a function of the Co-rich amorphous microwire parameters



dependence of $Z_{\varphi z}(f, H_{0z})$ on the applied magnetic field can be made only by means of numerical simulation [29, 30].

Figure 4.4 shows the results of the calculation of the $Z_{\varphi z}(f, H_{0z})$ component of Co-rich microwires with the same off-diagonal component of the residual quenching stress, $\sigma_{\varphi z} \rightarrow \sigma_{\varphi z}/\sigma_0 = 0.02$, but for various values of the magnetostriction constant and the magnetic damping parameter, because the magnetostriction constant, the amplitude of residual quenching stress, and the effective magnetic damping may depend on the annealing conditions.

As Fig. 4.4 shows, the maximum on the dependency of $Z_{\varphi z}(f,H_{0z})$ on H_{0z} corresponds approximately to the wire anisotropy field $H_{a,ef}$. At fixed amplitude of the residual quenching stress, the increase of the magnetostriction constant λ_s leads to an increase in the wire anisotropy field, and thus reduces the derivative $dZ_{\varphi z}/dH_{0z}$ in the linear region of the transfer characteristics of the GMI sensor. On the other hand, the decrease of the magnetic damping constant leads to a noticeable increase in the GMI sensor sensitivity.

4.5.2 The Role of Structural Defects and Bamboo Domain Walls

In the earlier theory [14] developed for a wire with a circular type of magnetic anisotropy, a linear dependence of the off-diagonal GMI component $Z_{\varphi z}(H_{0z})$ on the external magnetic field in a range of fields $|H_{0z}| \leq H_{a,ef}$ has been obtained. This linear relationship is particularly useful for creating sensitive sensor to measure weak magnetic fields of arbitrary sign.

The off-diagonal component of the impedance $Z_{\varphi z}$ was first explicitly measured in [20], where it was found that it exists only in the presence of circular magnetic field of dc bias current $I_{\rm dc}$. In the absence of the bias current, $I_{\rm dc}=0$, the measured

value of the $Z_{\varphi z}$ component turned out to be irregular and close to zero. This was attributed [20] to the presence of the bamboo domain structure in the Co-rich microwire in the absence of the dc bias current. Then, similar measurements were carried out in [22–25]. However, it is known [39] that in a perfect cylindrical Co-rich microwire the bamboo domain structure is energetically unfavorable. It can only exist as a metastable state. The appearance of bamboo domain walls and reverse circular domains in the wire in the absence of the bias current [25] can be explained by the presence of defects and magnetic imperfections. Note that in Fe-rich amorphous microwires of close diameters noticeable structural defects were found [40, 41] through the measurement of the local magnetic field for the reversed domain nucleation.

Let the uniform magnetic state of an amorphous wire with purely circular type of magnetic anisotropy is fixed in a strong axial magnetic field, $H_{0z} >> H_{a,ef}$. Since BDS is energetically unfavorable, in the absence of the defects there is no reason for the appearance of the bamboo domain walls in a perfect microwire during the reduction of the axial magnetic field to large negative values, $H_{0z} << -H_{a,ef}$ However, as shown in the present paper, the presence of a small off-diagonal component $\sigma_{\omega z}$ of the residual quenching stress leads to the jump of the circular magnetization component, and consequently, to probable appearance of the bamboo domain walls in the wire at the critical magnetic field, $H_{0z}^{*} < 0$. As Fig. 4.3 shows, in a sufficiently perfect Co-rich microwire one can confidently detect the off-diagonal GMI component $Z_{\varphi z}$ and its jump near the critical field ${H_{0z}}^*$ in the absence of the bias current, $I_{dc} = 0$. This means that in the entire magnetic field range from $H_{0z} >> H_{a,ef}$ up to $H_{0z} = H_{0z}^* < 0$ the BDS in the given wire is absent. Similar jumps of the $Z_{\omega z}$ GMI component under the changes of the axial magnetic field have been found previously [25] in a Co-rich wire in the presence of the external tensile stress.

As we mentioned above, the bamboo domain walls may appear in Co-rich amorphous wire with helical anisotropy accompanying the jump of the wire circular magnetization in the course of the longitudinal magnetization reversal. However, it remains unclear whether the bamboo domain walls exist only during a short transient period or they may present in a certain range of applied magnetic fields. Note that the very observation of the off-diagonal GMI component $Z_{\omega z}$ in Co-rich amorphous microwire is only possible in the absence of the bamboo domain walls, as the sign of the off-diagonal GMI component depends on the direction of magnetization in a circular cylindrical domain. Therefore, the average value of the off-diagonal GMI component is close to zero being averaged over a number of cylindrical magnetic domains of opposite signs. Recently [42], circular magnetization process in amorphous Co-rich microwire has been studied in more detail both theoretically and experimentally. Two different magnetization oscillation modes depending on the amplitude of alternating current flowing through the microwire have been observed in amorphous Co-rich microwire in the range of applied magnetic fields lower than the wire effective anisotropy field. The existence of these modes is explained by the presence of single circular domain in the ground state of a perfect Co-rich microwire.

4.6 Conclusion

In this paper a complete analysis of the electromagnetic properties of amorphous Co-rich microwire with a weak helical anisotropy has been carried out in a few necessary steps. First the calculation of residual quenching stresses in the microwire has been performed taking into account the specific conditions of the wire preparation, such as the wire cooling rate, the total wire diameter, and the thickness of the glass shell. Then, the magnetization distribution in the wire as a function of the applied magnetic field and the magnetic field of the dc bias current has been studied using numerical simulation. Finally, the components of the magneto-impedance tensor of the microwire have been calculated and the components of GMI tensor have been obtained taking into account the necessary boundary conditions at the wire surface. A weak helical anisotropy of the microwire has been introduced through a small off-diagonal correction to the residual stress tensor. In this way an adequate description of the results of experimental measurements of the diagonal and off-diagonal components of the wire GMI tensor at moderate frequency, f < 10 MHz, has been obtained.

Acknowledgments The authors wish to acknowledge the financial support of the Ministry of Education and Science of the Russian Federation in the framework of Increase Competitiveness Program of NUST "MISIS," Contract No. K2-2015-018. S. Gudoshnikov wishes to acknowledge a support of the program of the Russian Ministry of Education and Science "Organization of scientific research," Contract No. 2014/113.

References

- Jiles, C.: Recent advances and future directions in magnetic materials. Acta Mater. 51(19), 5907–5939 (2003)
- 2. Knobel, M., Vazquez, M., Kraus, L.: Giant magnetoimpedance. In: Buschow, K.H.J. (ed.) Handbook of Magnetic Materials, vol. 15, pp. 497–563. Elsevier, Amsterdam (2003)
- 3. Phan, M.-H., Peng, H.-X.: Giant magnetoimpedance materials: fundamentals and applications. Prog. Mater. Sci. **53**(2), 323–420 (2008)
- Larin, V.S., Torcunov, A.V., Zhukov, A.P., Gonzalez, J., Vazquez, M., Panina, L.V.: Preparation and properties of glass-coated microwires. J. Magn. Magn. Mater. 249(1-2), 39–45 (2002)
- 5. Chiriac, H., Ovari, T.A., Pop, G.: Internal stress distribution in glass-covered amorphous magnetic wires. Phys. Rev. B. **52**(14), 10104–10113 (1995)
- Velazquez, J., Vazquez, M., Zhukov, A.P.: Magnetoelastic anisotropy distribution in glasscoated microwires. J. Mater. Res. 11(10), 2499–2505 (1996)
- 7. Antonov, A.S., Borisov, V.T., Borisov, O.V., Prokoshin, A.F., Usov, N.A.: Residual quenching stresses in glass-coated amorphous ferromagnetic wires. J. Phys. D: Appl. Phys. **33**, 1161–1168 (2000)
- Panina, L.V., Mohri, K.: Magneto-impedance effect in amorphous wires. Appl. Phys. Lett. 65, 1189–1191 (1994)
- 9. Beach, R.S., Berkowitz, A.E.: Giant magnetic field dependent impedance of amorphous FeCoSiB wire. Appl. Phys. Lett. **64**, 3652–3654 (1994)

- Panina, L.V., Mohri, K., Uchiyama, T., Noda, M., Bushida, K.: Giant magneto-impedance in Co-rich amorphous wires and films. IEEE Trans. Magn. 31(2), 1249–1260 (1995)
- Yelon, A., Ménard, D., Britel, M., Ciureanu, P.: Calculations of giant magnetoimpedance and of ferromagnetic resonance response are rigorously equivalent. Appl. Phys. Lett. 69, 3084–3086 (1996)
- Vazquez, M., Hernando, A.: A soft magnetic wire for sensor applications. J. Phys. D: Appl. Phys. 29, 939–949 (1996)
- 13. Antonov, A., Dykhne, A., Lagar'kov, A., Perov, N., Usov, N., Furmonova, T.: The features of GMI effect in amorphous wires at microwaves. Physica A. 241, 420–424 (1997)
- Usov, N.A., Antonov, A.S., Lagar'kov, A.N.: Theory of giant magneto-impedance effect in amorphous wires with different types of magnetic anisotropy. J. Magn. Magn. Mater. 185, 159–173 (1998)
- 15. Kraus, L.: Theory of giant magneto-impedance in the planar conductor with uniaxial magnetic anisotropy. J. Magn. Magn. Mater. **195**(3), 764–778 (1999)
- Ménard, D., Yelon, A.: Theory of longitudinal magnetoimpedance in wires. J. Appl. Phys. 88, 379–393 (2000)
- Vazquez, M.: Giant magneto-impedance in soft magnetic wires. J. Magn. Magn. Mater. 226, 693–699 (2001)
- 18. Makhnovskiy, D.P., Panina, L.V., Mapps, D.J.: Field-dependent surface impedance tensor in amorphous wires with two types of magnetic anisotropy: helical and circumferential. Phys. Rev. B. **63**, 144424–144441 (2001)
- Zhukova, V., Chizhik, A., Zhukov, A., Torcunov, A., Larin, V., Gonzalez, J.: Optimization of giant magnetoimpedance in Co-rich amorphous microwires. IEEE Trans. Magn. 38(5), 3090–3092 (2002)
- Sandacci, S., Makhnovskiy, D., Panina, L., Mohri, K., Honkura, Y.: Off-diagonal impedance in amorphous wires and its application to linear magnetic sensors. IEEE Trans. Magn. 40(6), 3505–3511 (2004)
- Ciureanu, P., Melo, L.G.C., Seddaoui, D., Ménard, D., Yelon, A.: Physical models of magnetoimpedance. J. Appl. Phys. 102, 073908-1–073908-10 (2007)
- Zhukova, V., Ipatov, M., Gonzalez, J., Blanco, J.M., Zhukov, A.: Studies of magnetic properties and giant magnetoimpedance effect in ultrathin magnetically soft amorphous microwires. J. Appl. Phys. 103, 07E714-1–07E714-3 (2008)
- Ipatov, M., Zhukova, V., Zhukov, A., Gonzalez, J., Zvezdin, A.: Low-field hysteresis in the magnetoimpedance of amorphous microwires. Phys. Rev. B. 81, 134421-1-134421-8 (2010)
- 24. Ipatov, M., Zhukova, V., Zhukov, A., Gonzalez, J.: Magnetoimpedance sensitive to dc bias current in amorphous microwires. Appl. Phys. Lett. **97**, 252507-1–252507-3 (2010)
- Ipatov, M., Chizhik, A., Zhukova, V., Gonzalez, J., Zhukov, A.: Correlation of surface domain structure and magneto-impedance in amorphous microwires. J. Appl. Phys. 109, 113924–114100 (2011)
- Mohri, K., Honkura, Y.: Amorphous wire and CMOS IC based magneto-impedance sensors origin, topics, and future. Sens. Lett. 5, 267–270 (2007)
- 27. Zhukova, V., Ipatov, M., Zhukov, A.: Thin magnetically soft wires for magnetic microsensors. Sensors. 9, 9216–9240 (2009)
- Gudoshnikov, S., Usov, N., Nozdrin, A., Ipatov, M., Zhukov, A., Zhukova, V.: Highly sensitive magnetometer based on the off-diagonal GMI effect in Co-rich glass-coated microwire. Phys. Status Solidi A. 211, 980–985 (2014)
- Usov, N.A., Gudoshnikov, S.A.: Giant magneto-impedance effect in amorphous ferromagetic wire with a weak helical anisotropy: theory and experiment. J. Appl. Phys. 113, 243902-1–243902-10 (2013)
- Usov, N.A., Gudoshnikov, S.A.: Magnetization reversal process and peculiarities of giant magneto-impedance effect in amorphous ferromagnetic microwire with helical anisotropy. Phys. Status Solidi A. 211(5), 1055–1061 (2014)

- 31. Usov, N., Antonov, A., Dykhne, A., Lagar'kov, A.: Stress dependence of the hysteresis loops of Co-rich amorphous wire. J. Phys.: Condens. Matter. 10, 2453–2463 (1998)
- Aranda, G.R., Usov, N.A., Zhukova, V., Zhukov, A., Gonzalez, J.: Hysteretic properties of Co-rich amorphous microwires: theory and experiment. Phys. Status Solidi A. 205, 1800–1804 (2008)
- 33. Cristensen, R.M.: Theory of Viscoelasticity: An Introduction. Academic, New York (1971)
- 34. Landau, L.D., Lifshitz, E.M.: Theory of Elasticity. Pergamon Press, New York (1970)
- 35. Gudoshnikov, S., Churyukanova, M., Kaloshkin, S., Zhukov, A., Zhukova, V., Usov, N.A.: Investigation of the properties of Co-rich amorphous ferromagnetic microwires by means of small angle magnetization rotation method. J. Magn. Magn. Mater. 387, 53–57 (2015)
- 36. Narita, K., Yamasaki, J., Fukunaga, H.: Measurement of saturation magnetostriction of a thin amorphous ribbon by means of small-angle magnetization rotation. IEEE Trans. Magn. **16**(2), 435–439 (1980)
- Zhukov, A., Zhukova, V., Blanco, J.M., Cobeno, A.F., Vazquez, M., Gonzalez, J.: Magnetostriction in glass-coated magnetic microwires. J. Magn. Magn. Mater. 258-259, 151–157 (2003)
- 38. Brown Jr., W.F.: Micromagnetics. Interscience, New York (1963)
- 39. Usov, N., Antonov, A., Dykhne, A., Lagar'kov, A.: Possible origin for the bamboo domain structure in Co-rich amorphous wire. J. Magn. Magn. Mater. 174, 127–132 (1997)
- Ipatov, M., Usov, N.A., Zhukov, A., Gonzalez, J.: Local nucleation fields of Fe-rich microwires and their dependence on applied stresses. Physica B. 403(2-3), 379–381 (2008)
- Gudoshnikov, S.A., Grebenshchikov, Y.B., Ljubimov, B.Y., Palvanov, P.S., Usov, N.A., Ipatov, M., Zhukov, A., Gonzalez, J.: Local nucleation field and characteristic width of head to head domain wall in Fe-rich amorphous microwire. Phys. Status Solidi A. 206, 613–617 (2009)
- 42. Usov, N.A., Gudoshnikov, S.A.: Circular magnetization process in amorphous microwire with negative magnetostriction. J. Phys. D: Appl. Phys. 49, 16 (2016)

Chapter 5 **Tunable Magnetic Anisotropy** and Magnetization Reversal in Microwires

A. Chizhik, A. Stupakiewicz, and J. Gonzalez

5.1 Introduction

Understanding the physical nature of magnetic microwires on a wide-frequency regime led to a novel technologies based on magnetic sensors. In developing of the sensor technology it is very important to possess sensitive methods for investigations and detections of the magnetization states. In magnetic materials the interplay of magnetism and optics led to a high sensitivity magneto-optical experimental method. Being of a sub-micrometer spatial resolution, it brings new and complementary information in comparison with classical magnetometry, partly due to the high sensitivity of the magnetic signal from the microwire surface. The microwirebased sensors usually operate on the giant magneto-impedance (GMI) effect. The GMI effect was discovered 20 years ago [1]. In soft magnetic materials, such as composite amorphous thin wires, the impedance change is in the range of more than 100 % in the high-frequency band for the low external magnetic fields of 0.1 mT [2]. The surface magnetic anisotropy in microwire is originated by the distribution of internal stress which depends on the thermal and the mechanical prehistory of a wire [3]. Another words, the real distribution of magnetic anisotropy in microwires is determined by the sign and value of the magnetostriction originated in turn by the stress distribution [4–9].

The task of the determination of the limit angle of the helical anisotropy induced by the torsion stress exists since 90 years [10, 11], when it was demonstrated that the torsion stress is a sum of tension perpendicular stresses, each acting at 45°

A. Chizhik (⋈) • J. Gonzalez

Departmento Facultad de Quimica, Universidad del País Vasco UPV/EHU, San Sebastian,

e-mail: oleksandr.chyzhyk@ehu.es

A. Stupakiewicz

Laboratory of Magnetism, Faculty of Physics, University of Bialystok, Bialystok, Poland

© Springer International Publishing AG 2017

relative to the wire axis. The tensile stress is directed along one axis and while the opposite compressive stress is directed along another axis. The purpose of the present work is to demonstrate the limits of the torsion stress induced inclination of the helical anisotropy.

Taking into account that the GMI effect is based on the skin effect the circumferential permeability is essential for the observation of a high GMI effect in cylindrically shaped wires. The study of the formation and transformation of the surface magnetic structure in the presence of a high-frequency (HF) electric current is a fundamental task for the design of magnetic sensors. At the moment, the details of this transformation are under question. The temperature dependent behaviour of the domain structure (DS) in the microwire is also very important for stable sensor functioning. Considering the strong internal stresses arising from the difference in thermal expansion coefficients of glass and metallic alloy [2] we assumed that the surface magnetic structure should experience great transformation in a temperature range higher than room temperature.

The internal stress in microwires sufficiently affects the magnetization reversal process. In particular it limits the single domain wall (DW) propagation regime via the giant Barkhausen effect. Earlier we studied the single DW dynamics using magneto-optical Kerr effect (MOKE) modified Sixtus-Tonks method [12–14].

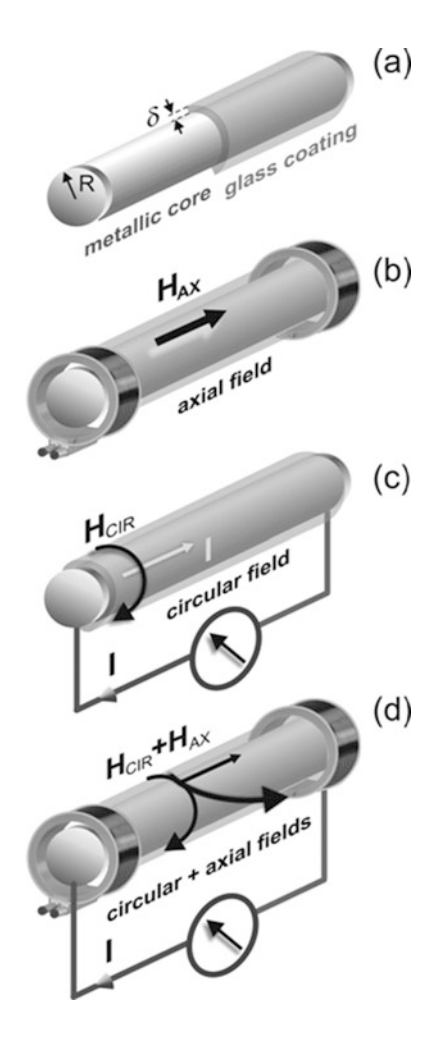
Recently, a number of studies of the DW motion in metallic microwires have used a Sixtus-Tonks method with a few pick-up magnetic coils to study the effect of the magnetoelastic anisotropy on the DW velocity [15] and the local DW nucleation [16] on a volume of the microwire. This technique does not present the direct visual observation of the DW dynamics. The MOKE microscopy permits a local observation of both the magnetic domain structures and the DW motion. In particular it allows analysis of the changing geometry of the DW under both circular and axial magnetic fields.

The present chapter consists of four parts: (1) "Experimental details"—describes the MOKE method in different geometries adapted to the cylindrically shaped glass covered microwires; (2) "Mechanical torsion stress effect"—presents the experimental results of the stress induced transformation of the surface magnetic structure. The limit of induced helical anisotropy also considered; (3) "Temperature effect"—is dedicated to the variety of the surface domain structures and magnetization reversal caused by the temperature variation; (4) "High-frequency electrical current effect" is devoted to influence of high-frequency electric current and circular magnetic field on the mechanism of surface magnetization reversal.

5.2 Experimental Details

The different geometries of observation of the surface magnetic domain structures and magnetization reversal process in cylindrical microwires using MOKE have been demonstrated. The separation of the magnetization components in the wire

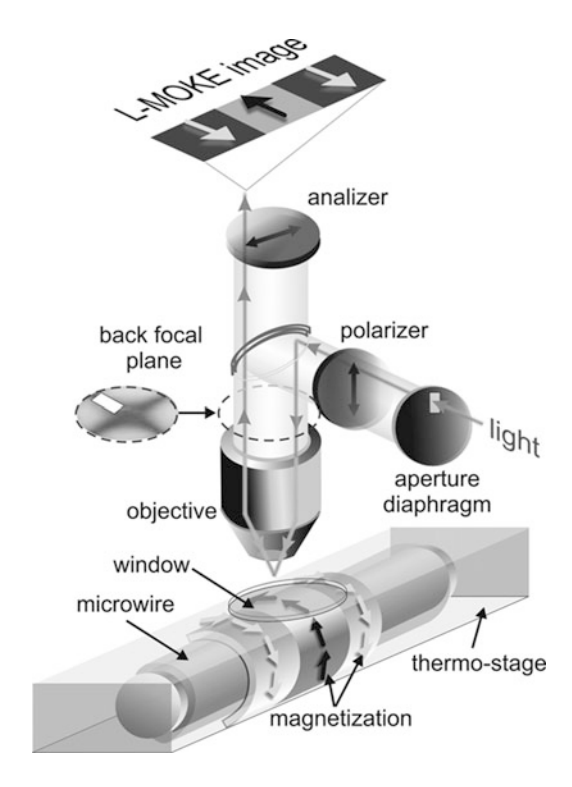
Fig. 5.1 The schematic configuration of the microwire (a), the orientation of the axial magnetic field (b), the orientation of the circular magnetic field (c), and the orientation by the helical direction of the field by the superposition of the orthogonally directed the circular and the axial magnetic fields



using vector magnetometry and analysis of both the hysteresis curves and the images of the magnetic domain structures were performed using these methods.

The investigations of the microwires (see Fig. 5.1a) were performed using MOKE microscopy with different configurations of the external magnetic field: (1) axial $(H_{\rm AX})$, (2) circular $(H_{\rm CIR})$, and (3) the sum $H_{\rm CIR}+H_{\rm AX}$. A pair of Helmholtz coils provided an external magnetic field, $H_{\rm AX}$, with an axial orientation at the microwire (see Fig. 5.1b). To produce the $H_{\rm CIR}$, an electric current was passed through the microwire (see Fig. 5.1c). In the static regime, the maximum amplitude of the current usually was <3 mA. At this value, the investigations were outside the regime that could induce over-heating. The circular magnetic field was calculated using the formula $H_{\rm CIR} = I/(2\pi R)$ where I is the electric current flowing through the microwire. To produce the superposition of the orthogonally directed the circular

Fig. 5.2 The experimental L-MOKE configuration for the observation of the magnetic domain structures in microwires at different temperature and the schematic localization of the main components for observation back focal plane using aperture diaphragm. Design of the skin on microwire marked by the magnetization orientation



and the axial magnetic fields were applied to the microwire. In result we obtained the helical direction of the magnetic field with amplitude $H_{\rm CIR}+H_{\rm AX}$ (see Fig. 5.1d).

The surface magnetic domain structures in all microwire were investigated using a high-resolution, wide-field magneto-optical polarizing microscope working in reflective mode. The essential components of the microscope and a ray diagram are shown in Fig. 5.2. A high-sensitive camera has a fast-frame rate with a thermoelectrical cooling CCD chip was used. Digital images of 1344×1024 pixels were captured with an exposure time between 10 and $100~\mu s$. The spatial resolution of the images was estimated to be 300~nm. The aperture diaphragm was used to control the incident angles of the light rays that reached the surface of the microwire and also determined the MOKE geometry at the microscope [17]. The plane of the aperture diaphragm is conjugate to the back focal plane of the objective lens. When the polarizer and the analyzer were crossed, the cross-shaped image defined the extinction area (the conoscopical image) that was observed in this plane. For the L-MOKE geometry, a slit aperture was displaced from the centre and oriented both parallel to the plane of light incidence.

The initial optical images of the microwire were recorded using a microscope with focusing objective lens close to the top metallic surface of the wire. In a microwire that has helical magnetic anisotropy, we can observe both circular and axial components of the magnetization under the external axial magnetic field,

 $H_{\rm AX}$. The visualization of the magnetic domain structure in the microwire was performed in both the P-MOKE and the L-MOKE geometries with out-of-plane and in-plane magnetization sensitivity, respectively [18].

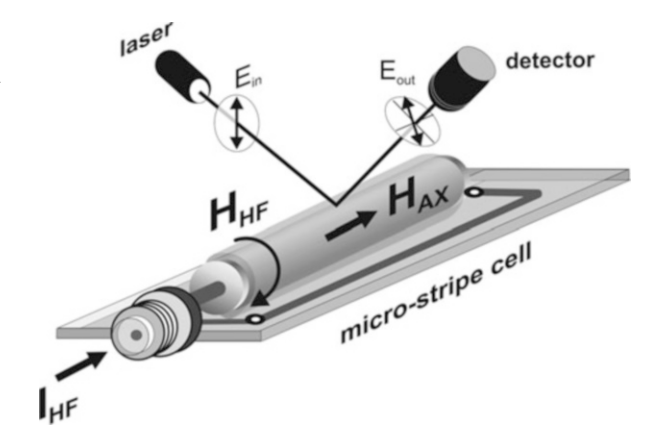
For our investigations we use mainly the L-MOKE configuration. The contrast in images of domain structures shows the difference between the in-plane magnetization components. The movement of the non-central position of the hole in aperture diaphragm (Fig. 5.2) leads to a change in the orientation of the plane of incidence of the light along the perpendicular or the parallel direction to the axial direction of the wire.

In the case where the direction of incidence was parallel to axial orientation of the wire, we observed the maximum magnetic contrast at the domains where the magnetization was in the direction of the wire. In the second case, when the direction of incidence was perpendicular to the axial orientation of the wire, the contrast at the domains in the axial direction of the magnetization decreased. The contrast of the domains with circular-only directions of the magnetization (that were perpendicular to the axial orientation) increased. Each of the in-plane magnetization components in the microwire was non-zero.

For the registration of the surface magnetic domains, we used the standard procedure that was developed to get contrast in the magnetic domains by subtracting the average images. The sample was initially saturated with relatively large amplitude of the magnetic field. When the mono-domain state appeared with this applied field, the image was recorded as the reference image. At the same time, the reference image was subtracted from next image, at the same saturation field. In the next step, the images were processed in real time while continuously varying magnetic field. Each image was the result of the difference between the image of the domain structure in a given external magnetic field and the reference image. It is significant that the "black and white" contrast on image of domain structure corresponds to the in-plane component of the magnetization (see Fig. 5.2).

The temperature change of magnetic domain structures in microwires was performed by means of MOKE microscope with a thermo-controlled system (see Fig. 5.3). This system consists of a thermo-stage and system controller operated

Fig. 5.3 Micro-strip cell used to MOKE study in the presence of a high-frequency electric current *I*_{HF}



within -0 to 300 °C temperature range. To observation of images of magnetic domain structure was used the same procedure of image processing.

To magnetization reversal process was studied using the MOKE magnetometer, where the L-MOKE and transversal (T-MOKE) configurations were employed. For the L-MOKE configuration, the rotation of the plane of the polarization of the light, reflected from the surface of microwire, is proportional to the axial component of the magnetization. For the T-MOKE configuration, the intensity of the reflected light is proportional to the magnetization, which is perpendicular to the plane of the light (circular projection of the magnetization). The details of the T-MOKE experimental setup have been presented elsewhere [18].

A polarized light from the He-Ne laser was reflected from the surface of the wire to the detector. The beam diameter was of 0.8 mm. For the transverse Kerr effect, the intensity of the reflected light is proportional to the magnetization oriented perpendicularly to the plane of the light polarization (the plane which contains the laser beam and the microwire). In the present experiments, the circular magnetization is the magnetization, which is perpendicular to the plane of the light polarization. Therefore, the light intensity is proportional to the circular projection of the magnetization in the surface area of the wire.

To apply the high-frequency (HF) electric current in the MHz–GHz band, the microwire was soldered in a specially designed micro-strip cell (Fig. 5.3). The HF current flows through the wire. This cell is usually used in GMI experiments.

5.3 Mechanical Torsion Stress Effect

Generally, the influence of the torsion stress on the coercive properties or magneto-impedance could be presented in the form of dependence on the value of the torsion angle [10, 11, 19]. Here we demonstrate the direct correlation between the torsion stress and the helical magnetic anisotropy [20]. Physically more informative the experimental results could be presented as a dependence on the helical anisotropy. Torsion stress induced limit of the angle of helical anisotropy has been theoretically shown earlier, but the experimental demonstration of this limit has not been demonstrated. Here we demonstrate experimentally the limits of the helical anisotropy induced by the torsion stress. The MOKE experiments have been performed in amorphous microwires of nominal composition $Co_{69.5}Fe_{3.9}Ni_1B_{11.8}Si_{10.8}Mo_2$ (metallic nucleus radius was 9.5 μ m, glass coating thickness was 2.6 μ m) supplied by TAMAG Iberica S.L.

The external torsion stress induces the transformation of the MOKE hysteresis loops (Fig. 5.4). We observe stress induced change of the amplitude and the sign of the jump of the MOKE intensity ΔI (another words, the circular magnetization $\Delta M_{\rm CIR}$). For example, for the stress of -2.2π rad m⁻¹ (Fig. 5.4b) there is no jump of $\Delta M_{\rm CIR}$. The application of high enough negative stress (-22π rad m⁻¹) causes the appearance of the jump circular magnetization of the opposite sign (Fig. 5.4a).

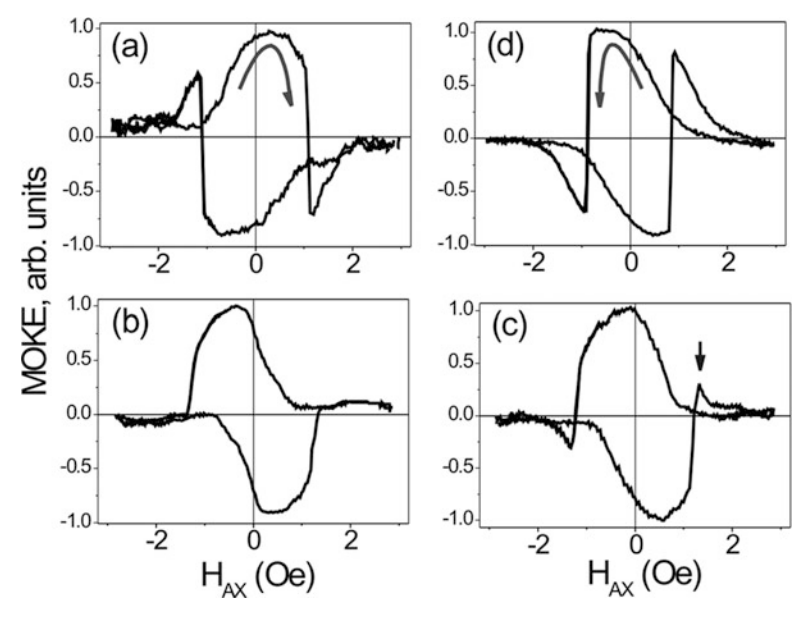


Fig. 5.4 T-MOKE dependencies in the presence of torsion stress: (a) $\tau = -22\pi$ rad m⁻¹, (b) $\tau = -2.2\pi$ rad m⁻¹, (c) $\tau = 0$, (d) $\tau = 8.9\pi$ rad m⁻¹. Reprinted with permission from [20] Chizhik, A., Zhukov, A., Blanco, J.M., Gonzalez, J., Gawronski, P.: J. Magn. Magn. Mater. 321, 803–805 (2009)

This transformation reflects the change of the surface helical anisotropy induced by the torsion stress.

Figure 5.5 demonstrates schematically the change of the surface helical anisotropy associated with the obtained MOKE experimental results. The normalized MOKE intensity is proportional to the normalized circular magnetization in the surface of the wire, i.e., $\Delta I/I_{\rm MAX} \sim \Delta M_{\rm CIR}/M_{\rm MAX}$ ($M_{\rm MAX}$ is the maximal value of the circular magnetization during the surface magnetization reversal, $I_{\rm MAX}$ is the maximal intensity of the MOKE signal during the magnetization reversal). In Fig. 5.6 we can see the experimentally obtained normalized value of the jump of the MOKE intensity $\Delta I/I_{\rm MAX}$ as a dependence on the external torsion stress. Knowing the jump of the circular magnetization we could determine experimentally the angle of helical anisotropy and establish the correlation between the surface hysteresis loop and this angle.

The calculation of the hysteresis loops has been performed taking into account that the helical magnetic anisotropy exists in the surface (outer shell) of the wire. While the curvature of the area of wire surface from which the light is reflected is about one angular degree, we consider in our calculations that the wire surface is a two-dimensional system. The external magnetic field H is a superposition of two orthogonal fields (H_{AX} and H_{CIR}), see Fig. 5.1d. The surface anisotropy changes the direction from axial to circular one. The energy of the system could be expressed as

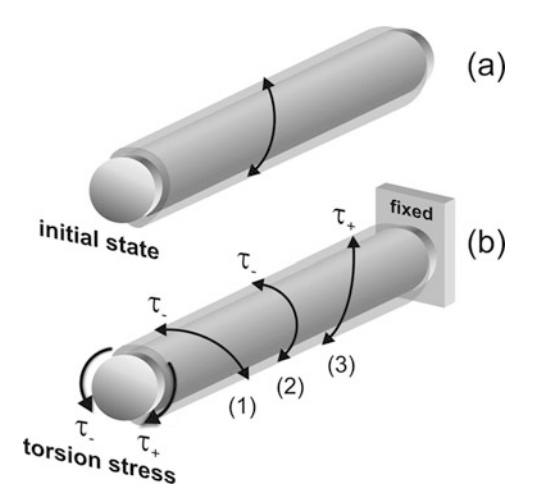
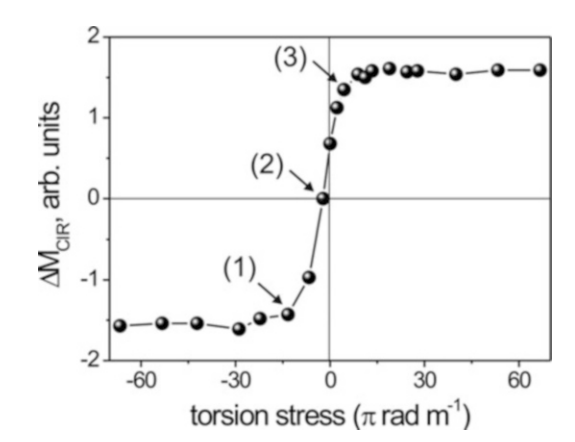


Fig. 5.5 Schematically pictures of the inclination of the axis of helical anisotropy induced by the torsion stress τ . The initial state of the microwire without stress (a) and alter right-hand τ_+ and left-hand τ_- torsion stress (b). The states (1, 2, 3) correspond to the magnetization states with helical component. Reprinted with permission from [20] Chizhik, A., Zhukov, A., Blanco, J.M., Gonzalez, J., Gawronski, P.: J. Magn. Magn. Mater. 321, 803–805 (2009)

Fig. 5.6 Experimental dependence of the normalized value of the jump of the Kerr intensity $\Delta I/I_{\rm MAX}$ on applied torsion stress. Reprinted with permission from [20] Chizhik, A., Zhukov, A., Blanco, J.M., Gonzalez, J., Gawronski, P.: J. Magn. Magn. Mater. 321, 803–805 (2009)



$$U = -K_{U\cos^{2}}(\theta - \varphi) - H \cdot M$$

$$= -K_{U\cos^{2}}(\theta - \varphi) - H_{AX}\cos(\theta) - H_{CIR}\sin(\theta)$$
(5.1)

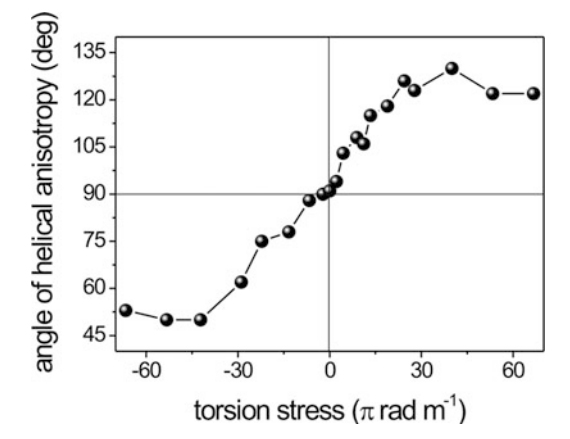
where K_U is uniaxial anisotropy constant, M is the saturation magnetization, φ is an angle between the anisotropy axis and the wire axis, and θ is the angle between the magnetic moment and the wire axis.

The numerical calculation was done by the coherent rotation approach [21]. The hysteresis loops were computed by the minimization of the energy term described by Eq. (5.1). For given values of the angle φ the minimization procedure can be

Fig. 5.7 Calculated dependence of the jump of the circular magnetization $\Delta M_{\rm CIR}/M_{\rm MAX}$ on the angle of helical anisotropy φ . Reprinted with permission from [20] Chizhik, A., Zhukov, A., Blanco, J.M., Gonzalez, J., Gawronski, P.: J. Magn. Magn. Mater. 321, 803–805 (2009)

2 1 1 - 2 45 60 75 90 105 120 135 angle of helical anisotropy (deg)

Fig. 5.8 Dependence of angle of helical anisotropy on applied torsion stress. Reprinted with permission from [20] Chizhik, A., Zhukov, A., Blanco, J.M., Gonzalez, J., Gawronski, P.: J. Magn. Magn. Mater. 321, 803–805 (2009)



outlined in the following way: each time the value of the axial field was changed, the search of the value of the angle θ that gave the minimal value of the energy term (Eq. (5.1)) was done.

The strong dependence of the jump of the circular magnetization on the angle of the helical anisotropy has been obtained as a result of the calculations. In Fig. 5.7 we present the calculated dependence of the $\Delta M_{\rm CIR}/M_{\rm MAX}$ on the angle of the helical anisotropy. When the magnetization is directed transversally the jump is equal zero. Two maximum for the values of the angle of 62° and 118° are observed in the calculated dependence.

Figure 5.8 is the result of the comparative analysis of the MOKE experiment (Fig. 5.6) and the calculations (Fig. 5.7).

There is a dependence of the angle of the helical anisotropy on the applied torsion stress. The surface anisotropy is directed almost to the transverse direction when the applied stress is absent. We have to mention that the small peak marked by arrow in Fig. 5.4c, means the small jump of circular magnetization. Therefore,

the angle of helical anisotropy is not exactly 90° . The application of stress of relatively small value of -2.2π rad m⁻¹ causes the disappearance of this small peak. Thus, at this value of the torsion stress the surface anisotropy has a transversal direction. The angle of the helical anisotropy increases when the external stress increases. This growth finishes at the applied stress of the value of about $\pm 40\pi$ rad m⁻¹. Therefore, in such a way we confirm the prediction [10, 11] that the torsion stress induced inclination of the helical anisotropy does have a natural limit of 45° from the transverse direction independently on the value of the applied stress.

5.4 Temperature Effect

We studied Fe- and Co-based glass-coated amorphous microwires with different compositions: (1) Fe_{71.7}B_{13.4}Si₁₁Nb₃Ni_{0.9} (metallic nucleus radius was 50 µm, glass coating thickness was 20 µm), (2) Fe_{3.5}Co₆₉B₁₅Si₁₀ (metallic nucleus radius was 37 µm, glass coating thickness was 4 µm), (3) Fe_{5.71}Co_{64.04}B_{15.88}Si_{10.94}Cr_{3.40}Ni_{0.03} (metallic nucleus radius was 50 µm, glass coating thickness was 20 µm). MOKE hysteresis loops were obtained from the Kerr intensity for different H_{AX} as a result of the images processing. The hysteresis curves reflect the transformation of surface magnetization in the axial magnetic field [18]. Observing the temperature induced transformations in the magnetic structure we have extracted the common properties and the specific features of every studied microwires. The MOKE hysteresis loops of three studied wires consist generally of two parts: (1) the part of coherent rotation of magnetization and (2) the switching magnetization part. The second part is determined by the transformation of the domain structure associated with the domain structure rearrangement or quick domain walls motion.

First we have studied the $Fe_{3.5}Co_{69}B_{15}Si_{10}$ microwire. Figure 5.9 presents the transformation of the MOKE hysteresis curves. The hysteresis loop consists of the

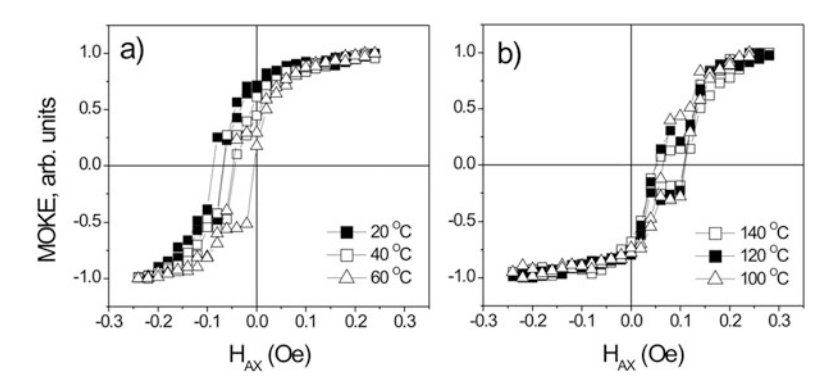


Fig. 5.9 Fe_{3.5}Co₆₉B₁₅Si₁₀ microwire. MOKE hysteresis loops obtained in the presence of an $H_{\rm AX}$ at different temperature: (a) 20 °C, 40 °C, and 60 °C; (b) 100 °C, 120 °C, and 140 °C

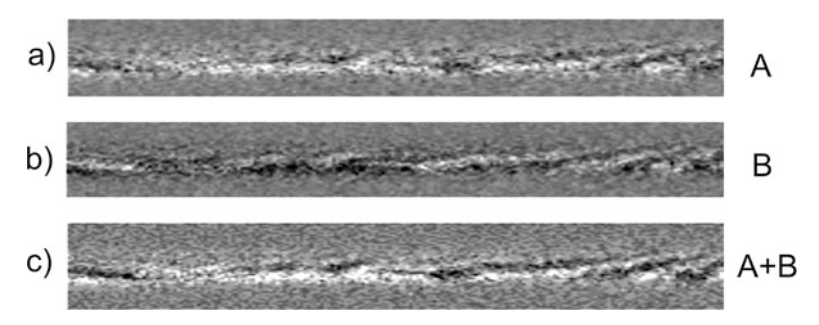


Fig. 5.10 The images of domain structures obtained at 20 °C: (a) $H_{\rm AX} = -0.08$ Oe; (b) $H_{\rm AX} = -0.1$ Oe. (c) result of the digital sum of (a) and (b). The size of images is 400 μ m \times 55 μ m

fluent and sharp parts within the temperature range of 20–140 °C. The sharp jumps changes with the temperature increase. The noticeable shift of the Kerr loops along the axis of $H_{\rm AX}$ (see Fig. 5.9) was fixed as an influence of the temperature.

Generally, as it was found earlier, dc circular magnetic field could be the reason of such type of hysteresis shifts, but we have not applied the circular field in our present experiments. Another possible reason of the directed shift is the surface helical anisotropy. From the value of this shift we determine the type of the surface domain structures. As it was found earlier [22], this shift reflects the surface magnetic helicality and the degree of helical structure could be extracted from it. Therefore, change of the angle of the surface helical structure induced by the temperature change takes place in the present experiment. The crossing of the "0" value of the axial magnetic field corresponds to the helical anisotropy of 90° . This configuration means the pure circular magnetic state.

Images presented in Figs. 5.10a, b have been obtained in short range of the external magnetic field containing the jump of the magnetization demonstrated in Fig. 5.9. Figure 5.10a, b differs only in the contrast of the domains—the black colour was changed to the white colour and vice versa. We have supposed that the domain walls have not moved during this jump. To verify this supposition we have produced the digital sum (Fig. 5.10c) of images (a) and (b). The resulting image confirms the suggestion: repeats the original domain configuration. It means that the quick jumps in the hysteresis loop are related to the transformation of the surface magnetic structure without the domain walls movement.

Figure 5.11 demonstrates the transformation of the Kerr hysteresis obtained in $Fe_{71.7}B_{13.4}Si_{11}Nb_3Ni_{0.9}$ microwire. The hysteresis loop consists of fluent rotation of the magnetization and jumps of the circular magnetization. The jump decreases with temperature disappears completely at 50 °C (Fig. 5.10b).

In difference with the $Fe_{3.5}Co_{69}B_{15}Si_{10}$ microwire, here we have fixed the quick motion of the domain walls (Fig. 5.12). The surface domain structure consists of two types of domain structures (type I and type II). They have different period of domain structure and different angle of the domain walls inclination relatively circular direction. The domain structure of the type I (central part of the image in Fig. 5.12) contains a DW with high mobility. The jumps of the Kerr signal are

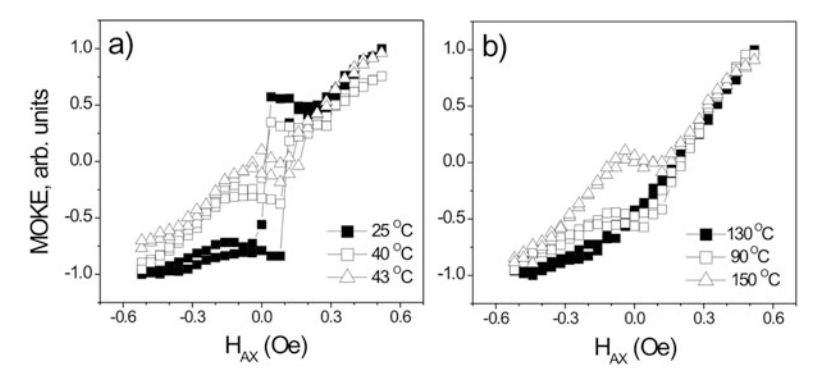


Fig. 5.11 Fe_{71.7}B_{13.4}Si₁₁Nb₃Ni_{0.9} microwire. MOKE hysteresis loops obtained in the presence of an H_{AX} at different temperatures: (a) 25 °C, 40 °C, and 43 °C; (b) 50 °C, 90 °C, and 130 °C



Fig. 5.12 The images of domain structures obtained at 40 °C: (a) $H_{\rm AX}=-0.5$ Oe; (b) $H_{\rm AX}=0.12$ Oe. The size of images is $600~\mu m \times 40~\mu m$

related to the quick motion of the solitary DW. The switching of the angle of the inclination is the characteristic feature of the structure II.

Figure 5.12a, b demonstrates the domain structures before and after the jump of the solitary domain wall realized in the domain structure I. Periodic domains are the samples of the structure II. Generally, structure II has helically inclined domains with two opposite directions of the inclination.

At the temperature of 50 °C the domain structure of I type disappears. This disappearance is correlated with the disappearance of the minor rectangular loop in the MOKE hysteresis (Fig. 5.11b).

It is evident that we have experimentally found coexistence of four helically oriented states which have been theoretically predicted in our paper [23]. The multidomains structure observed in this microwire is related to the internal stresses distribution inside the microwire. Because of difference between the thermal expansion coefficients of glass coating and metallic nucleus the glass coating introduces mentioned stresses [2]. Due to the magnetoelastic coupling between magnetization and internal stresses through magnetostriction, the internal stresses are the source of the magnetic anisotropy. These internal stresses are originated by high quenching rate and solidification process during the wire fabrication. The solidification usually proceeds from the wire surface causing the distribution of stresses along the wire depth.

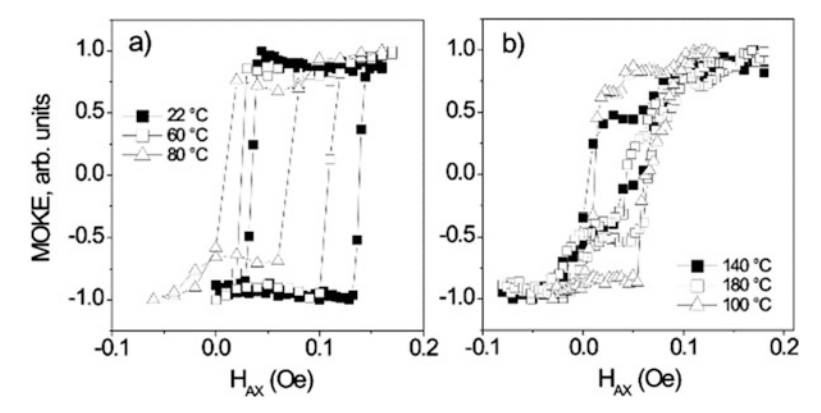


Fig. 5.13 Fe_{5.71}Co_{64.04}B_{15.88}Si_{10.94}Cr_{3.40}Ni_{0.03} microwire. MOKE hysteresis loops obtained in the presence of an $H_{\rm AX}$ at different temperatures: (**a**) 22 °C, 60 °C, 80 °C; (**b**) 100 °C, 140 °C, and 180 °C

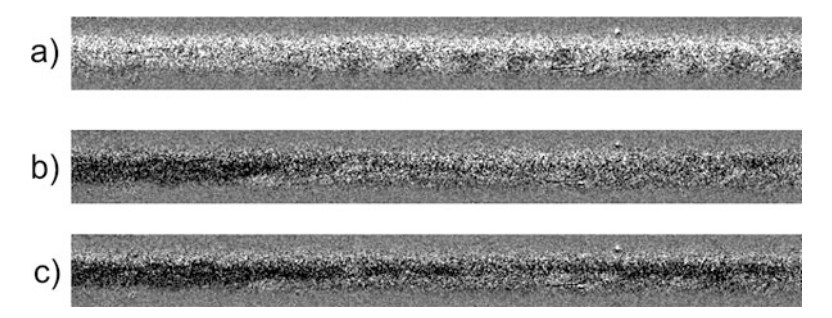


Fig. 5.14 The images of domain structures obtained at 100 °C: (a) $H_{\rm AX}=0.05$ Oe, (b) $H_{\rm AX}=0.07$ Oe, (c) $H_{\rm AX}=0.08$ Oe. The size of images is 500 μ m \times 50 μ m

The $Fe_{5.71}Co_{64.04}B_{15.88}Si_{10.94}Cr_{3.40}Ni_{0.03}$ microwire has rectangular hysteresis between the room temperature and 60 °C. This rectangularity means the existence of the effect of the circular bistability in this wire [24] (Fig. 5.13a). The heating process causes the transformation of the surface magnetic structure which is reflected in the hysteresis loop. The value of the jumps decreases with the temperature.

At high temperatures two types of domain structures have been found in this wire. The quick motion of the domain wall of type I is covered by the un-moved domains of type II. To demonstrate pure motion of the solitary domain wall we have performed the following image treatment. First, we have fixed the magnetic structure containing the small domains of the type II (Fig. 5.14a). Second step, we have used this image as a reference. Based on this reference image we have demonstrated the motion of the solitary domain wall (Fig. 5.14b, c). At the final part of the surface magnetization reversal the domains of the type II were observed again.

We consider that the temperature influence on the magnetic surface properties is stronger for the wire with the positive magnetostriction constant of 20×10^{-6} . It is related to the special magnetic structure of this wire: axially magnetized inner core, radially magnetized outer shell, and the helically magnetized surface closure domain structure. The coexistence of two types of surface domain structure takes place in very short temperature range. Two other magnetic microwires have basically helical magnetic structure with some distribution of the helicality. This structure is more homogeneous. Therefore, the temperature transformation of domain structures in these wires is weaker.

5.5 High-Frequency Electric Current Effect

The specially designed micro-strip cell has been used to apply the HF electric current $I_{\rm HF}$ in the MHz–GHz band (see Fig. 5.3). Usually this cell is used for GMI experiments [25].

Figures 5.15 and 5.16 present the MOKE hysteresis curves obtained in the presence of HF electric current of the MHz range. Figure 5.17 shows schematically the mechanisms of the surface magnetization reversal. The strong transformation of the hysteresis loop is observed that reflects the transformation of the magnetization reversal process. For the small value of the circular magnetic field ($I_{\rm HF}=2$ mA, Fig. 5.15) the hysteresis consists of the domain structure transformation and rotation of the magnetization in the surface (Fig. 5.17b). The electric current of 2 mA corresponds to the circular magnetic field of 0.35 Oe. An increase of the HF circular magnetic field ($I_{\rm HF}$ up to 10 mA) induces an asymmetric transformation of hysteresis loop. The following increase of the circular magnetic field amplitude ($I_{\rm HF}$ up to 20 mA) induces a change of the re-magnetization mechanism—the rotation of the magnetization dominates (Fig. 5.17a). We have to remark that this mechanism

Fig. 5.15 MOKE hysteresis loops in the presence of an HF electric current with 1 MHz frequency and varying amplitude of the current

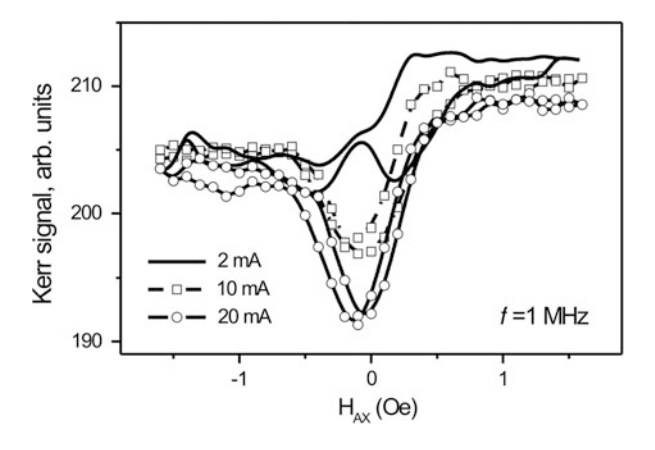


Fig. 5.16 MOKE hysteresis loops in the presence of an HF electric current. Comparison hysteresis loops in the presence of 1 MHz and 300 MHz frequency current

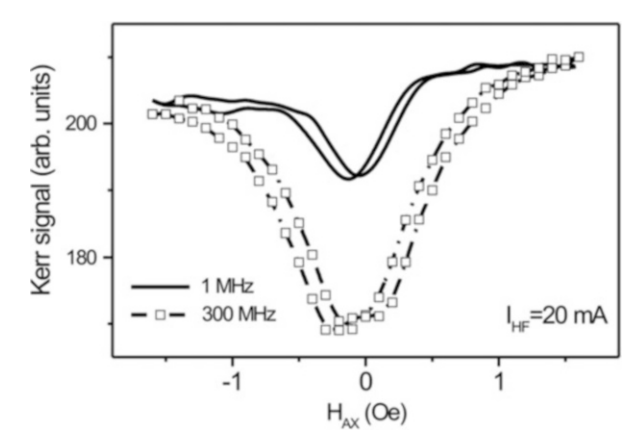
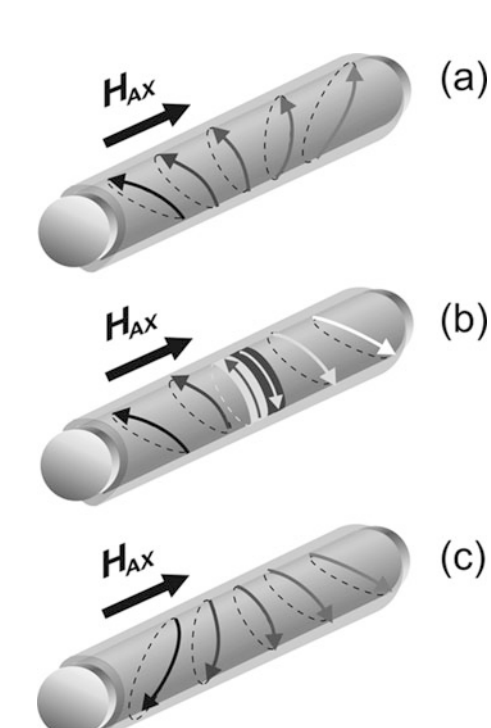


Fig. 5.17 Schematic pictures demonstrated mechanisms of the surface magnetization reversal under axial magnetic field $H_{\rm AX}$. The arrows schematically show the magnetization orientations



of the magnetization reversal is completely different from the magnetization reversal observed earlier in the presence of dc circular magnetic field [23].

To clear more deeply the details of the mechanism of the magnetization reversal, we have performed the following experiment. The MOKE hysteresis loops have been obtained in the presence of the HF electric current of the constant amplitude (20 mA). The frequency was changed in the band of 0.1–3 GHz (Fig. 5.18). The shape of the presented curves could be interpreted in the following way: the HF

Fig. 5.18 MOKE hysteresis loops obtained in the presence of an HF electric current of 20 mA for the different frequencies

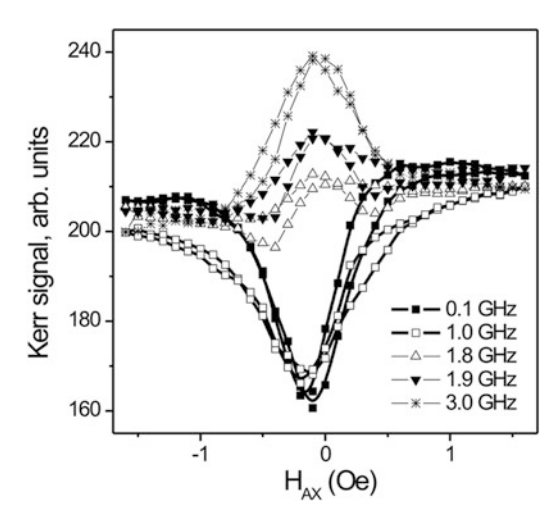


Fig. 5.19 Schematic of the magnetization vibration on the surface of the microwire



circular magnetic field causes such type of the energetic distribution that one of the surface circular phases is in an advantageous state, and the rotation of the magnetization in this domain is observed (Fig. 5.17a). The change of the frequency from 0.1 to 1 GHz only accelerates the rotation of the magnetization without changing of the essential of the mechanism. In this way, the circular field of 1 GHz causes a greater inclination of the circular magnetization from the axial direction than the circular field of 0.1 GHz.

Increasing the frequency we have found an unexpected effect. For the short band of the frequency (1.8–1.9 GHz) a strong transformation of the hysteresis loop takes place. For the frequency of 1.8 GHz, the MOKE hysteresis loop contains the regions which are interpreted as a clear rearrangement of the surface domain structure. For the frequency of 1.9 GHz, the opposite circular domain is the advantageous one and we observed coherent rotation of the magnetization in the surface of the wire. We explain this effect by the existence of a small initial helical anisotropy which exists originally in the studied wire (Fig. 5.19). Obviously, HF field induces an increase of the vibration of the magnetization. The meta-stable advantageous domain changes its sign to the opposite one when the vibrating helical magnetization overcomes the axial direction of the microwire.

For the frequency of 3 GHz, a pure rotation of the magnetization is also observed. The magnetic field of 3 GHz causes the following transformation: the meta-stable surface state becomes more inclined. The higher amplitude of the MOKE signal is the result of this effect of inclination. Generally, this effect finds the interpretation in the context of low field absorption and splitting between the ferromagnetic resonance and GMI effect [26].

We consider that the surface magnetic structure is the result of the superposition of the orthogonally directed HF circular and dc axial magnetic fields. The amplitude of the magnetic field generated by the exiting current of 20 mA is about 3.5 Oe in the wire surface that is higher than the quasi-static field applied in our experiments (about 2 Oe), while it is of the same order as the value of the static field applied typically in GMI experiments for such type of microwire [27, 28]. Following [29] we assume that for the high value of the HF circular field a microwave response of microwire is mainly associated with the inhomogeneous surface excitations of the magnetization vector. The dc axial field is smaller than the HF circular filed, but it is high enough to incline the equilibrium direction of helical magnetization relatively which the surface magnetization vibrates. The actual mechanism of the surface magnetization reversal is determined basically by the existence of four helical structures revealed earlier in [23]. The dynamic superposition of the two fields leads to the periodical change of the helical configuration. For the frequency of 1.9 GHz this change occurs as a magnetization switching.

5.6 Conclusion

The transformation of surface magnetic structures and magnetization reversal process have been studied in the Co- and Fe-rich amorphous microwires in the presence of the torsion stress, the temperature, and high-frequency electric current.

The analysis of the torsion stress induced transformation of hysteresis loops and domain structures has permitted us to establish the direct correlation between the angle of helical magnetic anisotropy and the value of the torsion stress. The real limit of the angle of the helical anisotropy has been determined. The earlier predicted value of 45° has been confirmed experimentally. Now we have an original method to present the results of the experiments with torsion stress as a dependence on the angle of helical anisotropy.

Taking into account the importance of circumferential permeability, we focus on the formation and the transformation of different types of magnetic domain structures induced by the HF circular magnetic field and the temperature.

The general regularities of the heating induced transformation of surface magnetization reversal and domain structure have been established. We have found that the surface magnetization reversal consists of the coherent rotation of the magnetization and the surface domain structure changes. In some microwires the quick directed solitary domain wall motion was observed while in other wires the rearrangement of domain structure rearranges in regular or irregular manner. The

quick jump in the MOKE hysteresis related to the domain wall motion disappears with temperature decrease. Another word, the heating suppresses the coexistence of two types of surface domain structures. The interplay of surface and internal mechanical stresses originated by the microwires fabrication process is the main reason of the domain structure transformation.

One of the observed essential effects in the presence of a low HF circular field is the sharp change in the direction of the magnetization in the existing domains. The contribution of this type of magnetization reversal is very essential to the circumferential permeability and, in turn, to the GMI amplitude. Also we have found that the HF circular magnetic field induces the existence of meta-stable inclined helical states. The sign of the inclined state and the degree of the helicity depend on the frequency and the amplitude of the HF magnetic field.

The temperature induced rearrangement of surface magnetic domain structure is examined in frame of providing the stable operation of the GMI device. It has been observed experimentally the coexistence of surface domain structures with different values of domain wall mobility. It has an ambivalent influence on the GMI effect. The increase of the number of inclined domain walls with temperature causes an increase of the GMI effect. In turn, it leads to an increase of the sensor sensitivity. On the other hand, a change in the number of domain walls causes evidently the instability of the magnetic sensor operation.

Acknowledgements This work was supported by Spanish Ministry of Economy and Competitiveness (MINECO) under Project No. MAT2013-47231-C2-1-P, the Basque Government under Saiotek 13 PROMAGMI (S-PE13UN014) and DURADMAG (S-PE13UN007) projects. A.C. acknowledges the financial support of Program of Mobility of the Investigating Personnel Basque Government MV-2015-1-15.

References

- Panina, L.V., Mohri, K.: Magneto-impedance effect in amorphous wires. Appl. Phys. Lett. 65, 1189–1191 (1994)
- Zhukov, A., Zhukova, V.: Magnetic Properties and Applications of Ferromagnetic Microwires with Amorphous and Nanocrystalline Structure. Nova Science Publishers, New York (2009)
- Chiriac, H., Ovari, T.A.: Switching field calculations in amorphous microwires with positive magnetostriction. J. Magn. Magn. Mater. 249, 141–145 (2002)
- Buznikov, N.A., Antonov, A.S., Granovsky, A.B.: Asymmetric magnetoimpedance in amorphous microwires due to bias current: effect of torsional stress. J. Magn. Magn. Mater. 355, 289–294 (2014)
- Xing, D., Chen, D., Liu, F., Liu, J., Shen, H., Ning, Z., Cao, F., SunT, J.: Torsion dependence of domain transition and MI effect of melt-extracted Co_{68.15}Fe_{4.35}Si_{2.25}B_{13.25}Nb₁Cu₁ microwires. Adv. Mater. Sci. Eng. 2015, 1–6 (2015)
- Gonzalez, J., Chen, I.P., Blanco, J.M., Zhukov, A.: Effect of applied mechanical stresses on the impedance response in amorphous microwires with vanishing magnetostriction. Phys. Status Solidi A. 189, 599–608 (2002)
- 7. Phan, A.H., Yua, S.C., Kim, C.G., Vazquez, M.: Origin of asymmetrical magnetoimpedance in a Co-based amorphous microwire due to dc bias current. Appl. Phys. Lett. **83**, 2871–2873 (2003)

- 8. Betancourt, I.: Magnetization dynamics of amorphous ribbons and wires studied by inductance spectroscopy. Materials. **4**, 37–54 (2011)
- Betancourt, I., Hrkac, G., Schrefl, T.: Micromagnetic study of magnetic domain structure and magnetization reversal in amorphous wires with circular anisotropy. J. Magn. Magn. Mater. 323, 1134–1139 (2011)
- Sablik, M.J., Jiles, D.C.: A modified Stoner-Wohlfarth computational model for hysteretic magnetic properties in a ferromagnetic composite rod under torsion. J. Phys. D: Appl. Phys. 32, 1971–1983 (1999)
- 11. Sablik, M.J., Jiles, D.C.: Modeling the effects of torsional stress on hysteretic magnetization. IEEE Trans. Magn. 35, 498–504 (1999)
- 12. Sixtus, K.J., Tonks, L.: Propagation of large Barkhausen discontinuities. Phys. Rev. 42, 419 (1932)
- Chizhik, A., Stupakiewicz, A., Maziewski, A., Zhukov, A., Gonzalez, J., Blanco, J.M.: Direct observation of giant Barkhausen jumps in magnetic microwires. Appl. Phys. Lett. 97, 012502 (2010)
- Chizhik, A., Zablotskii, V., Stupakiewicz, A., Dejneka, A., Polyakova, T., Tekielak, M., Maziewski, A., Zhukov, A., Gonzalez, J.: Circular domains nucleation in magnetic microwires. Appl. Phys. Lett. 102, 202406 (2013)
- Zhukov, A., Blanco, J.M., Ipatov, M., Chizhik, A., Zhukova, V.: Manipulation of domain wall dynamics in amorphous microwires through the magnetoelastic anisotropy. Nanoscale Res. Lett. 7, 223 (2012)
- Hudak, J., Blazek, J., Cverha, A., Gonda, P., Varga, R.: Improved Sixtus—Tonks method for sensing the domain wall propagation direction. Sens. Actuators A. 156, 292–295 (2009)
- 17. Hubert, A., Schäfer, R.: Magnetic Domains. Springer, Berlin (1998)
- Stupakiewicz, A., Chizhik, A., Tekielak, M., Zhukov, A., Gonzalez, J., Maziewski, A.: Direct imaging of the magnetization reversal in microwires using all-MOKE microscopy. Rev. Sci. Instrum. 85, 103702 (2014)
- 19. Chizhik, A., Gonzalez, J., Zhukov, A., Blanco, J.M.: Magnetization reversal of Co-rich wires in circular magnetic field. J. Appl. Phys. **91**, 537–539 (2002)
- Chizhik, A., Zhukov, A., Blanco, J.M., Gonzalez, J., Gawronski, P.: Experimental determination of limit angle of helical anisotropy in amorphous magnetic microwires. J. Magn. Magn. Mater. 321, 803–805 (2009)
- 21. Bertotti, G.: Hysteresis in Magnetism. Academic Press, San Diego (1998)
- 22. Chizhik, A., Gonzalez, J.: Magnetic Microwires: A Magneto-Optical Study. Pan Stanford Publishing Pte. Ltd., Singapore (2014)
- Chizhik, A., Zablotskii, V., Stupakiewicz, A., Gómez-Polo, C., Maziewski, A., Zhukov, A., Gonzalez, J., Blanco, J.M.: Phys. Rev. B. 82, 212401–212404 (2010)
- Chizhik, A., Gonzalez, J., Zhukov, A., Blanco, J.: Circular magnetic bistability in Co-rich amorphous microwires. J. Phys. D. Appl. Phys. 36, 419–422 (2003)
- Ipatov, M., Zhukova, V., Zhukov, A., Gonzalez, J., Zvezdin, A.: Low-field hysteresis in the magnetoimpedance of amorphous microwires. Phys. Rev. B. 81, 134421 (2010)
- Valenzuela, R., Zamorano, R., Alvarez, G., Gutiérrez, M.P., Montiel, H.: Magnetoimpedance, ferromagnetic resonance, and low field microwave absorption in amorphous ferromagnets. J. Non-Cryst. Solids. 353, 768–772 (2007)
- Zhukova, V., Chizhik, A., Zhukov, A., Torcunov, A., Larin, V., Gonzalez, J.: Optimization of giant magnetoimpedance in Co-rich amorphous microwires. IEEE Trans. Magn. 38, 3090–3092 (2002)
- 28. Tousignant, M., Zabeida, M.O., Rudkowska, G., Yelon, A.: Investigation of surface effect on giant magnetoimpedance in microwires. J. Magn. Magn. Mater. 349, 232–234 (2014)
- Nakayama, K., Chiba, T., Tsukimoto, S., Yokoyama, Y., Shima, T., Yabukami, S.: Ferromagnetic resonance in soft-magnetic metallic glass nanowire and microwire. J. Appl. Phys. 105, 202403 (2014)

Chapter 6 Tunable Electric Polarization of Magnetic Microwires for Sensing Applications

Larissa V. Panina, Dmitriy P. Makhnovskiy, Abdukarim Dzhumazoda, and Svetlana V. Podgornaya

6.1 Introduction

Miniature sensors with remote wireless operation are required in many technological areas including structural health monitoring, smart composites, embedded biosensors, etc. Microwave technologies have a high potential for remote sensing applications. In this chapter, tunable microwave electric polarization of magnetic microwires and its application in sensors are discussed. Recently, many applications of microwave interacting with ferromagnetic materials or metamaterials have been developed [1]. So far, the main uses of such materials are sensing applications [2, 3] and microwave shielding systems [4, 5].

In order to realize efficient tunable properties, magnetic microwires in amorphous state are considered. The glass forming alloy is based on CoFeSiB and may also contain additions such as Cr, Mn, Al, Cu, and Nb in order to refine magnetic and mechanical properties [6–8]. The absence of the crystalline structure is very useful since it is possible to induce a required magnetic anisotropy through magnetoelastic interaction. For microwave applications, the domain structure in the outer shell is important. For many sensing applications, a circumferential or

L.V. Panina (⋈)

National University of Science and Technology, MISIS, Moscow, Russian Federation

Institute for Design Problems in Microelectronics, Moscow, Russian Federation e-mail: drlpanina@gmail.com

D.P. Makhnovskiy Robat Ltd., Macclesfield, UK

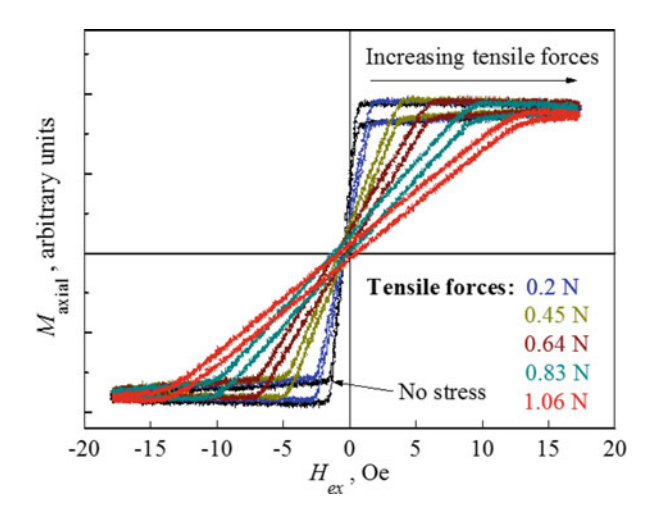
A. Dzhumazoda • S.V. Podgornaya National University of Science and Technology, MISIS, Moscow, Russian Federation L.V. Panina et al.

helical anisotropy is preferable, which can be established in Co-rich alloys with negative magnetostriction ($\lambda_s < 0$). In general, the magnetostrictive constant λ_s depends on the alloy composition. In the $(\text{Co}_{1-x}\text{Fe}_x)_{75}\text{Si}_{15}\text{B}_{10}$ series, λ_s is negative for x < 0.06 [8]. Therefore, around this compositional point, excellent soft magnetic properties can be realized. Thus, for a composition $\text{Co}_{68.15}\text{Fe}_{4.35}\text{Si}_{12.5}\text{B}_{15}$ the magnetostriction is almost zero (but still negative) $\lambda \sim -10^{-7}$. For such wires, the remagnetization behavior in an axial magnetic field less than the effective anisotropy field is almost linear, without hysteresis and with very high susceptibility.

Amorphous microwires with a diameter of 1–40 µm are produced in glass coating by a modified Taylor–Ulitovsky method [9]. For instance, MFTI LTD (Kishinev, Republic of Moldova; www.microwires.com) produces microwires of broad range of compositions. The drawing process of metal-glass composite wire introduces frozen-in tensile stress which is a source of the magnetic anisotropy in wires. This stress may be larger than other stresses occurring in the processes of rapid quenching. The ratio of the metal core and glass coating thickness determines the value of this stress. Therefore, controlling the metal core diameter and glass thickness, the magnetic properties of wires can be tailored [10]. Furthermore, since the metallic core is covered by a biocompatible Pyrex shell, microwires are suitable for biological and medical applications [11–13].

The external stress and temperature may also substantially modify the magnetic anisotropy and the magnetization processes as shown in Fig. 6.1 [14]. Tunable soft magnetic properties of amorphous microwires result in unique high frequency behavior, namely giant magnetoimpedance (MI) [15–17]. At MHz frequencies, MI is utilized in various magnetic and stress sensors. At GHz frequency, the MI effect can be used to control the scattering of electromagnetic waves from microwires with application to tunable electromagnetic composites and embedded sensors.

Fig. 6.1 Magnetization curves of $Co_{68}Fe_4Cr_3Si_{11}B_{14}$ microwire at different tensile forces applied to one end of the wire. The microwire had the total diameter of 33.3 μ m and the metal core diameter of 25.3 μ m



6.2 Electrical Dipole Moment of a Magnetic Wire

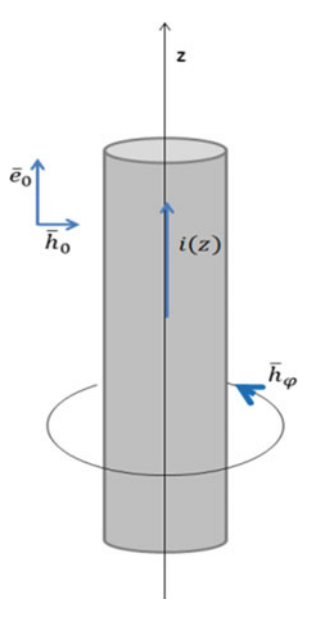
The use of metal inclusions in microwave applications is often justified by their larger electric polarizability in comparison with dielectrics. This enables one to obtain a strong response even from a single inclusion. The shape of metal particles significantly determines their polarization properties. A small metal sphere or ellipsoid is the simplest shape, the scattering on which can be analyzed by means of Mie's theory. However, the most wide variety of polarization effects are observed in the wire inclusions with different spatial configurations, beginning at needle-shaped [18–23] and ending with spirals or omega-particles [24, 25] which may form artificial magnetism and chiral effective properties [26, 27]. Here we consider the electromagnetic scattering from a rod-shaped thin magnetic conductor, namely magnetic microwires [28–30].

The wire of finite length is placed in the external microwave field as shown in Fig. 6.2. The external electrical field $e_0 \exp(-j\omega t)$ induces the current $i(z) \exp(-j\omega t)$ in the wire with some distribution along the wire length (z-axis). If the wire has a finite length, the current must be zero at the wire ends:

$$i\left(\pm\frac{1}{2}\right) = 0\tag{6.1}$$

Therefore, the field e_0 induces the dipole moment \mathcal{P} in the wire, which can be calculated using the continuity equation $\partial i(z)/\partial z = j\omega\rho(z)$ and integrating by parts (here ρ is the charge density per unit length):

Fig. 6.2 Geometry of scattering problem from a magnetic wire



L.V. Panina et al.

$$\mathcal{P} = \frac{j}{\omega} \int_{-1/2}^{1/2} i(z)dz \tag{6.2}$$

We can also introduce the electric polarizability of the wire:

$$\alpha = \frac{\mathcal{P}}{Ve_0} \tag{6.3}$$

where V is the wire volume.

6.2.1 Antenna Approximation and Impedance Boundary Conditions

The scattering problem for a thin conductor is typically solved within the antenna approximation [31]. The current in it induced by the electromagnetic radiation is replaced by an equivalent linear current flowing along the axis. So the current spatial distribution depends only on the axial (z) coordinate. This approximation can be used when the wavelength λ and the conductor length l are much larger than the conductor cross size $2a:2a\ll\lambda$ and $2a\ll l$. The incident electromagnetic wave is supposed to be of a plane type. In this case, the external magnetic field does not give a contribution to a circular magnetic field on the conductor surface. The incident wave having a longitudinal electric field \bar{e}_{0z} at the conductor surface induces a longitudinal current in it which determines the scattered electromagnetic field with longitudinal electric \bar{e}_z and circular magnetic \bar{h}_{φ} components on the conductor surface (cylindrical conductor is considered, φ is the azimuthal coordinate).

In the antenna approximation, the electromagnetic response from a thin conductor is fully determined by the external scattering problem with the boundary conditions imposed at the conductor surface, which involve the surface impedance matrix $\hat{\varsigma}$ [32]:

$$\bar{\boldsymbol{e}}_t = \widehat{\boldsymbol{\varsigma}}(\bar{\boldsymbol{h}}_t \times \boldsymbol{n}) \tag{6.4}$$

where n is the unit normal vector directed inside the conductor, \bar{e}_t and \bar{h}_t are the tangential vectors of the total electric and magnetic fields at the conductor surface, which include both the scattered and external fields. In the case of an ideal conductor with infinite conductivity ($\sigma = \infty$) condition (6.4) becomes zero: $\bar{e}_t = 0$, which is often used in the antenna problems. In the local cylindrical coordinate system (r, φ, z) condition (6.4) has a form

$$\bar{e}_z = \varsigma_{zz}\bar{h}_{\varphi} - \varsigma_{z\varphi}\bar{h}_z \tag{6.5a}$$

$$\bar{e}_{\varphi} = \varsigma_{\varphi z} \bar{h}_{\varphi} - \varsigma_{\varphi \varphi} \bar{h}_{z} \tag{6.5b}$$

It is interesting to notice that in a magnetic conductor the longitudinal electric field (and an electrical dipole moment) can also be induced by a longitudinal magnetic field owing to the existence of non-diagonal component $\varsigma_{z\varphi}$. Within the antenna approximation, the field $\bar{h}_{\varphi}(z)$ is originated only by the induced current with the linear density i(z). On the contrary, the longitudinal field \bar{h}_z is entirely defined by the excitation field.

The formalism for calculating the matrix $\hat{\varsigma}$ for a ferromagnetic wire with an arbitrary helical anisotropy was developed in [20, 21, 33]. In the case of a sufficiently strong skin-effect which is expected at GHz frequencies and considering that the surface layer of the wire has a helical magnetization with the constant angle θ (with respect to the wire axis), the components ς_{zz} , $\varsigma_{z\varphi}$ are of the form.

$$\varsigma_{zz} = \frac{c(1-i)}{4\pi\sigma\delta} \left(\sqrt{\widetilde{\mu}} \cos^2(\theta) + \sin^2(\theta) + \frac{\delta(1+i)}{4a} \right), \tag{6.6a}$$

$$\varsigma_{z\varphi} = \frac{c(1-i)}{4\pi\sigma\delta} \left(\sqrt{\widetilde{\mu}} - 1\right) \sin\left(\theta\right) \cos\left(\theta\right). \tag{6.6b}$$

Here c is the velocity of light, $\widetilde{\mu}$ is the permeability parameter composed of the components of the permeability tensor, σ is the wire conductivity, a is the wire radius, and $\delta = c/\sqrt{2\pi\sigma\omega}$ is the skin depth for non-magnetic wire.

6.2.2 Current Distribution in a Magnetic Wire (Antenna Equation with Impedance Boundary Condition)

The problem is formulated in terms of vector **A** and scalar φ potentials:

$$e = -\nabla \varphi - \frac{4\pi}{c^2} \frac{\partial \mathbf{A}}{\partial t}, \mathbf{h} = \frac{4\pi}{c} (\nabla \times \mathbf{A})$$
 (6.7)

The Lorentz gauge is imposed: $(\varepsilon_d \partial \varphi/\partial t + 4\pi \nabla \cdot \mathbf{A})$, where ε_d is the permittivity of the media around the wire. Then, the electric field in the frequency domain (assuming the time-dependence to be $\exp(-j\omega t)$) is expressed as:

$$e = \frac{4\pi j\omega}{c^2} \mathbf{A} - \frac{4\pi}{j\omega\varepsilon_d} \text{grad div } \mathbf{A}$$
 (6.8)

Potential A obeys the Helmholtz equation:

$$\Delta \mathbf{A} + k^2 \mathbf{A} = \mathbf{i} \tag{6.9}$$

L.V. Panina et al.

Here $k = (\omega/c)\sqrt{\varepsilon_d}$ is the wave number in the surrounding dielectric and i(z) is the current density. The solution of Eq. (6.9) can be written using the convolution of i(z) with the Green function G(r) (a more detailed formalism can be found in [29]):

$$\mathbf{A}(\mathbf{r}) = (G^* \mathbf{i}) = \int_V \mathbf{i}(z) G(r') dV_z$$

$$G(r) = \frac{\exp(jkr)}{4\pi r}$$
(6.10)

In (6.10) the integration is carried out over the total volume V containing i(z), that is over the wire volume, r' = |r - z| is the distance between r and the integration point z. The magnetic field induced by a linear current is found from Eqs. (6.7) and (6.10):

$$\boldsymbol{h}(\boldsymbol{r}) = \frac{1}{c} \int_{V} \frac{(1 - jkr')\exp(jkr')}{(r')^{3}} (\boldsymbol{i}(\boldsymbol{z}) \times \boldsymbol{r}') dV_{z}$$

$$\boldsymbol{r}' = \boldsymbol{r} - z$$
(6.11)

For a cylindrical symmetry and linear current i(z), the circular magnetic field at the wire surface is expressed as

$$\bar{h}_{\varphi}(z,a) = \frac{a}{c} \int_{-l/2}^{l/2} \frac{(1-jkr)\exp(jkr)}{r^3} i(s) ds$$
 (6.12)

where $r = \sqrt{(z-s)^2 + a^2}$. Contrary to the static case when the circular magnetic field is related to the total current $I(\bar{h}_{\varphi} = 2I/ac)$, Eq. (6.12) takes into account the retarding effects.

The longitudinal component of the vector potential A_z describes the scattered field from a straight conductor. With the use of Eqs. (6.7) and (6.10), the longitudinal component of the field $e_z(x, y, z)$ is expressed in terms of an integrodifferential operator, where the convolution is carried out for coordinate z:

$$e_{z}(x, y, z) = \frac{4\pi}{j\omega\varepsilon_{d}} \left(\frac{\partial^{2}}{\partial z^{2}} (G * i) + k^{2} (G * i) \right)$$

$$(G * i) = \int_{-1/2}^{1/2} i(s)G(r)ds, r = \sqrt{(z - s)^{2} + x^{2} + y^{2}}$$
(6.13)

At the wire surface $r = \sqrt{(z - s)^2 + a^2}$. Using the impedance boundary condition (6.5a) and Eq. (6.13), the integro-differential equation (generalized antenna equation) for the current density i(z) is finally obtained:

$$\frac{\partial^2}{\partial z^2}(G^*i) + k^2(G^*i) = \frac{j\omega\varepsilon_d}{4\pi}\bar{e}_{0z}(z) - \frac{j\omega\varepsilon_d\varsigma_{zz}}{2\pi ac}(G_{\varphi}^*i) + \frac{j\omega\varepsilon_d\varsigma_{z\varphi}}{4\pi}\bar{h}_{0z}(z)$$
(6.14)

In (6.14) \bar{e}_{0z} $\times \bar{h}_{0z}$ are the external electrical and magnetic fields taken at the wire surface. The function $G_{\varphi}(r)$ determines the scattered magnetic field $\bar{h}_{\varphi}(z,a)$ at the wire surface:

$$\bar{h}_{\varphi}(z,a) = \frac{2}{ac} \left(G_{\varphi} * i \right) = \frac{2}{ac} \int_{-l/2}^{l/2} G_{\varphi}(r) i(s) ds$$

$$G_{\varphi}(r) = \frac{a^2 (1 - jkr) \exp(jkr)}{2r^3}$$

$$(6.15)$$

Equation (6.15) is completed by the boundary conditions (6.1) at the wire ends $i(\pm l/2) = 0$. Antenna Eq. ((6.15)) involves the total losses including radiation and internal losses (resistive and magnetic). The internal losses are given by the impedance ς_{zz} and the convolution $(G_{\varphi} * i)$, whereas the imaginary part of (G * i) determines the radiation losses.

Along with this, there is an additional term in the right part of Eq. (6.16), related with the off-diagonal component $\varsigma_{z\varphi}$. Thus, the ferromagnetic conductor can be excited not only by a longitudinal electric field, but also by a longitudinal magnetic field.

The real parts of the Green functions G and G_{φ} , considered at the conductor surface, have a sharp peak at r=a. Thus, $\operatorname{Re}(G)$ and $\operatorname{Re}(G_{\varphi})$ give the main contribution to Eq. (6.14). However, the convolutions with the imaginary parts are important in the vicinity of the resonance and can be taken into account by an iteration procedure. For calculation of the convolutions with functions $\operatorname{Re}(G)$ and $\operatorname{Re}(G_{\varphi})$ an approximate method can be used:

$$(\text{Re}(G)^*i) \approx i(z) \int_{-l/2}^{l/2} \text{Re}(G(r))ds = i(z)Q,$$
 (6.16)

$$Q = \int_{-l/2}^{l/2} \text{Re}(G(r))ds \sim \frac{1}{4\pi} \int_{-l/2}^{l/2} \frac{ds}{\sqrt{s^2 + a^2}} \sim \frac{\ln(l/a)}{2\pi},$$
 (6.16a)

$$\left(\operatorname{Re}(G_{\varphi})^*i\right) \approx j(z) \int_{-l/2}^{l/2} \operatorname{Re}(G_{\varphi}(r)) ds = i(z) Q_{\varphi}$$
(6.17)

$$Q_{\varphi} = \int_{-l/2}^{l/2} \operatorname{Re}(G_{\varphi}(r)) ds \sim \frac{a^2}{2} \int_{-l/2}^{l/2} \frac{ds}{(s^2 + a^2)^{3/2}} + \frac{a^2 k^2}{2} \int_{-l/2}^{l/2} \frac{ds}{\sqrt{s^2 + a^2}} \sim (1 + a^2 k^2 \ln(l/a))$$

(6.17a)

L.V. Panina et al.

Equations ((6.16a)) and ((6.17a)) determine the positive form-factors Q and Q_{φ} . For the estimation of Q_{φ} it was taken into account that $ak \ll 1$ in the antenna approximation.

Using Eq. (6.14) together with the inequalities $|(\operatorname{Im}(G) * i)| \ll |(\operatorname{Re}(G) * i)|$ and $|(\operatorname{Im}(G_{\varphi}) * i)| \ll |(\operatorname{Re}(G_{\varphi}) * i)|$ we obtain a differential equation for the zero approximation $i_0(x)$ where the radiation losses are neglected:

$$\frac{\partial^{2}}{\partial z^{2}}i_{0}(z) + \left(\frac{\omega}{c}\right)^{2} \varepsilon_{d} \left(1 + \frac{jc\varsigma_{zz}}{2\pi a\omega} \frac{Q_{\varphi}}{Q}\right) i_{0}(z) \approx \frac{j\omega\varepsilon_{d}}{4\pi Q} \left(\bar{e}_{0z}(z) + \varsigma_{z\varphi}\bar{h}_{0z}(z)\right). \tag{6.18}$$

As it follows from Eq. (6.18), the implementation of the impedance boundary condition leads to the renormalization of the wave number which becomes:

$$\widetilde{k} = \frac{\omega}{c} \sqrt{\varepsilon_d} \left(1 + \frac{jc\varsigma_{zz}}{2\pi a\omega} \frac{Q_{\varphi}}{Q} \right)^{1/2}$$
(6.19)

The effective wave number \vec{k} defines the normalized resonance wavelength $(k_{\rm res} l = \pi (2n-1))$:

$$\lambda_{\text{res},n} = \frac{2l\sqrt{\varepsilon_d}}{2n-1} \text{Re}\sqrt{\left(1 + \frac{jc\varsigma_{zz}}{2\pi a\omega} \frac{Q_{\varphi}}{Q}\right)}, \quad n = 1, 2, 3 \dots$$
 (6.20)

Using Eqs. (6.16a) and (6.17a) for the form-factors, the resonance condition has the form:

$$\lambda_{\text{res},n} = \frac{2l\sqrt{\varepsilon_d}}{2n-1} \text{Re}\sqrt{\left(1 + \frac{jc\varsigma_{zz}}{a\omega \ln(l/a)}\right)}$$
(6.21)

The resonance frequency is defined as $f_{res,n} = c/\lambda_{res,n}$.

The resonance wavelengths defined by (6.21) depend on the wire magnetic properties. The condition of a moderate skin-effect is required in order to realize a substantial dependence of $\lambda_{\text{res},n}$ on the wire magnetic properties. If the magnetic skin depth is much smaller than the wire radius $(\delta_m/a << 1)$, the normalized wave number \widetilde{k} differs little from the wave number k of the free space. Substituting the high frequency impedance (6.6a) into (6.20) gives:

$$\widetilde{k} \sim \frac{\omega}{c} \sqrt{\varepsilon \mu} \left(1 + \frac{(1-j)}{2\mu \ln(l/a)} \frac{\delta}{a} \sqrt{\widetilde{\mu}} \cos^2(\theta) \right)^{1/2}$$
 (6.22)

From Eq. (6.22) it immediately follows that if $\delta/a < <1$ the wave number becomes $\widetilde{k} \approx \omega \sqrt{\varepsilon \mu}/c$, and does not depend on the wire properties.

The current distribution along the wire for different frequencies is shown in Figs. 6.3 and 6.4 considering the zero-order approximation (Eq. (6.18)) and the first

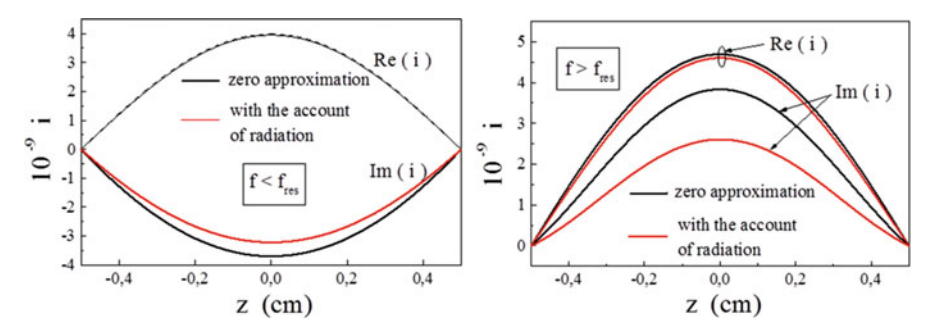


Fig. 6.3 Current distribution along the wire for frequencies below the resonance (at the right) and pass the resonance (at the left) for non-magnetic case ($\theta = \pi/2$ in Eqs. (6.6a) and (6.22)). The wire conductivity is $\sigma = 10^{16} \, \mathrm{s}^{-1}$. The frequency is in the GHz range

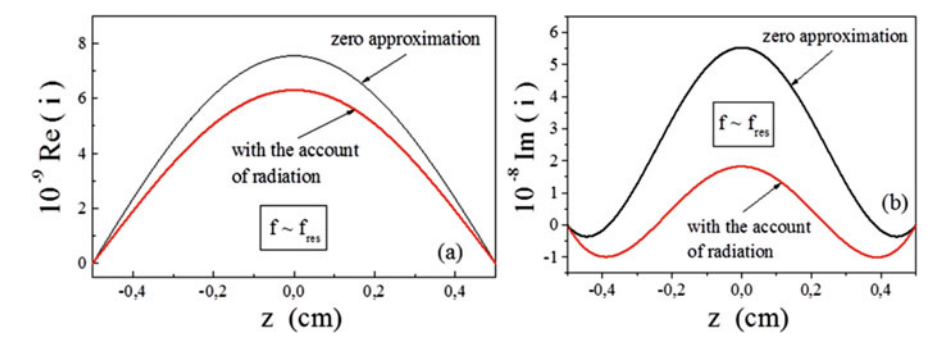


Fig. 6.4 Current distribution along the wire for frequency near the resonance: (a) real part, (b) imaginary part. The other parameters are the same as for Fig.6.3

order approximation obtained by the iteration procedure of solving Eq. (6.14) (for details of using the iteration procedure see [29, 30]). For this calculation, the wire magnetization is assumed to be in the circular direction, so the surface impedance has a minimum ($\theta = \pi/2$ in Eqs. (6.6a) and (6.22)). For amorphous alloy, the resistivity is relatively large so even in this case the skin depth is rather large and the resistive losses are also large. It is seen that the radiation losses appearing in the first order approximation is essential only at the antenna resonance frequency. Near the resonance the current distribution (its imaginary part) sharply changes its shape becoming positive after the resonance.

6.2.3 Tunable Polarizability of a Magnetic Wire

The current distribution allows the calculation of the wire dipole moment \mathcal{P} and the polarizability α according to Eqs. (6.2) and (6.3). If the radiation effects are

L.V. Panina et al.

neglected (zero-order approximation) the current distribution obeys Eq. (6.18) and the polarizability has a simple analytical form:

$$\alpha = \frac{1}{2\pi \ln(l/a) \left(\widetilde{k}a\right)^2} \left(\frac{2}{\widetilde{k}l} \tan\left(\widetilde{k}l/2\right) - 1\right)$$
 (6.23)

From Eq. (6.23) it is seen that the wire polarizability depends on the normalized wave number \tilde{k} which involves the wire surface impedance. The wire dipole moment determines the scattering of the electromagnetic waves from a conducting wire. If the surface impedance of the wire can be tuned by external factors, then it would be possible to control the scattering property.

The surface impedance of magnetic wires is sensitive to the change in the direction of the static magnetization. In the case of a circumferential or helical anisotropy which can be established in amorphous wires of Co-rich compositions the surface impedance shows large variations in the presence of a moderate magnetic field or stress which can be observed even at GHz frequencies [34–36] as shown in Figs. 6.5 and 6.6. It is seen in Fig. 6.5 that the impedance sensitively changes in the range of small fields when the static magnetization changes its direction from a circumferential to axial (there is change in the magnetization angle θ). When the external field H_{ex} sets the magnetization along the axis (which happens when $H_{ex} \cong H_K$, H_K is the anisotropy field) there is almost no change in the impedance since the apparent permeability parameter $\widetilde{\mu}$ changes little at GHz frequencies and moderate external fields.

The experimental results for MI at GHz frequencies confirm such behavior. Here we demonstrate the impedance behavior in a wire with a helical anisotropy in the presence of the external tensile stress (Fig. 6.6). For negative magnetostriction, this stress strengthens the circular anisotropy and rotates the magnetization towards the circular direction. The impedance behavior reflects the change in the magnetization direction but when the magnetization is set, the impedance does not show any

Fig. 6.5 Theoretical plots of the surface impedance of amorphous wires with a circumferential anisotropy. The wire has $10 \mu m$ diameter, conductivity $\sigma = 7.6 \times 10^{15} \text{ s}^{-1}$, anisotropy field $H_K = 2$ Oe, saturation magnetization $M_0 = 500$ G, and gyromagnetic constant $\gamma = 2 \times 10^7$ (rad/s)/Oe

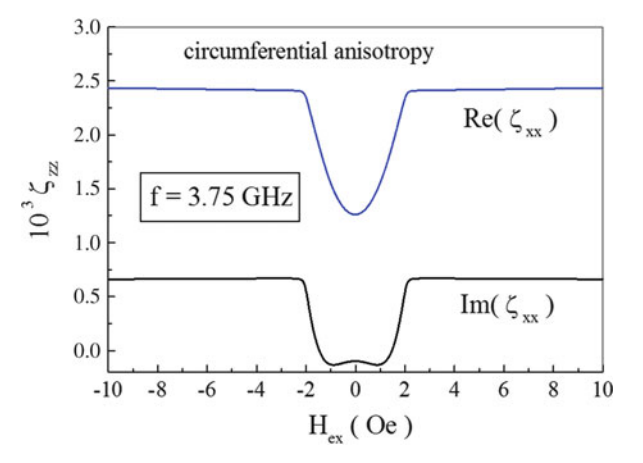
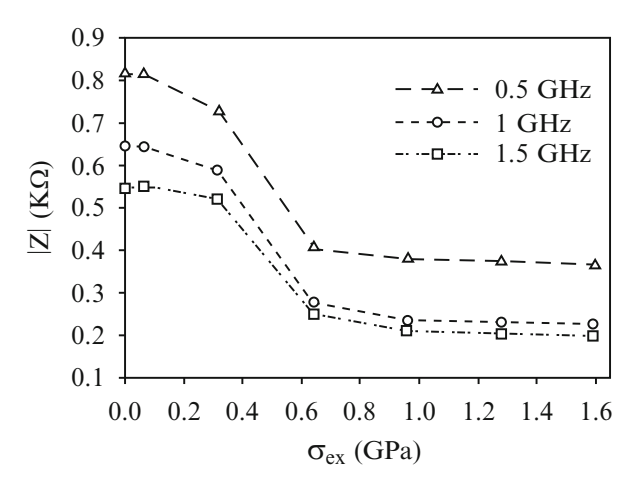


Fig. 6.6 Impedance vs. tensile stress in glass-coated amorphous wire of composition $Co_{69}Fe_3Cr_3Si_{10}B_{15}$ annealed and cooled under stress (30 kg/mm²) to establish a helical anisotropy. The plots are given for different frequencies. The metal core diameter is about 10 μ m, the total diameter is 14 μ m



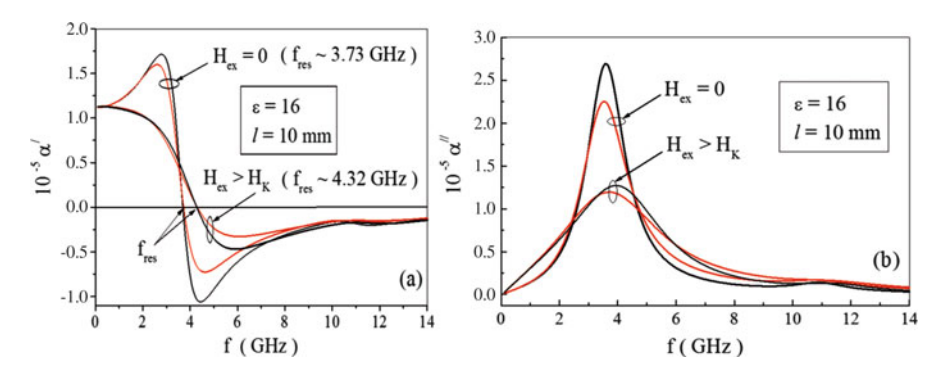


Fig. 6.7 Electrical polarizability of a magnetic vs. frequency: (a) real part and (b) imaginary part. The graphs are shown when no magnetic field is applied and in the presence of a magnetic field above the anisotropy field (the field when the magnetization saturates along the axis). The wire has a length of 1 cm and is placed in the dielectric matrix with a permittivity of 16. The antenna resonance frequency is 4.32 GHz. The magnetic, electric, and geometric parameters are the same as for Fig. 6.5: $a = 5 \mu m$, $\sigma = 7.6 \times 10^{15} \text{ s}^{-1}$, $H_K = 2 \text{ Oe}$, $M_0 = 500 \text{ G}$, $\gamma = 2 \times 10^7 \text{ (rad/s)/Oe}$

variations. Therefore, in magnetic amorphous wires the impedance at GHz frequencies sensitively changes with the change in the direction of the static magnetization. The transfer mechanism between the impedance and static magnetization involves the dynamic permeability which must be significantly different from unity. Certainly, this can be realized for not very high frequencies. For soft magnetic amorphous wires under consideration the frequency limit is about 10 GHz.

The modelled spectra of electric polarization of such wire are shown in Fig. 6.7. When no field is applied (the impedance has a minimum), the wire polarization shows a resonance behavior with the first resonance frequency defined by Eq. (6.21), which almost coincides with the half wavelength condition. In the presence of the external field which is larger than the effective anisotropy field

L.V. Panina et al.

 H_K the impedance and the losses increase resulting in a relaxation behavior of the polarizability. In this case the modelling is made for a short wire in a dielectric matrix to decrease the resonance wavelength. The use of short wires can be required for composite materials. In this case, if the matrix has a low permittivity, the resonance frequency could be too high to realize magnetic tuning.

6.3 Wireless Sensor Based on Tunable Wire Polarizability

Scattering from a single magnetic wire which possesses MI effect can be used for contactless sensing of external parameters such as magnetic field and stress [28]. The sensing experiment is based on S_{21} -parameter measurements. The wire is placed between two antennas attached to two ports of the analyzer as shown in Fig. 6.8.

The measured quantity

$$S_{21} = 20\log\frac{P_2}{P_1}$$

involves the power P_1 emitted by the antenna attached to the port 1 and power P_2 received by the antenna attached to the port 2. The last parameter is defined by the scattering of the wire which is proportional to the wire dipole moment \mathcal{P} since the scattered wave is generated by the electric current along the microwire. The P_2 -radiation also includes the emitted power. To avoid the effect of this contribution, an ac bias magnetic field very low frequency parallel to the axis of the microwire can be used so that the output will contain only the contribution from the scattering dependent on the wire magnetic properties. Such bias field is easy to create by

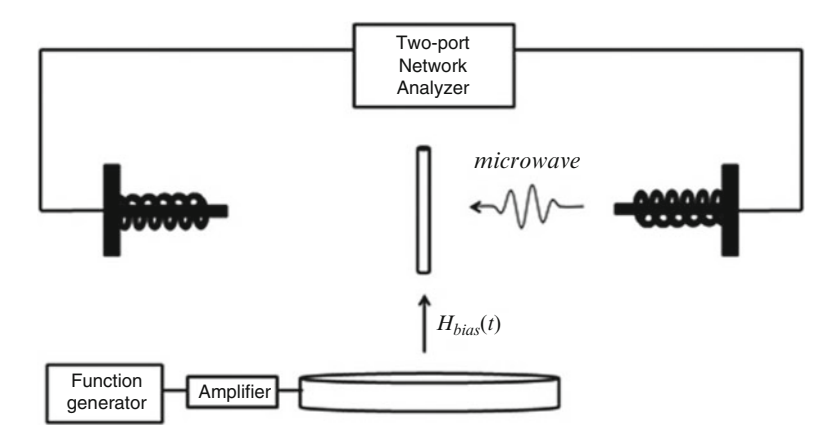


Fig. 6.8 Experimental arrangements for measuring scattering from a single magnetic wire which is placed between two antennas. The wire is subjected to ac bias magnetic field of low frequency which modulates the amplitude of scattered output signal

Fig. 6.9 Time modulation of S_{12} parameter based on scattering from a single magnetic microwire of composition $Fe_{2.25}Co_{72.75}Si_{10}B_{15}$ placed between two helical antennas. The distance between the antennas is 1.5 m, the antenna frequency is 1.2 GHz, and the ac bias field is 100 mHz

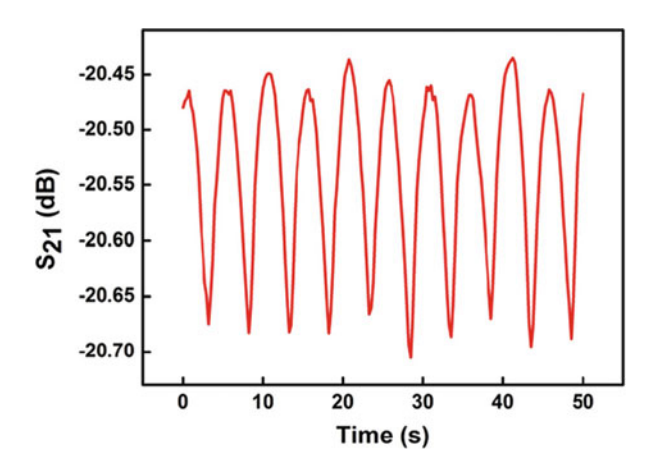
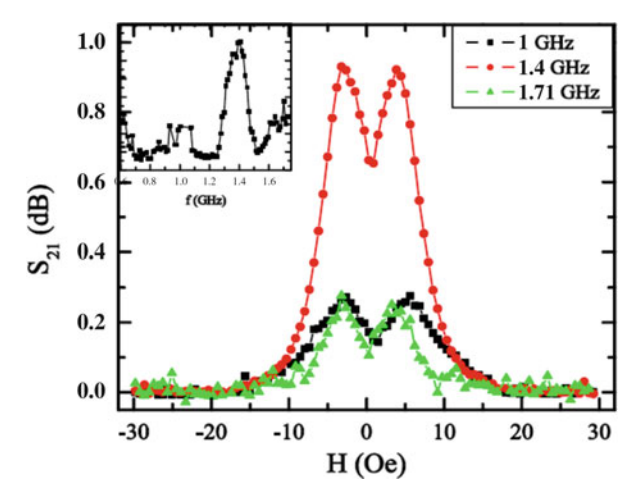


Fig. 6.10 Amplitude of the modulated S_{21} output as a function of a dc bias field. Insert shows the frequency spectra. The peak-to-peak value of the modulation field is 2.7 Oe. The signal increases with increasing the field reaching a maximum at 3 Oe which is about the anisotropy field found from inductive magnetization measurements



Helmholtz coils. The experiments were performed by applying a dc-magnetic field in addition to the above mentioned ac bias magnetic field also parallel to the axis of the microwire. Following this procedure, the field modulation driven around different magnetization states appears in the output signal as shown in Fig. 6.9. The frequency of the modulated signal is twice of that for ac bias fields. This doubled frequency is due to the symmetric shape of the impedance.

The amplitude of the modulation of the scattering coefficient as a function of the dc-applied field (sensed field) is given in Fig. 6.10. At large values of the dc field the modulated signal disappears since the wire impedance does not change if the field is higher than the anisotropy field. The insert shows the frequency spectrum of the modulated output at zero dc field for microwires of different length. The maximal response is obtained near antenna resonance frequency: 1.4 GHz for the 10 cm length and 1 GHz for the 15 cm microwire length. The distance between antennas is sufficiently large so the far field contribution due to dipole scattering dominates.

144 L.V. Panina et al.

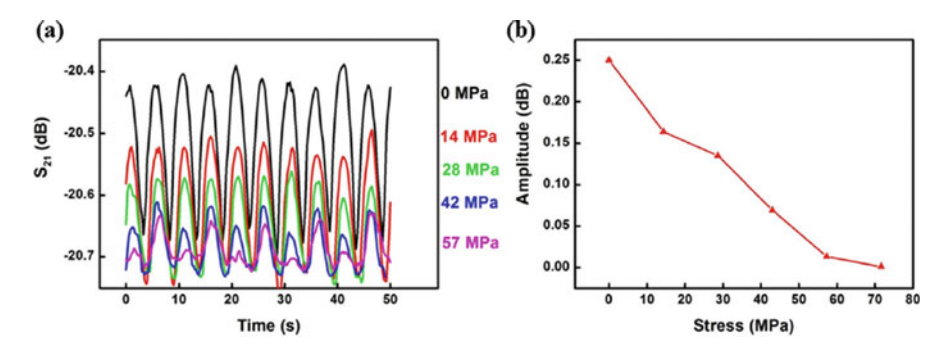


Fig. 6.11 Modulated scattered output from a single $Fe_{2.25}Co_{72.75}Si_{10}B_{15}$ amorphous microwire of 10 cm (metallic core radius is 33 µm and total radius is 50 µm) for different applied external stresses in (a). The amplitude of modulation as a function of the stress is shown in (b). The microwire was placed at 1.5 m from both antennas and orthogonal to the emission direction

The observed behavior suggests that the GHz scattering from magnetic wires can be used for wireless remote sensing which can be suitable for biological applications. The scattering from amorphous magnetic wires in which the magnetic structure is controlled by the magnetostrictive interactions will depend on the external stress. In this case the wire can be used as a remote embedded stress sensor, for example, for monitoring the stress state of human implants. The distance between the antennas is sufficient to place the human body between them. Figure 6.11 shows the modulated output as a function of the applied tensile stress. It can be noticed how the modulated pattern of S_{21} is modified under the application of the different mechanical stresses. In this case, the application of the stress alters the magnetostrictive contribution to anisotropy. Therefore, the amplitude of the modulation decreases since a larger field is needed to rotate the wire magnetization.

6.4 Tunable from Composites with Cut-Magnetic Wires

We now consider an artificial dielectric which consists of a matrix with a permittivity ε_d and embedded short pieces of ferromagnetic microwires with electric polarizability α . The wire length and the matrix permittivity should be chosen such that the antenna resonance in wires occurs in the frequency range of interest. If the wire concentration is very low so they do not interact the effective permittivity of the dielectric composite is

$$\varepsilon_{ef} = \varepsilon_d + 4\pi p\alpha \tag{6.24}$$

The modelling results with the external field as a parameter are shown in Fig. 6.12. It is seen that the permittivity of the wire medium has a strong frequency dispersion

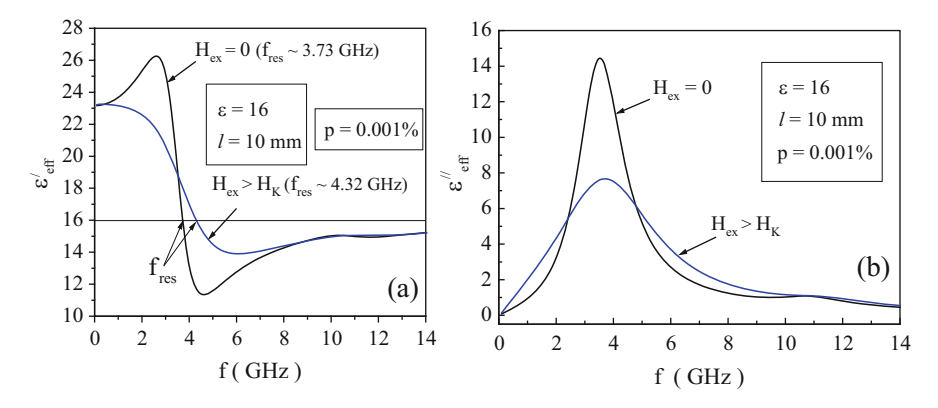


Fig. 6.12 Effective permittivity spectra vs. external field in composites containing short pieces of microwires embedded in a dielectric matrix with a permittivity of 16. Modelling is performed for wires with a circumferential anisotropy (anisotropy field $H_K = 500$ A/m). The other parameters are: resistivity—130 μΩ cm, magnetization—500 G, wire radius—20 μm, l = 1 cm, p = 0.001 %

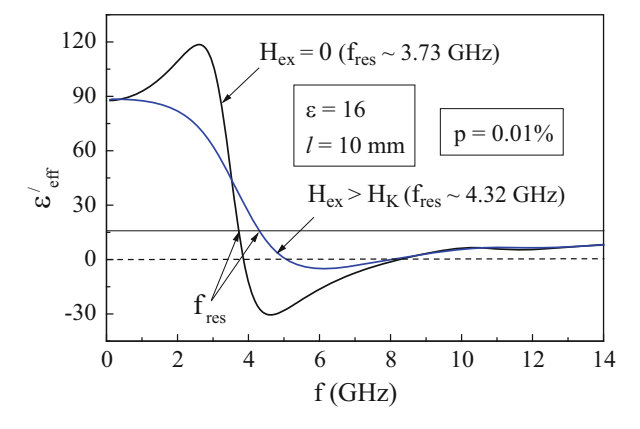


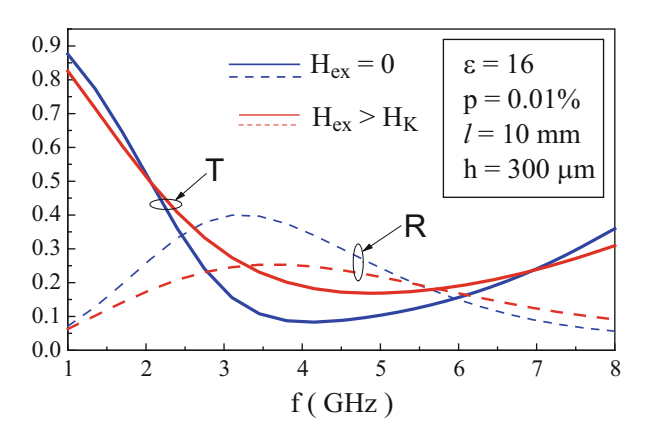
Fig. 6.13 Frequency dispersion of the real part of the effective permittivity in composites containing short pieces of microwires embedded in a dielectric matrix with a permittivity of 16 with higher volume concentration than in Fig. 6.12 (but the concentration is still very low so the wires do not interact with each other). The parameters are the same as for Fig. 6.12. The change in the permittivity in the presence of the external field $H_{ex} > H_K$ is also shown

near the first antenna resonance frequency. For wires with a circumferential anisotropy, if no field is applied the dispersion is of a well-pronounced resonance type which reflects the behavior of the wire dipole moments when the wire impedance is low (see Fig. 6.7, no field). In the presence of the external magnetic field which increases the wire impedance and losses in the system the dispersion region broadens and the permittivity behavior becomes even of a relaxation type.

If the concentration of wires is increased just to p = 0.01 %, it is possible to engineer artificial dielectrics which have negative values of the real part of the permittivity beyond the resonance as shown in Fig. 6.13. Such behavior could of

L.V. Panina et al.

Fig. 6.14 Modelled reflection and transmission parameters from thin sheets of magnetic wire composites



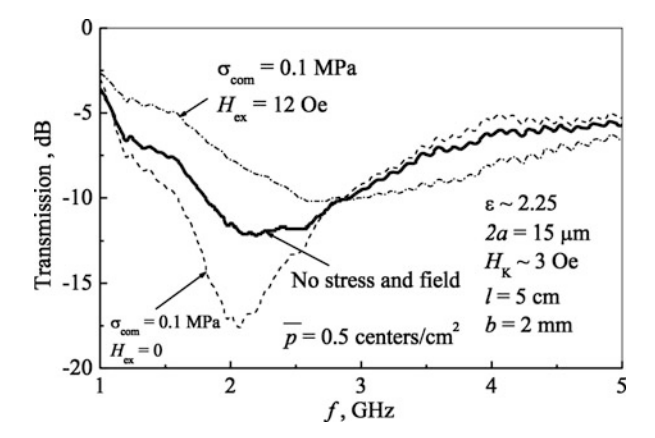


Fig. 6.15 Transmission spectra from a thin composite sheet with glass-coated microwires of composition $\text{Co}_{67.1}\text{Fe}_{3.8}\text{Ni}_{1.4}\text{Si}_{14.5}\text{B}_{11.5}\text{Mo}_{1.7}$ (total diameter of 21.4 μm and the metal core diameter of 15 μm). The matrix permittivity is 2.25, the wire length is 5 cm

interest for the creation of tuneable left-handed metamaterials which typically are considered with continuous wires [37–39]. In the case of composites with magnetic cut-wires with antenna resonances, it is possible to control the permittivity spectra in left-handed materials. The application of the magnetic field may even not allow the permittivity to have negative values which will strongly affect the propagation regime as shown in Fig. 6.13.

The microwave properties of wire composites can be investigated by free space techniques with the use of large samples (plane sheets of $50 \times 50 \text{ cm}^2$ for 1–10 GHz frequency range). The wire-composite sample is placed between the two antennas similar to the experimental arrangement shown in Fig. 6.8. The transmission spectra obtained from S_{21} parameter measurement are given in Figs. 6.14 and 6.15 [40]. The spectra are modified by using both the magnetic field and stress. The

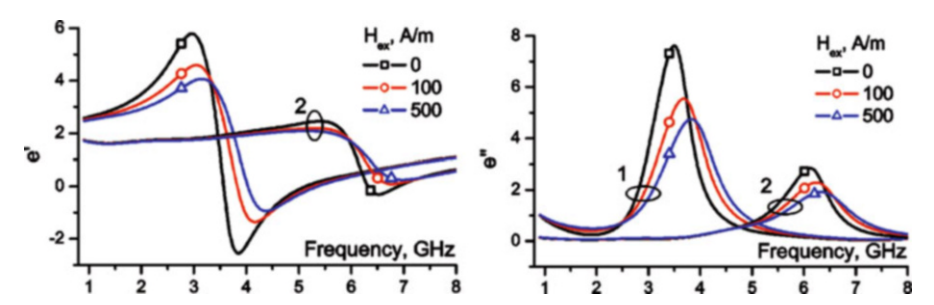


Fig. 6.16 Real and imaginary parts of ε_{ef} for cut wires composites of length 40 (1) and 20 (2) mm with the field H_{ex} as a parameter. Wires of the composition Co_{66} Fe_{3.5}B₁₆Si₁₁Cr_{3.5} with metal core radius of 20 μm coated with 10 μm glass sheath were glued in paper to form 50×50 cm² samples

wires are embedded in a silicon matrix with a high-elasticity module, which can be easily stretched with a small load (about 0.1 MPa) applied to the whole composite. This will produce sufficiently large stress acting on the wire via strain transfer. The tuning magnetic field can be generated with the help of a plane coil [40] having turns perpendicular to the electrical field in the incident wave. When a tensile stress is applied to the composite matrix this stress is transferred to the wire and the wire impedance decreases (see Fig. 6.6). The losses are reduced resulting in higher reflection and deep in the transmission spectra. Whilst the sample was under stress, a relatively large external field was applied to overcome the effect of the applied stress and saturate the magnetization along the axis, thus, realizing the condition of maximum impedance and increasing transmission. Using both the stress and the field the transmission parameter changes from -17 to -7 dB.

The effective permittivity spectra can be deduced from S-parameters with the help of special software (for example, Reflection/Transmission Epsilon Fast Model). Figure 6.16 shows the permittivity spectra for short-cut wire composites for different values of the external field. In agreement with the theory, the application of the field broadens the spectra since the wire impedance and losses increase. For composites with shorter wires this effect is much less pronounced, since the dispersion range shifts to higher frequencies where the wire permeability is nearly unity. Yet, adjusting the wire length and the matrix permittivity it could be possible to design the materials for multiparameter sensing using the wires with different magnetic properties which will respond at different frequencies.

For example, the wire dipole moment can be sensitive either to stress or to temperature. The magnetic structure and MI in microwires can be made highly temperature dependent in a practically important region of (50–200 °C) that gives a possibility to thermally control the microwave scattering from microwires. The high sensitivity to the temperature is observed in the vicinity of the compensation point where the magnetostriction changes its sign. Thus, in Fe $_{73}$ Cu $_1$ Nb $_3$ Si $_{16}$ B $_6$ nanocrystalline alloy the compensation point existing due to high volume fraction of bcc-FeSi is about 170 °C [41]. The magnetization of wires produced from such alloy will change from axial to circumferential direction when the temperature is increased beyond the compensation point resulting in decrease in the high frequency impedance.

L.V. Panina et al.

The other approach to realize temperature sensitive composites at ambient temperatures is based on the ferromagnetic-paramagnetic transition at Curie temperature T_c . This transition is characterized by the drastic change of properties such as magnetization, magnetic susceptibility, and anisotropy. It could be expected that MI ratio will also change near T_c , constituting basis for remote temperature detection through the microwave scattering. For majority of alloy systems, the Curie temperature of Fe- and Co-rich amorphous microwires is about 300–400 °C. Additions of Ni and Cr in the alloys make it possible to substantially decrease the Curie temperature [42, 43]. For example, the Curie temperature between 75 and 90 °C was reported for microwires with compositions $Co_{60.51}Fe_{3.99}Cr_{12.13}B_{13.53}Si_{9.84}$ and Co_{23.67}Fe_{7.14}Ni_{43.08}B_{13.85}Si_{12.26}. approaching T_c , the magnetization saturation M_s behaves as $(1 - T/T_c)^{\beta}$ and the magnetostriction which determines the anisotropy scales as M_s^3 . Then, the initial rotational permeability which is proportional to the ratio of the magnetization and anisotropy field will increase near T_c . The frequency dispersion of the permeability will shift towards lower frequencies. It means that the permeability values at high frequencies (parameter $\tilde{\mu}$ in Eq. (6.6a)) will decrease with temperature lowing the impedance and enhancing the scattering property.

6.5 Conclusion

We have discussed the potential of using magnetic microwires as wireless embedded sensors for magnetic field, stress, and temperature monitoring at microwave frequencies. The principle of operation is based on the antenna resonance in conducting wires, which is very sensitive to the wire static magnetic structure. The transfer function between the wire magnetic properties and microwave scattering is based on the magnetoimpedance (MI) effect. It is possible to use a single wire-sensor or a composite material with embedded wires. The technology of MI-wire structured composites is cost-effective and is suitable for large-scale applications. The magnetic wire composites may either provide information about the material's properties (stress, strain, temperature) or change the response in the desirable way. Such behavior is highly desirable for applications in NDT and control in civil engineering. The other large area of applications is related with their use as free space filters for secure wireless systems to obtain the desired band-pass or band-gap result.

References

- 1. Yang, S., Lozano, K., Lomeli, A., Foltz, H.D., Jones, R.: Composites Part A. 36, 691 (2005)
- Qin, F.X., Peng, H.X., Phan, M.H., Panina, L.V., Ipatov, M., Zhukov, A., Gonzalez, J.: Smart composites with short ferromagnetic microwires for microwave applications. IEEE Trans. Magn. 47, 4481–4484 (2011)

- 3. Vijayakumar, K., Wylie, S.R., Cullen, J.D., Wright, C.C., Ai-Shamma'a, A.I.: J. Phys.: Conf. Ser. **178**, 012033 (2009)
- Qin, F.X., Peng, H.X., Pankratov, N., Phan, M.H., Panina, L.V., Ipatov, M., Zhukova, V., Zhukov, A., Gonzalez, J.: Exceptional electromagnetic interference shielding properties of ferromagnetic microwires enabled polymer composites. J. Appl. Phys. 108, 044510 (2010)
- 5. Yuan, B., Yu, L., Sheng, L., An, K., Zhao, X.: J. Phys. D: Appl. Phys. 45, 235108 (2012)
- Chiriac, H., Pop, G., Ovari, T.-A., Barariu, F., Vazquez, M., Zhukov, A.P.: IEEE Trans. Magn. 33, 3346 (1997)
- Cobeno, F., Blanco, J.M., Zhukov, A.P., Gonzalez, J.: J. Magn. Magn. Mater. 249(1–2), 396 (2002)
- 8. Zhukov A.P., Blanco J.M., Gonzalez J., Garcia Prieto M.J., Pina E., Vazquez M.: J. Appl. Phys. 87, 1402 (2000)
- Larin, V.S., Torcunov, A.V., Zhukov, A.P., Gonzalez, J., Vazquez, M., Panina, L.V.: J. Magn. Magn. Mater. 249(1–2), 39 (2002)
- Zhukova, V., Chizhik, A., Zhukov, A., Torcunov, A., Larin, V., Gonzalez, J.: Optimization of giant magneto-impedance in Co-rich amorphous microwires. IEEE Trans. Magn. 38, 3090–3092 (2002)
- 11. Herrero-Gomez, C., Marin, P., Hernando, A.: Appl. Phys. Lett. 103, 142414 (2013)
- Kurlyandskaya, G.V., Sanchez, M.L., Hernando, B., Prida, V.M., Gorria, P., Tejedor, M.: Appl. Phys. Lett. 82, 3053 (2003)
- 13. Marın, P., Marcos, M., Hernando, A.: Appl. Phys. Lett. 96, 262512 (2010)
- 14. Makhnovskiy, D.P., Zamorovskii, V., Summerscales, J.: Composites Part A. 61, 216 (2014)
- 15. Kraus, L., Frait, Z., Pirota, K.R., Chiriac, H.: Giant magnetoimpedance in glass-covered amorphous microwires. J. Magn. Magn. Mater. **254-255**, 399–403 (2003)
- Mandal, K., Puerta, S., Vazquez, M., Hernando, A.: The frequency and stress dependence of giant magnetoimpedance in amorphous microwires. IEEE Trans. Magn. 36, 3257–3259 (2002)
- 17. Panina, L.V., Mohri, K.: Appl. Phys. Lett. **65**, 1189 (1994)
- 18. Lagarkov, A.N., Sarychev, A.K.: Phys. Rev. B. 53, 6318 (1996)
- Lagarkov, A.N., Matytsin, S.M., Rozanov, K.N., Sarychev, A.K.: J. Appl. Phys. 84, 3806 (1998)
- 20. Makhnovskiy, D.P., Panina, L.V., Mapps, D.J.: Phys. Rev. B. **63**, 144424 (2001)
- 21. Makhnovskiy, D.P., Panina, L.V., Mapps, D.J., Sarychev, A.K.: Phys. Rev. B. **64**, 134205 (2001)
- 22. Sarychev, A.K., Shalaev, V.M.: Phys. Rep. 335, 275–371 (2000)
- 23. Sarychev, A.K., McPhedran, R.C., Shalaev, V.M.: Phys. Rev. B. 62, 8531 (2000)
- Bohren, C.F., Huffman, D.R.: Absorption and Scattering of Light by Small Particles. Wiley, New York (1983)
- 25. van de Hulst, H.C.: Light Scattering by Small Particles. Dover, New York (1981)
- Serdyukov, A.N., Semchenko, I.V., Tretyakov, S.A., Sihvola, A.: Electromagnetics of Bi-anisotropic Materials: Theory and Applications. Gordon and Breach Science, Amsterdam (2001)
- 27. Tretyakov, S.A.: Analytical Modeling in Applied Electromagnetics. Artech House, Norwood (2003)
- 28. Herrero-Gomez, C., Aragon, A.M., Hernando-Rydings, M., Marın, P., Hernando, A.: Appl. Phys. Lett. 105, 092405 (2014)
- 29. Makhnovskiy, D.P., Panina, L.V.: J. Appl. Phys. 93, 4120 (2003)
- 30. Panina, L.V., Grigorenko, A.N., Makhnovskiy, D.P.: Phys. Rev. B. 66, 155411 (2002)
- 31. King, R., Smith, G.: Antennas in Matter. In: Fundamentals, Theory and Applications. The MIT Press, Cambridge (1981)
- 32. Landau, L.D., Lifshitz, E.M.: Electrodynamics of Continuous Media. Pergamon Press, New York (1975)
- 33. Ipatov, M., Zhukova, V., Zhukov, A., González, J., Zvezdin, A.: Low-field hysteresis in the magnetoimpedance of amorphous microwires. Phys. Rev. B. 81, 134421–134428 (2010)

- 34. Lofland, S.E., Baghat, S.M., Garcia-Beneytez, J.M., et al.: Low field microwave magnetoimpedance in amorphous microwires, J. Appl. Phys. **85**, 4442 (1999)
- Popov, V., Zhukova, V., Ipatov, M., García, C., Gonzalez, J., Ponomarenko, V., Berzhansky, V., Vinogorodsky, D., Zhukov, A.: Studies of giant magnetoimpedance effect of Co-rich microwires in wide frequency range. Phys. Status Solidi A. 206, 671–673 (2009)
- Sandacci, S., Makhnovskiy, D.P., Panina, L.V., Larin, V.: Valve-like behavior of the magnetoimpedance in the GHz range. J. Magn. Magn. Mater. 272/276, 1855–1857 (2004)
- 37. Pendry, J.B., Holden, A.J., Robbins, D.J., Stewart, W.J.: Low frequency plasmons in thin-wire structures. J. Phys.: Condens. Matter. 10, 4785–4809 (1998)
- 38. Reynet, O., Adent, A.-L., Deprot, S., Acher, O., Latrach, M.: Effect of the magnetic properties of the inclusions on the high-frequency dielectric response of diluted composites. Phys. Rev. B. **66**, 94412–94421 (2002)
- Smith, D.R., Padilla, W.J., Vier, D.C., Nemat-Nasser, S.C., Schultz, S.: Composite medium with simultaneously negative permeability and permittivity. Phys. Rev. B. 84, 4184–4187 (2000)
- Makhnovskiy, D.P., Panina, L.V., Garcia, C., Zhukov, A., Gonzalez, J.: Experimental demonstration of tunable scattering spectra at microwave frequencies in composite media containing CoFeCrSiB glass-coated amorphous ferromagnetic wires and comparison with theory. Phys. Rev B. 74, 064205-064215 (2006)
- 41. Hong Duong, V., Sato Turtelli, R., Grossinger, R., Hiebl, K., Rogl, P.: IEEE Trans. Magn. 32, 4821 (1996)
- 42. Trémolet de Lacheisserie, E., Gignous, D., Schlenker, M.: Magnetism: Materials and Applications, vol. 2. Springer, New York (2005)
- Zhukova V., Blanco J.M., Ipatov M., Zhukov A., Garcia C., Gonzalez J., Varga R., Torcunov A. (2007) Sens. Actuators, B: 318 318

Chapter 7 Soft Ferromagnetic Microwires with Excellent Inductive Heating Properties for Clinical Hyperthermia Applications

Rupin Singh, Javier Alonso, Jagannath Devkota, and Manh-Huong Phan

7.1 Introduction

7.1.1 Overview

Although the spread of cancer continues to decline, down twenty-two percent in the USA over the past two decades [1], it is still the leading cause of death worldwide, accounting for 8.2 million deaths in 2012 alone [2]. Therefore, there is a pressing need to improve and develop cancer treatments to continue to improve survival rates and patient well-being. The unregulated growth of cells associated with cancer normally causes a low pH and hypoxia to occur in the tumors and surrounding tissue [3]. These are not ideal conditions for radiation therapy or cytotoxic drugs as their delivery is severely hindered to a much lower concentration. Additional treatment cannot be done without doing harm to the patient as well, such as inducing high levels of radiation to patients. Magnetic hyperthermia is one alternative avenue researchers are investigating to improve cancer treatments success rates and reduce patient discomfort.

The use of magnetic nanoparticles in medicine is rapidly growing due to their variability in size, shape, coating, and ability to perform noninvasive procedures. They can be used as a means to monitor chemical and biological systems as magnetic sensors, to perform deep tissue penetration for drug delivery, magnetic cell separation and purification, magnetic resonance imaging contrast enhancement,

R. Singh • J. Devkota • M.-H. Phan (🖂)

Department of Physics, University of South Florida, Tampa, FL 33620, USA e-mail: rupin@mail.usf.edu; jagan.devkota@gmail.com; phanm@usf.edu

I Alonso

Department of Physics, University of South Florida, Tampa, FL 33620, USA

BCMaterials Edificio No. 500, Parque Tecnológico de Vizcaya, Derio 48160, Spain e-mail: jalonsomasa@gmail.com

[©] Springer International Publishing AG 2017
A. Zhukov (ed.), *High Performance Soft Magnetic Materials*, Springer Series in Materials Science 252, DOI 10.1007/978-3-319-49707-5_7

purification, bioassay, gene transfer, and hyperthermia of cancerous tissue [4–6]. For magnetic hyperthermia, however, magnetic nanoparticles present some limitations. It has been reported that if the nanoparticles are injected intravenously they tend to be covered with proteins (opsonized), thus encouraging their phagocytosis. The nanoparticles can also be recognized as "foreign bodies" and eliminated by the reticuloendothelial system [7]. To avoid the action of the immune system, there is an increasing need for controlling their size, surface functionality, aggregation, and size distribution. It has also been reported that once the treatment is finished, the nanoparticles tend to accumulate in the liver and spleen, with possibly unwanted toxic effects [8]. Therefore, alternative materials have recently been proposed. In particular, the use of ferromagnetic implants or needles for magnetic hyperthermia, which was recognized a few decades ago as a promising approach [9], has brought renewed interest in the scientific community [10].

Soft ferromagnetic glass-coated microwires (GCMWs) of 5–150 µm diameter have emerged as one of the most promising soft magnetic materials, owing to their outstanding magnetic properties (e.g., magnetic bistability, giant magneto-impedance (GMI) effect, fast domain wall propagation, and Hopkinson effect) for a wide variety of applications in magnetic sensors, microelectronics, security, and biomedical engineering [10–14]. The continuous microwires up to few kilometers can easily be fabricated from 1 gram of master alloy [11]. The extremely large saturation magnetization and shape anisotropy coupled with their strong responses to AC magnetic fields suggest that the GCMWs can be a promising candidate for use in magnetic hyperthermia. The glass coating itself provides electrical insulation and also improves biocompatibility [14].

In this study, we aim to explore radio frequency field responses of magnetically soft Co-rich glass-coated microwires for clinical hyperthermia applications while investigating the effect of multiple variables of interest including metal composition, core diameter, glass-coating diameter, orientation, and multiple microwire interactions.

7.1.2 Magnetic Hyperthermia

Magnetic hyperthermia mediated by magnetic structures is based on raising the temperature of a localized tumor area in order to impede or kill malignant cells within the body. Normally performed synergistically with more common treatments such as radiotherapy and chemotherapy [3, 6, 15], hyperthermia is usually carried out at defined local hyperthermic levels, i.e., temperatures around 42–45 °C. In this temperature range, hyperthermia does not induce cell death, only disrupts cellular metabolism, and impedes cancer proliferation. On the other hand, thermoablation relies on the use of hyperthermia in order to induce rapid cell death at temperatures above 50 °C. At this point, vital proteins of the cancer cell become damaged and the cell membrane partially dissolves into the aqueous solution surrounding it [15]. This technique has a high risk of severe or persistent side-effects and can potentially lead to dire consequences depending on the size of

the target region. Thermoablation may be feasible for some cancer morphologies but as long as one can assure side-effects are reduced to reasonable levels.

The basic magnetic hyperthermia involves injecting a ferrofluid, i.e., a stable colloidal dispersion of iron magnetic particles in an aqueous media, or inserting wires into the cancerous body [3, 6]. The cancerous location in the body is remotely targeted from active or passive external magnetic field gradients and then subsequently an external alternating magnetic field (usually between a few kHz to 1 MHz) is applied to the localized site in order to heat cancer cells. Contemporary research demonstrates an ability to increase specificity and reliability of magnetic structures for hyperthermia by altering delivery methods, synthesis methods, optimization of their coating, optimization of their size to heat delivered ratio, and attempts to reduce the indirect heating of healthy tissue [16].

The use of fine magnetic particles for magnetic hyperthermia has not only been known for decades but also has been an active field of research for over 50 years [10]. Early research by Dr. Gilchrist was first done in 1965 to kill lymph node metastases [17]. It was an attempt to treat colon cancer by applying an alternating magnetic field of 55 kHz to the ferrite nanoparticles of size 100–500 nm. Gilchrist demonstrated that by applying an external AC field, the nanoparticles gave rise to heat losses proportional to the frequency of the field [17]. The targeted tissue is mainly heated by two physical phenomena: eddy currents and magnetic hysteresis [3, 6]. The eddy currents, the primary heat source in typical bulk magnetic structures, oppose the applied magnetic field and by the Joule effect, produce heating [18]. In ferromagnetic materials, such as magnetic particles, the heating is mainly due to magnetic hysteresis losses originated by the lag between the magnetic moments of the particles and the oscillating magnetic field [19]. The advantages of using modern hyperthermia systems are huge and all are important to the patient's safety and well-being.

In addition to the use of fine magnetic particles, ferromagnetic implants, i.e., needles or micro/nanowires, have been developed for enhanced hyperthermia. It has recently been reported that the magnetic needles show even higher heating efficiency rates, as compared to iron oxide nanoparticles [20]. Therefore, it is more important than ever to be able to control the spatial distribution of heat to be both very strong and homogenous. Additionally, ferromagnetic microwires have demonstrated the ability to be self-regulated because of their tailored Curie temperatures [21]. Some materials proposed outside microwires include Fe-based amorphous ribbons, biocompatible Mg-Fe-based ceramics, and nickel-zinc nanoparticles [21].

7.1.3 Soft Ferromagnetic Glass-Coated Microwires

Glass-coated microwires are a composite material that consists of a metallic nucleus and a glass coating. The metallic nucleus ranges from 100 nm to 50 μ m in diameter while the glass-coated thickness ranges from 2 to 20 μ m [12]. As a result

of their amorphous structure, glass-coated microwires are characterized by low magnetic anisotropy. Their magnetic properties are mainly dictated by magnetoelastic and shape anisotropy. Overall, amorphous microwires possess large shape anisotropy, magnetoelastic anisotropy, and ultra-soft magnetic properties such as a high permeability, large saturation magnetization (M_s), and low magnetic field anisotropy (H_s). They have a characteristic core/shell structure that dictates their magnetic properties [11–13].

Soft ferromagnetic amorphous glass-coated microwires are particularly interesting because thus far their research has been limited to other applications such as GMI and microwave sensing [13, 22, 23]. Their applications in hyperthermia could open a new avenue for biocompatible hyperthermic treatments without the need for carefully crafted magnetic nanoparticles and nanowires. Their commercial availability and cheap/efficient preparation increase the access institutions to have for the treatment which can ultimately lower the cost of care for both the health care provider and the patient. During the production of these amorphous glass-coated microwires, a combination of axial and tensile radial stresses affects their magnetic properties [12, 13]. This is usually dependent on the metallic composition of the alloy causing them to be divided into three groups: positive magnetostrictive, negative magnetostrictive, and low magnetostrictive.

Positive magnetostrictive wires are Fe-rich alloys, negative magnetostrictive wires are Co-rich (mainly CoSiB-based microwires), and low magnetostrictive wires are usually CoFeSiB-based microwires with 3–5 % Fe-based. The domain structures for each of these are shown in Fig. 7.1. It can be seen that amorphous magnetic microwires form a core-shell type of domain structure but in different patterns and orientations depending on their magnetostriction. The positive magnetostrictive microwires have longitudinal core domains oriented along the wire axis while the shell forms radial domains (Fig. 7.1a). Due to this domain structure,

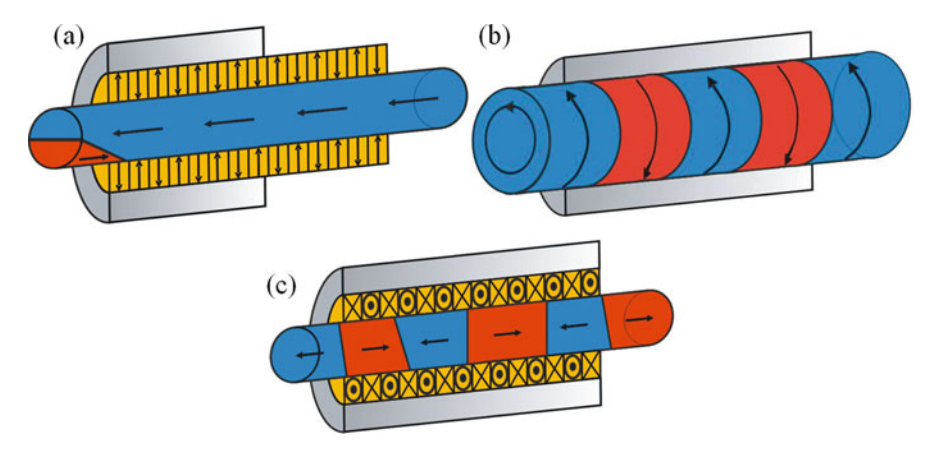


Fig. 7.1 Schematic domain structures of glass-coated microwires with (a) positive magnetostriction, (b) negative magnetostriction, and (c) low magnetostriction. Reprinted with permission from [24]

the magnetization process propagates along the entire microwire in a single Barkhausen jump, forming a rectangular-shaped magnetic hysteresis loop. Due to this, they are easy to detect and are commonly used in the construction of small sensors. Negative magnetostrictive alloys form circular domains perpendicular to the domain axis (Fig. 7.1b). Therefore, magnetization in the axial direction along the microwire causes rotations of magnetic moments inside the domains so their magnetization is proportional to the applied magnetic field.

The hysteresis loops of negative magnetostrictive microwires are small due to the perpendicular alignment of the magnetic moments in an external magnetic field. The low magnetostrictive alloys have less defined domain structures, as visible in Fig. 7.1c, but still show circular domains below the surface of the nucleus and an axial domain in the center of the wire [13]. These nearly zero magnetostrictive microwires demonstrate normal-shaped hysteresis loops due to the balance between the magnetoelastic and magnetostatic energies.

To exhibit an excellent hyperthermic effect, microwires should have extremely soft magnetic properties, large but well-defined anisotropy, and negative magnetostriction [10, 14]. Considering this, we have selected the two following materials for our study, CoMnSiB and CoFeSiBCrNi, both of them exhibiting negative magnetostriction. Once an external magnetic field is applied, the effects of orientation to the magnetic field and interactions between different microwires have been tested to see if the domain structures have a positive or negative effect on the field's effectiveness. In addition, we have also investigated how the thickness of the glass coating and the core diameter affect the hyperthermia efficiency of these microwires. Finally, the effect of having multiple microwires interacting among each other has been analyzed.

7.2 Experimental

7.2.1 Fabrication and Characterization

The Co-rich amorphous glass-coated microwires used in this experiment were fabricated by the Taylor-Ulitovsky technique, a more advanced form of the normal Taylor-wire spinning synthesis [25]. The glass-coated microwires come in two different alloy compositions which we will describe using their manufacturer labels, 1675 and 1597. Both are soft magnetic amorphous Co-rich microwires with complex magnetic characteristics. The composition of each microwire is outlined in Tables 7.1 and 7.2. The tables show that alloy number 1675 is $Co_{68}B_{15}Si_{10}Mn_7$ and alloy number 1597 is $Co_{64.61}B_{16}Si_{11}Fe_{4.97}Cr_{3.4}Ni_{0.02}$.

These microwires have high curie temperatures and crystallization temperatures, making them ideal for hyperthermia because of their ability to maintain their magnetization properties at high temperatures. For example, the Curie temperature of 1597 is 250 °C and the crystallization temperature is 520 °C. The density of each

R. Singh et al.

Table 7.1 Composition of alloy number 1675

Metal	Mass (%)	Atomic (%)
Со	82.90	68.00
В	3.40	15.00
Si	5.80	10.00
Mn	7.90	7.00

Table 7.2 Composition of alloy number 1597

Metal	Mass (%)	Atomic (%)	
Fe	5.85	4.97	
Co	80.26	64.61	
В	3.62	16.00	
Si	6.48	11.00	
Cr	3.76	3.40	
Ni	0.02	0.02	

of these microwire alloys was estimated based on their mass percent. The estimation is normally only useful for crystalline alloys rather than amorphous ones but provides good estimation of the true density without physically removing the glass coating and measuring the densities in the lab. The formula used to estimate the density is shown below:

$$\frac{1}{D_f} = \sum_{1}^{n} \frac{x_n}{D_n} \tag{7.1}$$

where D_f is the final density of the allow, n is the number of metals that make up the allow, x is the mass fraction of that metal in the alloy, and D is the density of the pure metal. The estimated density of alloy 1675 is 6.98 g/cm³ and the estimated density of alloy 1597 is 6.84 g/cm³.

In addition to using two different alloys, wires of different core diameters and glass thicknesses were used to determine how each affects the inductive heating efficiency. As a side-effect of the synthesis technique, the microwires do not have the same diameter across the entire length of the wire. The average diameter, however, has been calculated and is used as the measuring point. Each thickness was given a number label that corresponds to its alloy. #1–4 correspond to alloy number 1675, while #5–12 correspond to alloy number 1597. The average diameters of the total, core, and glass coating for each microwire tested are summarized in Table 7.3.

To further characterize the structural characteristics of these microwires, we employed a combination of X-ray diffractometry (XRD) and scanning electron microscopy (SEM). For XRD, a Bruker AXS D8 diffractometer with Cu K_{α} 1.5418 A was used in a $\theta\!-\!2\theta$ mode in order to get information about crystal phases of the Co-rich microwires. The XRD data gave us information about how amorphous the microwires used in this experiment truly are. On the other hand, a JEOL JSM-6390LV SEM was used to image the surface morphology of the Co-rich

Alloy and label	Total thickness (µm)	Core thickness (µm)	Glass thickness (µm)
1675-1	28.8	22.8	6.0
1675-2	20.2	12.9	7.3
1675-3	21.7	15.6	6.1
1675-4	32.5	25.3	7.2
1597-7	26.9	16.9	10.0
1597-8	18.2	12.7	5.5
1597-10	23.4	16.5	6.9
1597-11	22.7	16.7	6.0
1597-12	19.8	14.2	5.6

Table 7.3 Average thicknesses of the microwires

microwires. SEM was only used to image a single microwire as a representative sample to describe the general structure of these microwires including both their glass coating and their inner amorphous metal core.

Finally, the magnetic characterization of the microwires presented in this experiment was performed in a physical property measurement system (PPMS) from Quantum Design with an installed vibrating sample magnetometer probe. The system can measure properties in a temperature range of 2–350 K and induce magnetic fields up to ± 7 T.

7.2.2 Magnetic Hyperthermia

In order to perform the hyperthermia experiments, the Co-rich microwires were cut into 5 mm strands. Multiple different configurations of microwire alloy, diameter, orientation, quantity, and separation were examined. The single microwire examinations were done for alloys number 1675 1–4 and 1597 7, 8, 10, 11, and 12. Alloys number 1675 1–4 were studied for their general differences in microwire diameter as both the core diameter and the glass thickness varied between the four samples. The samples from alloy number 1597 were carefully selected to investigate the effects of core diameter while the glass thickness was held constant and the effects of the glass thickness while the core diameter was held constant. Alloys number 1597 7, 10, and 11 demonstrated the former effect while 1597-8 and 1597-12 demonstrated the latter effect. Additionally, the sample that demonstrated the best heating was used for additional experiments including orientation, i.e., horizontal versus vertical, and the effects of using multiple microwires.

The single microwire samples were prepared by inserting a single microwire of 5 mm in length into a glass vial filled with 1 mL of deionized water. To test for orientation, the single microwire was placed into a 2 % agar solution that would maintain the orientation of the microwire even under high magnetic fields. The orientation was imposed by the use of a small external permanent magnet and physically aligning it in solution before the agar cooled completely. Tests on

R. Singh et al.



Fig. 7.2 Magnetic hyperthermia system employed. Generator on the *left* and radio frequency amplifier on the *right*

multiple microwires were done both in water and in agar. The tests in water would demonstrate natural microwire orientation in movement in a random distribution. On the other hand, the tests in agar were specifically done in different distributions or orientations, i.e., in situations where the wires are together, separated, and horizontal. The microwires in the multiple microwire experiments were also 5 mm in length.

In this experiment, we have used an Ambrell Easyheat system that can generate an alternating magnetic field at a frequency between 150 and 400 kHz. Figure 7.2 shows an image of the water refrigerated multi-turn helical coil connected to a radio frequency power amplifier. Power to the system is provided by a generator. During the hyperthermia experiments, for each sample, the temperature evolution with time has been monitored while applying an external AC field, between 400 and 800 Oe, at a constant frequency of 310 kHz. The temperature was monitored by using a fiber optic temperature probe which automatically recorded the data to the PC.

The heating efficiency, also known as the specific absorption rate (SAR), of the microwires has been estimated following calorimetric methods: the initial slope $\Delta T/\Delta t$ of the sample has been obtained from the measured heating curves, and the SAR values have been derived from the following formula:

$$SAR = C_p \cdot \frac{\Delta T}{\Delta t} \phi \tag{7.2}$$

where φ corresponds with the concentration of magnetic material, C_p is the heat capacity of water, and $\Delta T/\Delta t$ is the initial slope. To remove the heating contribution coming from the coil, we have subtracted the slope measured for the vial without sample from all our measurements. The initial slope was taken shortly after heating began, i.e., when the temperature increase was nearly linear.

Due to the small mass of these microwires (10^{-5} g) , the final concentration value φ (0.01 mg/mL) is much smaller than those typically reported in the case of magnetic nanoparticles (0.5–5 mg/mL). This is a considerable error source for the calculation of the SAR, and therefore, in those cases in which we are only working with one microwire, we have normalized the measurements to the maximum SAR value and just focused on the evolution of SAR as a function of the analyzed parameter (glass thickness, core diameter, wire alignment, etc.).

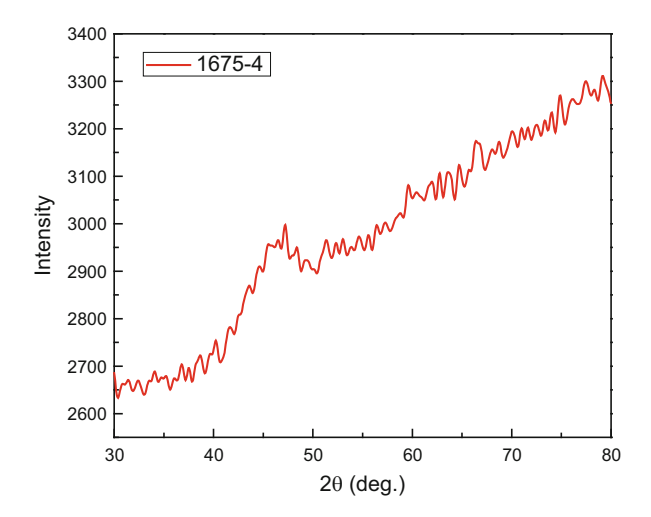
7.3 Results and Discussion

This section consists of the results of the structural characterization methods of XRD and SEM, magnetic properties of all the microwires, and their effectiveness as hyperthermia agents. The tests include discussions of the effects of different variables including metallic core diameter, glass-coating thickness, microwire number, separation, and orientation.

7.3.1 Structural Analysis

Figure 7.3 shows the XRD pattern for a 5 mm long single microwire sample of alloy number 1675-4. It can be observed that the XRD pattern exhibits only one broad peak around $2\theta = 45^{\circ}$, which is often known as a diffuse halo, indicating that the microwires prepared are amorphous in nature. It has been reported that the amorphous magnetic microwires are more desirable for many applications due to their good mechanical properties as compared to their crystalline counterparts [13]. In our study, the microwires used are Co-based, so their particular magnetic domains are reserved if the wires are amorphous rather than crystalline.

Fig. 7.3 XRD pattern of a glass-coated amorphous microwire 1675-4, i.e., $Co_{68}B_{15}Si_{10}Mn_7$ from 20° to 80°



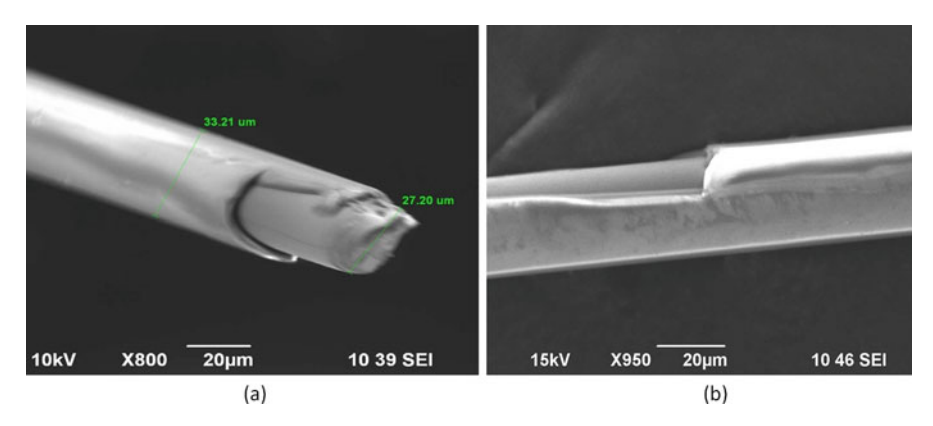


Fig. 7.4 SEM images of a glass-coated amorphous microwire 1675-4, i.e., $Co_{68}B_{15}Si_{10}Mn_7$ for two different segments (**a**, **b**)

7.3.2 Surface Morphology

Figure 7.4a, b shows the SEM images of a soft ferromagnetic amorphous glass-coated microwire for two different segments.

The SEM images taken of 1675-4 are representative of all the glass-coated microwires used in this experiment. The average diameter of the metallic core and the average thickness of the glass layer can be determined from these images. It can be seen that the entire length of the microwire has a slightly variable diameter. While the surface of the glass-coating layer is not very smooth, the surface of the metallic core is rather smooth. Therefore, we can expect these microwires to exhibit good magnetic properties. Since the magnetic property of a microwire depends sensitively on both the metallic core and the glass thickness, it is essential to investigate the effects of varying core diameter and glass thickness on the magnetic softness of the microwires studied in this work.

7.3.3 Magnetic Properties

The room temperature magnetic hysteresis M(H) loops were collected for all the microwires. The wires were then split into comparison views for the tests performed, i.e., the effects of differences in thickness of either the core as shown in Fig. 7.5a or the glass coating as shown in Fig. 7.5b. It is generally observed that all microwires have negligible coercivity (H_c) and large saturation magnetization (M_s) indicative of their soft ferromagnetic characteristics. Upon closer inspection of the wires of comparative value, differences do begin to emerge about their M_s . As one can see clearly in Fig. 7.5a, 1675-4 has the largest M_s (~100 emu/g) and 1675-2 has the smallest M_s (~75 emu/g) among the four samples compared.

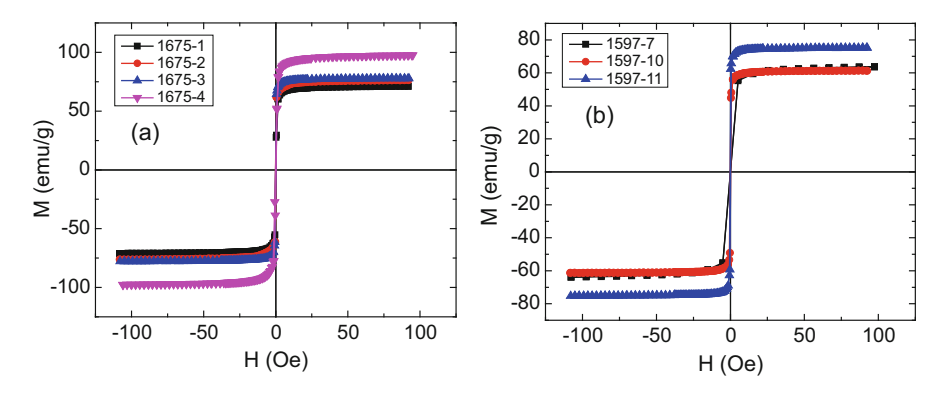


Fig. 7.5 Room temperature magnetic hysteresis M(H) loops of the glass-coated amorphous microwires $Co_{68}B_{15}Si_{10}Mn_7$ and $Co_{64.61}B_{16}Si_{11}Fe_{4.97}Cr_{3.4}Ni_{0.02}$. (a) Hysteresis loops of only 1675-1, 2, 3, and 4 that vary by core diameter. (b) Hysteresis loops of only 1597-7, 10, and 11 that vary only by glass thickness

This is attributed to the increased magnetic volume of the wire as the metallic core is increased while keeping the same glass thickness. The largest value of M_s suggests in principle a better heating efficiency for the wire 1675-4, since the SAR is proportional to the M_s [3, 6].

Figure 7.5b shows the M(H) loops for the wires used in the comparison of the effect of glass thickness. Once again, there is a clear outlier for M_s as the wire 1579-11 is ~75 emu/g while neither 1579-7 nor 1579-10 is ~65 emu/g. This clearly demonstrates that for wires having the same diameter of the metallic core, the M_s is larger when the glass thickness is smaller. In the literature, this effect has been attributed to internal stresses arising from the difference in the thermal expansion coefficients of metallic nucleus and glass coating [26]. Since the heating efficiency is proportional to the M_s , one can expect significant effects of the metal core diameter and glass thickness on magnetic hyperthermia response.

7.3.4 Inductive Heating Properties

Next, we have analyzed the inductive heating properties of these microwires for magnetic hyperthermia applications. In Fig. 7.6a we have plotted the heating curves for one microwire, sample 1675-4, in 1 mL of water (0.01 mg/mL) measured at different fields, and as can be observed, the heating rate appreciably increases with increasing field. We note that the relatively low temperature values reached in all these measurements (<32 °C after 5 min), in comparison with those typically obtained in hyperthermia measurements with magnetic nanoparticles, can be explained considering the small mass of the individual microwires. Therefore, by increasing their mass or their number, the heating rate could in principle be increased to reach the desirable temperature window for therapeutic cancer treatment.

R. Singh et al.

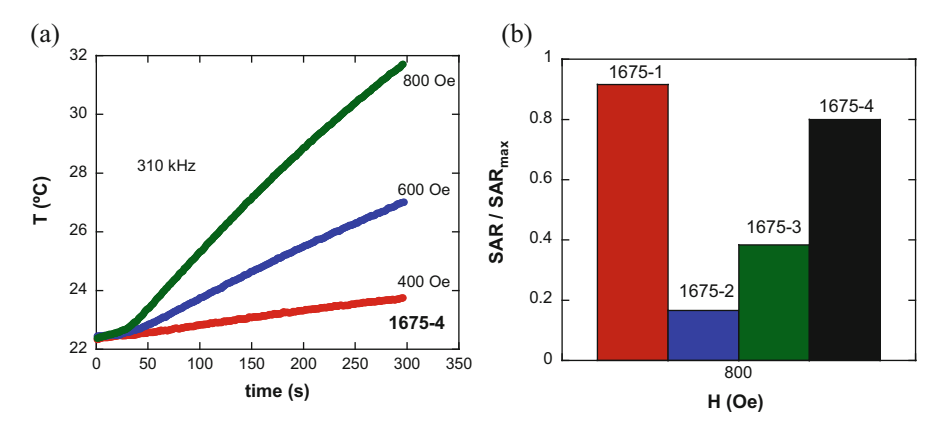


Fig. 7.6 (a) Temperature curves as a function of time at different AC fields (400–800 Oe) for sample 1675-4; (b) Normalized SAR values for 800 Oe for four samples of the same alloy (1675) with almost the same glass thickness and varying metal core diameters

Concerning the mechanism behind the heating of the microwires, as mentioned before, it could be related either to eddy current or hysteresis loss, although in principle it has been reported that in the case of soft ferromagnetic glass-coated microwires, the eddy current damping is often negligible due to the amorphous nature of the microwire presenting high electrical resistivity [12, 24].

In this study, we have analyzed the overall effects of changes in microwire dimensions using four samples of the same alloy: 1675-1, 1675-2, 1675-3, and 1675-4. All the microwires are coated with glass, which acts as an insulating barrier and enhances the biocompatibility of these materials. In Fig. 7.6b we have represented the SAR values for the four microwires that have almost the same glass thickness and varying metal core diameters. It can be observed that the SAR values of the samples 1675-1 and 1675-4 (22.8 and 25.3 μm core) are considerably larger compared to the samples 1675-2 and 1675-3 (12.9 and 15.6 μm core). In connection with the magnetization data, it is concluded that the 1675 wires with larger metal cores exhibit larger M_s and hence larger SAR. A similar trend has been observed for the samples 1597-8 and 1597-12, with the same composition and the same glass thickness (~5.5 μm), but different core diameters, 12.7 and 14.2 μm , respectively.

After this evaluation of the heating responses of the microwires, we have studied how the heating efficiency, SAR, evolves depending on the core diameter, glass thickness, and relative orientation for different applied fields (Fig. 7.7).

As observed in Fig. 7.7a, at 600 Oe, the thicker sample presents a better heating efficiency, but at higher fields, 800 Oe, the SAR values are similar, suggesting that at sufficiently high fields, the effect of the core diameter is less important than that at lower fields. Therefore, we have analyzed the effect of the glass thickness on the heating efficiency of these microwires.

In Fig. 7.7b, we have represented the SAR values for two samples, 1597-7 and 1597-10, with the same composition, the same diameter (\sim 16.7 μ m), but different

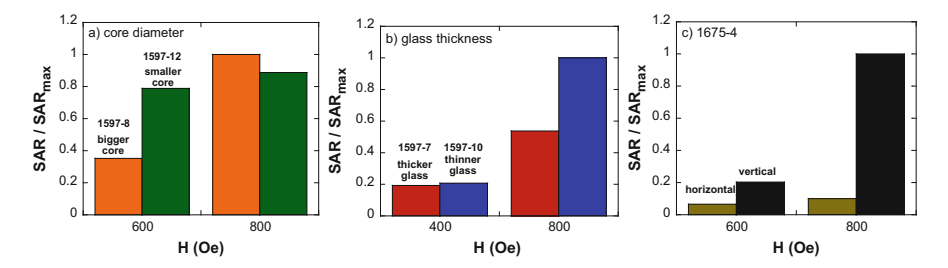


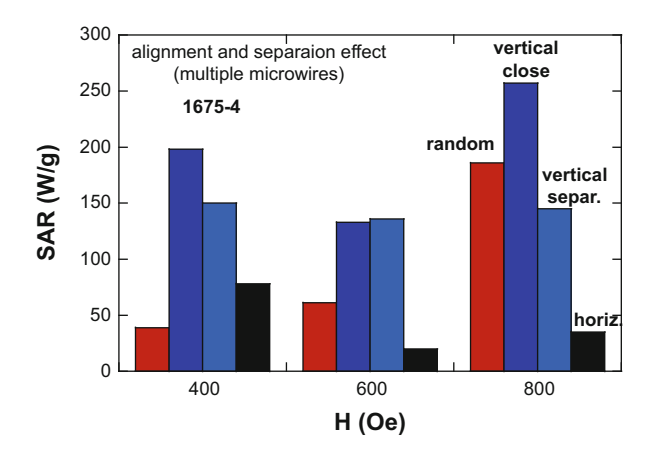
Fig. 7.7 Normalized SAR values at different fields (600 and 800 Oe) for samples with (a) the different core diameters and the same glass thickness, (b) the different glass thicknesses and the same core diameter, and (c) different orientations of the microwire with respect to the applied field

glass thicknesses, 10 and 7 µm, respectively. As can be seen in this figure, with increasing glass thickness and increasing field the SAR values tend to decrease, indicating that the glass coating partially hinders the external heat transmission from the internal metallic core. Therefore, from the point of view of hyperthermia applications, the glass coating must be kept as thin as possible to enhance the heating efficiency of the microwires. Next, we have analyzed how the alignment of the wires affects the SAR values for the sample 1675-4. In order to carry out this study, we aligned the wires in agar, both in vertical (parallel to the AC field) and horizontal (perpendicular to the AC field) directions. The agar allows us to fix the direction of the wire and make sure that the orientation does not change during the hyperthermia experiments. As observed in Fig. 7.7c, the heating efficiency is maximal when the wires are aligned in the direction of the field, and it greatly diminishes in the perpendicular direction. This is attributed to the strong shape anisotropy along the axis of the microwires. Based on this effect, we can propose a new method for controlling the heating and manipulating the inductive heating efficiency of the microwire by simply rotating the microwire by an angle ($\alpha < 90^{\circ}$) with respect to the direction of the AC applied field, while keeping a constant AC field. Instead of rotating the microwire, rotating an inductive coil about its axis to vary the direction of the AC field appears to be more efficient for practical use. Future research should thus be performed to fully exploit this novel approach.

Finally, we have measured the heating efficiency for multiple microwires (five). As we noted above, the mass of the individual microwires is too small to produce enough heating to reach the therapeutic window. Therefore, one strategy to overcome this problem is using multiple microwires for the hyperthermia treatment instead of a single microwire. In this study, we have compared how the SAR changes as a function of the orientation (vertical and horizontal) and as a function of the relative separation between the microwires. In this case, the absolute values of SAR have been given since by increasing the number of wires, the previously commented error in the SAR determination appreciably diminishes. As can be seen in Fig. 7.8, the results indicate that the heating efficiency of the microwires randomly oriented in water is lower than that of the microwires aligned in the

R. Singh et al.

Fig. 7.8 SAR values for the 1675-4 samples containing five microwires in different alignments and separations



field direction, due to the effect of the shape anisotropy. It can also be observed that the heating efficiency is higher for the microwires being in direct contact than for the microwires being well separated. These results suggest that the closer the microwires, the stronger the dipolar interactions (the induced magnetostatic anisotropy), thus giving rise to an enhanced heating efficiency. The obtained SAR values are relatively high if we compare them with those typically reported for magnetic nanoparticles [27].

7.4 Concluding Remarks and Future Scope

Throughout this chapter, we have systematically demonstrated the potential of soft ferromagnetic glass-coated microwires for clinical hyperthermia applications. In particular, we have demonstrated appreciable heating rates for microwires when bundled together. We have also demonstrated the conditions that permit glass-coated microwires to perform most efficiently based on size, thickness, orientation, and distribution to develop new glass-coated microwires that balance the best aspects from each of these studies. The important results from our study are summarized below.

We have investigated the use of glass-coated microwires as an alternative to magnetic nanoparticles. With their magnetic bistability, enhanced magnetic softness, GMI effect, fast domain wall propagation, and Hopkinson effect, glass-coated microwires are a very promising alternative that does not require difficult and expensive synthesis techniques, and avoid possible biocompatibility issues and toxic effects due to accumulation in body organs. Magnetization measurements demonstrated negligible coercivity ($H_c \sim 0.2$ Oe) and high magnetization saturation ($M_s \sim 100$ emu/g) of the microwires. Additionally, we have demonstrated that single microwires show an increasing trend in heating efficiency with increased applied fields for both $Co_{64.61}B_{16}Si_{11}Fe_{4.97}Cr_{3.4}Ni_{0.02}$ and $Co_{68}B_{15}Si_{10}Mn_7$. Due to

the small mass of these glass-coated microwires, however, their SAR values are only comparable to nanoparticles when measuring multiple wires at a time.

We have studied the effects of varying levels of glass coating, varying from 6 to $10~\mu m$ in diameter, on hyperthermia efficiency of $Co_{64.61}B_{16}Si_{11}Fe_{4.97}Cr_{3.4}Ni_{0.02}$ microwires. As expected, increasing the external magnetic field from 400 to 800 Oe, the microwire with the thicker glass coat led to a decrease in SAR. 1597-7's higher SAR value demonstrates a more efficient release of heat than 1597-10. This provides some evidence that the glass coating does hinder the heat transfer between the metallic core and the surrounding environment. For biomedical applications, however, the glass-coat is important to retain the wires biocompatible. Further investigation must be done to determine the critical thickness that the glass-coat must be in order to maintain biocompatibility but still allow for efficient heat transfer. It is another controllable variable to continue to improve clinical hyperthermia optimization.

Further optimization can be accomplished by controlling the diameter of the metallic core. We have studied the influence of varying the metallic core diameter while retaining the same glass thickness in Co_{64.61}B₁₆Si₁₁Fe_{4.97}Cr_{3.4}Ni_{0.02} microwires. As predicted, alloy number 1597-12, with its thicker metallic core, demonstrated higher SAR values at lower magnetic fields and approximately equal SAR values at higher magnetic fields. This indicates that a thicker microwire may be possible to implement at lower magnetic fields to achieve the same effect if higher magnetic fields are unavailable or are hazardous to the patient. Once again, however, a balance must be achieved because extremely thick microwires may result in rejection by the body, increase the difficulty in injecting the wires, or limit microwire movement to the target location.

We have also investigated the effects of orientation of the microwires, perpendicular and parallel, to the AC field for both a single microwire and for a group of five microwires. Systematically, we have shown that the vertical orientation produces far better SAR values at all magnetic fields. This is the expected result based on the microwire's domain structure. With alternating circular domains perpendicular to the domain axis, these negative magnetostrictive alloys would perform best when the applied field was not interfering with the natural domain alignment. By acting in the axis of orientation, the external magnetic field is not impeded by the internal structure. We have also determined that the closer the microwires, the greater the heating efficiency.

Having given a broad but limited study on the heating effects of amorphous soft ferromagnetic microwires, our study opens up innovative directions for further research into the hyperthermia applications of this class of microwire. Some examples are given below:

 Our study provided insight into the difficulties in studying heat loss of single and small microwires. Therefore, future studies could limit their analysis to testing the same variables using single microwires with large magnetic cores (>50 μm) or multiple microwires where the effects of error are decreased significantly. Those studies also can expand the use of multiple microwires from five to ten or more.

- 2. Proper studies on matching the real-life scenarios of clinical hyperthermia should be done with glass-coated microwires. In these tests, the microwires should be tested to investigate the time it takes to reach the clinical hyperthermia temperature range, how well the temperature can be maintained, and the distribution of heat between the target location and the surrounding environment/tissue. Different alloys, different glass thicknesses, and different numbers of microwires could be tested.
- 3. While the Co-rich microwires were studied in this study, Fe-based microwires with appropriate compositions and dimensions could also be a competitive candidate for clinical hyperthermia applications. Suitable annealing of these Fe-based microwires could potentially improve their magnetic softness and hence inductive heating responses. Further research should thus be performed to exploit this class of microwires fully.

Acknowledgements The research was supported by the College of Arts and Science—University of South Florida Research Grant (Magnetic and hyperthermia measurements). Javier Alonso acknowledges the financial support provided through a postdoctoral fellowship from Basque Government. We thank Professors Hariharan Srikanth and Pritish Mukherjee of the University of South Florida for their useful comments and discussions. Microfir TehnologiiIndustriale (www.microwires.com) is acknowledged for providing the soft ferromagnetic glass-coated microwires for this study.

References

- 1. Alteri, R., Bertaut, T., Brooks, D., et al.: Cancer Facts & Figures 2015. American Cancer Society, Atlanta (2015)
- 2. Stewart, B., Wild, C.P.: World Cancer Report 2014. World Health Organization, Lyon (2014)
- 3. Ortega, D., Pankhurst, Q.A.: Magnetic hyperthermia. Nanoscience. 1, 60 (2013)
- Chertok, B., Moffat, B.A., David, A.E., et al.: Iron oxide nanoparticles as a drug delivery vehicle for MRI monitored magnetic targeting of brain tumors. Biomaterials. 29, 487 (2008)
- 5. Colombo, M., Carregal-Romero, S., Casula, M.F., et al.: Biological applications of magnetic nanoparticles. Chem. Soc. Rev. **41**, 4306 (2012)
- Périgo, E.A., Hemery, G., Sandre, O., et al.: Fundamentals and advances in magnetic hyperthermia. Appl. Phys. Rev. 2, 041302 (2015)
- 7. Pankhurst, Q.A., Connolly, J., Jones, S.K., et al.: Applications of magnetic nanoparticles in biomedicine. J. Phys. D. Appl. Phys. **36**, R167 (2003)
- 8. Skyes, E.A., Dai, Q., Tsoi, K.M., et al.: Nanoparticle exposure in animals can be visualized in the skin and analyzed via skin biopsy. Nat. Commun. **5**, 3796 (2013)
- 9. Stauffer, P.R., Cetas, T.C., Flectcher, A.M., et al.: Observations on the use of ferromagnetic implants for inducing hyperthermia. IEEE Trans. Biomed. Eng. 31, 76 (1984)
- Zuchini, R., Tsai, H.W., Chen, C.Y., et al.: Electromagnetic thermotherapy using fine needles for hepatoma treatment. Eur. J. Surg. Oncol. 37, 604 (2011)
- 11. Vázquez, M.: Soft magnetic wires. Physica B. 299, 302 (2001)
- 12. Zhukov, A., Zhukova, V.: Magnetic Properties and Applications of Ferromagnetic Microwires with Amorphous and Nanocrystalline Structure. Hauppauge, New York (2009)
- 13. Phan, M.H., Peng, H.X.: Giant magnetoimpedance materials: fundamentals and applications. Prog. Mater. Sci. **53**, 323 (2008)

- Hudak, R., Varga, R., Hudak, J., et al.: Influence of fixation on magnetic properties of glasscoated magnetic microwires for biomedical applications. IEEE Trans. Magn. 51, 5200104 (2015)
- Banobre-Lopez, M., Teijeiro, M., Rivas, J.: Magnetic nanoparticle-based hyperthermia for cancer treatment. Rep. Prac. Oncol. Radiother. 18, 397 (2013)
- Jordan, A., Wust, P., Fahling, H., et al.: Inductive heating of ferrimagnetic particles and magnetic fluids—physical evaluation of their potential for hyperthermia. Int. J. Hyperth. 9, 51 (1993)
- 17. Gilchrist, R.K., Shorey, W.D., Hanselman, R.C., et al.: Effects of electromagnetic heating on internal viscera: a preliminary to the treatment of human tumors. Ann. Surg. 161, 890 (1965)
- 18. Lucia, O.: Induction heating and its applications: past developments, current technology, and future challenges. IEEE Trans. Ind. Electron. 61, 2509 (2014)
- Figuerola, A., Di Corato, R., Manna, L., et al.: From iron oxide nanoparticles towards advanced iron-based inorganic materials designed for biomedical applications. Pharmacol. Res. 62, 126 (2010)
- Gómez-Polo, C., Larumbe, S., Pérez-Landazabal, J.I., et al.: Magnetic induction heating of FeCr nanocrystalline alloys. J. Magn. Magn. Mater. 324, 1897 (2012)
- Gómez-Polo, C., Larumbe, S., Pérez-Landazabal, J.I., et al.: Analysis of heating effects (magnetic hyperthermia) in FeCrSiBCuNb amorphous and nanocrystalline wires. J. Appl. Phys. 111, 07A314 (2012)
- Qin, F.X., Peng, H.X.: Ferromagnetic microwires enabled multifunctional composite materials. Prog. Mater. Sci. 58, 183 (2013)
- 23. Colosimo, P., Chen, A., Devkota, J., Srikanth, H., Phan, M.H., et al.: Sensing RF and microwave energy with fiber Bragg grating heating via soft ferromagnetic glass-coated microwires. Sens. Actuators A. 210, 25 (2014)
- Varga, R.: Magnetization processes in glass-coated microwires with positive magnetostriction.
 Acta Phys. Slov. 62, 411 (2012)
- 25. Ulitovsky, A.V.: Micro-technology in design of electric devices. Leningrad. 7, 6 (1951)
- Chizhik, A., Zhukova, V.: Magneto-optical and magnetic studies of Co-rich glass-covered microwires. Phys. Res. Int. 2012, 690793 (2012)
- Kolhatkar, A.G., Jamison, A.C., Litvinov, D., et al.: Tuning the magnetic properties of nanoparticles. Int. J. Mol. Sci. 14, 15977 (2013)

Chapter 8 Magnetically Bistable Microwires: Properties and Applications for Magnetic Field, Temperature, and Stress Sensing

Rastislav Varga, Peter Klein, Rudolf Sabol, Kornel Richter, Radovan Hudak, Irenej Polaček, Dušan Praslicka, Miroslav Šmelko, Jozef Hudak, Ivan Mikita, Giovanni Andrea Badini-Confalonieri, Rhimou El Kammouni, and Manuel Vazquez

8.1 Introduction

Amorphous glass-coated microwires with positive magnetostriction are composite materials which consist of metallic nucleus and glass-coating (see Fig. 8.1a) and they are ideal materials for applications in various sensors (magnetic field, temperature, stress, position, etc.) [1–4]. They are prepared by the modified Taylor–Ulitovsky technique by simultaneously drawing and quenching of molten master alloy [5]. Domain structure is governed by two dominant anisotropies: (1) magnetoelastic and (2) shape anisotropy. As a result of magnetoelastic

R. Varga () • P. Klein • R. Sabol

Faculty of Science, Institute of Physics, UPJS, Park Angelinum 9, 041 54 Košice, Slovakia

RVmagnetics s.r.o., Hodkovce 21, 04421 Kosice, Slovakia

e-mail: rastislav.varga@upjs.sk; peter.klein@upjs.sk; rudolf.sabol@upjs.sk

K. Richter

Faculty of Science, Institute of Physics, UPJS, Park Angelinum 9, 041 54 Košice, Slovakia e-mail: kornel.richter@upjs.sk

R. Hudak • I. Polaček

Department of Biomedical Engineering and Measurement, Faculty of Mechanical Engineering, Technical University of Košice, Košice 042 00, Slovakia e-mail: radovan.hudak@tuke.sk; irenej.polacek@tuke.sk

D. Praslicka • M. Šmelko • J. Hudak • I. Mikita

Department of Aviation Technical Studies, Faculty of Aeronautics, Technical University of Košice, Košice 040 01, Slovakia

e-mail: dusan.praslicka@tuke.sk; miroslav.smelko@tuke.sk; jozef.hudak@tuke.sk; ivan. mikita@tuke.sk

G.A. Badini-Confalonieri • R. El Kammouni • M. Vazquez

Instituto de Ciencia de Materiales de Madrid, CSIC, Cantoblanco, Sor Juana

Inés de la Cruz 3, Madrid 28049, Spain

e-mail: giovanni.badini@rub.de; elkammounirhimou@gmail.com; mvazquez@icmm.csic.es

[©] Springer International Publishing AG 2017

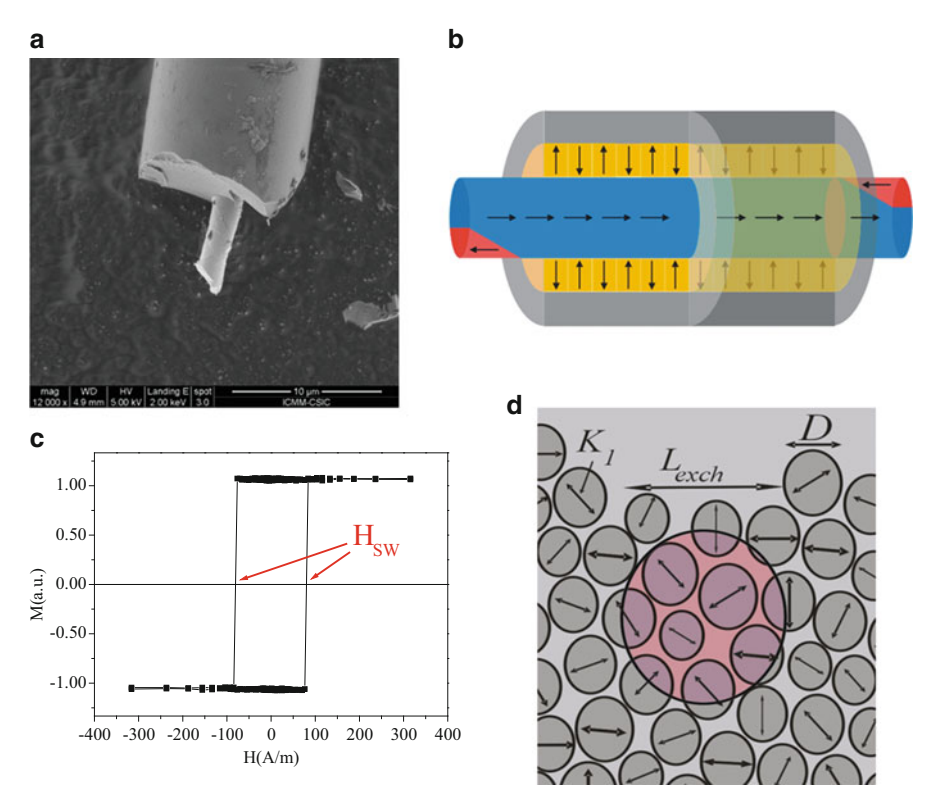


Fig. 8.1 (a) SEM picture of glass-coated microwire, (b) Schematic domain structure of amorphous or nanocrystalline microwire with positive magnetostriction, (c) Rectangular hysteresis loop of bistable microwire, (d) Schematic picture of the nanocrystalline grains embedded in the residual amorphous matrix

anisotropy, the domain structure of microwires with positive magnetostriction consists of a single axial monodomain in the center of the metal core, which is surrounded by radial domain structure. Due to the shape anisotropy, small closure domains appear at both ends of the microwire in order to decrease the stray fields (Fig. 8.1b). Such a peculiar domain structure is reflected in magnetic bistability (see rectangular hysteresis loop in Fig. 8.1c). The magnetization in axial monodomain has only two states: $+M_S$ or $-M_S$. Switching between these two states is driven by the domain wall propagation at the field called switching field H_{sw} , which is sensitive to many external parameters, such as stress, temperature, magnetic field, and so on [6–9]. Naturally, idea to employ microwires for microsensors of temperature, stress, and so on arises.

However, amorphous microwires are unstable, their main disadvantage is change of magnetic properties with time (aging) and temperature. One possible solution is to use nanocrystalline materials [10]. Nanocrystalline microwires are prepared by controlled annealing from the amorphous precursors, and they consist

of small randomly oriented nanocrystalline grains embedded in the residual amorphous matrix (see Fig. 8.1d) [11]. Magnetocrystalline anisotropy in nanocrystalline material is averaged out if distance between crystalline grains is smaller than ferromagnetic exchange length L_{ex} [6]. Thus, dominant anisotropy is magnetoelastic one. Microwires with nanocrystalline microstructure exhibit excellent temperature stability of the switching field and domain wall dynamics [12, 13].

8.2 Theoretical Background of the Switching Field

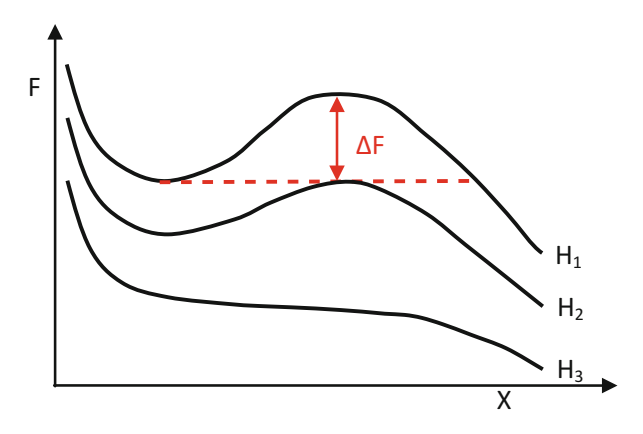
8.2.1 Switching Field of Closure Domain Wall

The magnetization process of magnetically bistable amorphous microwires runs by a single giant Barkhausen jump between two stable remanent states (Fig. 8.2). Therefore, the depinning of a domain wall from the closure structure at one end is responsible for the coercivity mechanism. The switching field of closure domain wall in microwire is given by the shape of the domain wall potential. Without the action of the external magnetic field, the position x of the pinned 180° domain wall is given by its potential W(x) minimum which in amorphous materials is mainly determined by magnetoelastic interaction of magnetic moments with local stresses induced during production process. Under the action of the applied magnetic field H the total free energy F(x) of the domain wall is given by [14]:

$$F(x) = W(x) - 2\mu_0 M_S H S_{dw} x, \tag{8.1}$$

where μ_0 is permeability of vacuum, M_S is saturation magnetization, and S_{dw} is the area of domain wall (which is assumed to be constant in this case). If the applied magnetic field H is lower than the switching field H_{sw} , the equilibrium position of the domain wall is given by the local minimum of its total free energy F (see Fig. 8.2). The energy barrier ΔF exists, which does not allow the domain

Fig. 8.2 Dependence of the free energy F of closure domain wall on its position x at different external magnetic field $H_1 < H_2 < H_3$



172 R. Varga et al.

wall to jump into a more favorable position. When the external field H reaches the value of the switching field H_{sw} , the domain wall depinns from its original position and starts to propagate along entire length of the microwire.

In equilibrium, the domain wall occupies the position that is given by a minimum of free energy F:

$$\frac{\partial F}{\partial x}|_{H} = 0. ag{8.2}$$

Hence, the switching field will be given by a maximum of the first derivation of the domain wall potential W(x):

$$H_{sw} = \frac{1}{2\mu_0 M_s S_{dw}} \frac{\partial W}{\partial x}|_{\text{max}}.$$
 (8.3)

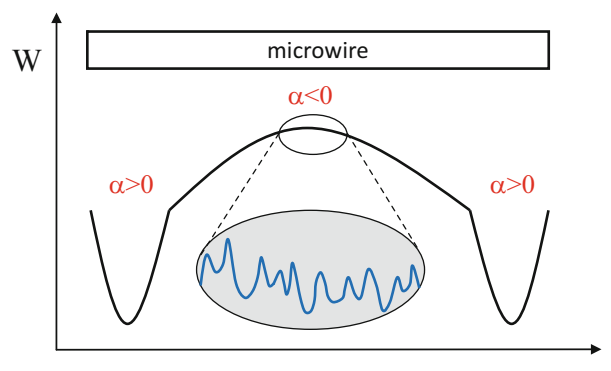
Because μ_0 , M_S , and S_{dw} are constants for given material, the main parameter which affects switching field will be maximal value of derivation of its potential. From Eq. (8.3) is apparent that switching field is not given by depth of the potential of the domain wall but it is given by its gradient.

If we suppose parabolic shape of the domain wall potential $(W(x) = 1/2\alpha_d x^2)$, Eq. (8.3) is simplified to the following form:

$$H_{sw} = \frac{\alpha_d x_{cr}}{2\mu_0 M_S S_{dw}},\tag{8.4}$$

where α_d is restoring force acting on the domain wall in potential well (for clarify, restoring force on the domain wall becomes positive values at both ends in contrary to the middle part of the microwire, see Fig. 8.3) and x_{cr} is critical deflection of the domain wall. When domain wall reaches position at x_{cr} then it overcomes energetic barriers and leaves the local minimum at the end.

Fig. 8.3 Schematic picture of domain wall potential *W* in amorphous or nanocrystalline microwire



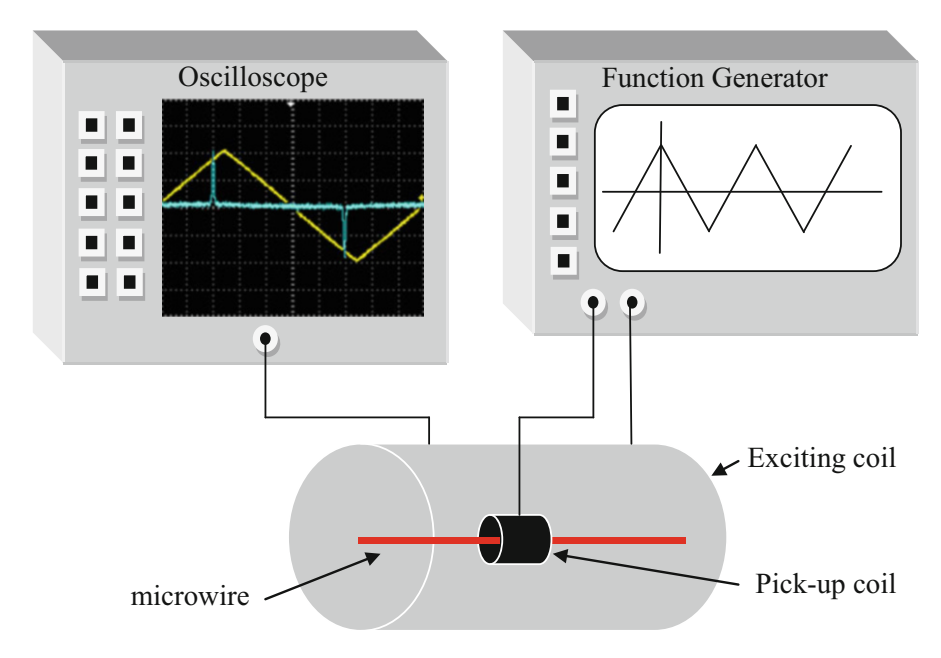


Fig. 8.4 Schematic picture of apparatus for measuring the switching field by induction method

8.2.2 Experimental Method

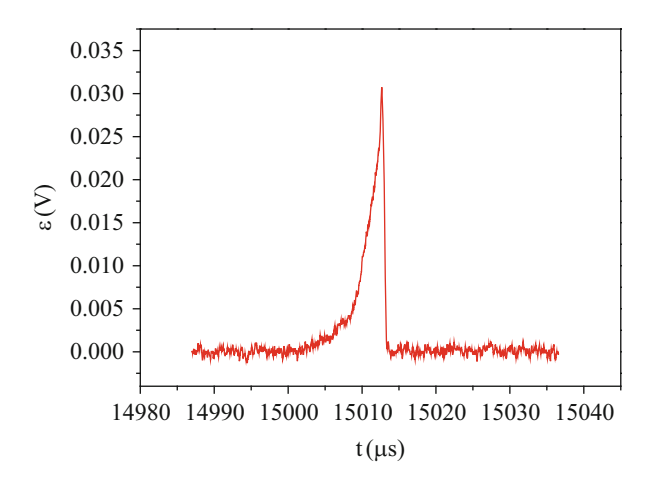
The advantage of magnetization process in bistable microwire (single Barkhausen jump) is that one can use a simple induction method to measure the switching field (Fig. 8.4) [15, 16]. Primary coil is fed by triangular shape signal in order to produce linearly increasing magnetic field. When the external field exceeds the switching field, domain wall propagates along the wire (placed coaxially in the primary and pick-up coil) and *emf* maximum is induced in the pick-up coil. Switching field can be easily estimated from the position of maximum. Whole system can be placed into the cryostat and the switching field can be measured in a wide temperature range from 80 K up to 450 K.

Such a method can be successfully employed also in practical applications. However, the induced signal must be high enough to be distinguished from the noise. The induced signal voltage U_i in the pick-up coil obeys a Faraday's law:

$$U_i = -\frac{\partial \Phi}{\partial t} \tag{8.5}$$

where $\delta\Phi$ is the variation of the magnetic flux within the time interval δt . In case of microwires, the variation of magnetic flux is low due to their small volume. However, the magnetization process is very fast and so δt is extremely short. As a result, the *emf* maximum induced in the pick-up coil is well distinguishable from the background noise (see Fig. 8.5).

Fig. 8.5 Voltage peak induced by the propagating domain wall



Fast magnetization process is a result of extremely fast domain wall that was observed in microwires [17, 18]. Its velocity reaches up to 20 km/s [17], which makes it sometimes faster than a sound speed in microwires and supersonic boom can be observed [19]. Such fast velocity has three reasons: (1) low magnetic anisotropy of amorphous microwires (due to a lack of magnetocrystalline anisotropy); (2) existence of two perpendicular anisotropies (with respect to each other)—axial one from drawing the wire and radial one from quenching the wire during production [5], and (3) existence of radial domain structure as demonstrated in Fig.8.1b, that shields the domain wall from the pinning at the surface roughness. Playing with these parameters, one can increase the domain wall velocity even in the wire with relatively slow domain wall. For example, it is possible to obtain the domain wall velocity up to 9 km/s by application of perpendicular magnetic field. Such velocity is moreover independent from the applied magnetic field [20]. Moreover, the enhancement of the domain wall velocity can be obtained by properly selected parameters of thermal treatment under applied magnetic field or electrical current.

8.2.3 Contributions to the Switching Mechanism

Knowledge of temperature dependence of the switching field can be used very simply for construction of temperature sensor. Therefore it is very important to know switching field mechanism. Temperature dependence of the switching field was already studied by many authors [21–23]. As was shown before, temperature dependence of the switching field can be explained using two pinning mechanisms of closure domain wall. First mechanism is magnetoelastic interaction of magnetic moments with mechanical stresses induced during production process together with additional stresses from glass-coating and especially stresses arising from different

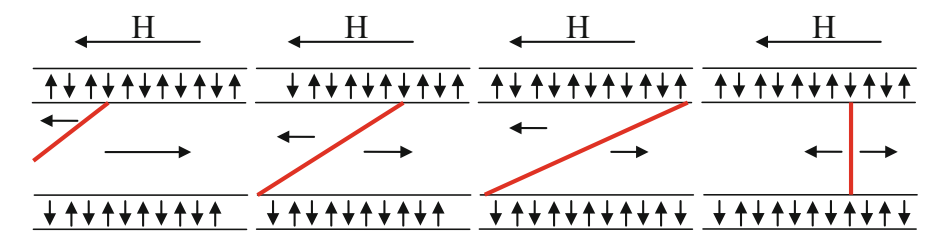


Fig. 8.6 Schematic picture of closure domain structure at the end of the microwire in external applied magnetic field. Closure domain wall just before its depinning and propagation from left side to the right side

thermal expansion coefficients of metallic nucleus and glass-coating. Energy of the domain wall can be expressed in the form:

$$E_{DS} = \pi \sqrt{A \cdot K} \tag{8.6}$$

where K is anisotropy energy density within the wall and A is exchange energy constant.

Potential energy of ferromagnetic body in external magnetic field H can be expressed in the form:

$$E_{\rm POT} = -\mu_0 M_{\rm S} H \cos \varphi \tag{8.7}$$

where φ is the angle between magnetization in axial monodomain M_S and applied external magnetic field H (see Fig. 8.6).

Firstly, energy of external applied magnetic field H is consumed to increase the volume of already existing closure domain wall at the end of the microwire. After domain wall is formed from complicated closure domain structure. Equations (8.6) and (8.7) can be given into equality at moment before closure domain wall depinn and propagates in the direction of external applied magnetic field:

$$E_{DS} = E_{POT}$$

$$\pi \sqrt{A \cdot K} = \mu_0 M_S H$$

We know that magnetoelastic anisotropy K is equal to $3/2\lambda_S\sigma$. After simple rearrangement it is possible to express value of the switching field, which should be proportional to the square root of the applied tension stresses in full accordance to the nucleation propagation model [24–26]:

$$H_{sw} \propto \frac{\sqrt{\lambda_S \sigma}}{\mu_0 M_S}$$
 (8.8)

where σ being stresses. In our case σ is equal to $\sigma = \sigma_g(T) + \sigma_r$, where σ_r are residual intrinsic stresses coming from production process of simultaneously of quenching and drawing, and $\sigma_g(T)$ are the stresses which presently depend on the temperature and arise from the different thermal expansion coefficients of the glass-coating and metallic nucleus. These stresses can be expressed as:

$$\sigma_{g}(T) \approx E(\alpha_{g} - \alpha_{m})\Delta T,$$
 (8.9)

where E is the Young modulus of the glass, α_g and α_m are thermal expansion coefficients of glass and metallic core, respectively.

As early found in previous works [27], the temperature dependence of the magnetostriction of amorphous alloys can be described by the so-called scaling law:

$$\lambda_S = cM_S^k \tag{8.10}$$

Here, c is a constant and the power exponent k depends on the mechanism of magnetostriction and is expected to take value of 3 for Fe-based amorphous alloys, when the magnetostriction originates from a single-ion anisotropy of uniaxial character and 2 for Co-based amorphous alloys where the magnetostriction originates from an anisotropic two-ion exchange contribution of uniaxial symmetry [28]. Thus, Eq. (8.8) can be simplified into the form:

$$H_{sw}^{\sigma} \propto p M_S^{3/2}(T) (1 + r(\Delta T))^{1/2}.$$
 (8.11)

where p is a constant proportional to residual stress σ_r and r is proportional to the difference between the thermal expansion coefficient of metallic nucleus and glass-coating $(r \sim E_{gl}(\alpha_g - \alpha_m)/\sigma_r)$.

As was early showed strong increase of the switching field at low temperatures cannot be explained only by temperature dependence of the magnetoelastic contribution to the switching field and therefore another mechanism must be responsible in soft magnetic amorphous alloys. Second biggest contribution to the coercivity mechanism that arises from structural relaxation (also called magnetic after-effect or directional ordering) leads to the stabilization of the domain structure. It is worth to note that amorphous structure is very metastable (contains a lot of free volumes and mobile defects). In such amorphous structure mobile defect (or atoms) can relax (or change its position) in order to decrease of overall interaction energy (see Fig. 8.7a).

Interaction energy of the mobile atom pairs is given by the following equation:

$$\varepsilon = \varepsilon_0 \cos^2 \varphi, \tag{8.12}$$

where ε_0 is an interaction energy constant, and φ is angle between local spontaneous magnetization and the axis of mobile atom pair. Two orientations of the atom

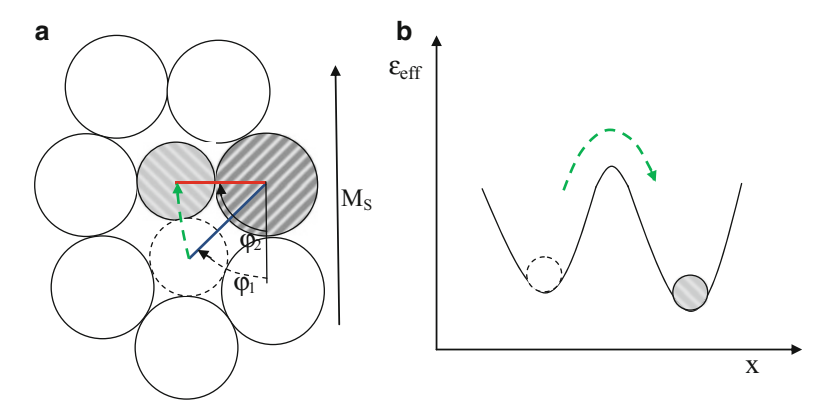


Fig. 8.7 (a) Schematic picture of structural relaxation of mobile defect in amorphous structure, (b) Schematic picture of two level energetic model

pair are separated by an energetic barrier (activation energy Q) that could be overcome by thermal activation or by tunneling process. Such transition can be demonstrated by a two level energetic model (see Fig. 8.7b). In Fig. 8.7a atom changed his position from former (*dotted circle*) into new and more stable one (*gray circle*). Moreover, interaction energy in more stable position is much lower because interaction energy becomes minimal value in the case when angle between local spontaneous magnetization and axis of mobile atom pair is 90° . Structural relaxation can be reversible or irreversible.

Atom pair reorientation is characterized by relaxation time, which is given by Arrhenius law:

$$\tau_r = \tau_0 e^{Q/kT},\tag{8.13}$$

where τ_0 is pre-exponential factor, Q is activation energy of mobile defects.

By very simple calculations using Arrhenius law in amorphous material based on iron it is possible to show that annealing at $300\,^{\circ}\text{C}$ for 1 h leads to the same structural changes which normally take more than one million years at room temperature.

Structural relaxation is manifested by induced anisotropies (in case of amorphous glass-coated microwires: annealing in strong perpendicular magnetic field, annealing by current, annealing under stress, annealing in torsion, or many others). Moreover, annealing must be performed under Curie temperature because interaction energy in paramagnetic state becomes equal in both atom pair orientations.

Such structural relaxation contribution can be expressed as

$$H_{sw}^p(T) \propto \frac{1}{M_S} \frac{\varepsilon_p^2 \rho_p}{kT} \left(1 - e^{(-t/\tau_r)} \right),$$
 (8.14)

where ε_p is the interaction energy of mobile defects with local spontaneous magnetization, ρ_p is density of mobile defects, t is time of measurements, τ_r is relaxation time, which is given by Arrhenius equation (see Eq. (8.13)).

Both above mentioned contributions (magnetoelastic contribution and structural relaxation contribution) can be simply summed and therefore final expression for temperature dependence of the switching field is obtained:

$$H_{sw}(T) = pM_S^{3/2} (1 + r(\Delta T))^{1/2} + n\left(1 - e^{(-t/\tau_r)}\right) / (M_S T), \tag{8.15}$$

where $n \approx \left(\varepsilon_p^2 \rho_p / k\right)$ is proportional to the number of defects. Both contributions are sufficient for describing of temperature dependence of the switching field in whole range of measured temperatures.

The two above described contributions have also different stress dependence [29]. Therefore, there are also two mechanisms of the closure domain wall responsible for the stress dependence of the critical field H_{sw} :

1. Firstly, it is a long-range magnetoelastic contribution arising from mechanical stresses induced during the preparation process and from the additional stresses applied by external load. Assuming the magnetoelastic anisotropy constant K_{σ} (=(3/2) $\lambda_s \sigma$), the corresponding stress dependence of the critical field was evaluated [30]:

$$H_0^r \approx \pi \lambda_S(\sigma + \sigma_0)/M_S \mu_0,$$
 (8.16)

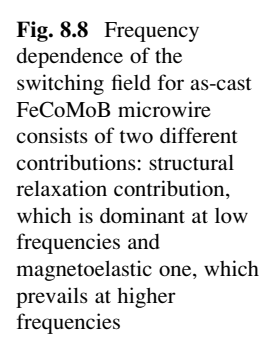
where σ_0 is a residual stress and σ an externally applied tension stress.

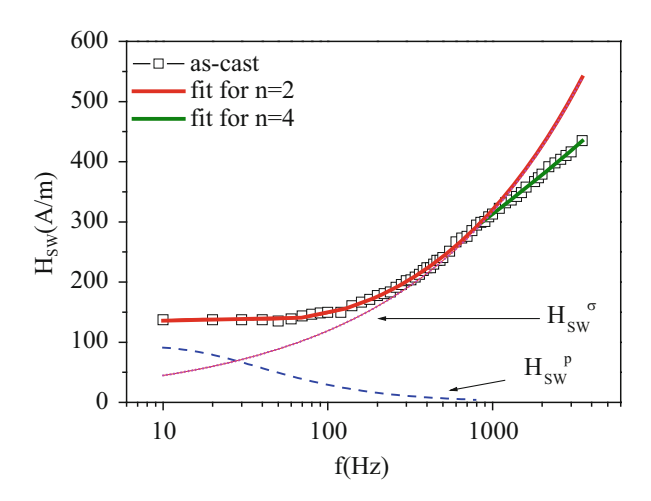
2. Secondly, the short-range pinning of the closure domain on the local defects was shown to be responsible for an increase of a critical propagation field especially at low temperatures [31]:

$$H_0^S \approx \varepsilon_{eff}^2 c_0 (1 - \exp(-t/\tau)) / M_S kT. \tag{8.17}$$

It has been shown that both contributions can be controlled by frequency or temperature [32].

Moreover, both above described contributions have different dependence on the frequency of applied field [16] (Fig. 8.8). It was shown that at low frequencies (below 50 Hz) short-range pinning contribution prevails, while at frequencies above 50 Hz the magnetoelastic contribution becomes the dominant one [16]. As a result, their relative contribution to the total switching field and hence their influence on the final temperature and stress dependence of H_{sw} can be tailored by simply changing the frequency of the applied field [32, 33].





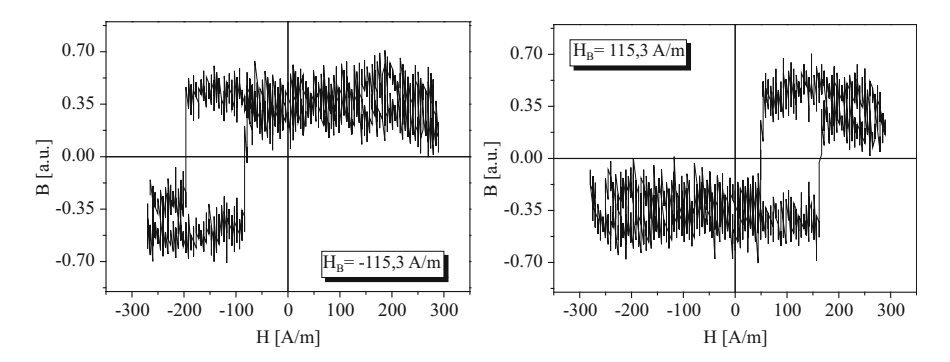


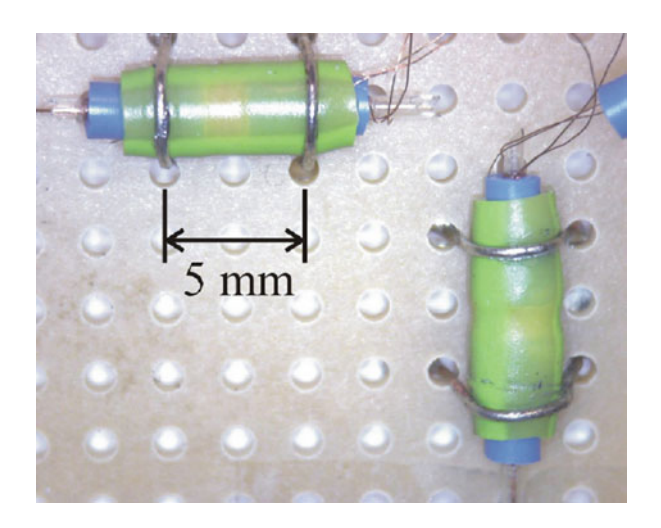
Fig. 8.9 Application of external magnetic field leads to the displacement of whole hysteresis loop of bistable microwires according to the direction of applied field

8.3 Magnetic Field Sensing Applications

Application of external parasitic magnetic field (e.g., Earth's magnetic field) leads to the displacement of whole hysteresis loop of bistable microwire according to direction of the field (Fig. 8.9). In such cases, the measured switching field is a sum of external parasitic and intrinsic switching field. Both components can be distinguished when the switching field is measured in both directions of applied excitation field. Hence, two values of the switching field will be measured, H_{sw}^+ when excitation field increases and H_{sw}^- when excitation field decreases. Finally, the intrinsic switching field, H_{sw} , is proportional to the difference of both components [2]:

$$H_{sw} = \frac{H_{sw}^+ - H_{sw}^-}{2},\tag{8.18}$$

Fig. 8.10 2D magnetometer based on orthogonally placed bistable microwire



while external parasitic field, H_{ext} , is given by a sum of both components:

$$H_{\text{ext}} = \frac{H_{sw}^{+} + H_{sw}^{-}}{2}.$$
 (8.19)

Such a method is particularly interesting for applications, since two variables can be obtained from single measurements: (1) amplitude of axial (with respect to the wire's axis) magnetic field (that in some cases defines also the position of object) and (2) intrinsic switching field that is influenced by temperature, mechanical stress, etc.

The dimensions of microwires allow to produce very small 2D measuring system [34] that consists of two complex coil systems place orthogonally (Fig. 8.10). Each system consists of a single excitation and single pick-up coil—as described in Sect. 8.2.2. Both excitation coils are connected in series in order to produce same fields. In contrary, pick-up coil is connected in anti-serial configuration. Hence one pick-up coil gives maximum, while the other one induces minimum when the domain walls propagate along both wires (Fig. 8.11). This gives us possibility to recognize two signals from two pick-up coils using a single input on oscilloscope. Apart from this, such configuration leads to the compensation of the signal from the excitation coils and hence well-defined maxima are observed that are far from the background signal (Fig. 8.11).

Another advantage of magnetometer based on bistable microwire is a linear response of the switching time on external parasitic magnetic field (Fig. 8.12). The precision of magnetometer depends on how precisely the switching time is measured and the range of measured magnetic field is defined by the excitation field, which should be higher than the sum of the switching field and external parasitic field.

Fig. 8.11 Induced signal from primary (*yellow*) and pick-up coils. Special design allows to recognize the signal from each pick-up coil using single input (see the text)

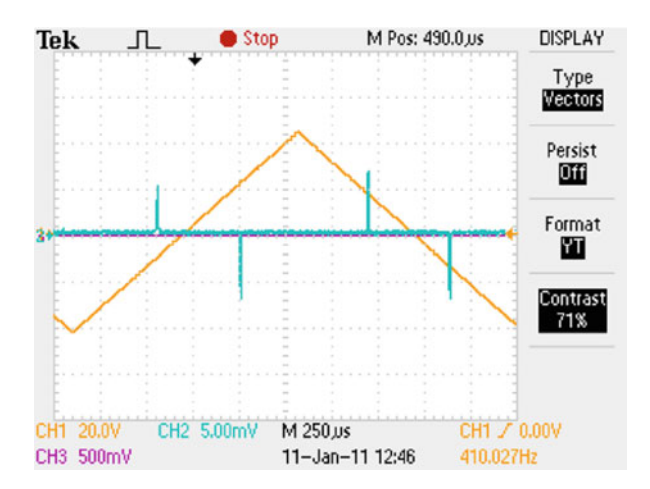
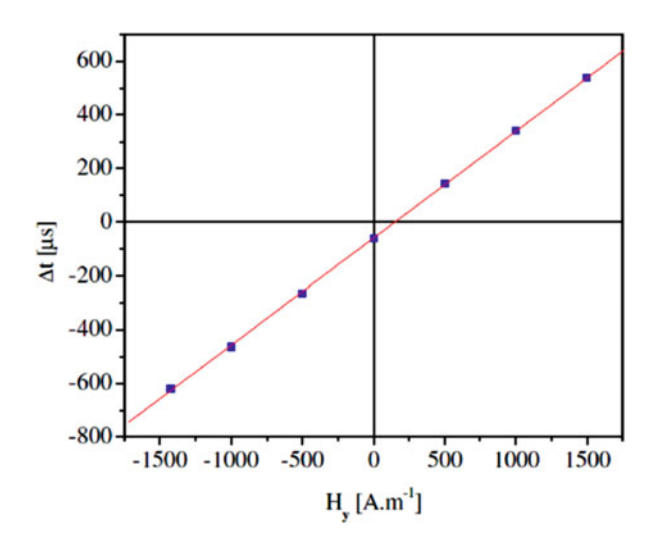


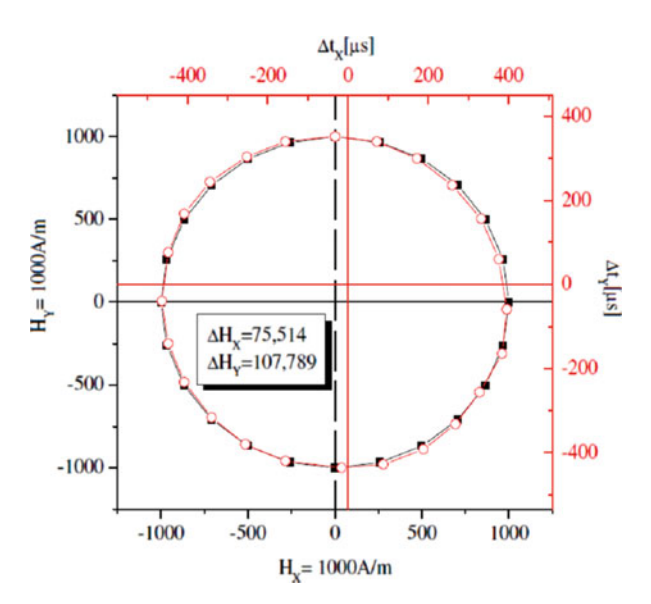
Fig. 8.12 Response of the switching time on the switching field is perfectly linear in a whole measuring range



An example of the response of 2D magnetometer on the application of rotation of 2D magnetic field with amplitude 1000 A/m is given in Fig. 8.13. One can see that two circles fit perfectly to each other. From the displacement of both circles centers, the external parasitic field can be estimated (see inset of Fig. 8.13).

Such magnetometer has few advantages. Firstly, their dimensions are given by the dimensions of microwires. Secondly, it is the linear response of the switching time on the magnetic field. Thirdly, any kind of the bistable microwire can be used—the shift of the switching time with respect to the external parasitic field does not depend on the switching field. Finally, it is its multifunctionality—when using properly selected bistable microwire, one can obtain also temperature, stress, or other parameters apart from magnetic field as given by Eqs. (8.18) and (8.19).

Fig. 8.13 Response of 2D magnetometer to the applied rotational 2D magnetic field. From the displacement of both circles centers, the external parasitic field can be estimated (see *inset*)



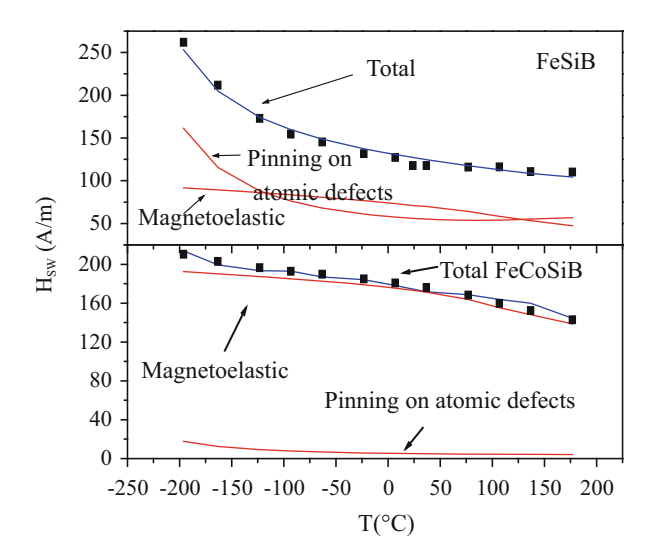
8.4 Temperature Dependence of the Switching Field for Industrial Applications

The biggest advantage of glass-coated microwires is their small dimensions that allow embedding of microwire into the many materials without destroying its mechanical properties. For example, they can be introduced inside the glass or carbon-based composites and sense the temperature during the production. Moreover, the applicable temperature range is extremely wide—microwires can be used within the temperatures from absolute zero ($-273~^{\circ}$ C) up to the temperatures as high as 600 $^{\circ}$ C (depending on their Curie temperature). Their temperature dependence can be tailored properly by composition, thermal treatment, or by properly selected measuring condition. In the following section we give an overview of selected microwires that were tested for the industrial temperatures range from -200 to $200~^{\circ}$ C.

8.4.1 Effect of Compositions on Temperature Dependence of the Switching Field

One possibility how to tailor the temperature dependence of the switching field is to select appropriate chemical composition, playing with the appropriate materials constant. Figure 8.14 shows the results for two different chemical compositions that differ by magnetostriction and concentration of the defects that can play the role of the pinning centers for the domain wall propagation [35]. The switching field

Fig. 8.14 Temperature dependence of the switching field for two different composition of metallic core (FeSiB and FeCoSiB) of amorphous glass-coated microwires



amplitude of the amorphous $Fe_{77.5}Si_{7.5}B_{15}$ microwire (which is characterized by high value of the magnetostriction constant ~25 \times 10⁻⁶ [36]) shows strong increase when the temperature decreases, which can be ascribed to the increase of the relaxation time of the mobile defects. They loose their mobility and increase the local anisotropy. With increasing the temperature, the mobility of the defects increases and the coercivity decreases. Above $-100\,^{\circ}\text{C}$, the magnetoelastic pinning dominates in the coercivity mechanism because of high saturation magnetization of $Fe_{77.5}Si_{7.5}B_{15}$ composition. In this case, the switching field decreases to its half amplitude in the temperature range from -193 up to $177\,^{\circ}\text{C}$.

The different situation is in the amorphous $Fe_{38}Co_{40}Si_{13}B_{11}$ microwire with relatively high magnetostriction constant ~15 \times 10⁻⁶ [37] where magnetoelastic pinning dominates over all temperature range. The contribution from structural relaxation is ten times smaller than magnetoelastic one and can be registered only at lowest temperatures as a small increase of coercivity. It was found on the ribbons of the similar composition [38] that low temperature relaxation has very small effect on the coercivity in amorphous $Fe_{38}Co_{40}Si_{13}B_{11}$ alloys with the same compound of Fe and Co. The high temperature annealing is necessary to see the effect of magnetic relaxation in this composition [39]. In the case of $Fe_{38}Co_{40}Si_{13}B_{11}$ microwire, the switching field decreases almost linearly by one quarter of its value in the temperature range from -193 up to 177 °C.

8.4.2 Amorphous and Nanocrystalline FeNiMoB Microwires

As given in the previous part, structural relaxation strongly influences the temperature dependence of the switching field in bistable microwire. However, it makes it

strongly non-linear, which is rarely desirable for practical applications. In the case, where linear response of the switching field on temperature is necessary, it is desired to hinder the structural relaxation. One possible solution can be found in terms of nanocrystalline structure that provides high structural stability together with low magnetocrystalline anisotropy.

It has been shown that partial crystallization of Fe₄₀Ni₃₈Mo₄B₁₆ ribbon leads to the formation of nanocrystalline materials with fcc-(Fe,Ni) nanocrystals (ferromagnetic phase characterized by low value of positive magnetostriction) having diameter of 10 nm [40]. It has also been shown that optimum annealing temperature is $T_a = 425$ °C to obtain nanocrystalline Fe₄₀Ni₃₈Mo₄B₁₆ alloy with optimized soft magnetic properties (lowest magnetostriction, lowest coercive field, and highest initial susceptibility) [41, 42]. Optimum annealing temperature range for nanocrystallization in FeNiMoB alloy is much lower in comparison to the typical nanocrystalline materials as FINEMET (from 520 up to 550 °C) [43–46]. Annealing at higher temperatures than optimum one is undesirable because compressive stresses applied by the glass-coating after annealing are very strong in the case of FeNiMoB microwires and even they suppress the grain growths [7]. It has been demonstrated before that Fe₄₀Ni₃₈Mo₄B₁₆ alloy composition can be used to produce soft magnetic nanocrystalline microwires with positive magnetostriction [7]. Moreover, the glass-coating of microwires improves the fragility of nanocrystalline metallic nucleus.

The drawing and rapid quenching applied during production of amorphous microwires as precursor for nanocrystalline ones results in a strong and complex stress distribution applied on metallic nucleus. Moreover, additional stresses are applied on nucleus due to different thermal expansion coefficient of metallic nucleus and glass-coating of amorphous microwires (Fig. 8.15). As a result, complex temperature dependence is obtained in as-cast amorphous FeNiMoB microwire (see Fig. 8.16).

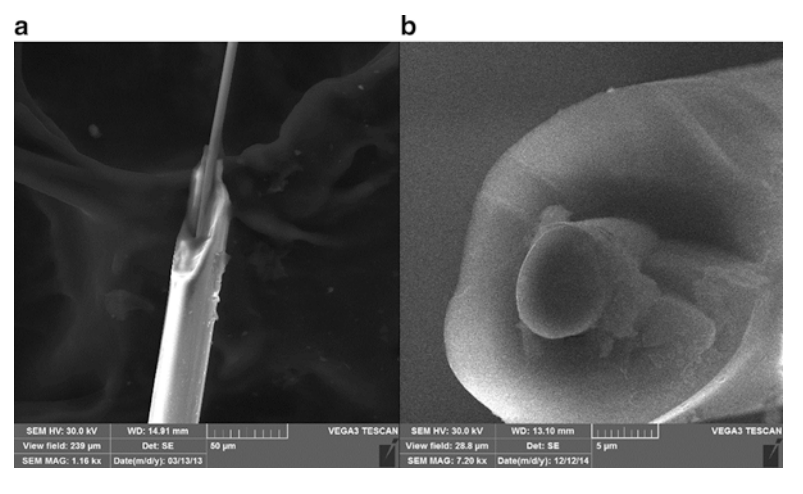


Fig. 8.15 Scanning electron microscopy (SEM) images of (a) as-cast FeNiMoB microwire, (b) cross-section of nanocrystalline FeNiMoB microwire annealed at 400 °C for 1 h

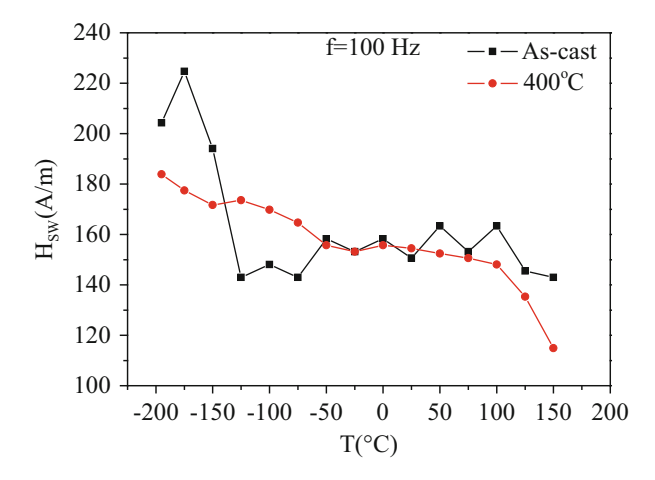


Fig. 8.16 Temperature dependence of the switching field for amorphous and nanocrystalline FeNiMoB microwires measured in as-cast and nanocrystalline state

Annealing at 400 °C leads to the optimum nanocrystalline state of metallic nucleus [7] with lower magnetostriction [41]. It is worth to note that both residual amorphous phase and the fcc-FeNi nanograins are characterized by positive magnetostriction. However, magnetostriction of fcc-FeNi nanograins is positive but very low. Therefore, magnetostriction decreases as a result of nanocrystallization process. However, the amorphous structure is relaxed and contains very few mobile defects. Therefore, the temperature dependence of the switching field is very continuous and shows weak monotonous decrease with temperature (see Fig. 8.16).

Such behavior is very desirable for temperature sensors. However, the disadvantage of nanocrystalline FeNiMoB-based microwires is their relatively small magnetization, low Curie temperature, and the very narrow range of annealing temperatures to reach optimum nanocrystalline microstructure. Solution can be found in modification of chemical composition of nanocrystalline microwire.

8.4.3 Amorphous and Nanocrystalline FeCoMoB Microwires

In contrary to nanocrystalline FeNiMoB, nanocrystalline HITPERM-based alloys prepared by controlled annealing from amorphous precursors are characterized by high value of saturation magnetization, saturation magnetostriction, high Curie temperature (above 1000 °C) and as well as by high stability of magnetic properties as coercive field [47–51]. Therefore, they are suitable material for high temperature

applications. Bcc-(Fe,Co) nanograins appear after annealing above crystallization temperature ~425 °C. It is worth to note that magnetostriction increases with nanocrystallization process because both bcc-(Fe,Co) grains together with residual amorphous matrix exhibit positive magnetostriction (from 17×10^{-6} in as-cast state up to 33×10^{-6} in advanced nanocrystalline state as was found in ribbons with similar composition) [52].

We have studied microwires with nominal compositions of Fe₄₀Co₃₈Mo₄B₁₈, which is slightly different from the typical HITPERM-based composition. Firstly, no Cu was used to enhance the early crystallization because Cu addition has weak effect of on size of grains [53, 54] and secondly effect of addition of molybdenum is in decreasing of crystallization temperature what is very important because glass-cover applies strong compressive stresses on metallic nucleus of microwires after annealing [7]. In general, the goal is obtain stable nanocrystalline microstructure in metallic core after annealing at lowest possible temperature.

FeCoMoB-based nanocrystalline microwires are particularly suitable for applications where wide range of temperature is desired. After annealing at optimum temperature, bcc-(Fe,Co) grains with diameter between 11 and 13 nm are observed [11]. Moreover, it was shown that the increase of crystalline phase volume is a result of nucleation of new grains rather than existing grain growth [6]. Additionally, FeCoMoB-based microwires do not lose their bistability even in advanced nanocrystalline state [6]. Finally, the optimum annealing temperature to obtain soft magnetic properties (switching field) is in wide temperature range from 450 up to 600 °C [6].

In addition, nanocrystalline microwires are characterized by high domain wall velocities up to 10 km/s [55, 56]. High temperature stability of transverse domain wall dynamics in nanocrystalline FeCoMoB microwires (which does not depend on the annealing method) has also been observed [13, 57].

Similarly to the FeNiMoB microwires, there is a complex stress distribution induced in the as-cast microwire. Therefore, the temperature dependence of switching field is also complex (Fig. 8.17). Firstly, it decreases at low temperature, then it arises, close to the $0\,^{\circ}$ C, showing discontinuous behavior at high

Fig. 8.17 Temperature dependence of the switching field for amorphous and nanocrystalline Fe₄₀Co₃₈Mo₄B₁₈ microwires measured at frequency of 50 Hz

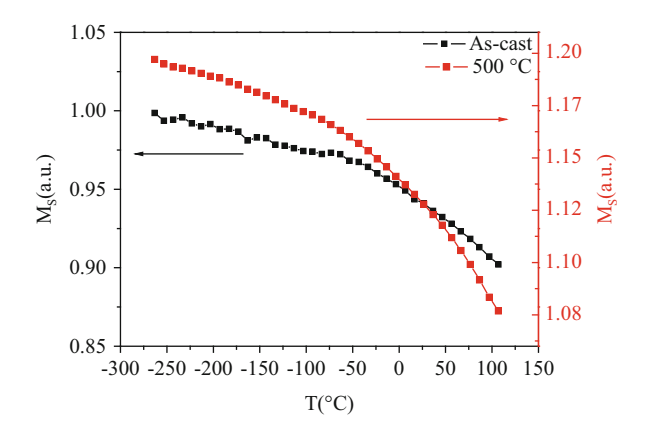
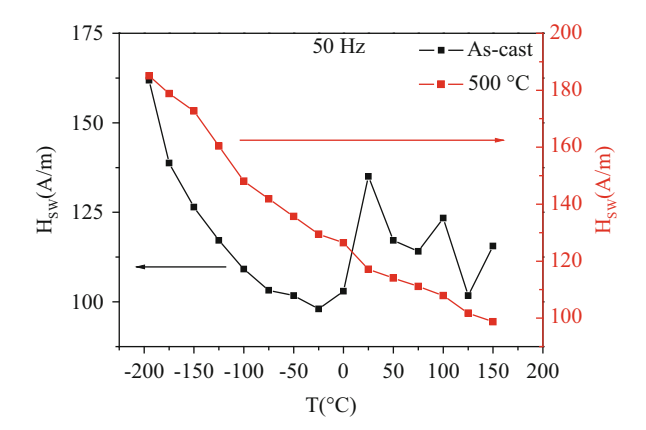


Fig. 8.18 Temperature dependence of the saturation magnetization for as-cast and heat-treated FeCoMoB microwire $(T_a = 500 \, ^{\circ}\text{C})$



temperatures. Such temperature dependence can be understood taking into account the complex stress distribution and the additional stresses applied on microwire due to a different thermal expansion coefficient of metallic nucleus, α_m , and glass-coating, α_g . Varying the temperature of microwires, the complex stress distribution in as-cast microwires varies, too. Moreover, the switching field consists of two different contributions: structural relaxation contribution and magnetoelastic one. Structural relaxation contribution is dominant at low temperatures (see also Sect. 8.4.1).

Similar behavior can be found from the measurement of saturation magnetization M_s (Fig. 8.18). Small discontinuities in the saturation magnetization are visible at low temperatures. The temperature dependence of magnetization is not smooth reflecting the changes in the complex stress distribution due to stress coming from glass-coating. However, the applied field 1 T is strong enough to saturate the sample and such laborious behavior is observed only below -70 °C. At higher temperature, the temperature dependence of M_s is smooth.

Annealing at the temperatures higher than 420 °C leads to the appearance of nanocrystalline structure [6] that is characterized by the small crystalline grains (smaller than exchange length) embedded in the residual amorphous matrix. Exchange interaction of crystalline grains leads to the averaging out of magnetocrystalline anisotropy that results in a magnetic softness (switching field decreases). On the other side, magnetoelastic anisotropy becomes dominant. FeCoMoB composition was selected due to its high positive magnetostriction in order to obtain bistable hysteresis loop. Therefore, the temperature dependence of H_{sw} is driven mainly by magnetoelastic interaction of magnetic moments with the stress applied due to the glass-coating. And the temperature dependence of the switching field becomes almost linear and relative variation of the switching field within the studied interval is 87.5 %.

The another advantage of FeCoMoB composition is that magnetic softness obtained by annealing is almost independent on the temperature of annealing within wide range of temperatures from 450 up to 600 °C. The temperature dependence of H_{sw} is also similar for different temperature of annealing within this range

[6]. Moreover, the saturation magnetization of nanocrystalline microwires is also higher than that of amorphous one (Fig. 8.18).

All these parameters point to the fact that FeCoMoB nanocrystalline microwires are suitable for temperature sensing in a wide range of temperatures. Theoretically, the switching field can be measured almost up to the Curie temperature, which is much above the crystallization one.

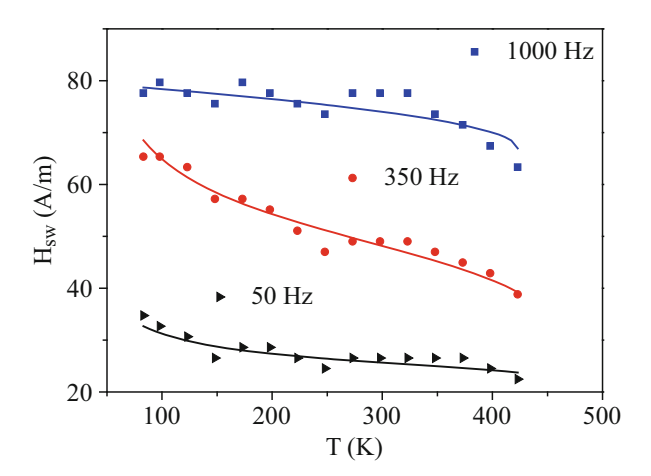
8.4.4 Amorphous and Nanocrystalline FeSiBNb Microwires

In contrary to classic basic FeSiB system used elsewhere [3, 4, 58, 59] addition of Nb increases corrosion resistance and glass forming ability [60], which results in the increase of structural relaxation effects.

Moreover, addition of Nb into classical Fe-Si-B system leads to the increasing of crystallization temperature. Hence, Nb alloying stabilizes amorphous structure which is consistent with earlier reports [61–63]. Nb addition also decreases the value of saturation magnetization and value of coercive field [64, 65].

All the above-mentioned properties enhance the effect of structural relaxation on the switching field [32]. Combining the frequency dependence of the switching field with its temperature dependence one can get interesting results shown in Fig. 8.19. At low frequencies (50 Hz), the switching field decreases firstly at low temperatures but is temperature independent in the range from 270 to 370 K. It is because at low frequencies the structural relaxation contribution is not negligible and defines the temperature dependence of the switching field. On the other hand, high frequency (1000 Hz) temperature dependence shows almost temperature independent range up to 325 K that is followed by the decrease of the switching field. At higher frequencies, the structural relaxation vanishes and the overall temperature dependence of the switching field is given by the temperature dependence of its magnetoelastic contribution.

Fig. 8.19 Temperature dependence of the switching field for three different excitation frequencies



At intermediate frequencies, both contributions contribute to the temperature dependence of the switching field in amorphous microwires. In such a way, almost linear dependence of the switching field on the temperature can be obtained by measuring at 350 Hz (see Fig. 8.19). Such behavior is desired in case where temperature dependence of the switching field must be suppressed or enhanced. In the given case, it can be done by simple variation of the frequency of excitation field without affecting the hardware of sensing elements.

8.4.5 Amorphous FeSiBCr Microwires

Another possibility how to improve the temperature dependence of the switching field is to employ the alloys with high stability and low Curie temperature. Typical example is $Fe_{67.5}Si_{7.5}B_{15}Cr_{10}$ microwire [66]. Given composition has some specific properties. Firstly, addition of Cr decreases magnetostriction (from $\lambda_S \sim 35 \times 10^{-6}$ for classical FeSiB system up to $\lambda_S \sim 6 \times 10^{-6}$ for $Fe_{68}Si_9B_{13}Cr_{10}$) [37] and also the Curie temperature. The Curie temperature has been reported to be 398 K, close to room temperature, in amorphous ribbons with the same chemical composition as the studied microwires [67]. However, the Curie point of the amorphous microwire will be higher due to strong internal stresses introduced during production process [68]. Small Curie temperature increases the sensitivity of the switching field to the external parameters (like temperature, stress) at room temperature. Secondly, addition of chromium stabilizes amorphous structure (due to the higher Cr affinity to B atoms) [69] that is highly desirable for practical applications.

As a result, the stress distribution will also show high structural stability in a wide range of temperatures as confirmed from magnetization measurements that shows very continuous dependence of saturation magnetization on the temperature (Fig. 8.20). The same is valid for remanent magnetization M_r [66].

Fig. 8.20 Temperature dependence of saturation magnetization M_S for FeCrSiB microwire shows high stability of stress distribution

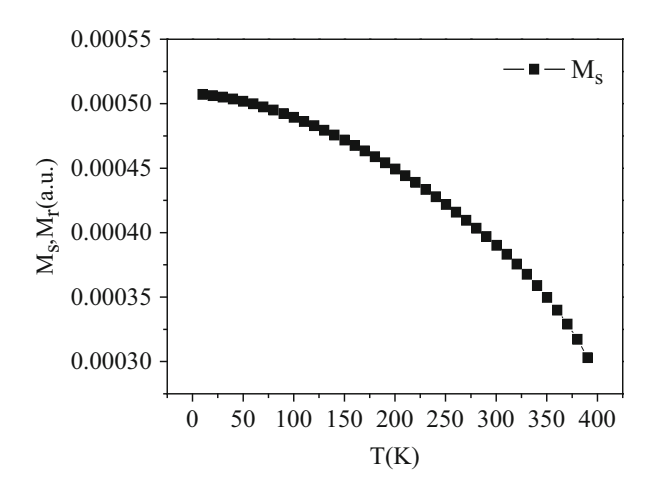
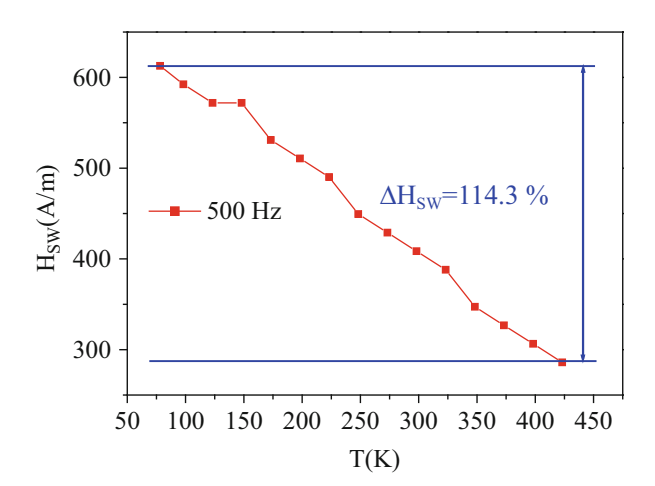


Fig. 8.21 Temperature dependence of the switching field of as-cast amorphous FeCrSiB microwire measured at frequency of 500 Hz



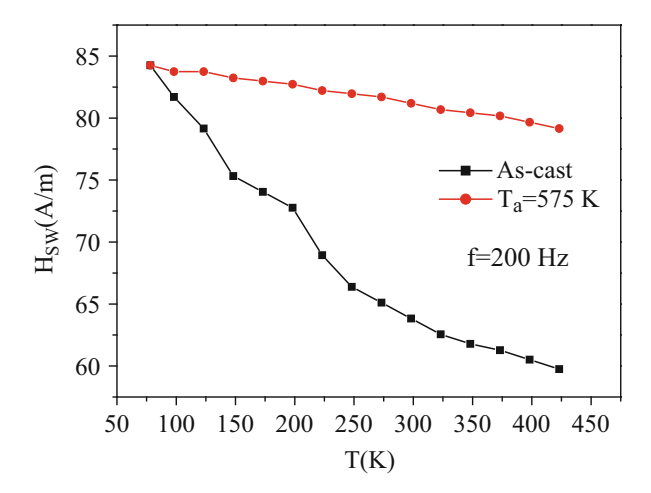
These features result in a strong and almost linear temperature dependence of the switching field in a wide temperature range from 80 up to 425 K (see Fig. 8.21) [66]. Generally, the switching field decreases with temperature, reflecting the relief of the stresses induced by the glass-coating due to different thermal expansion coefficient comparing to metallic nucleus. Here, the temperature dependence of the switching field is enhanced by the low value of the Curie temperature. Close to the Curie temperature, the anisotropy decreases steeply and this results in an enhancement of the switching field reduction. Finally, the switching field decreases from 612 A/m at 80 K down to 286 A/m at 425 K. So, it shows a variation of almost 114.3 % compared with the high temperature value. As previously shown, the temperature dependence of the switching field in amorphous microwires can be tuned by the frequency of the applied field [32], as a result of the different frequency dependence of both contributions to the switching field. In the case of FeSiBCr microwire, the temperature dependence of the switching field is not influenced by the frequency since the structural relaxation contribution is very small (see Fig. 8.21).

8.4.6 Amorphous FeSiBP Microwires

Alloys based on $Fe_{76}Si_9B_{10}P_5$ composition are characterized by high value of magnetostriction constant ($+3 \times 10^{-5}$), high glass forming ability due to presence of phosphorus, high saturation magnetization, and low coercive field [70]. Moreover, domain wall dynamics have been studied in microwires with such composition and fast velocities of the domain wall up to 4.5 km/s were observed [71–74].

The temperature dependence of the switching field for as-cast and annealed FeSiBP-based microwires is showed in Fig. 8.22. As-cast sample is very

Fig. 8.22 Temperature dependence of the switching field for as-cast amorphous microwire and amorphous microwire annealed at 575 K for 1 h measured at frequency of 200 Hz



unhomogenous and strong stresses from production process (simultaneous drawing and quenching) are present in metallic core. Switching field in as-cast sample monotonously decreases from 84.2 A/m at lowest measured temperature (78 K) to 59.7 A/m at highest measured temperature (425 K). Variation of the switching field in as-cast sample in whole measured temperature range is more than 41 %.

Annealing at 300 °C for 1 h leads to the relaxation of strong stresses from production process, to the homogenization of amorphous structure, and to the stabilization of the domain structure. Selected temperature of 575 K is much below crystallization temperature of bcc-Fe(Si) grains (818 K), and as well as it is temperature at which stresses from different thermal expansion coefficient of glass-coating and metallic nucleus are not so high in comparison to higher temperatures, i.e., 500 °C and more. Moreover, selected temperature of 575 K is optimum annealing temperature for relax of stresses from production process.

Variation of the switching field in annealed sample is much lower (only 5 A/m) most probably as a result of the domain structure stabilization caused by annealing. Particularly, switching field decreases by almost linear way from 84.2 A/m at lowest measured temperature (78 K) to 79.1 A/m at highest measured temperature (425 K).

8.4.7 Amorphous FeNiCrB Microwires

In real applications, a compromise must be found between excellent magnetic properties and mechanical strength in order to guarantee long-life performance of sensors. Nickel-based superalloys are an exceptional combination of high temperature strength, toughness, and resistance to degradation in corrosive or oxidizing environments. These materials are widely used in aircraft and power-generation turbines, rocket engines, and other challenging environments, including nuclear power and chemical processing plants, such as turbine discs, for high pressure stages [75, 76].

Typical widely used FeNiCr-based alloy is Elinvar, which consists of 59 % iron, 36 % nickel, and 5 % chromium. Elinvar is almost nonmagnetic and corrosion resistant. The largest application of Elinvar was in balance spring for mechanical watches and chronometers. Main reason of application of Elinvar is low temperature coefficient of expansion in comparison to the ordinary steels. In general, FeNiCr-based alloys possess superior high temperature mechanical strength, oxidation, and corrosion resistance. Moreover, they are more manufacturable than ferritic stainless steels. Only one disadvantage is that FeNiCr-based alloys are generally more expensive. On the other hand, FeNiCr-based alloys exhibit resistance towards aggressive media and due to their high biocompatibility they are excellent candidate for developing cheap biodevices [77]. Finally, FeNiCr-based alloys are widely used as coating material due to their excellent anticorrosion effect [78].

However, little bit another situation is in amorphous FeNiCr-based alloys [79–81]. Amorphous ribbons based on FeNiCr composition also attract attention of many authors [82, 83]. They found very interesting fact that atom pair ordering of Fe and Ni atoms leads to the increasing of Curie temperature [14], while opposite effect was observed by replacing the Fe by Cr atoms [84, 85]. Additionally, small addition of Chromium into FeNi-based alloy leads to the decrease of saturation magnetization and as well as to the decrease of thermal expansion coefficient, while crystallization temperature is not affected. Finally, amorphous FeNiCr-based alloys are characterized by better mechanical properties (mechanical hardness, high yield strength, and low Young's modulus) in comparison to the crystalline counterpart while other excellent properties remain [85].

Good mechanical properties and small thermal expansion coefficient make FeNiCr-based alloys an excellent candidate for metallic nucleus of glass-coated microwires. In given contribution, we focus our attention on amorphous FeNiCr-based microwires in order to employ them as precise temperature and magnetic field sensor. Thermal annealing is always necessary for real applications in order to prevent aging of magnetic properties. Therefore, two series of microwires with different chromium content (and therefore with two different Curie temperatures) were produced to check the effect of Cr on annealing process. It is shown that a variation of only 1 at.% of Cr significantly changes the sensitivity of the switching field to the temperature after annealing. The switching field decreases almost linearly with temperature for Fe₄₉Ni₂₇Cr₆B₁₈ annealed microwires, while there is almost temperature independent part of the switching field for annealed Fe₄₆Ni₂₉Cr₇B₁₈ microwire.

Firstly, the SEM-analysis was performed in order to investigate amorphous nature of studied microwires. In Fig. 8.23, cross-section pictures of amorphous as-prepared Fe₄₉Ni₂₇Cr₆B₁₈ and Fe₄₆Ni₂₉Cr₇B₁₈ microwires are showed.

The Curie temperature was estimated from magnetization measurements to be 290 and 350 °C for $Fe_{46}Ni_{29}Cr_7B_{18}$ and $Fe_{49}Ni_{27}Cr_6B_{18}$ microwires, respectively. According to estimated T_C , the annealing temperature was chosen to be 300 °C, which was also shown in other microwires to be optimal temperature for releasing the stresses introduced during production of the wire [8].

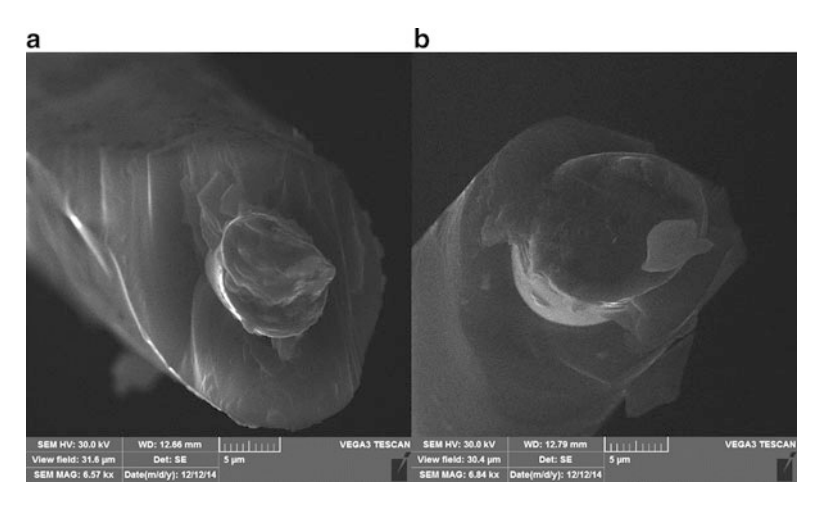


Fig. 8.23 SEM pictures of cross-section of amorphous as-cast (a) $Fe_{49}Ni_{27}Cr_6B_{18}$ and (b) $Fe_{46}Ni_{29}Cr_7B_{18}$ microwires

Such temperature is also well below the crystallization temperature of fcc-(Fe,-Ni) phase (which is approximately in interval from 420 up to 445 °C for amorphous ribbons with very similar composition [80, 86]).

The domain structure of the glass-coated microwire with positive magnetostriction is the result of the strong and complex stress distribution introduced during microwire production (σ_i) [87, 88] and by the stresses arising from different thermal expansion coefficient of metallic nucleus and glass-coating.

It is worth to note that the internal stresses strength in the core of glass-coated microwires is mostly determined by the ratio between the metallic nucleus diameter and the total composite wire diameter ($\rho=d/D$) [89]. In general, the strength of the internal stresses increases as the ρ -ratio decreases [89]. Therefore it was observed unusual behavior because switching field is higher (212 A/m at room temperature) in Fe₄₆Ni₂₉Cr₇B₁₈ microwire with higher ρ -ratio (0.56) in comparison to the lower switching field (189 A/m at room temperature) in Fe₄₉Ni₂₇Cr₆B₁₈ microwires with lower ρ -ratio (0.46).

The temperature dependence of the switching field for as-cast $Fe_{49}Ni_{27}Cr_6B_{18}$ microwire decreases in an almost linear way with increasing temperature (see Fig. 8.24a) reflecting the temperature dependence of the stresses applied on microwire during its production. Particularly, the switching field decreases from 189 A/m at room temperature to 154 A/m at 165 °C. Observed variation of the switching field with temperature is almost 23 % in the given temperature range. Moreover, the switching field decreases by almost linear way in as-cast sample (see Fig. 8.24a).

Annealing of the microwire at 300 °C for 1 h leads to stresses relief and homogenization of the sample [8, 90] which is accompanied by the decrease of switching field. As a result, the value of the switching field decreases from 162 A/m

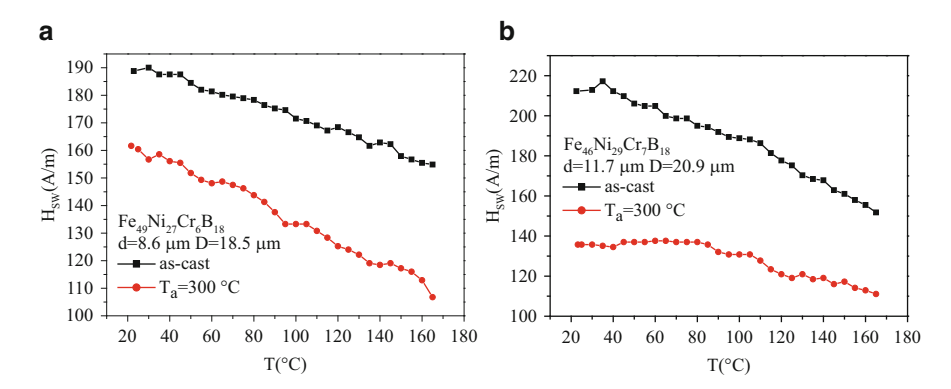


Fig. 8.24 (a) Temperature dependence of the switching field for as-cast amorphous $Fe_{49}Ni_{27}Cr_6B_{18}$ microwire and annealed at 300 °C for 1 h, (b) Temperature dependence of the switching field for amorphous $Fe_{46}Ni_{29}Cr_7B_{18}$ microwire and annealed at 300 °C for 1 h

at room temperature to 107 A/m at temperature 165 °C and variation of the switching field is much higher \sim 52 % in comparison to the as-cast sample. From this reason, annealed Fe₄₉Ni₂₇Cr₆B₁₈ microwires can be used as precise temperature sensor. On the other hand, the shape of the temperature dependence of switching field does not vary and its linearity is even enhanced (see Fig. 8.24a). This could be a result of the stabilization of the domain structure through the atom pair ordering of Fe and Ni atoms during annealing.

Fig. 8.24b shows temperature dependence of the switching field for as-cast amorphous $Fe_{46}Ni_{29}Cr_7B_{18}$ microwire. The switching field decreases from 212 A/m at room temperature to 151 A/m at 165 °C. Observed variation of the switching field with temperature is equal to 40 % in the given temperature range (see Fig. 8.24b). Moreover, the switching field decreases with temperature by almost linear way in as-cast $Fe_{46}Ni_{29}Cr_7B_{18}$ microwire.

In contrary to $Fe_{49}Ni_{27}Cr_6B_{18}$ microwire, the Curie temperature of $Fe_{46}Ni_{29}Cr_7B_{18}$ microwire is just below 290 °C. Hence, annealing of the $Fe_{46}Ni_{29}Cr_7B_{18}$ microwire at 300 °C above Curie temperature for 1 h leads to the destabilization of the domain structure due to the random atom pair ordering of Fe and Ni atoms [14]. As a result, the temperature dependence of the switching field becomes non-monotonous showing slight increase at low temperature and jerky decrease at temperature above 80 °C. This is a result of temperature dependence of magnetoelastic anisotropy that arises from interaction of magnetic moment with complex stress distribution in an unstabilized domain structure. Observed variation of the switching field in the temperature range from 80 up to 165 °C is equal to 23 %.

8.4.8 Amorphous and Nanocrystalline FeMoBCu Microwires

The temperature dependence of the switching field can be enhanced in terms of special nanocrystalline microwires based on FeMoBCu composition. In contrary to previous works [66], microwire with low Curie temperature is used here, that employ another mechanism to increase of temperature dependence of the switching field based on effect of superparamagnetism, which has already been observed in nanocrystalline ribbons with similar composition [91–94].

Temperature dependence of saturation magnetization shows monotonous decrease up to the Curie temperature of amorphous precursor that was estimated to be 165 °C (see Fig. 8.25). Increase of the temperature up to 400 °C leads to the formation of nanocrystalline α -Fe grains with the Curie temperature over 700 °C. This is represented by increase of magnetization. The crystallization temperature has been estimated from dM/dT curve to be 400 °C. Such crystallization temperature is consistent with the ones obtained for similar FeCoMoB and FeNiMoB nanocrystalline microwires [6, 7].

Strong and complex stress distribution is introduced into the metallic nucleus of microwire during its production. As a result, the temperature dependence of the switching field for amorphous precursor is not continuous and shows various local minima (Fig. 8.26).

When approaching the Curie temperature (at about $165~^{\circ}$ C), the magnetic bistability disappears. The low Curie temperature is also responsible for a high variation of the switching field in the given temperature range that is reduced from 70~A/m down to 40~A/m.

Annealing at 400 °C for 1 h leads to formation of early nanocrystalline state with low crystalline volume fraction, in which the small crystalline grains are well separated. As a result of structural transformation, the temperature dependence of

Fig. 8.25 Temperature dependence of magnetization of FeMoBCu microwire

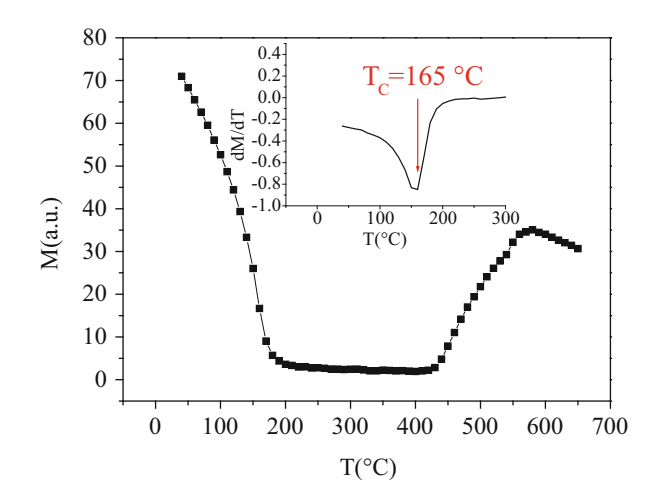
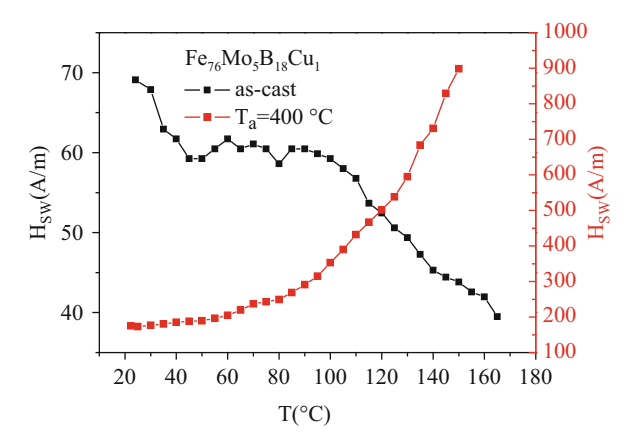


Fig. 8.26 Temperature dependence of the switching field for as-cast amorphous FeMoBCu and nanocrystalline FeMoBCu microwire annealed at 400 °C for 1 h, respectively.



the switching field changes drastically, showing the monotonous and marked increase (Fig. 8.26). The absolute value of the switching field increases from 175 A/m at room temperature up to 900 A/m at 150 °C. Above this temperature, the magnetic bistability is lost due to the transition of amorphous matrix into the paramagnetic state. Such a huge variation (more than 400 %) in a quite narrow temperature range is a result of lost of coupling between the ferromagnetic grains with rising temperature, which has been observed in soft magnetic nanocrystalline materials [91–94]. In general, the exchange ferromagnetic length L_{ex} in nanocrystalline materials is expressed as [91]:

$$L_{ex} = \left(\frac{\gamma A}{\langle K \rangle}\right)^{\frac{1}{2}} \tag{8.20}$$

where γ is a scaling parameter, A is an exchange stiffness constant, and $\langle K \rangle$ is average structural anisotropy. At low temperature (well below the Curie temperature), the crystalline grains are coupled through the amorphous matrix since the exchange length of amorphous matrix is longer than the intergranular distance. However, the exchange stiffness constant A is proportional to the square of magnetization. Hence it will decrease with temperature close to the Curie temperature due to a sharp decrease of magnetization. As a result, the crystalline grains decouple. Instead, they start to play a role of the pinning centers for the domain wall propagation. As a result, the switching field drastically increases, which makes this materials excellent candidates for very sensitive sensors.

8.5 Temperature Dependence of the Switching Field for Biomedical Application

This part is devoted to the searching for suitable composition of microwire metallic core and suitable thermal treatment in order to use microwire as sensor of temperature for biomedical applications. These applications require the material with very

special parameters. Particularly, they require very sensitive magnetic property within the very narrow temperature range from 35 to 45 $^{\circ}$ C.

In generally, it is well known that the switching field is sensitive to the temperature. One possible way how to increase such sensitivity of switching field is to employ the materials with low Curie temperature [68]. Below Curie temperature, the magnetic characteristics (magnetization, magnetic anisotropy) vary strongly. Unfortunately, so does the saturation magnetostriction, too. And this affects the possibility to produce the bistable microwire with low Curie temperature strongly.

8.5.1 Amorphous FeWB Microwires

As a first approach the amorphous $Fe_{80}W_3B_{17}$ microwire has been chosen because Wolfram decreases the Curie temperature of amorphous alloys and also reduces the effect of structural relaxation (see Fig. 8.27) [95]. On the other hand, magnetoelastic anisotropy decreases, too.

Temperature dependence of the switching field shows monotonous decrease from 1000 A/m at 20 °C down to 750 A/m at 170 °C (see Fig. 8.28). Such high values are very strange for amorphous materials and could be a result of strong stresses introduced on the metallic nucleus. This is confirmed by the annealing at 300 °C/1 hod that leads to the stress relief and homogeneization of the metallic nucleus. After annealing, the switching field drops down to 750 A/m at room temperature and monotonously decreases down to 500 A/m at 170 °C.

Fig. 8.27 Scanning electron microscopy image of as-cast Fe₈₀W₃B₁₇ microwire

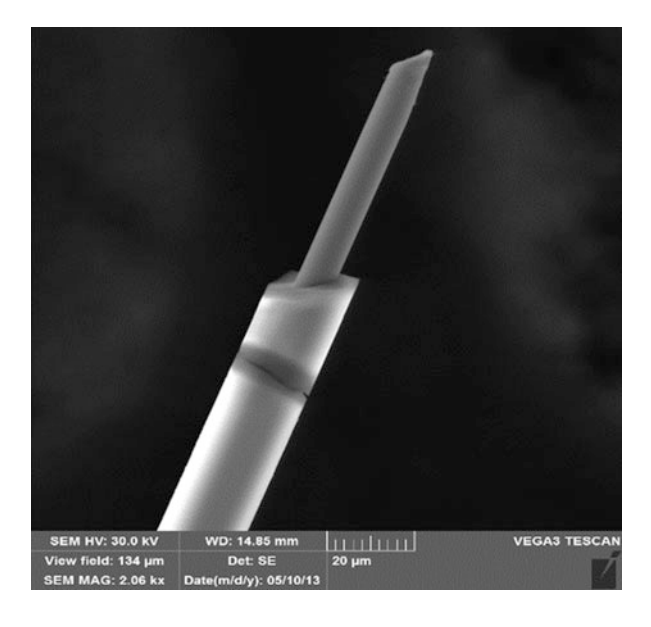


Fig. 8.28 Dependence of the switching field on annealing temperature for amorphous Fe₈₀W₃B₁₇ microwires in the as-cast and annealed state

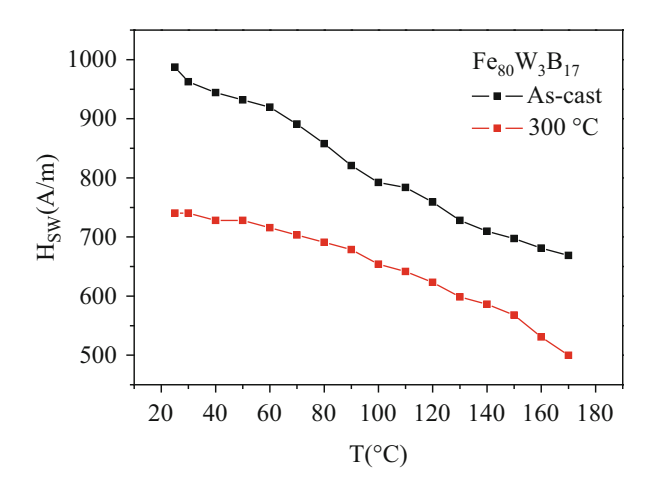
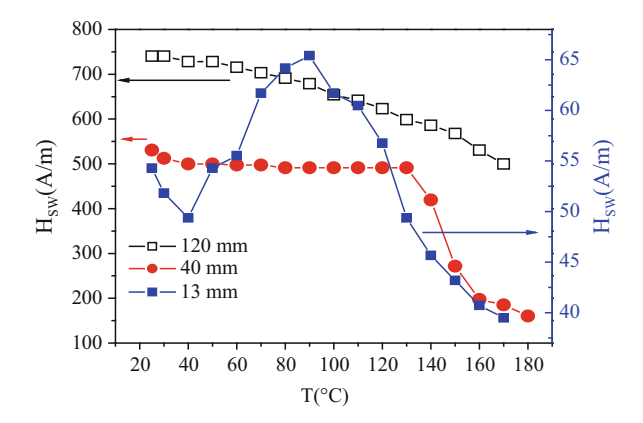


Fig. 8.29 Temperature dependence of the switching field for long and short Fe₈₀W₃B₁₇ microwires annealed at 300 °C for 1 h



Glass-coating applies strong stresses on metallic nucleus up (to 1 GPa [96]). One possible solution is to decrease the length of the microwire. As a result of reduced length, magnetoelastic anisotropy should decrease, too. Therefore, the temperature dependence of the switching field in microwires with various lengths was studied.

Temperature dependence of the switching field for FeWB microwires with 120, 40, and 13 mm lengths is shown in Fig. 8.29. As a result of strong stresses introduced during microwires production, the amplitude of the switching field is high ~750 A/m at room temperature for longest microwire (12 cm). As a result of reduction of the stresses applied by glass-coating, the switching field decreases with temperature monotonously.

Decrease of the length of microwire leads to the switching field reduction down to 540 A/m for microwire of length of 4 cm. The glass-coating induces high mechanical stresses on the metallic core up to 1 GPa [88]. These stresses decrease significantly with decreasing the length of the sample. Moreover, shape anisotropy

(that decreases with decreasing length of the microwire) also plays very important role. On the other hand, the temperature dependence of the switching field becomes more complex showing strong decrease above 130 $^{\circ}$ C. At this temperature, the anisotropy decreases steeply as it approaches the Curie temperature (this microwire looses bistability above 180 $^{\circ}$ C).

However, situation is more complex for very short FeWB microwires with length 13 mm (see Fig. 8.29). The switching field decreases steeply down to 55 A/m due to much smaller mechanical stresses applied by glass-coating. Moreover, the temperature dependence of switching field becomes complex. Firstly, switching field increases with increasing temperature up to 90 °C. Then, switching field decreases with increasing temperature mainly due to low value of the Curie temperature. Such temperature dependence approves that magnetoelastic anisotropy is no more dominant. However, strong variations of the switching field could be employed for sensing the temperature.

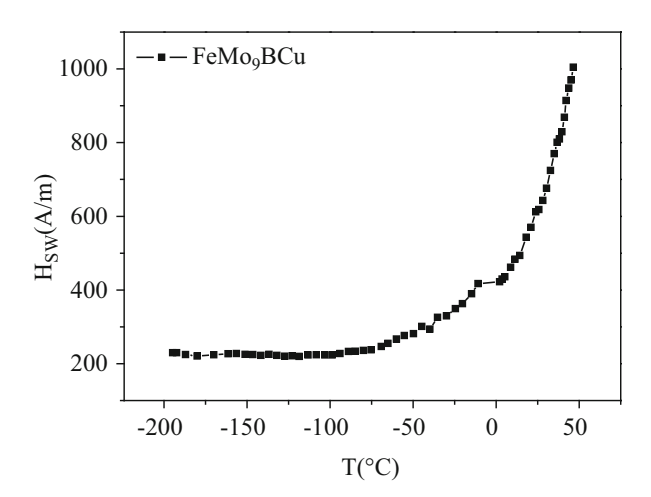
8.5.2 Amorphous and Nanocrystalline FeMoBCu Microwires with High Content of Molybdenum

In order to increase the sensitivity of the switching field for biomedical applications, the enhancement effect of superparamagnetism in early stage of process of nanocrystallization at lower applied temperatures was employed (similarly as in Sect. 8.4.8). In order to decrease the Curie temperature down to the bio-temperature range the amount of Mo was increased to 9 at.% in Fe₇₆Mo₉B₁₈Cu₁ microwire [97]. The Curie temperature for FeMo₉BCu microwire is 37 °C and crystallization temperature of α -Fe grains as 461 °C.

The problem is that as-cast amorphous microwire is not bistable at room temperature and not even at very low temperature. Moreover, such microwire is not bistable even after annealing out at $300\,^{\circ}\text{C}$ for 1 h at room temperature and even at low temperatures up to $-195\,^{\circ}\text{C}$.

However, situation is changed after annealing of FeMo₉BCu microwire under axial tensile stress of 309 MPa above crystallization temperature (~461 °C) at 500 °C for 1 h (Fig. 8.30). Such annealing leads to the appearance of bistability even at room temperature. Moreover, such annealed microwire does not loose its bistability even at 46.5 °C due to stable nanocrystalline state of metallic core. Particularly, switching field is almost constant ~223 A/m in the temperature range from -195 °C up to -100 °C. However, switching field above -102 °C starts to drastically increase due to effect of superparamagnetism (which was described above) from 223 A/m at -102 °C up to 1004 A/m at 46 °C. Anyway, it is important that switching field changes noticeably in the temperature range from 35 °C up to 42 °C what is important temperature region for biomedical applications. Observed variation of the switching field in such temperature range is more than 18 % which is reasonable for biomedical applications.

Fig. 8.30 Temperature dependence of the switching field for annealed FeMo₉BCu microwire at 500 °C for 1 h under axial stress of 309 MPa



8.5.3 Applications

Compared to the other sensor, such as radio frequency identification sensors [98], the microwires have a significant advantage due to their small dimensions (~ 2 cm $\times 50$ µm). Only 2 cm piece of microwire is needed for the functional sensor and such sensor almost does not interfere with inner implant structure. Finally, the switching field values can be easily read by using contact less method [2, 99].

One possible application of glass-coated microwires is in various titanium implants (dental, knee joint, replacement of damaged skull part, reparation of femur, etc.) see Fig. 8.31. Value of the switching field can give us information whether inflammatory process starts or if body accepts the implant. For this purpose, one needs highest possible variation of the switching field in desired temperature range from 35 up to 42 °C for high accuracy of sensor.

Moreover, glass-coating serves as chemical (it avoids oxidation at higher temperatures) and electrical insulator. In addition, Pyrex glass-coated microwire can be considered as biocompatible materials.

First test of magnetic microwires for sensing the temperature of Ti implants was made using FeWB microwire [100, 101]. It was shown that the sensitivity of the switching field on temperature can even be enhanced by proper fixation of the wire on Ti implant. In this way, the sensitivity of the switching field was enhanced to 30% in the temperature range from 30 to 50% (see Fig. 8.32).

8.6 Stress Dependence of the Switching Field

8.6.1 Theory

As the magnetic properties of amorphous glass-coated microwires are determined by the magnetoelastic interaction of magnetic moment with the mechanical stresses, the switching field in microwires with high and positive magnetostriction

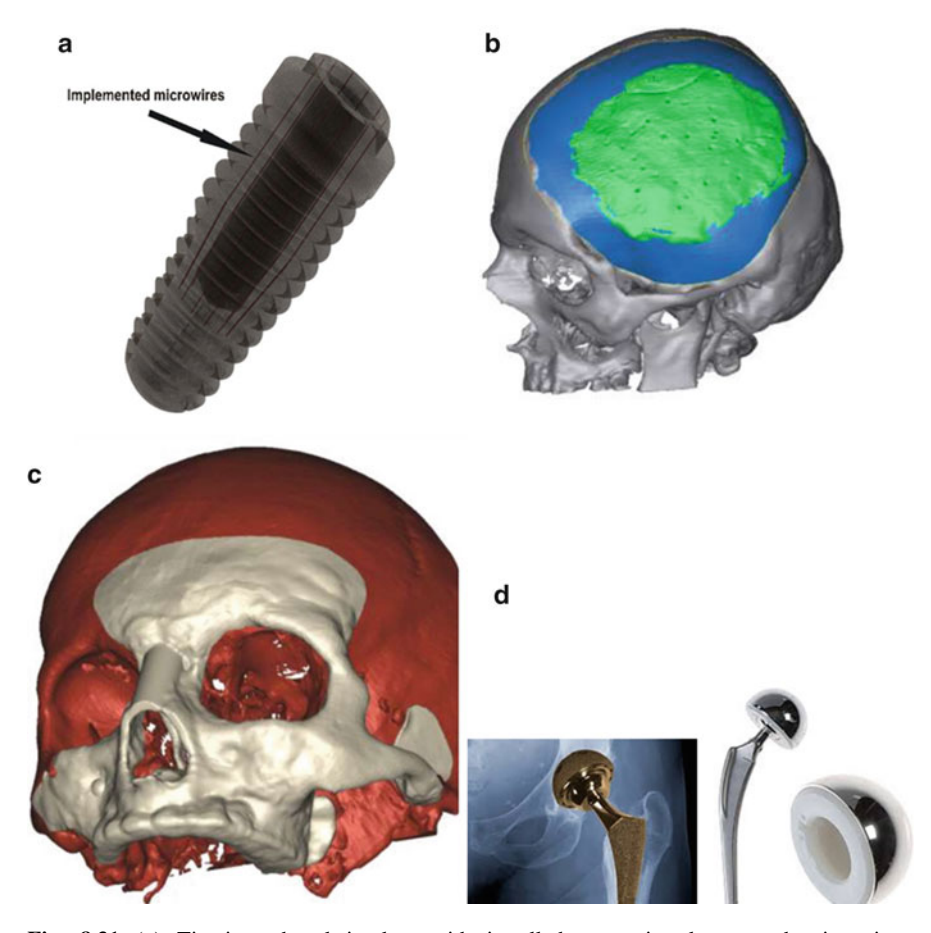
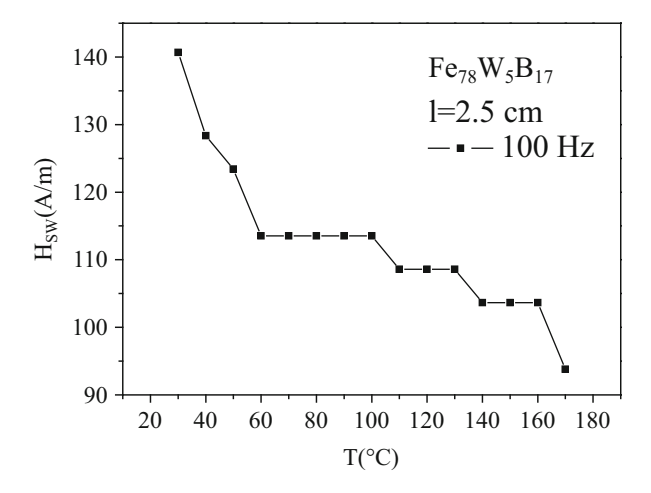


Fig. 8.31 (a) Titanium dental implant with installed magnetic glass-coated microwires, (b) titanium cranial implant, (c) titanium maxillofacial implant, and (d) titanium hip implant

Fig. 8.32 Temperature dependence of the switching field in the microwire fixed along the whole length



is very sensitive to the applied mechanical stress. Due to the different thermal expansion coefficient of the metallic nucleus and glass-coating, additional stresses are applied on metallic nucleus, hence the switching field is sensible to temperature, too. Apart from the magnetoelastic contribution to the switching field, there exists another contribution that arises from the structural relaxation of amorphous microwires. Such a contribution is sensitive not only to the temperature but also to the frequency of the exciting magnetic field. Hence, the variation of the frequency results in variation of the switching field temperature dependence. In such a way, one can tailor the temperature dependence—independence of the switching field according to desired conditions [32]. At constant frequency and temperature this contribution of stress to the switching field is proportional [24]:

$$H_{SW}^{\sigma} \approx \frac{\sqrt{\lambda_S \sigma}}{\mu_0 M_S},$$
 (8.21)

where M_s is the saturation magnetization, λ_s is the saturation magnetostriction, μ_0 is the magnetic permeability of vacuum, and σ is total stress.

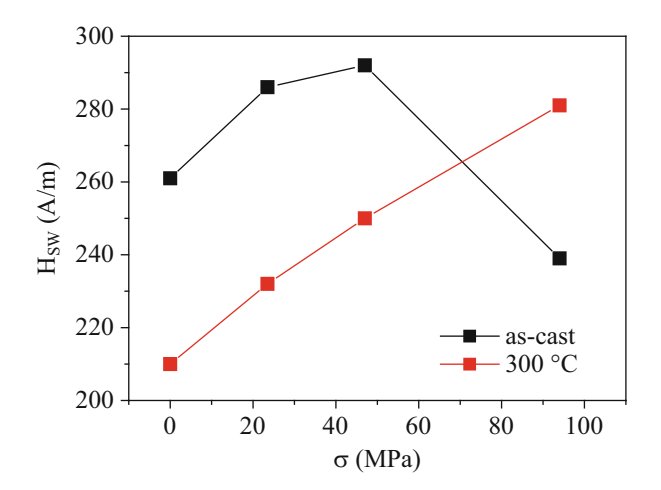
Few groups have been dedicated to the study of the stress dependence of the magnetic properties in glass-coated microwires [8, 26, 33, 102–106]; however, various results were obtained. In fact, the total stress σ in Eq. (8.8) is given by the sum of the stresses inducted during the microwires production (σ_i) together with the stresses applied on the microwire by glass-coating due to different thermal expansion coefficients of metallic nucleus and glass-coating (σ_{Δ}) and the stress applied on the microwires during measurement (σ_a):

$$\sigma = \sigma_i + \sigma_\Delta + \sigma_a \tag{8.22}$$

The strong and complex distribution of the stresses is introduced by drawing and rapid quenching into the wire during its production. As a result, the stress dependence of the switching field could also be complex giving the increase of the switching field at lower stresses and decrease at higher ones (Fig. 8.33) [8]. Also, the variation of the switching field is not so high as expected for the microwire with high magnetostriction. However, it can be enhanced by annealing out of the induced stress. Figure 8.33 shows that after annealing, the switching field amplitude decreases reflecting the relaxation of the structure. Moreover, the stress dependence of the switching field becomes pronounced reflecting the change in the relative strength of induced σ_i and applied σ_a stress on metallic nucleus of microwire. This points to the fact that stress dependence of the switching field can be induced in or induced out even after the production of the wire by properly selected post-production annealing.

The stress dependence of the switching field is also affected by the frequency. As it was given in Sect. 8.2.3, the two contributions to the switching field (magnetoelastic one and structural relaxation one) can be selectively pronounced by the frequency of excitation magnetic field. The stress dependence of the magnetoelastic contribution is given by the variation of the stress in Eq. (8.8). On the other hand, the stress dependence of the relaxation contribution is

Fig. 8.33 Stress dependence of the switching field for amorphous Fe-Ni-Si-B microwires annealed at different temperatures



represented by the stress dependence of the interaction energy of the mobile defects with spontaneous magnetization ε_p (as given in Eq. (8.12)). The interaction energy ε_p is given by a sum of three terms: magnetoelastic (ε_s), exchange (ε_{ex}), and dipole–dipole contribution (ε_d) [31, 107]:

$$\varepsilon_p = \varepsilon_S + \varepsilon_{ex} + \varepsilon_d \tag{8.23}$$

The most important in our case is the magnetoelastic contribution, ε_s , that is given by a local magnetoelastic energy:

$$\varepsilon_S \approx \lambda_S \sigma_i$$
 (8.24)

where σ_i denotes the local stress that surrounds the relaxing defects.

The stress dependence of the switching field for two different frequencies of external magnetic field is given in Fig. 8.34. At low frequency (50 Hz), the structural relaxation contribution prevails, which sensitivity to the stress is reduced in comparison to the magnetoelastic one. Hence, the switching field is weakly dependent on magnetic field. At high frequency (2 kHz), the magnetoelastic contribution to the switching field prevails. As a result, the switching field increases in the whole studied interval giving a variation of up to 100 % of the switching field within studied interval.

8.6.2 Applications

Once we are able to control the stress dependence of the switching field, it is possible to employ the microwires with positive magnetostriction as miniaturized sensing elements for stress monitoring.

Fig. 8.34 Stress dependences of the switching field measured at two different frequencies of the applied magnetic field

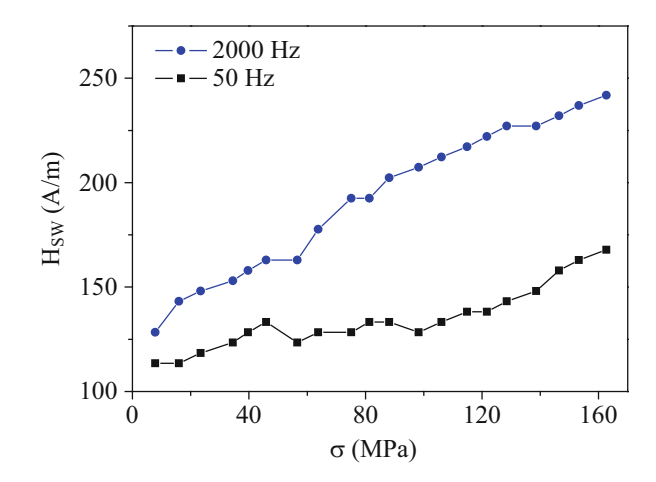


Fig. 8.35 The diameter of the microwire is smaller than size of sand's grains in concrete. The red arrows show the position of the wire



The first example is the use of microwires to monitor the stress in the concrete [108]. The diameter of the wire is smaller than the size of sand's grains and hence it does not act as a defect for the concrete (Fig. 8.35). Figure 8.36 shows the stress dependence of the switching field embedded into the concrete block when compressive stress was applied. It could be seen that the stress dependence follows the square root law given by Eq. (8.8).

Another possibility for application of the stress dependence of the switching field is the Structural Health monitoring in the glass- or carbon-fiber composites. The size of microwires is smaller than the glass-fibers and hence they can be successfully embedded inside the composite structure [2]. Figure 8.37 shows the comparison of two responses of the switching field on applied tensile stress in two glass-fiber composites. On the left side, there is a response in the composite where sliding appears between the glass-fibers. On the right side, there is a response of the switching field on tensile stress in correctly produced composite.

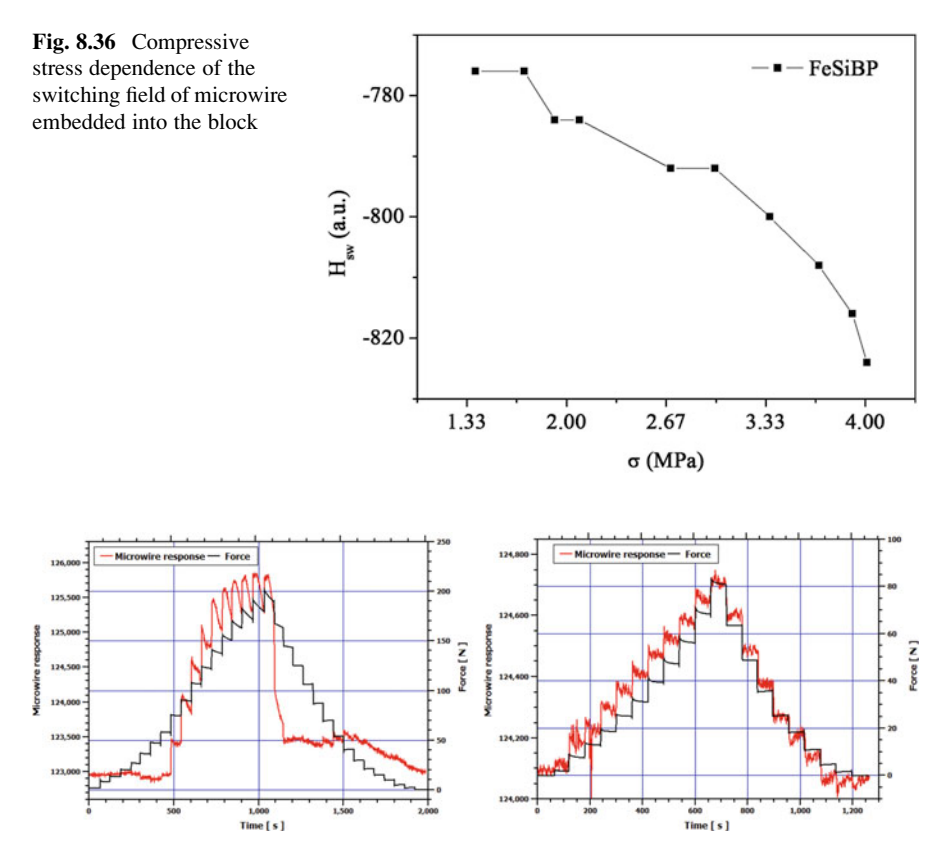


Fig. 8.37 Response of the switching field on the applied tensile stress in bad composite where the sliding between glass-fibers appeared (*left*) and correct composite (*right*)

8.7 Conclusions

Amorphous microwires with positive magnetostriction are characterized by magnetic bistability. The switching between the two stable magnetic configurations appears at the switching field. The switching field depends on the various external parameters like magnetic field, electrical current, temperature, mechanical stress, etc.

Almost any composition of microwires having positive magnetostriction can be used to sense magnetic field. Such a sensor is perfectly linear in a wide range of measured field. The range of the measured fields is determined only by excitation field.

The desired temperature dependence can be obtained by properly selecting the composition of the wire in order to enhance or to avoid one of the two contributions to the switching field (as both contributions have different temperature dependence). The required temperature dependence can even be annealed in or annealed

out. Finally, the temperature dependence of the switching field can also be tailored by the frequency of excitation magnetic field employing the different frequency dependencies of both contributions to the switching field.

When particular sensitivity of the switching field in selected temperature range is required, it can be obtained by playing with the Curie temperature. However, decrease of the Curie temperature leads to the decrease of saturation magnetostriction and to the lost of magnetic bistability. In such cases another effects must be considered (e.g., superparamagnetic effect in nanocrystalline structure).

Magnetoelastic anisotropy is the one that plays decisive role in determination of magnetic properties in microwires with positive magnetostriction. This act allows the easy application of microwires as sensing elements for monitoring the stress.

There are few more advantages of glass-coated microwires: Firstly, it is their simple production process that allows the production of large amount of microwires in a very short time. One of the biggest advantages of glass-coated microwires is their small dimensions that allow embedding of microwire into monitored material without destroying its mechanical properties. Additionally, glass-coating provides electrical and chemical insulation as well as biocompatibility. Finally, fast response on various external conditions is also important advantage.

All the above mentioned facts make the glass-coated microwires ideal materials for construction of miniaturized sensors.

Acknowledgments This work was supported by the project NanoCEXmat Nr. ITMS 26220120019, Slovak VEGA Grant Nos. 1/0164/16, 2/0192/13, APVV-0027-11, APVV-0266-10, and APVV-0492-11.

References

- Hudák, R., Varga, R., Živčák, J., Hudák, J., Blažek, J., Praslička, D.: Application of magnetic microwires in titanium implants—conception of intelligent sensoric implant. In: Madarász, L., Živčák, J. (eds.) Aspects of Computational Intelligence: Theory and Applications Topics in Intelligent Engineering and Informatics, pp. 413–434. Springer, Berlin, Heidelberg (2013)
- Praslička, D., Blažek, J., Šmelko, M., Hudák, J., Čverha, A., Mikita, I., Varga, R., Zhukov, A.: Possibilities of measuring stress and health monitoring in materials using contact-less sensor based on magnetic microwires. IEEE Trans. Magn. 49, 128–131 (2013). doi:10.1109/ TMAG.2012.2219854
- Vázquez, M.: Advanced magnetic microwires. In: Kronmüller, H., Parkin, S.S.P. (eds.) Handbook of Magnetism and Advanced Magnetic Materials, pp. 2193–2226. Wiley, Chichester (2007)
- Zhukov, A., Gonzalez, J., Vazquez, M., Larin, V., Torcunov, A.: Nanocrystalline and amorphous magnetic microwires. In: Nalwa, H.S. (ed.) Encyclopedia of Nanoscience and Nanotechnology, p. 23. Valencia, CA, American Scientific Publishers (2004)
- 5. Taylor, G.F.: A method of drawing metallic fillaments and a discussion of their properties and uses. Phys. Rev. 23, 655–660 (1924). doi:10.1103/PhysRev.23.655
- Klein, P., Varga, R., Vojtanik, P., Kovac, J., Ziman, J., Badini-Confalonieri, G.A., Vazquez, M.: Bistable FeCoMoB microwires with nanocrystalline microstructure and increased Curie temperature. J. Phys. D: Appl. Phys. 43(4), 045002-1–045002-6 (2010). doi:10.1088/0022-3727/43/4/045002

- Komova, E., Varga, M., Varga, R., Vojtanik, P., Bednarcik, J., Kovac, J., Provencio, M., Vazquez, M.: Nanocrystalline glass-coated FeNiMoB microwires. Appl. Phys. Lett. 93(6), 062502-1–062502-3 (2008). doi:10.1063/1.2969057
- Varga, R., Gamcova, J., Klein, P., Kovac, J., Zhukov, A.: Tailoring the switching field dependence on external parameters in magnetic microwires. IEEE Trans. Magn. 49(1), 30–33 (2013). doi:10.1109/TMAG.2012.2218224
- Li, L., Bao, C., Feng, X., Liu, Y., Fochan, L.: Fast switching thyristor applied in nanosecondpulse high-voltage generator with closed transformer core. Rev. Sci. Instrum. 84(2), 024703 (2013). doi:10.1063/1.4792593
- 10. Herzer, G.: Modern soft magnets: amorphous and nanocrystalline materials. Acta Mater. **61** (3), 718–734 (2013). doi:10.1016/j.actamat.2012.10.040
- Michalik, S., Gamcova, J., Bednarčík, J., Varga, R.: In situ structural investigation of amorphous and nanocrystalline Fe₄₀Co₃₈Mo₄B₁₈ microwires. J. Alloys Compd. **509**(7), 3409–3412 (2011). doi:10.1016/j.jallcom.2010.12.098
- Klein, P., Varga, R., Badini-Confalonieri, G.A., Vazquez, M.: Study of domain structure and magnetization reversal after thermal treatments in Fe₄₀Co₃₈Mo₄B₁₈ microwires. J. Magn. Magn. Mater. 323(24), 3265–3270 (2011). doi:10.1016/j.jmmm.2011.07.027
- Klein, P., Varga, R., Vázquez, M.: Stable and fast domain wall dynamics in nanocrystalline magnetic microwire. J. Alloys Compd. 550, 31–34 (2013). doi:10.1016/j.jallcom.2012.09. 098
- 14. Cullity, B.D.: Introduction to Magnetic Materials. Wiley, Hoboken (1972)
- Varga, R., Garcia, K.L., Zhukov, A., Vazquez, M., Vojtanik, P.: Temperature dependence of the switching field and its distribution function in Fe-based bistable microwire. Appl. Phys. Lett. 83, 2620 (2003). doi:10.1063/1.1613048
- Klein, P., Varga, R., Badini-Confalonieri, G.A., Vazquez, M.: Study of the switching field in amorphous and nanocrystalline FeCoMoB microwire. IEEE Trans. Magn. 46, 357–360 (2010). doi:10.1109/TMAG.2009.2033348
- Varga, R., Zhukov, A., Zhukova, V., Blanco, J.M., Gonzalez, J.: Supersonic domain wall in magnetic microwires. Phys. Rev. B. 76, 132406-1–132406-3 (2007). doi:10.1103/PhysRevB. 76.132406
- Varga, R., Garcia, K.L., Vazquez, M., Vojtanik, P.: Single-domain wall propagation and damping mechanism during magnetic switching of bistable amorphous microwires. Phys. Rev. Lett. 94, 017201 (2005). doi:10.1103/PhysRevLett.94.017201
- Varga, R., Richter, K., Zhukov, A., Larin, V.: Domain wall propagation in thin magnetic wires. IEEE Trans. Magn. 44(11), 3925–3930 (2008). doi:10.1109/TMAG.2008.2001997
- Richter, K., Varga, R., Badini-Confalonieri, G.A., Vazquez, M.: The effect of transverse field on fast domain wall dynamics in magnetic microwires. Appl. Phys. Lett. 96, 182507 (2010). doi:10.1063/1.3428367
- Olivera, J., Sánchez, M.L., Prida, V.M., Varga, R., Zhukova, V., Zhukov, A.P., Hernando, B.: Temperature dependence of the magnetization reversal process and domain structure in Fe_{77.5-x}Ni_xSi_{7.5}B₁₅ magnetic microwires. IEEE Trans. Magn. **44**(11), 3946–3949 (2008). doi:10.1109/TMAG.2008.2002194
- Vazquez, M., Zhukov, A., Pirota, K.R., Varga, R., Garcia, K.L., Luna, C., Provencio, M., Navas, D., Martinez, J.L., Hernandez-Velez, M.: Temperature dependence of remagnetization process in bistable magnetic microwires. J. Non-Cryst. Solids. 329, 123–130 (2003). doi:10.1016/j.jnoncrysol.2003.08.025
- Vázquez, M., Zhukov, A.P., Garcia, K.L., Pirota, K.R., Ruiz, A., Martinez, J.L., Knobel, M.: Temperature dependence of magnetization reversal in magnetostrictive glass-coated amorphous microwires. Mater. Sci. Eng. A. 375–377, 1145–1148 (2004). doi:10.1016/j.msea. 2003.10.200
- Vazquez, M., Hernando, A.: A soft magnetic wire for sensor applications. J. Phys. D: Appl. Phys. 29, 939–949 (1996). doi:10.1088/0022-3727/29/4/001

- Gonzalez, J., Blanco, J.M., Vazquez, M., Barandiaran, J.M., Rivero, G., Hernando, A.: Influence of the applied tensile stress on the magnetic properties of current annealed amorphous wires. J. Appl. Phys. 70, 6522–6524 (1991). doi:10.1063/1.349894
- Aragoneses, P., Blanco, J.M., Dominguez, L., Gonzalez, J., Zhukov, A., Vazquez, M.: The stress dependence of the switching field in glass-coated amorphous microwires. J. Phys. D: Appl. Phys. 31(21), 3040–3045 (1998). doi:10.1088/0022-3727/31/21/009
- O'Handley, R.C.: Magnetostrictin of transition-metal-metalloid glasses: temperature dependence. Phys. Rev. B. 18, 930–938 (1978). doi:10.1103/PhysRevB.18.930
- Hernando, A., Madurga, V., Núnez de Villavicencio, C., Vazquez, M.: Temperature dependence of the magnetostriction constant of nearly zero magnetostriction amorphous alloys. Appl. Phys. Lett. 45(7), 802 (1984). doi:10.1063/1.95371
- Richter, K., Varga, R., Zhukov, A.: Influence of the magnetoelastic anisotropy on the domain wall dynamics in bistable amorphous wires. J. Phys.: Condens. Matter. 24, 296003 (2012). doi:10.1088/0953-8984/24/29/296003
- Chen, D.X., Dempsey, N.M., Vazquez, M., Hernando, A.: Propagating domain wall shape and dynamics in iron-rich amorphous wires. IEEE Trans. Magn. 31(1), 781–790 (1995). doi:10.1109/20.364597
- 31. Kronmüller, H.: Theory of the coercive field in amorphous ferromagnetic alloys. J. Magn. Magn. Mater. 24(2), 159–167 (1981). doi:10.1016/0304-8853(81)90010-X
- Sabol, R., Varga, R., Hudak, J., Blazek, J., Praslicka, D., Vojtanik, P., Badini, G., Vazquez, M.: J. Appl. Phys. 111, 053919 (2012). doi:10.1063/1.3691961
- Sabol, R., Varga, R., Hudak, J., Blazek, J., Praslicka, D., Vojtanik, P., Badini, G., Vazquez, M.: Stress dependence of the switching field in glass-coated microwires with positive magnetostriction. J. Magn. Magn. Mater. 325, 141–143 (2013). doi:10.1016/j.jmmm.2012. 08.030
- 34. Sabol, R.: Technické aplikácie magnetických mikrodrôtov. Dissertation, Faculty of Aeronautics, Technical University of Kosice (2012)
- 35. Varga, R., Garcia, K.L., Luna, C., Zhukov, A., Vojtanik, P., Vazquez, M.: Distribution and temperature dependence of switching field in bistable magnetic amorphous microwires. Recent Res. Dev. Non-Cryst. Solids. 3, 85 (2003)
- Chiriac, H., Ovari, T.A.: Switching field calculations in amorphous microwires with positive magnetostriction. J. Magn. Magn. Mater. 249(1–2), 141–145 (2002). doi:10.1016/S0304-8853(02)00522-X
- 37. Mohri, K., Humprey, F.B., Kawashima, K., Kimura, K., Mizutani, M.: Large Barkhausen and Matteucci effects in FeCoSiB, FeCrSiB, and FeNiSiB amorphous wires. IEEE Trans. Magn. **26**(5), 1789 (1990). doi:10.1109/20.104526
- Vojtanik, P., Degro, J., Nielsen, O.V.: Magnetic after effects in (Co_{1-x}Fe_x)₇₅Si₁₅B₁₀ metallic glasses. Acta Phys. Slov. 42(6), 364–369 (1992)
- Degro, J., Vojtanik, P., Nielsen, O.V.: Effect of field annealing on compositional dependences of some magnetic properties in (Co_{1-x}Fe_x)₇₅Si₁₅B₁₀ metallic glasses. Phys. Status Solidi A. 132(1), 183–189 (1992). doi:10.1002/pssa.2211320120
- Ramanujan, R.V., Du, S.W.: Nanocrystalline structures obtained by the crystallization of an amorphous Fe₄₀Ni₃₈B₁₈Mo₄ soft magnetic alloy. J. Alloys Compd. 425(1–2), 251–260 (2006). doi:10.1016/j.jallcom.2005.10.096
- Andrejco, R., Varga, R., Marko, P., Vojtanik, P.: Magnetic properties of amorphous and nanocrystalline Fe-Ni-Mo-B alloys. Czech. J. Phys. 52(1), A113–A116 (2002). doi:10.1007/ s10582-002-0026-z
- Li, J., Su, Z., Wei, F., Yang, Z., Hahn, H., Wang, T., Ge, S.: Magnetic properties of nanostructured Fe₄₀Ni₃₈Mo₄B₁₈. Chin. Phys. Lett. 16(3), 211–213 (1999). doi:10.1088/ 0256-307X/16/3/020
- 43. Vojtanik, P., Varga, R., Andrejco, R., Agudo, P.: The evolution of magnetic properties of Fe_{73.5}Cu₁Nb₃Si_{13.5}B₉ microwires during the devitrification process. J. Magn. Magn. Mater. **249**(1–2), 136–140 (2002). doi:10.1016/S0304-8853(02)00521-8

- 44. Yoshizawa, Y., Oguma, S., Yamauchi, K.: New Fe-based soft magnetic alloys composed of ultrafine grain structure. J. Appl. Phys. **64**, 6044 (1988). doi:10.1063/1.342149
- 45. Hernando, B., Olivera, J., Sánchez, M.L., Prida, V.M., Pérez, M.J., Santos, J.D., Gorria, P., Belzunce, F.J.: Soft magnetic properties, magnetoimpedance and torsion-impedance effects in amorphous and nanocrystalline FINEMET alloys: comparison between ribbons and wires. Phys. Met. Metallogr. 102(1), S13–S20 (2006). doi:10.1134/S0031918X06140043
- 46. Olivera, J., Varga, R., Prida, V.M., Sanchez, M.L., Hernando, B., Zhukov, A.: Domain wall dynamics during the devitrification of Fe_{73.5}CuNb₃Si_{11.5}B₁₁ magnetic microwires. Phys. Rev. B. 82(9), 094414 (2010). doi:10.1103/PhysRevB.82.094414
- McHenry, M.E., Willard, M.A., Laughlin, D.E.: Amorphous and nanocrystalline materials for applications as soft magnets. Prog. Mater. Sci. 44(4), 291–433 (1999). doi:10.1016/ S0079-6425(99)00002-X
- 48. Li, H.F., Laughlin, D.E., Ramanujan, R.V.: Nanocrystallisation of an Fe_{44.5}Co_{44.5}Zr₇B₄ amorphous magnetic alloy. Philos. Mag. **86**(10), 1355–1372 (2006). doi:10.1080/14786430500380142
- Mohanta, O., Ghosh, M., Mitra, A., Panda, A.K.: Enhanced ferromagnetic ordering through nanocrystallization in cobalt incorporated FeSiBNb alloys. J. Phys. D: Appl. Phys. 42(6), 065007 (2009). doi:10.1088/0022-3727/42/6/065007
- Gercsi, Z.S., Mazaleyrat, F., Varga, L.K.: High-temperature soft magnetic properties of Co-doped nanocrystalline alloys. J. Magn. Magn. Mater. 302(2), 454–458 (2006). doi:10. 1016/j.jmmm.2005.10.014
- Škorvanek, I., Švec, P., Marcin, J., Kovac, J., Krenicky, T., Deanko, M.: Nanocrystalline Cu-free HITPERM alloys with improved soft magnetic properties. Phys. Status Solidi A. 196 (1), 217–220 (2003). doi:10.1002/pssa.200306390
- 52. Vlasak, G., Pavuk, M., Mrafko, P., Janičkovič, D., Švec, P., Butvinova, B.: Influence of heat treatment on magnetostrictions and electrical properties of (Fe₁Co₁)₇₆Mo₈Cu₁B₁₅. J. Magn. Magn. Mater. 320(20), e837–e840 (2008). doi:10.1016/j.jmmm.2008.04.168
- 53. Conde, C.F., Conde, A.: Microstructure and magnetic properties of Mo containing Nanoperm-type alloys, Rev. Adv. Mater. Sci. **18**(6), 565–571 (2008)
- 54. Ping, D.H., Wu, Y.Q., Hono, K., Willard, M.A., McHenry, M.E., Laughlin, D.E.: Microstructural characterization of $(Fe_{0.5}Co_{0.5})_{88}Zr_7B_4Cu_1$ nanocrystalline alloys. Scr. Mater. **45** (7), 781–786 (2001). doi:10.1016/S1359-6462(01)01096-X
- 55. Klein, P., Varga, R., Vazquez, M.: Domain wall dynamics in nanocrystalline microwires. Phys. Status Solidi C. 11(5–6), 1139–1143 (2014). doi:10.1002/pssc.201300707
- Klein, P., Varga, R., Vazquez, M.: Enhancing the velocity of the single domain wall by current annealing in nanocrystalline FeCoMoB microwires. J. Phys. D: Appl. Phys. 47, 255001 (2014). doi:10.1088/0022-3727/47/25/255001
- 57. Klein, P., Varga, R., Komanicky, V., Badini-Confalonieri, G.A., Vazquez, M.: Effect of current annealing on domain wall dynamics in bistable FeCoMoB microwires. Solid State Phenom. 233–234, 281–284 (2015). doi:10.4028/www.scientific.net/SSP.233-234.281
- Chiriac, H., Ovari, T.A.: Amorphous glass-covered magnetic wires: preparation, properties, applications. Prog. Mater. Sci. 40, 333–407 (1996). doi:10.1016/S0079-6425(97)00001-7
- 59. Chiriac, H., Lupu, N., Dobrea, V., Corodeanu, S.: Mechanical properties of magnetic Fe-based and Co-based amorphous wires and microwires. Phys. Status Solidi A. **206**, 648–651 (2009). doi:10.1002/pssa.200881269
- 60. Inoue, A.: Stabilization of metallic supercooled liquid and bulk amorphous alloys. Acta Mater. 48(1), 279–306 (2000). doi:10.1016/S1359-6454(99)00300-6
- Kaloshikin, S.D., Tomilin, I.A., Jalnin, B.V., Kekalo, I.B., Shelekhov, E.V.: The influence of amorphous alloys composition on kinetics of crystallization with the nanocrystalline structure formation. Mater. Sci. Forum. 179–181, 557–562 (1995). doi:10.4028/www.scientific.net/ MSF.179-181.557

- 62. Mattern, N., Danzig, A., Muller, M.: Influence of additions on crystallization and magnetic properties of amorphous Fe_{77.5}Si_{15.5}B₇. Mater. Sci. Forum. **179–181**, 539–544 (1995). doi:10. 4028/www.scientific.net/MSF.179-181.539
- Mattern, N., Danzig, A., Muller, M.: Effect of Cu and Nb on crystallization and magnetic properties of amorphous Fe_{77.5}Si_{15.5}B₇ alloys. Mater. Sci. Eng. A. 194(1), 77–85 (1995). doi:10.1016/0921-5093(94)09666-X
- Zhang, Y.R., Ramanujan, R.V.: The effect of niobium alloying additions on the crystallization of a Fe-Si-B-Nb alloy. J. Alloys Compd. 403(1-2), 197-205 (2005). doi:10.1016/j.jallcom.2005.05.019
- 65. Naohara, T.: The role of Nb in the nanocrystallization of amorphous Fe-Si-B-Nb alloys. Acta Mater. 46(2), 397–404 (1998). doi:10.1016/S1359-6454(97)00271-1
- Klein, P., Richter, K., Varga, R., Vazquez, M.: Frequency and temperature dependencies of the switching field in glass-coated FeSiBCr microwire. J. Alloys Compd. 569, 9–12 (2013). doi:10.1016/j.jallcom.2013.03.040
- 67. Varga, R., Vojtanik, P., Kovac, J., Agudo, P., Vazquez, M., Lovas, A.: Influence of Cr on magnetic and structural properties of amorphous Fe_{80-x}Cr_xSi₆B₁₄ (x=0-14) alloys. Acta Phys. Slovaca. **49**(5), 901–904 (1999)
- Lupu, N., Chiriac, H., Corodeanu, S., Ababei, G.: Development of Fe–Nb–Cr–B glassy alloys with low curie temperature and enhanced soft magnetic properties. IEEE Trans. Magn. 47 (10), 3791–3794 (2011). doi:10.1109/TMAG.2011.2158528
- 69. Varga, R., Vojtanik, P.: Temperature dependence of the magnetic properties of amorphous Fe_{80-x}Cr_xSi₆B₁₄ (x=0-14) alloys. J. Magn. Magn. Mater. **196–197**, 230–232 (1999). doi:10. 1016/S0304-8853(98)00777-X
- 70. Makino, A., Kubota, T., Chang, C., Makabe, M., Inoue, A.: FeSiBP bulk metallic glasses with high magnetization and excellent magnetic softness. J. Magn. Magn. Mater. **320**(20), 2499–2503 (2008). doi:10.1016/j.jmmm.2008.04.063
- Richter, K., Varga, R., Infante, G., Badini-Confalonieri, G.A., Vazquez, M.: Domain wall dynamics in thin magnetic wires under the influence of transversal magnetic field. IEEE Trans, Magn. 46(2), 210–212 (2010). doi:10.1109/TMAG.2009.2032517
- Infante, G., Varga, R., Badini-Confalonieri, G.A., Vázquez, M.: Locally induced domain wall damping in a thin magnetic wire. Appl. Phys. Lett. 95, 012503 (2009). doi:10.1063/1. 3174919
- Varga, R., Infante, G., Badini-Confalonieri, G.A., Vázquez, M.: Diffusion-damped domain wall dynamics. J. Phys.: Conf. Ser. 200, 042026 (2010). doi:10.1088/1742-6596/200/4/ 042026
- Varga, R., Infante, G., Richter, K., Vázquez, M.: Anomalous effects in the domain-wall dynamics in magnetic microwires. Phys. Status Solidi A. 208, 509–514 (2011). doi:10.1002/ pssa.201026371
- 75. Chateau, E., Remy, L.: Oxidation-assisted creep damage in a wrought nickel-based superalloy: experiments and modelling. Mater. Sci. Eng. A. **527**(7–8), 1655–1664 (2010). doi:10. 1016/j.msea.2009.10.054
- Pollock, T.M., Tin, S.: Nickel-based superalloys for advanced turbine engines: chemistry microstructure and properties. J. Propul. Power. 22(2), 361–374 (2006). doi:10.2514/1.18239
- 77. Romankiw, L.T.: A path: from electroplating through lithographic masks in electronics to LIGA in MEMS. Electrochim. Acta. **42**(20–22), 2985–3005 (1997). doi:10.1016/S0013-4686 (97)00146-1
- 78. Zhang, Z.Y., Liang, B.N.: Tribological properties of FeNiCr coatings with the addition of La₂O₃ on 1045 carbon steel. Adv. Mater. Res. 852, 219–222 (2014). doi:10.4028/www. scientific.net/AMR.852.219
- Du Trémolet De Lacheisserie, E., Krishnan, R.: An improved capacitance method of measuring thermal expansion and magnetostriction of amorphous ribbons: application to FeNiCr metallic glasses. Rev. Phys. Appl. 18(11), 727–730 (1983)

- 80. Krishnan, R., Dancygier, M., Tarhouni, M.: Magnetization studies of Cr concentration effects in amorphous Fe–Ni–Cr–B–Si ribbons. J. Appl. Phys. **53**, 7768–7770 (1982). doi:10.1063/1. 330200
- 81. Chen, W., Zhou, S., Chen, J.: Magnetic properties of Fe- and FeNi-based amorphous composite ribbons. J. Mater. Sci. Technol. **16**(02), 151–152 (2000)
- Lovas, A., Böhönyey, A., Kiss, L.F., Kováč, J., Németh, P.: Some new results on amorphous Curie-temperature relaxation. Mater. Sci. Eng. A. 375–377, 1097–1100 (2004). doi:10.1016/j.msea.2003.10.143
- 83. Németh, P., Böhönyey, A., Tichý, G., Kiss, L.F.: Anomalous Curie-point relaxation in a Cr-containing amorphous alloy. J. Magn. Magn. Mater. **320**(5), 719–723 (2008). doi:10. 1016/j.jmmm.2007.08.025
- 84. Alvarez-Alonso, P., Santos, J.D., Perez, M.J., Sanchez-Valdes, C.F., Sanchez Llamazares, J. L., Gorria, P.: The substitution effect of chromium on the magnetic properties of (Fe_{1-x}Cr_x)₈₀Si₆B₁₄ metallic glasses (0.02≤x≤0.14). J. Magn. Magn. Mater. **347**, 75–78 (2013). doi:10.1016/j.jmmm.2013.07.048
- 85. Hilzinger, R., Rodewald, W.: Magnetic Materials: Fundamentals, Products, Properties, Applications. Publicis MCD Verlag, Erlangen (2013)
- Antonione, C., Battezzati, L., Lucci, A., Riontino, G., Tabasso, M., Venturello, G.: Effect of composition in (Fe,Ni,Cr)(P,B) and (Fe,Ni,Mo)B metallic glasses. J. Phys. Colloq. 41, C8-131–C8-134 (1980). doi:10.1051/jphyscol:1980834
- 87. Chiriac, H., Ovári, T.A., Pop, G.: Internal stress distribution in glass-covered amorphous magnetic wires. Phys. Rev. B. 52, 10104–10113 (1995). doi:10.1103/PhysRevB.52.10104
- Antonov, A.S., Borisov, V.T., Borisov, O.V., Prokoshin, A.F., Usov, N.A.: Residual quenching stresses in glass-coated amorphous ferromagnetic microwires. J. Phys. D: Appl. Phys. 33(10), 1161–1168 (2000). doi:10.1088/0022-3727/33/10/305
- Larin, V.S., Torcunov, A.V., Zhukov, A., Gonzalez, J., Vazquez, M., Panina, L.: Preparation and properties of glass-coated microwires. J. Magn. Magn. Mater. 249(1–2), 39–45 (2002). doi:10.1016/S0304-8853(02)00501-2
- Klein, P., Varga, R., Vazquez, M.: Temperature dependence of magnetization process in bistable amorphous and nanocrystalline FeCoMoB microwires. Acta Phys. Pol. A. 118, 809–810 (2010)
- 91. Hernando, A., Marin, P., Vazquez, M., Barandiaran, J.M., Herzer, G.: Thermal dependence of coercivity in soft magnetic nanocrystals. Phys. Rev. B. **58**(1), 366–370 (1998). doi:10.1103/PhysRevB.58.366
- 92. Škorvánek, I., O'Handley, R.C.: Fine-particle magnetism in nanocrystalline Fe-Cu-Nb-Si-B at elevated temperatures. J. Magn. Magn. Mater. 140-144(1), 467–468 (1995). doi:10.1016/0304-8853(94)00734-9
- 93. Škorvánek, I., Kováč, J., Kötzler, J.: Temperature evolution of coercive field and thermal relaxation effects in nanocrystalline FeNbB alloys. J. Magn. Magn. Mater. **272–276**, 1503–1505 (2004). doi:10.1016/j.jmmm.2003.12.553
- 94. Franco, V., Conde, C.F., Conde, A., Kiss, L.F., Kemény, T.: Transition to superparamagnetism in a Cr-containing Finemet-type alloy. IEEE Trans. Magn. 38(5), 3069–3074 (2002). doi:10.1109/TMAG.2002.802115
- 95. Varga, R., Vojtanik, P., Lovas, A.: Time and thermal stability of magnetic properties of amorphous Fe₈₀TM₃B₁₇ alloys. J. Phys. IV (France). **08**, Pr2-63–Pr2-66 (1998)
- Gonzalez, J., Zhukov, A., Zhukova, V., Cobeno, A.F., Blanco, J.M., de Arellano-Lopez, A.R., Lopez-Pombero, S., Martinez-Fernandez, J., Larin, V., Torcunov, A.: High coercivity of partially devitrified glass-coated Finemet microwires: effect of geometry and thermal treatment. IEEE Trans. Magn. 36(5), 3015–3017 (2000). doi:10.1109/20.908660
- 97. Hudak, R., Varga, R., Polacek, I., Klein, P., Skorvanek, I., Komanicky, V., del Real, R.P., Vazquez, M.: Addition of a Molybdenum into a amorphous glass-coated microwires usable as a temperature sensors in biomedical application. Phys. Status Solidi A. **213**, 377–383 (2015)

- 98. Bergmann, G., Graichen, F., Dymke, J., Rohlmann, A., Duda, G.N., Damm, R.: High-tech hip implant for wireless temperature measurements in vivo. PLoS One. **7**(8), e43489 (2012). doi:10.1371/journal.pone.0043489
- Sabol, R., Rovnak, M., Klein, P., Vazquez, M., Varga, R.: Mechanical stress dependence of the switching field in amorphous microwires. IEEE Trans. Magn. 51, 2000304-1–2000304-4 (2015). doi:10.1109/TMAG.2014.2357580
- 100. Hudak, R., Varga, R., Hudak, J., Praslicka, D., Polacek, I., Klein, P., El Kammouni, R., Vazquez, M.: Influence of fixation on magnetic properties of glass-coated magnetic microwires for biomedical applications. IEEE Trans. Magn. 51(1), 5200104 (2015). doi:10.1109/TMAG.2014.2359498
- 101. Hudak, R., Varga, R., Hudak, J., Praslicka, D., Blazek, J., Polacek, I., Klein, P.: Effect of the fixation patterns on magnetic characteristics of amorphous glass-coated sensoric microwires. Acta Phys. Pol. A. 126(1), 417–418 (2014). doi:10.12693/APhysPolA.126.417
- 102. Gamcova, J., Varga, R., Hernando, B., Zhukov, A.: The study of magnetization process in amorphous FeNiSiB microwires. Acta Phys. Pol. A. 118(5), 807–808 (2010)
- 103. Komova, E., Varga, M., Varga, R., Vojtanik, P., Torrejon, J., Provencio, M., Vazquez, M.: Frequency dependence of the single domain wall switching field in glass-coated microwires. J. Phys.: Condens. Matter. 19(23), 236229 (2007). doi:10.1088/0953-8984/19/23/236229
- 104. Varga, R.: Magnetization processes in glass-coated microwires with positive magnetostriction. Acta Phys. Slovaca. 62(5), 411–518 (2012). doi:10.2478/v10155-012-0002-5
- 105. Komova, E., Varga, M., Varga, R., Vojtanik, P., Torrejon, J., Provencio, M., Vazquez, M.: Stress dependence of the switching field in glass coated microwires. Acta Phys. Pol. A. 113 (1), 135–138 (2008)
- 106. Olivera, J., Varga, R., Anaya, J., Zhukov, A.: Stress dependence of switching field during the devitrification of Finemet-based magnetic microwires. Key Eng. Mater. 543, 495–498 (2013). doi:10.4028/www.scientific.net/KEM.543.495
- 107. Kronmüller, H., Fähnle, M.: Micromagnetism and the Microstructure of the Ferromagnetic Solids. Cambridge University Press, Cambridge (2003)
- 108. Olivera, J., González, M., Fuente, J.V., Varga, R., Zhukov, A., Anaya, J.J.: An embedded stress sensor for concrete shm based on amorphous ferromagnetic microwires. Sensors. 14, 19963–19978 (2014). doi:10.3390/s141119963

A Amorphous alloys ribbons, 49 microwire, 2–20, 26, 27, 53, 54, 66, 67, 69, 70, 72, 85, 92–95, 97, 99, 101, 104–106, 116, 120, 127, 132, 144, 148, 154, 159–161, 170, 171, 174, 184, 189–191,	B Bamboo domain walls, 92, 105–106 Biocompatible, 132, 153, 154, 165, 200 Biomedical application, 165, 196–200 Bistability, 2, 14, 15, 18, 24, 123, 152, 164, 170, 186, 195, 196, 199, 205, 206
199, 202, 205 structure, 21, 25, 154, 176, 177, 185, 188, 189, 191 wire, 2, 3, 60, 64, 71, 78–80, 85, 96–104,	C Cobalt (Co) alloys, 33, 60, 132 Coordinate: 8, 11, 20, 24, 26, 160, 164, 171
106, 140, 141 Anisotropy	Coercivity, 8, 11, 20, 24, 26, 160, 164, 171, 176, 183
Anisotropy constant, 93, 94, 118, 178 field, 9, 10, 13, 35, 39, 42, 44, 46, 48, 77, 78, 81, 86, 93–95, 98, 100, 101, 105, 132, 140, 141, 143, 145, 148 helical, 44, 91–107, 111, 112, 116–121, 126, 127, 131, 135, 140, 141 induced, 14, 39, 41–44, 49 magnetoelastic, 3, 5, 17, 27, 33, 112, 154, 169, 175, 178, 187, 194, 197–199 transverse induced, 9, 40, 46, 48, 49	176, 183 Cold drawn, 71–75, 78, 79, 85 Composite, 1, 53, 86, 111, 131, 132, 142, 144–148, 153, 169, 182, 193, 204, 205 Contact-less sensing, 142, 200 Co-rich microwire, 5, 9, 10, 14, 18, 27, 92–107, 156, 157, 166 Crystallization, 4, 20–26, 28, 37, 42, 44, 48, 63, 155, 184, 186, 188, 191–193, 195, 199
Annealing current, 10, 12, 34, 36, 40–41, 46–49, 177 stress, 36, 40–41, 44, 49, 177 temperature, 9, 11, 20, 21, 23, 24, 36, 183–186, 191, 192, 198 time, 9, 10, 21, 46	D DC bias current, 39, 44, 99, 100, 103–105, 107 Demagnetizing field, 93, 96 Devitrification, 4, 24, 26 Differential scanning calorimetry (DSC), 37, 38

Domain structure, 14, 18, 25, 44, 75, 79, 106, 112, 114, 115, 120–124, 126, 127, 131, 154, 155, 165, 169, 170, 174–176, 191, 193, 194 Domain wall (DW) nucleation, 112 propagation, 2, 8, 13, 14, 26, 27, 112, 152, 164, 170, 182, 196 velocity, 2, 13, 15–19, 112, 174 Ductility, 71–73, 85	H Heating inductive, 151–166 Joule, 46–48 High-frequency properties, 99 Hitperm, 26, 28, 29, 185, 186 Hyperthermia, 151–166 Hysteresis loop, 2–14, 18, 21, 24, 26, 27, 29, 38–39, 42, 82, 116–118, 120–127, 155, 161, 170, 179, 187
E Easy anisotropy axis, 93, 98 Eddy current, 17, 153, 162 Electrodynamics properties, 92, 101	I Impedance diagonal, 41–44, 46 imaginary, 43
Electromagnetic field, 134	non-diagonal, 39, 43–45, 104 real, 43–45
radiation, 134 wave, 132, 134, 140 Electro-motive force (EMF), 95, 104	Industrial application, 1, 4 Inflammatory process, 200
Exchange constant, 96	J
F	Joule effect heating, 153
Ferromagnetic material, 36, 131, 153	
resonance, 35, 42, 43, 48, 49, 127 Fracture, 64–70, 72, 75, 85 Frequency, 8, 33–49, 69, 94, 111, 132, 152, 178	L Landau–Lifshitz–Gilbert (LLG) equation, 34, 35, 97
requercy, 6, 55–47, 07, 74, 111, 152, 152, 176	Losses hysteresis, 153, 162
G Giant magneto-impedance (GMI) effect	magnetic, 137, 145
diagonal, 34, 41, 42, 44, 78, 91, 97, 101, 103, 107	M
off-diagonal, 34, 43, 91, 92, 97, 98, 100, 103–106 ratio, 2, 9–11, 13, 34, 47, 48, 75–78, 80, 81,	Magnetic anisotropy, 9, 10, 13, 14, 36, 40, 41, 46, 48, 49, 77, 78, 91–98, 101, 105, 106,
86, 91 Glass-coated microwire, 2–5, 7–9, 18, 20, 25, 91, 93, 94, 152–155, 160, 162, 164–166,	111–113, 115, 117–121, 123, 124, 126–128, 131, 132, 154, 174, 197 charge, 96
169, 170, 177, 182, 183, 192, 193, 200–202, 206	damping constant, 92, 98, 102, 103, 105 defects, 92
Glass-coating, 6, 152, 153, 165, 169, 174, 176, 184, 187, 190, 191, 193, 198, 199, 202, 206	entropy, 83, 84 field, 2, 34, 75, 91, 111, 132, 152, 169–206
Glass transition point, 94 Grain size, 4, 20, 23, 25, 26	materials, 1, 4, 9, 33, 40, 75, 111, 152, 158 sensors, 1, 33, 111, 112, 128, 151, 152

Magnetization	P
circular, 92, 95, 97–101, 106, 116, 117,	Penetration depth, 2, 34
119, 121, 126	Permeability, 1, 9, 11, 16, 26, 34, 35, 40, 42,
longitudinal, 43, 95, 106	44, 48, 80, 92, 98, 101–103, 112,
remanent, 8, 171, 189	127, 128, 135, 140, 141, 147, 148,
reversal, 99, 100, 103, 106, 111–113, 115,	154, 171, 202
117–121, 123, 124, 126–128	Permittivity, 135, 141, 142, 144–147
rotation, 35, 94, 100	Plasticity, 66, 67
saturation, 164, 185	Polarization
vector, 78, 93, 95–97, 99–101, 103, 127 Magnetocaloric	electric, 131–138, 140–142, 144, 145, 147, 148
effect, 81	147, 140
property, 81–84, 86	
Magnetoelastic energy, 3, 6, 9, 17, 77, 78,	Q
98, 203	Quenching, 2, 5, 25, 36, 38, 53, 72, 77, 78,
Magnetostatic properties, 93, 96	91–96, 98, 101, 104–107, 122, 132, 169,
Magnetostriction, 1–2, 4, 5, 13, 15, 20, 25,	174, 176, 184, 191, 202
26, 33, 38–41, 46, 78, 91, 93, 111, 132,	
140, 148, 154, 155, 169, 176, 182,	
184–187, 189, 197, 200, 202,	R
203, 205, 206	Rapid quenching, 2, 5, 25, 36, 92, 132,
Magnetostriction constant, 3–5, 7, 14,	184, 202
16, 26, 78, 81, 91–93, 104, 105, 124, 183, 190	Relaxation, 14, 17, 20, 26, 35, 36, 41, 49, 69, 94, 97, 142, 145,
Mechanical properties, 64–75, 85, 131, 159,	177–179, 183, 187, 188, 190,
182, 192, 206	191, 197, 202, 203
Melt	Residual quenching stress, 78, 91–96, 98, 101,
extraction, 53–57, 60–62, 71, 72, 85	104–107
spinning, 36–38, 56, 61	Resonance frequency, 35, 42, 43, 138, 139,
Melting, 2, 36, 55, 58	141, 143–145
Metallic core, 6, 132, 144, 159–161, 163, 165,	
176, 183, 186, 191, 196, 198, 199	
Metamaterials, 131, 146	S
Micromagnetic equilibrium	Saturation magnetization, 7, 20, 35, 39, 81, 82,
equation, 96, 97, 103	93, 95, 118, 152, 154, 160, 171, 183,
Microwire	185, 187–190, 192, 195, 202
glass shell, 94, 107 impedance, 104	Scanning electron microscopy (SEM), 37, 38, 55, 56, 71, 80, 156, 159, 160, 170, 184,
nucleus, 2–7, 93, 94, 104, 153, 184, 186,	193, 197
187, 192, 193, 195, 198, 202	Sensitivity, 66, 92, 104, 105, 111, 115, 128,
107, 172, 173, 173, 170, 202	147, 189, 192, 197, 199, 200, 203, 206
	Sensor, 1, 2, 33, 34, 44, 53, 86, 91, 92, 104,
N	105, 111, 112, 131, 132, 142–144, 148,
Nanocrystalline structure, 20, 21, 26, 28, 184,	151, 152, 155, 169, 174, 185, 191, 192,
187, 206	194, 196, 200, 205, 206
Nanocrystallization, 4, 20–26, 28, 29, 36, 37,	Sensor sensitivity, 111, 128
72, 184–186	Skin effect, 35, 40, 99, 112, 135, 138
Network analyzer, 39	Small angle magnetization rotation (SAMR),
Nucleus	39, 94
metallic, 2–7, 20, 25, 94, 96, 99, 100, 102,	Soft magnetic materials, 1, 33, 75, 111, 152
104, 116, 120, 122, 153, 161, 169, 175, 176, 184, 186, 187, 190–193, 195, 197,	magnets, 1–9, 11–18, 20, 21, 23–26, 28, 29,
198, 202	33–44, 46, 48, 49, 54, 75, 80, 81, 111,
Numerical simulation, 99, 105, 107	132, 141, 152, 155, 176, 184, 186, 196
, ,	

Specific absorption rate (SAR), 158, 159,	Titanium implant, 200, 201
161–165	Transmission, 37, 39, 72, 74, 146, 147, 163
Strain, 64, 66–72, 147, 148	
Stress	
applied, 8, 14, 16–19, 69, 119, 147,	U
187, 202	Unit magnetization vector, 78, 93, 95–97,
internal, 3, 5, 6, 8–10, 15–20, 24, 33, 111,	99–101, 103
112, 122, 161, 189, 193	
monitoring, 144, 148, 203, 204	
tensile, 8, 14, 40, 41, 66, 67, 69, 71–73,	V
78–80, 93, 95, 106, 112, 132, 140, 141,	Viscoelasticity, 94
144, 147, 199, 204, 205	
Superparamagnetism, 195, 199	
Switching field, 8, 170	W
	Wire
	amorphous, 2, 3, 60, 64, 71, 78–80, 85,
T	96–104, 106, 140, 141
Temperature, 4, 36, 58, 94, 112, 132, 152,	glass-coated, 1–29
169–206	magnetic, 1-4, 133-148
Tensor	melt extracted, 53-58, 60-67, 69-73, 75,
of GMI components, 98, 101, 105	77–86
of residual stress components, 104	nanocrystalline, 1-9, 11-18, 20, 21, 23-26,
Thermal conductivity, 75	28, 29, 85
Thermal expansion coefficient, 3, 6, 112, 122,	
161, 174, 176, 184, 187, 190–193, 202	
Thermal treatments, 40–41, 49, 174, 182, 196	X
Thermoelastic stress, 94	X-ray diffraction, 37, 72, 74